Development of a Numerical Strategy for 2nd Gradient Continuum Porous Media based on Iso-Geometric Finite Element. Application to Partially Saturated Media

Carlos Plúa

Communauté
UNIVERSITÉ Grenoble Alpes

THÈSE

Pour obtenir le grade de

DOCTEUR DE LA COMMUNAUTÉ UNIVERSITÉ GRENOBLE ALPES

préparée dans le cadre d'une cotutelle *entre la Communauté Université Grenoble Alpes* et les Universités degli Studi di Firenze, Perugia et Pisa

Spécialité : **Matériaux, Mécanique, Génie Civil, Electrochimie**

Arrêté ministériel : le 6 janvier 2005 – 25 mai 2016

Présentée par

Carlos PLÚA

Thèse dirigée par **Claudio Tamagnini** et codirigée par **Pierre BÉSUELLE**

préparée au sein des **Laboratoire Sols, Solides, Structures; Risques** et **Dipartimento di Ingegneria Civile e Ambientale** dans **l'École Doctorale IMEP2** et **Università delgi Studi di Perugia**

Développement d'une stratégie d'implémentation numérique pour milieu continu poreux de 2nd gradient basée sur les éléments finis isogéométriques, application à un milieu partiellement saturé

Thèse soutenue publiquement le **5 Mars 2018**,
devant le jury composé de :

Mr Panagiotis KOTRONIS
Professeur, École Centrale de Nantes, Président
Mr Frédéric COLLIN
Professeur, Université de Liège, Rapporteur
Mr Claudio di PRISCO
Professeur, Politecnico di Milano, Rapporteur
Mr Carlo CALLARI
Professeur, Università degli studi del Molise, Examinateur
Mr Denis CAILLERIE
Professeur émérite, Université Grenoble Alpes, Examinateur
Mr Massimiliano LUCCHESI
Professeur, Università degli studi di Firenze, Examinateur
Mr Claudio TAMAGNINI
Professeur, Università degli studi di Perugia, Directeur de thèse
Mr Pierre BÉSUELLE
CR HDR, CNRS UMR 5521, Co-Directeur de thèse

Dedicated to my grandmas Mariana and Blanca

Abstract

During the last decade, Isogeometric Analysis (IGA) has drawn the attention of the Finite Element community to its superior capabilities over the standard Finite Element Method (FEM). The IGA concept uses the same basis functions used in Computed Aided Design (CAD) for the approximation of the unknown fields such as displacements, pore pressure or temperature in the Finite Element solution of a (possibly coupled) thermo–hydro–mechanical problem. Among the most relevant features of IGA, its smoothness, its convergence rate and particularly its intrinsic higher–order continuity between elements represent a definite improvement over the standard FEM, which allow to obtain significant computational advantages in terms of accuracy of the solution and computational efficiency.

This work attempts to exploit the characteristics of IGA for the numerical solution of coupled hydro–mechanical (HM) problems in saturated and partially saturated second gradient poro–elastoplastic geomaterials. On one hand, the second gradient model belonging to the theory of continua with microstructure ensures the objectivity of the results in presence of strain localization phenomena in terms of mesh independence of the numerical solution, which cannot be achieved with classical constitutive models without an internal length scale. On the other hand, the C^1–continuity achievable by means of IGA basis functions allows a straightforward implementation of such higher order constitutive models, within a HM formulation derived from the classical mixture approach. In addition, the smoothness of the IGA basis functions proved to be very efficient in the modeling of coupled processes characterized by strong hydraulic gradients – such as the simulation of the downward propagation of a saturation front in a partially saturated slope subject to rainfall infiltration. Last but not least, it is worth noting that, as compared to the existing approaches based on Lagrange multipliers, the IGA approach to the solution of coupled hydro-mechanical (HM) problems in saturated and partially saturated second gradient materials allows a dramatic reduction in the number of degrees of freedoms required to achieve the same level of accuracy. This not only results in a significant increase of the computational efficiency, but also allows to extend the complete second gradient formulation to the analysis of realistic 3D problems, the solution of which has been presented in this work for the first time.

The local second gradient poro–elastoplastic formulation developed in this work is implemented in the research–oriented code GeoPDEs, a Matlab open source IGA–FEM code developed at the University of Pavia. Based on the results obtained in a large series of representative 2D and 3D initial–boundary value problems analyzed in this work, it can be concluded that the combination of IGA and the second gradient elastoplasticity represents a powerful tool for the numerical simulation of geotechnical problems characterized by strong multiphysics couplings, highly nonlinear behavior of the soil, and strongly localized displacement and pore pressure gradients.

Keywords: Isogeometric Analysis, second gradient continuum, poro–elastoplasticity, partially saturated soils, strain localization

Résumé

Au cours de la dernière décennie, la méthode d'analyse isogéométrique (AIG) a attiré l'attention des chercheurs grâce à ses capacités supérieures à la méthode standard des éléments finis (MEF). Le concept AIG utilise les mêmes fonctions de base que celles utilisées dans la conception assistée par ordinateur (CAO) pour l'approximation des champs inconnus tels que les déplacements, pression interstitielle ou la température dans la solution des éléments finis d'un problème thermo–hydro–mécanique (éventuellement couplé). Parmi les caractéristiques les plus importantes d'AIG, la régularité, le taux de convergence et surtout sa continuité intrinsèque d'ordre supérieur représentent une nette amélioration par rapport à la méthode standard des éléments finis, permettant d'obtenir des avantages computationnels significatifs en termes de précision de la solution et de efficacité.

Ce travail tente d'exploiter les caractéristiques d'AIG pour la résolution numérique des problèmes hydromécaniques (HM) couplés dans les géomatériaux de second gradient de type poro–élastoplastiques partiellement saturés. D'une part, le modèle second gradient appartenant à la théorie des milieux continus avec microstructure assure l'objectivité des résultats en présence de phénomènes de localisation de la déformation en termes d'indépendance de maillage de la solution numérique, ce qui ne peut être réalisé avec des modèles constitutifs classiques qui n'implique pas l'intervention d'une longueur interne. D'autre part, la continuité C^1 réalisable au moyen de fonctions de base AIG permet une implémentation directe de tels modèles constitutifs d'ordre supérieur, dans une formulation HM dérivée de l'approche de mélange classique. De plus, la régularité des fonctions de base AIG s'est révélée très efficace dans la modélisation de processus couplés caractérisés par de forts gradients hydrauliques – comme la simulation de la propagation d'un front de saturation dans une pente partiellement saturée. Dernier point, mais non des moindres, il convient de noter que, par rapport aux approches existantes basées sur les multiplicateurs de Lagrange, la méthode AIG pour résoudre les problèmes hydromécaniques (HM) couplés dans les matériaux du second gradient saturé et partiellement saturé permet une réduction considérable du nombre de degrés de libertés requis pour atteindre le même niveau de précision. Cela entraîne non seulement une augmentation significative de l'efficacité de calcul, mais permet également d'étendre la

formulation du second gradient à l'analyse de problèmes réalistes en 3D, dont la solution a été présentée pour la première fois dans ce travail.

La formulation poro–élastoplastique du second gradient développée dans ce travail est mise en œuvre dans le code orienté vers la recherche GeoPDEs, un code IAG–MEF open source écrit en Matlab et développé à l'Université de Pavia. Sur la base des résultats obtenus dans une large série de problèmes aux limites en 2D et 3D analysées dans ce travail, on peut conclure que la combinaison de AIG et d'élastoplasticité du second gradient représente un outil puissant pour la simulation numérique de problèmes géotechniques caractérisés par de forts couplages multiphysiques, un comportement fortement non linéaire du sol, et des gradients de déplacement et de pression interstitielle fortement localisés.

Mots clés: Analyse Isogéométrique, milieu continu du second gradient, matériau élasto–plastique poreux, sols partiellement saturés, localisation de la déformation

Acknowledgements

During these long journey, as any Ph.D student, I have been through tough times where I felt that I was making no progress or the outcomes of my work were not the ones I expected. In those moments, I always found my supervisors' support. Feeling that your supervisors trust you means a lot for a Ph.D student. I will keep with me during my Post–Ph.D life those moments of Claudio sitting down besides me writing down on a notebook with a pencil the different equations that we would need to extend our FE code no matter what time it took. And Pierre's meetings giving me a different perspective of how to understand the results that we got.

I would also like to express all my gratitude to Cino. He was the first person who relied on me and understood my passion for the Finite Element Method. Without him none of the great things that have happened to me along these four years and a half in Grenoble could have been possible.

My friends at 3SR lab have also contributed to make this journey unforgettable. Specially thanks to Ivan and Aina for teaching me how to ski, climb and share the wonderful experience of making the summit of Gran Paradiso.

Finally, to my family, for always taking care of me. Thanks to them I never felt alone no matter the distance we were apart.

Carlos Plúa
Grenoble, May 2018

Contents

List of Figures

List of Tables

List of Symbols

General notation

$(\cdot)^*$	Virtual quantity $(\cdot)$
$(\cdot)^e$, $(\cdot)^p$	Elastic and plastic components of quantity $(\cdot)$
$(\cdot)^t$	Current value of quantity $(\cdot)$ at a given time t
$(\cdot)^0$, $(\cdot)^1$	Quantity $(\cdot)$ outside and inside a shear band
$(\cdot)_0$	Initial value of quantity $(\cdot)$
$\Delta(\cdot)$	Increment of quantity $(\cdot)$
$\dot{(\cdot)}$	Time derivative of quantity $(\cdot)$

Operators

$(\cdot)^T$	Transpose of matrix $(\cdot)$
$(\cdot)^{-1}$	Inverse of matrix $(\cdot)$
$\det(\cdot)$	Determinant of matrix $(\cdot)$
$\frac{\mathrm{d}(\cdot)}{\mathrm{d}t}$	Material derivative of $(\cdot)$
$\nabla(\cdot) := \frac{\partial(\cdot)}{\partial x_i}$	Gradient operator
$\nabla\nabla(\cdot) := \frac{\partial^2(\cdot)}{\partial x_i x_j}$	Second gradient operator
$\nabla^2(\cdot) := \nabla \cdot \nabla(\cdot)$	Laplacean operator
$\nabla^s(\cdot)$	Symmetric gradient operator
$\|(\cdot)\|$	Euclidean norm
$\overset{s}{\nabla}(\cdot) := \nabla(\cdot) - D(\cdot) \otimes \boldsymbol{n}$	Tangential gradient operator

$\mathrm{sym}(\cdot)$	Symmetric part of matrix $(\cdot)$	
$\mathrm{tr}(\cdot)$	Trace of matrix $(\cdot)$	
$D(\cdot) := \frac{\partial(\cdot)}{\partial x_i} n_i$	Normal gradient operator	
$\boldsymbol{a} \cdot \boldsymbol{b} := a_i b_i$	Dot product of two vectors	
$\boldsymbol{A} \cdot \boldsymbol{B} := A_{ij} B_{ij}$	Contraction product of two tensors of 2nd order	
$\boldsymbol{\mathcal{A}} \cdot \boldsymbol{\mathcal{B}} := \mathcal{A}_{ijk} \mathcal{B}_{ijk}$	Inner product of two tensors of 3rd order	
$\boldsymbol{a} \otimes \boldsymbol{b} := a_i b_j$	Dyadic product of two vectors	
$\boldsymbol{a} \times \boldsymbol{b} := e_{ijk} a_j b_k$	Cross product of two vectors	

Roman letters

$\mathbf{1} := \delta_{ij}$	Identity tensor	
a_f, a_g	Milan model parameters	
a_{sw}	Van Genuchten parameter, inverse of air entry pressure	$[\mathrm{M}^{-1}\mathrm{LT}^2]$
$\mathcal{B}$	Porous material domain	$[\mathrm{L}^3]$
$\boldsymbol{b}$	Body force vector	$[\mathrm{LT}^{-2}]$
c	Nonlocal gradient parameter	$[\mathrm{L}^2]$
C_s	Specific moisture content	$[\mathrm{M}^{-1}\mathrm{LT}^2]$
cu	Undrained shear strength	$[\mathrm{ML}^{-1}\mathrm{T}^{-2}]$
C_w	Liquid compressibility coefficient	$[\mathrm{M}^{-1}\mathrm{LT}^2]$
$\boldsymbol{D}^e$, $\boldsymbol{D}$	Elastic and elastoplastic consistent tangent tensor	$[\mathrm{ML}^{-1}\mathrm{T}^{-2}]$
$\boldsymbol{D}^e_{sg}$	Second gradient elastic consistent tangent tensor	$[\mathrm{MLT}^{-2}]$
$\boldsymbol{D}_{sg}$	Second gradient elastoplastic consistent tangent tensor	$[\mathrm{MLT}^{-2}]$
D^{sg}	Second gradient elastic parameter	$[\mathrm{MLT}^{-2}]$
$\mathrm{d}v$	Material volume	$[\mathrm{L}^3]$
$\boldsymbol{e}$	Deviatoric strain	
e	Void ratio	
$E := \|\boldsymbol{e}\|$	Norm of deviatoric strain/ Young modulus	[–/ $\mathrm{ML}^{-1}\mathrm{T}^{-2}$]
e_{lim}	Prandtl–Reuss model parameter	

$\boldsymbol{F}$	(Macro) deformation gradient field	
$\boldsymbol{f}$	Microkinematic gradient field	
G, G_0, G_1	Shear modulus	$[\mathrm{ML}^{-1}\mathrm{T}^{-2}]$
G_2	Prandtl–Reuss model plastic parameter	$[\mathrm{ML}^{-1}\mathrm{T}^{-2}]$
G_r	Milan model parameter that controls the rate of change in p''_m	
$\boldsymbol{h} := \frac{\partial f_{ij}}{\partial x_k}$	Microkinematic second gradient field	$[\mathrm{L}^{-1}]$
H_ε	Prandtl–Reuss model parameter, plastic modulus	$[\mathrm{ML}^{-1}\mathrm{T}^{-2}]$
H_γ	Second gradient parameter, plastic modulus	$[\mathrm{MLT}^{-2}]$
K	Prandtl–Reuss model parameter, bulk modulus	$[\mathrm{ML}^{-1}\mathrm{T}^{-2}]$
k	Milan model parameter	
$\boldsymbol{k}_{sat}$	Permeability tensor in saturated conditions	$[\mathrm{L}^2]$
$\boldsymbol{k}_w$	Permeability of liquid phase	$[\mathrm{L}^2]$
k_w^{rel}	Relative permeability of liquid	
$\mathcal{L}(\cdot)$	Non–linear tensor value function	
$L_{k,p_\zeta}(\zeta)$	Univariate B–spline basis function of order p_ζ in the ζ–direction	
$\boldsymbol{M}$	Consistent tangent tensor of environmental variables	
m_f, m_g	Milan model parameters	
M_{fc}, M_{gc}	Milan model parameters	
M_{fe}, M_{ge}	Milan model parameters	
m_i	Multiplicity of knot i	
$M_{j,p_\eta}(\eta)$	Univariate B–spline basis function of order p_η in the η–direction	
m_{sw}	Van Genuchten parameter	
$\boldsymbol{m}_w$	Fluid mass flow	$[\mathrm{ML}^{-2}\mathrm{T}]$
M_w	Fluid mass inside unit volume $\mathrm{d}v$	$[\mathrm{ML}^{-3}]$
$\boldsymbol{n}$	Normal unit vector	
$\boldsymbol{n}^{(i)}$	ith unit eigenvector of elastic strain field $\boldsymbol{\varepsilon}^e$	

n	Porosity	
$N_{i,p_\xi}(\xi)$	Univariate B–spline basis function of order p_ξ in the ξ–direction	
n_{sw}	Van Genuchten parameter	
$\overline{\boldsymbol{P}}$	External double traction force	$[\mathrm{MT}^{-2}]$
$\overline{\boldsymbol{p}}$	External (classical) traction force per unit area	$[\mathrm{ML}^{-1}\mathrm{T}^{-2}]$
p	Polinomial oder of univariate and multivariate basis functions	
p''	Isotropic generalized stress invariant	$[\mathrm{ML}^{-1}\mathrm{T}^{-2}]$
p_g	Pore gas pressure	$[\mathrm{ML}^{-1}\mathrm{T}^{-2}]$
$\boldsymbol{P}_i$, $\boldsymbol{P}_{ij}$, $\boldsymbol{P}_{ijk}$	Control polygon, net and lattice	
p''_m	Internal variable of Milan model that accounts for the effects of interparticle bonding	$[\mathrm{ML}^{-1}\mathrm{T}^{-2}]$
p_{ref}	Milan model parameter, reference mean stress	$[\mathrm{ML}^{-1}\mathrm{T}^{-2}]$
p''_s	Internal variable of Milan model that plays the role of the preconsolidation pressure	$[\mathrm{ML}^{-1}\mathrm{T}^{-2}]$
p_w	Pore liquid pressure	$[\mathrm{ML}^{-1}\mathrm{T}^{-2}]$
p_ξ, p_η, p_ζ	Polynomial order of basis functions in ξ–, η–, ζ–directions	
$\boldsymbol{q}$	Internal variable vector	
q	Deviatoric stress invariant	$[\mathrm{ML}^{-1}\mathrm{T}^{-2}]$
$\overline{q}_w$	Prescribed fluid flow per unit area	$[\mathrm{ML}^{-2}\mathrm{T}]$
Q_w	Sink term of fluid mass	$[\mathrm{ML}^{-3}\mathrm{T}]$
$\boldsymbol{R}$	(Macro) rotation field	
$\boldsymbol{r}$	Microrotation field	
R^{sg}	Second gradient parameter, double yield stress	$[\mathrm{MT}^{-2}]$
R^{sg}_{max}	Second gradient parameter, maximum double yield stress	$[\mathrm{MT}^{-2}]$
$S := \|\boldsymbol{\sigma}_{\mathrm{dev}}\|$	Norm of deviatoric stress	$[\mathrm{ML}^{-1}\mathrm{T}^{-2}]$
$s := p_g - p_w$	Matric suction	$[\mathrm{ML}^{-1}\mathrm{T}^{-2}]$
S_e	Effective water degree of saturation	

S_g	Degree of saturation of gas phase	
S_{max}	Maximum water degree of saturation	
S_{res}	Residual water degree of saturation	
S_w	Degree of saturation of liquid phase	
S_y	Prandtl–Reuss model parameter, yield stress	$[\mathrm{ML}^{-1}\mathrm{T}^{-2}]$
$S_{y,min}$	Prandtl–Reuss model parameter, minimum yield stress	$[\mathrm{ML}^{-1}\mathrm{T}^{-2}]$
$\overline{\boldsymbol{T}}$	External double traction force per unit area	$[\mathrm{ML}^{-1}\mathrm{T}^{-2}]$
$\bar{\boldsymbol{t}}$	External traction force per unit area	$[\mathrm{ML}^{-1}\mathrm{T}^{-2}]$
$\boldsymbol{u}$	Displacement field	[L]
$\boldsymbol{v}^s$, $\boldsymbol{v}^w$ and $\boldsymbol{v}^g$	Velocity of the solid, liquid and gas phases	$[\mathrm{LT}^{-1}]$
v	Unit volume of porous material	$[\mathrm{L}^3]$
v_s, v_w, v_g	Volume fractions of the solid, liquid, and gas phases	$[\mathrm{L}^3]$
v_v	Volume fraction of void	$[\mathrm{L}^3]$
W_e^*, W_i^*	External virtual work and internal virtual work	$[\mathrm{ML}^2\mathrm{T}^{-2}]$
$\boldsymbol{w}^w$	Darcy velocity of the pore water	$[\mathrm{LT}^{-1}]$
$\boldsymbol{x} := \{x, y, z\}^T$	Physical coordinates	
l_D, l_H	Second gradient elastic parameters	[L]

Greek letters

α	Milan model elastic parameter	
$\boldsymbol{\alpha}$	Environmental process variable vector	
$\boldsymbol{\beta} := -\overset{s}{\nabla}\boldsymbol{n}$	Second fundamental form of the surface $\partial\mathcal{B}$	
χ	Bishop's effective stress parameter	
$\partial\mathcal{B}$	Porous material boundary	$[\mathrm{L}^2]$
$\partial\mathcal{B}_{q_w}$	Part of $\partial\mathcal{B}$ on which input water mass q_w is prescribed	$[\mathrm{L}^2]$
$\partial\mathcal{B}_\sigma$	Part of $\partial\mathcal{B}$ on which external traction forces $\bar{\boldsymbol{t}}$ and $\overline{\boldsymbol{T}}$ are applied	$[\mathrm{L}^2]$
$\partial\mathcal{B}_T$	Part of $\partial\mathcal{B}$ on which external double traction force $\bar{\boldsymbol{T}}$ is applied	$[\mathrm{L}^2]$

$\partial\mathcal{B}_t$	Part of $\partial\mathcal{B}$ on which external traction force $\bar{\boldsymbol{t}}$ is applied	$[\mathrm{L}^2]$
Δt, Δt_c	Time step size and critical time step size	$[\mathrm{T}]$
$\boldsymbol{\varepsilon}$	(Macro) strain field	
$\tilde{\varepsilon}$	Nonlocal strain invariant measure	
$\boldsymbol{\varepsilon}^m$	Microstrain field	
ε_s	Equivalent deviatoric strain	
ε_v	Volumetric strain	
$\boldsymbol{\eta}$	Unit deviatoric tensor normal to the yield surface	
$\boldsymbol{\gamma} := \nabla\nabla\boldsymbol{u}$	Second gradient of displacement field	$[\mathrm{L}^{-1}]$
$\hat{\kappa}$	Milan model elastic parameter	
κ	Internal variable	
λ	Arc–length parameter	
$\boldsymbol{\lambda}$	Lagrange multiplier field	$[\mathrm{ML}^{-1}\mathrm{T}^{-2}]$
$\dot{\lambda}_\gamma$	Second gradient plastic consistency parameter	
$\dot{\lambda}_\varepsilon$	Plastic consistency parameter	
μ_w	Dynamic viscosity of the liquid	$[\mathrm{ML}^{-1}\mathrm{T}^{-1}]$
ν	Poisson's ratio	
ψ	Nonlocal spatial averaging weight function	
ρ	Average mass density of the porous material	$[\mathrm{ML}^{-3}]$
ρ_m	Milan model hardening parameter related to the internal variable p''_m	
ρ_s	Mass density of solid phase/Milan model hardening parameter related to the internal variable p''_s	$[\mathrm{ML}^{-3}$ /–
ρ_w, ρ_g	Mass density of liquid and gas phases	$[\mathrm{ML}^{-3}]$
$\boldsymbol{\Sigma}$	Double stress	$[\mathrm{MT}^{-2}]$
$\boldsymbol{\sigma}$, $\boldsymbol{\sigma}'$, $\boldsymbol{\sigma}''$	Cauchy total stress, Terzaghi's efective stress and generalized efective stress	$[\mathrm{ML}^{-1}\mathrm{T}^{-2}]$
$\boldsymbol{\varsigma}$	Velocity gradient field of a shear band	$[\mathrm{T}^{-1}]$

$\boldsymbol{\sigma}_{\text{dev}} := \frac{\boldsymbol{\sigma}_{\text{dev}}}{S}$	Deviatoric stress	$[\text{ML}^{-1}\text{T}^{-2}]$
$\boldsymbol{\tau}$	Microstructure stress field (microstress)	$[\text{ML}^{-1}\text{T}^{-2}]$
θ	Lode's angle	[rad]
$\boldsymbol{\xi} := \{\xi, \eta, \zeta\}^T$	Parametric coordinates	
$\tilde{\boldsymbol{\xi}} := \left\{\tilde{\xi}, \tilde{\eta}, \tilde{\zeta}\right\}^T$	Parent coordinates	
ξ_m	Milan model hardening parameter related to the internal variable p''_m	
ξ_s	Milan model hardening parameter related to the internal variable p''_s	
$\Xi_\xi, \Xi_\eta, \Xi_\zeta$	Knot vectors in ξ–, η–, ζ–directions	

Part I

Introduction and motivations

Chapter 1

Introduction

The description of the behavior of partially saturated (also called unsaturated) porous media such as soils and rocks in geomechanics is of primary importance when modeling natural slopes subjected to environmental changes, stability of excavations, bearing capacity for shallow foundations and so on. Since a partially saturated medium is composed of different phases such as solid, fluid and gas, nonlinear behaviors and coupling effects of different physical processes (*e.g.* solid phase influences the fluid phase due to changes of hydraulic properties such as porosity, permeability, and water storage capacity) have to be taken into account for numerical modeling in order to obtain realistic results. In this regard, the degree of saturation plays a key role since it strongly affects the mechanical response of the medium. A typical example is the wetting process due to rainfall infiltration into an initially partially saturated slope leading to failure (collapse of the slope) as a consequence of a reduction of the soil strength.

Finite element method (FEM) has been successfully applied to model engineering problems involving partially saturated media and has received wide acceptance. However, FEM does not properly reproduce the failure mechanism when modeling strain softening materials as it generally happens in geomaterials. In these cases, the failure mechanism consists of a clearly defined localized zones characterized by narrow bands of high strains; this phenomenon is called strain localization. If the FEM is not enhanced with a regularization technique, the numerical solutions show spurious mesh dependency with

vanishing width of shear bands and no convergence of the global response of the problem is achieved.

The use of second gradient models is one of these regularization techniques that has proven to be efficient in modeling strain localization by introducing an implicit internal length scale. On the one hand, it has the advantage that any classical constitutive model can be extended to a second gradient model in a straightforward manner. But on the other hand, the second gradient finite elements require square–integrability of generalized second derivatives and so C^1–continuous elements need to be used; a property that classical finite elements using Lagrange polynomials do not have. As a consequence, the alternatives adopted to circumvent the need for C^1–continuous elements imply the use of mixed elements and Lagrange multipliers leading to expensive numerical computations. For this reason, elements with intrinsic C^1–continuous are more convenient in terms of numerical implementation and computer time.

Isogeometric Analysis (IGA) consisting in the use of basis functions with high degree of inter–element continuity for the geometry and the approximation of the physical fields seems a promising alternative. IGA has become popular not only for its good control of continuity, but also for its other properties such as exact geometry representation, smoothness, and superior accuracy to traditional finite element analysis. The main difference between IGA and standard FEM is the application of B–splines (or Non-uniform rational B–splines, T–splines, etc.) as basis functions.

The main objective of this research is to develop a second gradient model for partially saturated porous media that is able to deal not only with the physical coupling between the different phases but also with the strain localization. To this end, the second gradient formulation will be implemented in the research–oriented code GeoPDEs, a Matlab open source code developed at the University of Pavia that uses IGA functions for the solution of partial differential equations. The second gradient model adopted is based on two independent plastic mechanisms. The classical constitutive model describing the first gradient (standard) part is a three-invariant isotropic–hardening elastoplastic model for bonded soils and a hardening rule accounting for the effect of changes in the degree of saturation on the plastic yield function. The second gradient part will be described by a simple elastoplastic model.

This thesis is arranged into four parts:

- Part I. Following this introduction, chapter 2 is devoted to a review of the experimental observations of strain localization, giving special attention in recent field measurement techniques like x–ray computed tomography and digital image correlation. Then, the bifurcation theory is presented as a theoretical background for the onset of strain localization. Chapter 3 introduces the concept of *objectivity* and summarizes the different regularization techniques found in literature that model strain localization ensuring objective results. Chapter 4 focuses on the second gradient model, a regularization technique based on a special case of micromorphic materials and chapter 5 provides the main features of Isogeometric analysis and discusses the particularities and differences to traditional FE analysis.

- Part II. Chapter 6 develops the balance equations needed for the description of the behavior of partially saturated porous media. Chapter 7 presents the mechanical and hydraulic constitutive laws required for the full description of the balance equations in chapter 6. Chapter 8 contains the numerical implementation of the governing equations based on chapters 6 and 7. Chapter 9 presents the numerical integration of the mechanical constitutive equations (in rate form) for the first and second gradient parts, presented in chapter 7, via an implicit return mapping scheme.

- Part III. Chapter 10 presents five benchmark problems in order to validate the IGA–FEM code for monophasic and biphasic media, the latter, under fully and partially saturated conditions. Chapter 11 studies the effects of the 2nd gradient model on biaxial compression test problem, in particular, the evolution of the shear band width. Chapter 12 studies the failure mechanisms of two geotechnical problems involving only the solid phase. And Chapter 13 presents two geotechnical problems on multiphase media: a strip footing problem of a calcarenite layer under fully saturated conditions, and a partially saturated slope stability problem under rainfall conditions in which the classical constitutive tensor is influenced by suction effects.

- Part IV. Chapter 14 concludes this work with a summary of the main results and the main contributions; future lines of research are outlined in order to enhanced the capabilities of the IGA–FEM tool.

Chapter 2

Strain localization in geomaterials

Failure of geotechnical structures (retaining walls, dams, foundations, embankments, slopes etc.) are generally associated to a localized deformation field that is characterized by one or several narrow zones of high strains. In geomaterials, this translates into concentration or coalescence of cracks, slip lines, shear bands or rupture zones followed by a rapid loss of the overall strength. This phenomenon is generally called *strain localization* and it is of a primary importance to take it into account when modeling geotechnical problems.

In order to properly characterize the mechanisms of strain localization and develop a mathematical model, numerous experimental studies performed on geomaterials have been devoted to this phenomenon during the last years. This chapter first addresses the experimental observations of shear band localization. And then, the bifurcation theory is presented as a theoretical background which specifies the condition for triggering and forming shear band localization in a material.

2.1 Experimental evidence

Strain field measurements are needed to characterized the onset and development of strain localization. To this end, the first studies mainly focused on the pure mechanical problem (dry or globally drained conditions at low strain rate) or the hydromechanical

problem (undrained or globally drained at fast strain rate), especially for sand specimens [*i.e.* 52, 56, 64, 78, 178]. They showed that strain localization is affected by various factors, such as porosity, confining pressure, size and shape of both grains and specimens and anisotropy of the granular deposit. It was also shown that the severe shearing in regions of localized deformation may be accompanied by dilation (inelastic volume increase) and/or comtraction (inelastic volume decrease), under either drained or undrained conditions.

Biaxial tests on sands revealed that the localization process starts to develop before or/at the peak stress of the global response [52, 55, 56]. These studies among others were carried out by techniques like acoustic emissions, false relief stereophotogrammetry, grid points on the specimen membrane, photographically tacking individual grain motion, etc. during the 70s until the 90s. However, these techniques have become obsolete since they are not sufficient to detect the start of the localization when the size of the microcracks are too small to be observed or are not superficial. More recent high resolution techniques such as X–ray computed tomography, neutron tomography, ultrasonic tomography, digital image correlation, etc. have been capable of capturing the developing mechanisms at the grain–scale. Good evidence of this can be found in the works of Andò [4] and Lanatà [104], in which the combination of X–ray computed tomography with digital image correlation has been effective to show pre–peak deformation patterns in soils and rocks.

In the following, a short overview of three techniques used in the field of experimental geomechanics during the last forty years are presented along with some illustrative results of the transition from diffuse to localized deformation in soils.

2.1.1 False relief stereophotogrammetry

In the early 70s, false relief stereophotogrammetry (FRS) was used by Butterfield et al. [31], based on the use of successive pairs of photographs of a deformable object taken from a fixed viewpoint. The photographs correspond to different deformation states of an object and they record the local displacement of some points on the specimen surface perpendicular to the shooting direction. In order to reduce measurement errors,

the samples have to be tested under plane strain conditions which makes the method limited to two–dimensional problems.

Desrues [52] performed a drained biaxial test on a Hostun RF sand specimen and took several photographs during the specimen shortening. These photographs were analyzed by the FRS. Results are presented in Fig. 2.1. After having a reasonably homogeneous loading during the firsts steps, it can be seen that the initiation of localization takes place between steps 3 and 4 (just before the peak load).

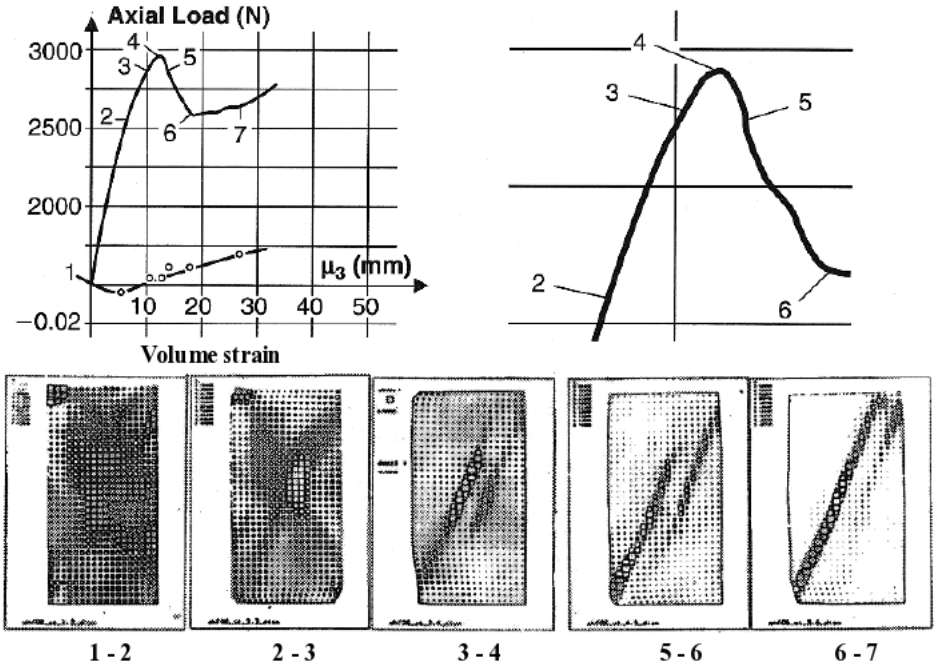

Figure 2.1: Strain localization in a drained test on Hostun RF sand [52].

The low spatial resolution of FRS made way for high spatial resolution techniques such as digital image correlation capable of performing deformation analysis at the grain–scale.

2.1.2 X–ray Computed Tomography

X-ray computed tomography (X–ray CT) was developed by Hounsfield [88] in the field of medicine. Transmission radiographs taken while rotating an object allows three–dimensional fields of attenuation to be reconstructed inside the scanned domain. This technique derives quantitative measurements of local density through correlation with

measured radiation attenuations [*e.g.* 54]. It is especially effective at delineating subtle material density variations, such as the lower density of sand within a shear band, and thus enables precise quantifications of shear band patterning, inclination and thickness.

During the last years, the technique of micro–computed tomography (μ–CT), including micro–focus X–ray CT, and micro–CT with synchrotron radiation has enabled precise detection of individual sand grains, providing detailed particle position as well as contact maps and calculation of void ratios [*e.g.* 79, 82, 83, 127, 166].

In general the CT method does not yield kinematic data such as strain increments. This is why the combination of X–ray CT with full field measurement methods, such as digital image correlation, is a much more powerful tool for the quantification of the displacement field, and not only the mass density change (volume strain field).

2.1.3 Digital Image Correlation

Digital image correlation (DIC) technique was originally proposed at the University of South Carolina [41, 135] to obtain the full–field surface displacements in materials under deformation by comparing the digital images of the specimen surface in the reference and the deformed states. A field can be a plane 2D field, a 3D surface field or a volume (3D) field. Once DIC provides a displacement field measurement between two images of a specimen, the strain tensor field can be deduced from the displacement vector field using spatial derivation methods for a discrete field.

Applications of three–dimensional DIC can be found in soft rocks and sand during triaxial compression tests using CT images [77, 106, 183] in which internal full–field deformations are provided by tracking the movement of the volume unit; the method is referred to as volumetric DIC.

An illustrative example of this last technique is given by Andò [4], where a triaxial compression test was performed on the Caicos ooid sand. Fig. 2.2 shows the stress–strain response and the global volume curve measured for the test. X–ray CT provided the images that were used to measure the kinematic field with the volumetric DIC. Fig. 2.3 shows the strain field transition from an initial homogenous strain field to a localized regime with an active shear band.

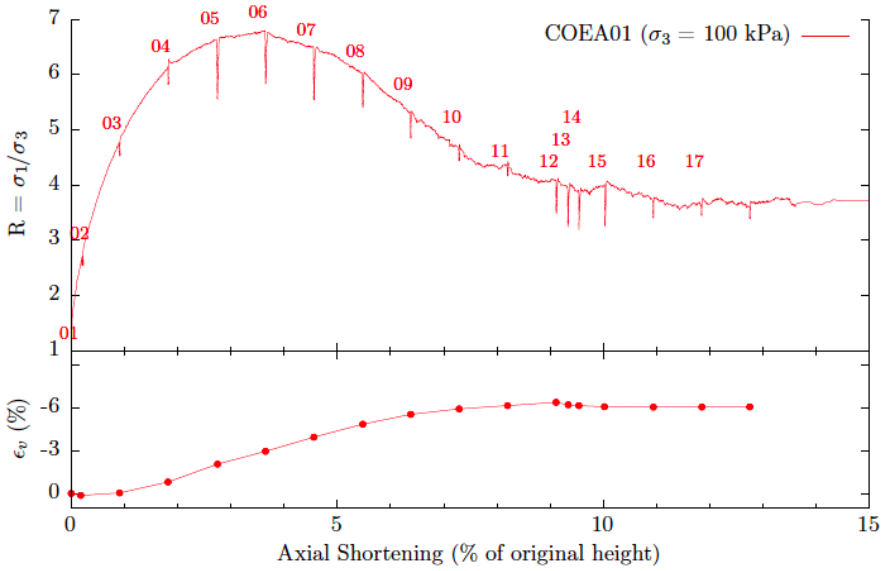

Figure 2.2: Stress strain response; the numbers noted on curve are the X–ray CT scan numbers [4].

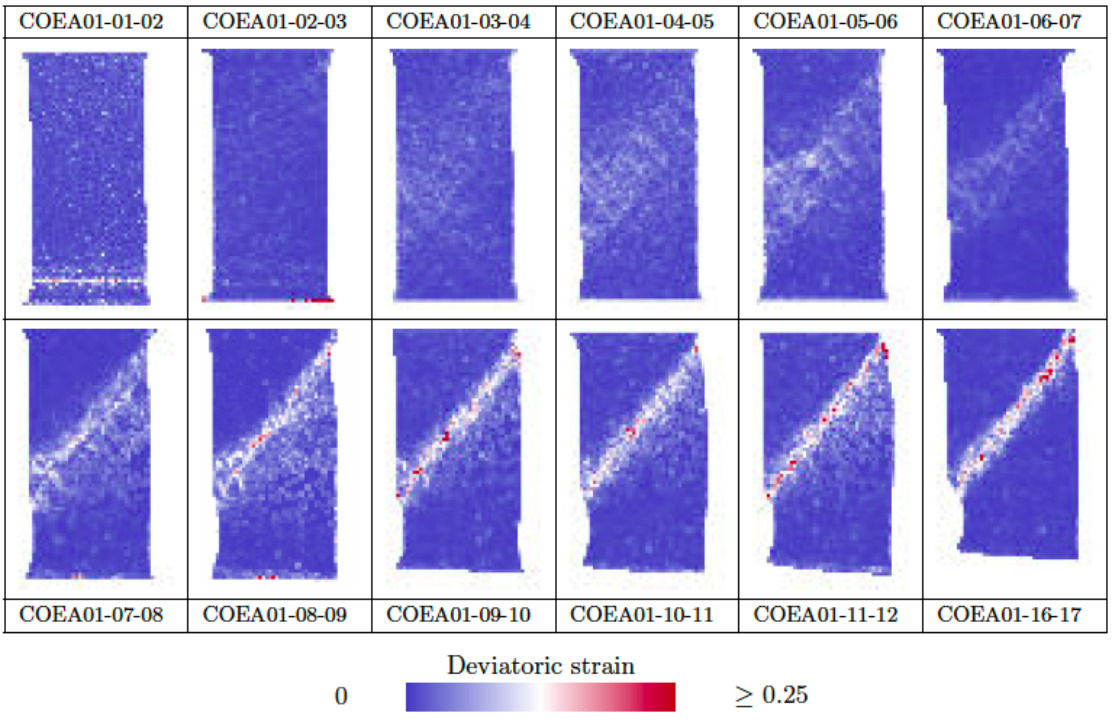

Figure 2.3: Slice of the strain field, measured by a continuous volumetric DIC [4].

These advances have also allowed to study the strain localization behavior in partially saturated soils. Higo et al. [84] performed a triaxial test on a partially saturated sand specimen showing very thin localized shear deformation before shear bands become visible in the macroscopic observations by using microfocus X–ray CT and DIC.

2.2 Theoretical framework: the onset of strain localization

The onset conditions for strain localization can be described by the bifurcation theory as a non uniqueness condition [144]. This approach have been particularized for soils by many authors [*e.g.* 145, 177], then for soft rocks by Bésuelle [18], Sulem et al. [165], Vardoulakis [176], non–associative laws [22, 23] and hypoplastic laws [34, 53, 102, 170]. The conditions for the emergence of localization are thus established by seeking the possible critical conditions for which an alternative solution, corresponding to localized deformation in planar band, is possible. If so, then the solution is not unique and the occurrence of localization is connected with loss of uniqueness [21].

Here we summarize the basis of the ideas proposed by Rice [144]. The development of a shear band bifurcation in a initially homogeneous deforming body, submitted to a load rate, is completely defined in terms of the following kinematic condition.

2.2.0.1 Kinematical condition

Denoting the indexes 1 and 0 for the quantities inside and outside the shear band, a solution involving the existence of a shear band is given by:

$$\nabla \dot{\boldsymbol{u}}^1 = \nabla \dot{\boldsymbol{u}}^0 + \boldsymbol{\varsigma} \otimes \boldsymbol{n} \tag{2.1}$$

where $\nabla \dot{\boldsymbol{u}}$ is the spatial velocity gradient and $\boldsymbol{n}$ is the normal vector to the shear band and $\boldsymbol{\varsigma}$ is the velocity gradient in the direction $\boldsymbol{n}$.

2.2.0.2 Static condition

Let $\dot{\boldsymbol{\sigma}}^1$ and $\dot{\boldsymbol{\sigma}}^0$ be the Cauchy stress rates inside and outside the shear band, respectively. Along the boundaries of the band, equilibrium equations in rate form can be written as:

$$\dot{\boldsymbol{\sigma}}^1 \boldsymbol{n} = \dot{\boldsymbol{\sigma}}^0 \boldsymbol{n} \tag{2.2}$$

2.2.0.3 Bifurcation condition

Under rather general assumptions, the constitutive equation can be written in the following general form

$$\dot{\boldsymbol{\sigma}} = \mathcal{L}\left(\nabla \dot{\boldsymbol{u}}\right) \tag{2.3}$$

where $\dot{\boldsymbol{\sigma}}$ is the stress rate and $\mathcal{L}(\cdot)$ is a non–linear tensor value function depending on the state of the material and of the velocity gradient.

Hence, using the kinematical condition, eq. (2.1), the static condition, eq. (2.2) and the constitutive equation, eq. (2.3), the shear band bifurcation is possible if there exists some unit normal vector $\boldsymbol{n}$ and a vector $\boldsymbol{\varsigma} \neq \boldsymbol{0}$ such that

$$\left(\mathcal{L}\left(\nabla \dot{\boldsymbol{u}}^0 + \boldsymbol{\varsigma} \otimes \boldsymbol{n}\right) - \mathcal{L}\left(\nabla \dot{\boldsymbol{u}}^0\right)\right) \boldsymbol{n} = \boldsymbol{0} \tag{2.4}$$

If we particularize eq. (2.3) for the linear case, we define the fourth–rank tensor $\boldsymbol{D}$ such that

$$\dot{\boldsymbol{\sigma}} = \boldsymbol{D} \nabla \dot{\boldsymbol{u}} \tag{2.5}$$

then, the bifurcation condition reads

$$\left(\boldsymbol{D}\left(\boldsymbol{\varsigma} \otimes \boldsymbol{n}\right)\right) \boldsymbol{n} = \boldsymbol{0} \tag{2.6}$$

eq. (2.6) has to be satisfied for $\boldsymbol{\varsigma} \neq \boldsymbol{0}$. Hence, the acoustic tensor, defined as $\boldsymbol{nDn}$, has a zero determinant:

$$\det\left(\boldsymbol{nDn}\right) = 0 \tag{2.7}$$

which is usually called the bifurcation criterion or localization condition [144]. The zero determinant of the acoustic tensor by eq. (2.7) corresponds to a change in the type of partial differential governing equations from elliptic to hyperbolic [86].

Chapter 3

Objective modeling of strain localization: regularization techniques

In the previous chapter, a review of different imaging techniques used during experimental tests has proved their usefulness for the characterization localized failure process of geomaterials. Above all, high resolution techniques have shown that triggering and forming shear band localization in a material are linked to the micro–scale mechanisms such as development of defects and imperfections like pre-existing micro–cracks. Hence, the development of constitutive models can not neglect the influence of such micro–mechanisms.

Classical constitutive models are able to reproduce qualitatively shear bands. However, numerical modeling of shear bands also implies practical aspects such as the definition of the shear band thickness and orientation, and since they do not account for the deformation mechanisms at the micro–scale these models suffer from a pathological problem of *mesh dependency* or *lack of objectivity* when making use of finite element solutions. This means that the thickness of the shear band will concentrate in a narrow band zone which corresponds to the element size of the mesh used to approximate the geometry of the problem [see *e.g.* 13]. As a consequence, the global response of the studied problem may be affected leading to non–objective results since no convergence will be achieved.

To overcome the aforementioned difficulties, various techniques have been developed to ensure objective description of strain localization. This chapter looks at six of these regularization techniques; special emphasis is made on the third group in which a subclass model is chosen in this thesis. The first four techniques introduce an explicit or an implicit internal length scale at the level of the constitutive model. On the other hand, the last two ones avoid the need to introduce an internal length scale by enriching the finite element formulation, and treat the localization zone as a zero–thickness localization band. These two techniques model the band with either a jump in the strain field, a *weak discontinuity*, or in the displacement field, a *strong discontinuity*, and are mainly used into the field of fracture mechanics.

3.1 Nonlocal integral theory

The nonlocal theory was originally proposed by Pijaudier-Cabot and Bažant [137]. It has been applied to concrete [14] and to soils [30] regularizing boundary value solutions when strain localization takes place in the form of shear zones and cracks. The nonlocal integral theory consists in that the response of the material is determined not only by the state at the point under consideration but also by the state of its neighboring points. And it is done by using a weighted spatial averaging function of a suitable state variable; this averaging function contains the internal length which regularizes the numerical solution.

Following De Borst et al. [50], the yield condition with isotropic hardening, for the sake of simplicity, can be written as follows:

$$f(\tilde{\varepsilon}, \kappa) = \tilde{\varepsilon} - \kappa \tag{3.1}$$

where the nonlocal strain invariant measure $\tilde{\varepsilon}$ replaces the equivalent deviatoric strain ε_s and κ is an internal variable. The nonlocal strain $\tilde{\varepsilon}$ is spatially averaged in the following form

$$\tilde{\varepsilon}(\boldsymbol{x}) = \frac{1}{\Psi(\boldsymbol{x})} \int_{\mathcal{B}} \psi(\boldsymbol{y}, \boldsymbol{x}) \varepsilon_s(\boldsymbol{y}) \, \mathrm{d}v \qquad \Psi(\boldsymbol{x}) = \int_{\mathcal{B}} \psi(\boldsymbol{y}, \boldsymbol{x}) \, \mathrm{d}v \tag{3.2}$$

where $\psi(\boldsymbol{y}, \boldsymbol{x})$ is a given nonlocal weight function which is usually assumed to be homogeneous and isotropic, so that it only depends on the norm $s = ||\boldsymbol{x} - \boldsymbol{y}||$. Other

alternatives may consider that the internal variable κ is treated as a nonlocal function instead of ε_s in eq. (3.1).

Due to the nonlocal character of the constitutive relation, the band width of the tangential stiffness is much larger than in standard FEM, since a higher number of nodes are connected to each other De Borst et al. [50]. Secondly, symmetry can be lost [138].

Few works on applications to multiphase porous media using nonlocal integral theory can be found in the literature, one of them is the work of Lazari [105] that combines nonlocal integral theory with a viscoplastic approach in partially saturated soils.

3.2 Gradient plasticity models

The gradient–dependent plasticity theory that evolved from the original ideas of Aifantis [1] is considered as the differential counterpart of the nonlocal integral theory [94]. The constitutive model takes into account the microstructure by incorporating the influence of gradients (of the first or higher order) of internal variables.

If we consider the expansion of ε_s and truncate after the second–oder terms, under the assumption of isotropy, the following relation ensues:

$$\tilde{\varepsilon} = \varepsilon_s + c\nabla^2\varepsilon_s \tag{3.3}$$

where c is a gradient parameter of dimension $\left[L^2\right]$.

Eq. (3.3), known as the explicit gradient model, requires the use of C^2–continuous finite elements due to the presence of second derivatives of the strain tensor, which involves first order derivatives of the displacements [50]. For this reason, new developments indicate that this can be overcome by implicit gradient models. Such formulations, first proposed for gradient damage [133], have been also adapted for gradient plasticity [60]. The implicit gradient model has a similar structure to the explicit nonlocal model, but the nonlocal equivalent strain $\tilde{\varepsilon}$ is defined as the solution of the Helmholtz differential equation:

$$\tilde{\varepsilon} - c\nabla^2\tilde{\varepsilon} = \varepsilon_s \tag{3.4}$$

which becomes formally identical to a fully nonlocal integral theory for a specific choice of the weight function ψ.

In the framework of multiphase porous media, gradient plasticity models have been used for example in Zhang and Schrefler [189] to analyze dynamic instabilities in fully and partially saturated granular material, and in Stankiewicz [164], who enhanced the Cam–clay model by introducing suitable higher–order deformation gradients.

3.3 Continua with microstructure

Continua with microstructure, also called micromorphic media, descend from the works of Germain [72, 73], Mindlin [118, 119], Toupin [172]. They use an enriched kinematic description of the continuum, with respect to classical continua, in order to incorporate a characteristic length. In addition to the displacement field, $\boldsymbol{u}$, a second–order tensor, the microkinematic gradient $\boldsymbol{f}$, is introduced to describe the strains and the rotation of the grains themselves.

Within the theories with micromorphic media, the displacement gradient, $\boldsymbol{F} = \nabla \boldsymbol{u}$, is referred to as the (macro) deformation gradient. The (macro) strain and the (macro) rotation are defined as

$$\boldsymbol{\varepsilon} = \frac{1}{2}\left(\boldsymbol{F} + \boldsymbol{F}^T\right), \qquad \boldsymbol{R} = \frac{1}{2}\left(\boldsymbol{F} - \boldsymbol{F}^T\right) \tag{3.5}$$

The microkinematic gradient $\boldsymbol{f}$ is an additional field, independent of the deformation gradient, which can be decomposed as follows

$$\boldsymbol{f} = \boldsymbol{\varepsilon}^m + \boldsymbol{r} \tag{3.6}$$

where $\boldsymbol{\varepsilon}^m$ is the microstrain and $\boldsymbol{r}$ is the microrotation:

$$\boldsymbol{\varepsilon}^m = \frac{1}{2}\left(\boldsymbol{f} + \boldsymbol{f}^T\right), \qquad \boldsymbol{r} = \frac{1}{2}\left(\boldsymbol{f} - \boldsymbol{f}^T\right) \tag{3.7}$$

The internal virtual work, consistent to the classical models, is considered as a linear form with respect to the virtual macro strain $\boldsymbol{\varepsilon}^*$, the virtual macro deformation gradient $\boldsymbol{F}^*$

(both tensors depending on a virtual displacement field $\boldsymbol{u}^*$), the virtual microkinematic gradient $\boldsymbol{f}^*$, and its gradient, denoted $\boldsymbol{h}^* := \nabla \boldsymbol{f}^*$ in the following. Thus, internal virtual work W_i^* for any kinematically admissible fields ($\boldsymbol{u}^*$, $\boldsymbol{f}^*$) is given by:

$$W_i^* = \int_{\mathcal{B}} \{\boldsymbol{\sigma} \cdot \boldsymbol{\varepsilon}^* + \boldsymbol{\tau} \cdot (\boldsymbol{f}^* - \boldsymbol{F}^*) + \boldsymbol{\Sigma} \cdot \boldsymbol{h}^*\} \, \mathrm{d}v \tag{3.8}$$

where $\boldsymbol{\sigma}$ is the Cauchy stress, $\boldsymbol{\tau}$ is a second–order stress tensor associated to the microstructure, also called the microstress, and $\boldsymbol{\Sigma}$, the double stress, which is related to $\boldsymbol{h}$.

The external virtual work W_e^* can be defined as follows (only classical body forces, $\boldsymbol{b}$, are assumed):

$$W_e^* = \int_{\mathcal{B}} \rho \boldsymbol{b} \cdot \boldsymbol{u}^* \, \mathrm{d}v + \int_{\partial \mathcal{B}_\sigma} \left(\overline{\boldsymbol{p}} \cdot \boldsymbol{u}^* + \overline{\boldsymbol{P}} \cdot \boldsymbol{f}^*\right) \mathrm{d}a \tag{3.9}$$

where $\overline{\boldsymbol{p}}$ is the external (classical) traction force per unit area and $\overline{\boldsymbol{P}}$ is an additional external (double) traction force, applied on $\partial \mathcal{B}_t$ and $\partial \mathcal{B}_T$, respectively. $\partial \mathcal{B}_t$ and $\partial \mathcal{B}_T$ are parts of the boundary of $\mathcal{B}$, which can be regrouped in $\partial \mathcal{B}_\sigma$. The additional boundary condition (on $\partial \mathcal{B}_T$) allows to produce solutions with boundary layers.

The variational formulation is obtained by equating the internal virtual work eq. (3.8) and the external virtual work eq. (3.9).

A large set of models can be derived by introducing some mathematical constraints on the microkinematic field [see 36]. We report two of these simplified models. First, the Cosserat model, that can be seen as a micromorphic media for which the microstrain $\boldsymbol{\varepsilon}^m$ vanishes. And then, the (local) second gradient model which assumes that the microkinematic gradient $\boldsymbol{f}$ is equal to the deformation gradient $\boldsymbol{F}$.

3.3.1 Cosserat models

Following Germain [72] or Mühlhaus and Vardoulakis [122], Cosserat theory can be seen as simplifications of the theory of micromorphic media. If the internal virtual work eq. (3.8) is written in its equivalent form:

$$W_i^* = \int_{\mathcal{B}} \{\boldsymbol{\alpha} \cdot \boldsymbol{\varepsilon}^* + \boldsymbol{\tau} \cdot (\boldsymbol{f}^* - \boldsymbol{R}^*) + \boldsymbol{\Sigma} \cdot \boldsymbol{h}^*\} \, \mathrm{d}v \tag{3.10}$$

with $\boldsymbol{\alpha} := \boldsymbol{\sigma} - \boldsymbol{\tau}$. Then, the Cosserat theory assumes that the microstrain $\boldsymbol{\varepsilon}^m$ vanishes. This means that $\boldsymbol{f} = \boldsymbol{r}$ and that $\boldsymbol{h}$ has then only nine independent components because it is antisymmetric with respect to its first two indices. Eq. (3.10) now reads

$$W_i^* = \int_{\mathcal{B}} \{\boldsymbol{\alpha} \cdot \boldsymbol{\varepsilon}^* + \boldsymbol{\tau} \cdot (\boldsymbol{r}^* - \boldsymbol{R}^*) + \boldsymbol{\Sigma} \cdot \boldsymbol{h}^*\} \, \mathrm{d}v \tag{3.11}$$

The assumption of microrotation equal to macro rotation is usually only effective on granular materials with rigid grains as it is indicated by Calvetti et al. [33] and Matsushima et al. [116].

Applications of the Cosserat theory can be found in papers by Mühlhaus and Vardoulakis [122] and Vardoulakis and Sulem [178]; and Ehlers and Volk [59] in the framework of multiphase porous media.

3.3.2 Second gradient models

The works of Chambon et al. [35], its extension to two–dimensional problems [115], Shu et al. [155] and Fleck and Hutchinson [65] belong to this subclass of models. The main assumption in second gradient models is that the microkinematic gradient is equal to the deformation gradient.

$$\boldsymbol{f} = \boldsymbol{F} \tag{3.12}$$

and consequently

$$\boldsymbol{f}^* = \boldsymbol{F}^* \tag{3.13}$$

having this in mind in eq. (3.8), the virtual work for every kinematic admissible field $\boldsymbol{u}^*$ reads:

$$\int_{\mathcal{B}} (\boldsymbol{\sigma} \cdot \boldsymbol{\varepsilon}^* + \boldsymbol{\Sigma} \cdot \nabla\nabla \boldsymbol{u}^*) \, \mathrm{d}v = \int_{\mathcal{B}} \rho \boldsymbol{b} \cdot \boldsymbol{u}^* \, \mathrm{d}v + \int_{\partial \mathcal{B}_\sigma} \left(\overline{\boldsymbol{p}} \cdot \boldsymbol{u}^* + \overline{\boldsymbol{P}} \cdot \nabla \boldsymbol{u}^*\right) \, \mathrm{d}a \tag{3.14}$$

Several works during the last fifteen years have proved that second gradient model is a competitive alternative to not only model strain localization in monophasic media [*e.g.* 19, 38, 115] but also in multiphasic media [*e.g.* 44, 132]. This model will be further explained in chapter 4.

3.4 Rate dependent models

The adoption of rate dependent models by replacing the plasticity with viscoplasticity and by using the time dependent viscosity parameter has proven to be efficient when dealing with strain localization in rate–dependent problems [110, 123, 140, 162, 185].

Needleman [123] showed in a one–dimensional case study that viscoplastic regularization can remove the pathological mesh dependency associated to strain localization. The mentioned work demonstrated that viscoplastic regularization implicitly introduces a length scale into the constitutive model for slightly rate–dependent solids under both quasi–static and dynamic loading conditions. However some numerical instabilities exist when the rate–independent limit is approached. These instabilities reflect the actual tendency for shear bands to be as narrow as possible. Díez et al. [57] found similar results concluding that when the load velocity decreases the viscoplastic solution tends to the elastoplastic one, which means that the viscoplastic regularization vanishes for rate–independent problems. Therefore, the band width is not determined exclusively by the material parameters but it mostly depends on the load velocity.

Lazari [105] used the viscoplastic approach for modeling strain localization in partially saturated soils. The difficulty of rate–independency explained in the previous paragraph was circumvented by extending the viscoplastic model to the nonlocal integral theory.

3.5 Strong–discontinuity approach

When a shear band evolves as a fault, making it impossible for the material to support highly localized strains, the strong–discontinuity approach has proven to be an effective alternative. This approach falls within the framework of assumed enhanced strain methods (AES) described in Simo and Rifai [160]. It models the crack growth implicitly by a jump in the displacement field enhancing the affected elements with resulting additional degrees of freedom statically condensed out of the equations and without affecting the neighboring elements. The approximation of the displacement field $\boldsymbol{u}^h(\boldsymbol{x})$ in the neighborhood of these discontinuities can be represented as the sum of the standard finite

element approximation $\boldsymbol{u}^{\mathrm{FE}}$ and an enriched term, $\boldsymbol{u}^{\mathrm{enr}}$

$$\boldsymbol{u}^h(\boldsymbol{x}) = \underbrace{\sum_{i=1}^{n_{nodes}} N_i(\boldsymbol{x})\boldsymbol{d}_i}_{\boldsymbol{u}^{\mathrm{FE}}} + \underbrace{\sum_{e=1}^{n_{el}} \mathcal{M}_S \boldsymbol{a}_e}_{\boldsymbol{u}^{\mathrm{enr}}} \tag{3.15}$$

where n_{nodes} is the number of nodes, n_{el} is the number of elements, N_i are the standard FE shape functions, $\boldsymbol{d}_i$ are the standard nodal degrees of freedom, $\boldsymbol{a}_e$ are the degrees of freedom describing the elemental displacement jump and and $\mathcal{M}_S$ is the so–called elemental unit jump function, Oliver et al. [128].

This feature makes much easier to capture a propagating crack without remeshing, unlike with standard elements. This approach has been tested with good results for deviatoric plasticity models with a constant post–localization softening modulus [9, 70, 157, 159]. Applications to geomechanics problems are provided by the works of Borja and Regueiro [26, 27, 139]. An extension of the strong–discontinuity approach to the coupled cases of saturated and partially saturated media considered by in Armero and Callari [8] and Callari et al. [32], respectively.

This approach provides a better kinematic description of discontinuous displacement fields than pure continuum models that smear the displacement jumps uniformly over the entire element, but they still have certain limitations. Their main disadvantage is that the strain approximations in the two parts of the element separated by a discontinuity are not independent [93]. The use of higher order elements may reduce this behavior but this issue can not be completely removed.

3.6 Extended Finite Element Method

The Extended Finite Element Method (XFEM) is an alternative approach capable of dealing with strong discontinuities and overcome the drawback pointed out in the previous approach. XFEM was first developed by Belytschko and Black [17] in the framework of fracture mechanics and is considered as a local version of the partition–of–unity method (PUM) [117]. XFEM differs from the strong–discontinuity approach in that only the nodal displacements surrounding the discontinuities are enriched and not the

elements (see Fig. 3.1). Oliver et al. [129] made a comparative study between these two methods in terms of accuracy and performance for one and multiple cracks and Borja [28] also compared them through numerical examples involving tangential sliding.

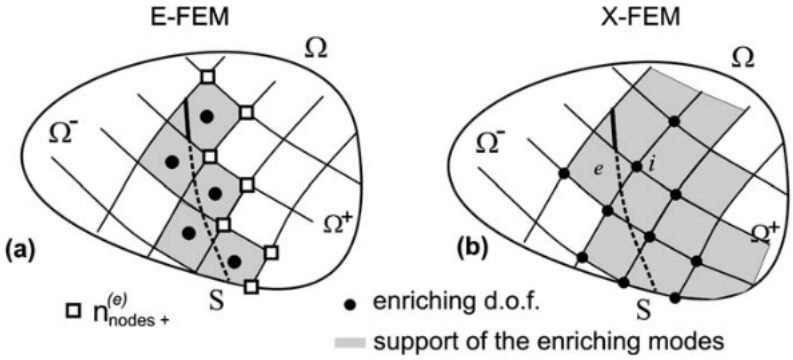

Figure 3.1: Nodal and elemental enrichments [129].

The enriched displacement approximation is written in the form

$$\boldsymbol{u}^h(\boldsymbol{x}) = \underbrace{\sum_{i=1}^{n_{nodes}} (N_i(\boldsymbol{x})\boldsymbol{d}_i)}_{\boldsymbol{u}^{\mathrm{FE}}} + \underbrace{\sum_{i=1}^{n_{nodes}} (\mathcal{H}_S N_i(\boldsymbol{x})\boldsymbol{a}_i)}_{\boldsymbol{u}^{\mathrm{enr}}} \tag{3.16}$$

where $\boldsymbol{a}_i$ is the nodal displacement jump vector and $\mathcal{H}_S$ is the Heaviside step function shifted to the discontinuity surface S.

The use of XFEM for modeling shear bands as strong discontinuities within a continuum mechanics context has been done by Samaniego and Belytschko [147] and Areias and Belytschko [5]. Khoei and Karimi [100] employed XFEM within a higher–order continuum model based on the Cosserat theory to simulate shear band localization. Daneshyar and Mohammadi [48] and Liu [109] worked on the modeling the shear band localization using non–associated plasticity models.

Works on the shear band evolution in saturated porous media can be found in Réthoré et al. [143], Khoei and Haghighat [99]; the fluid flow in partially saturated porous media was treated by Réthoré et al. [141, 142] and Mohammadnejad and Khoei [120].

Chapter 4

Finite Element modeling of strain localization with second gradient model

Among the different regularization techniques presented in the previous chapter, we propose in the following to use the second gradient model developed in Grenoble [35, 36], a subclass of continua with microstructure, for modeling saturated and partially saturated soils. It is based on the assumption that the microkinematic gradient is equal to the deformation gradient. The second gradient model introduces an implicit internal length scale that removes the pathological mesh dependence when strain localization occurs. And as we will see through this chapter, this model has been extensively applied in different geomechanics and engineering applications with satisfactory results.

This chapter aims to review the existing literature related to the second gradient model. First, the variational formulation for monophasic media presented in the previous chapter is revisited. Second gradient models contain second order derivatives of displacements in the virtual power principle which means that C^1–continuity between elements is required; this has been circumvented by employing Lagrange multipliers to enforce the kinematic relation between the displacement and displacement gradient fields yielding to three unknown fields: displacement field, displacement gradient field and Lagrange multipliers. Then, this formulation will be extended to biphasic materials; the main assumptions are

presented regarding the second gradient effects. Finally, recent advances related to this regularization technique will be outlined.

4.1 Second gradient model for monophasic medium

Recalling the variational formulation for the second gradient model. We have that for every kinematic admissible field $\boldsymbol{u}^*$:

$$\int_{\mathcal{B}} (\boldsymbol{\sigma} \cdot \nabla^s \boldsymbol{u}^* + \boldsymbol{\Sigma} \cdot \nabla\nabla \boldsymbol{u}^*) \, \mathrm{d}v = \int_{\mathcal{B}} \rho \boldsymbol{b} \cdot \boldsymbol{u}^* \, \mathrm{d}v + \int_{\partial \mathcal{B}_\sigma} \left(\overline{\boldsymbol{p}} \cdot \boldsymbol{u}^* + \overline{\boldsymbol{P}} \cdot \nabla \boldsymbol{u}^* \right) \mathrm{d}a \tag{4.1}$$

where $\boldsymbol{\sigma}$ is the Cauchy stress, $\boldsymbol{\Sigma}$ is the double stress, $\overline{\boldsymbol{p}}$ is the external (classical) traction force per unit area and $\overline{\boldsymbol{P}}$ an additional external (double) traction force.

Due to the fact that $\boldsymbol{u}^*$ and $\nabla \boldsymbol{u}^*$ are not independent ($\boldsymbol{u}^*$ and its tangential derivatives along the boundary can not vary independently), $\overline{\boldsymbol{p}}$ and $\overline{\boldsymbol{P}}$ can not be taken independently. After some algebra, the variational formulation of the general expression of micromorphic media yields the following expression of the virtual power equation [see 36, 38]; for any kinematically admissible field $\boldsymbol{u}^*$:

$$\int_{\mathcal{B}} (\boldsymbol{\sigma} \cdot \nabla^s \boldsymbol{u}^* + \boldsymbol{\Sigma} \cdot \nabla\nabla \boldsymbol{u}^*) \, \mathrm{d}v = \int_{\mathcal{B}} \rho \boldsymbol{b} \cdot \boldsymbol{u}^* \, \mathrm{d}v + \int_{\partial \mathcal{B}_\sigma} \left(\overline{\boldsymbol{t}} \cdot \boldsymbol{u}^* + \overline{\boldsymbol{T}} \cdot D\boldsymbol{u}^* \right) \mathrm{d}a \tag{4.2}$$

The external traction force per unit area $\overline{\boldsymbol{t}}$ and the additional external (double) traction force per unit area $\overline{\boldsymbol{T}}$ can be chosen independently and are defined as follows:

$$\overline{\boldsymbol{t}} = (\boldsymbol{\sigma} - \nabla \cdot \boldsymbol{\Sigma}) \, \boldsymbol{n} - (\overset{s}{\nabla} \cdot \boldsymbol{\Sigma}) \boldsymbol{n} + \boldsymbol{\Sigma} \left\{ \boldsymbol{\beta} - \mathrm{tr} \left(\boldsymbol{\beta} \right) \boldsymbol{n} \otimes \boldsymbol{n} \right\} \tag{4.3a}$$

$$\overline{\boldsymbol{T}} = \boldsymbol{\Sigma} \left(\boldsymbol{n} \otimes \boldsymbol{n} \right) \tag{4.3b}$$

where $\boldsymbol{\beta}$ is the so–called *second fundamental form* of the surface $\partial \mathcal{B}$.

$$\boldsymbol{\beta} := -\overset{s}{\nabla} \boldsymbol{n} \tag{4.4}$$

In the above equations, D and $\overset{s}{\nabla}$ denote the normal gradient and tangential gradient of the unspecified field $(\cdot)$, respectively:

$$D(\cdot) := \nabla(\cdot)\boldsymbol{n}, \qquad D(\cdot) := \frac{\partial(\cdot)}{\partial x_i} n_i \tag{4.5a}$$

$$\overset{s}{\nabla}(\cdot) := \nabla(\cdot) - D(\cdot) \otimes \boldsymbol{n} = \nabla(\cdot) - (\nabla(\cdot)\boldsymbol{n})\,\boldsymbol{n} \tag{4.5b}$$

and $\overset{s}{\nabla} \cdot \boldsymbol{\Sigma}$ is the surface divergence of $\boldsymbol{\Sigma}$, with components:

$$(\overset{s}{\nabla} \cdot \boldsymbol{\Sigma})_{ij} = \frac{\partial \Sigma_{ijk}}{\partial x_k} - \frac{\partial \Sigma_{ijk}}{\partial x_l} n_k n_l \tag{4.6}$$

Using the divergence theorem and after two integrations by part of eq. (4.2), the balance equations read:

$$\nabla \cdot (\boldsymbol{\sigma} - \nabla \cdot \boldsymbol{\Sigma}) + \rho \boldsymbol{b} = \boldsymbol{0} \tag{4.7}$$

The kinematically admissible field $\boldsymbol{u}^*$ as well as the displacement field $\boldsymbol{u}$, have has to be two times differentiable which is a real difficulty in finite element since it implies the use of C^1 finite elements.

The second gradient model introduces an internal length scale which, in elasticity, is proportional to the ratio of the two constitutive moduli defined by the first and the second gradient constitutive laws.

Regarding the constitutive laws, Chambon et al. [36] proposed a generalization of the flow theory of plasticity for media with microstructure. The authors first considered a one plastic mechanism in which there exists only one yield function, f, depending on the macro stress $\boldsymbol{\sigma}$, the microstress $\boldsymbol{\tau}$ (neglected in the case of second gradient models), the double stress $\boldsymbol{\Sigma}$ and one single internal variable κ; f has to remain negative or null:

$$f(\boldsymbol{\sigma}, \boldsymbol{\tau}, \boldsymbol{\Sigma}, \kappa) \leq 0 \tag{4.8}$$

They also presented a multi–mechanism plastic theory, in particular three mechanisms (two mechanisms in the case of the second gradient model) with three plastic multipliers

with their respective and independent yield functions:

$$f^{\sigma}(\boldsymbol{\sigma}, \kappa^{\sigma}) \leq 0 \qquad f^{\tau}(\boldsymbol{\tau}, \kappa^{\tau}) \leq 0 \qquad f^{\Sigma}(\boldsymbol{\Sigma}, \kappa^{\Sigma}) \leq 0 \tag{4.9}$$

This approach assumes that these three mechanisms are independent on each other, based on the fact that the microstress would be linked to grain straining and the macro stress to rearrangement of grains. One of the advantages of local second gradient models is the fact that all quantities remain local in the constitutive equations in both cases. Thus, it is straightforward to formulate a second gradient extension of any classical models in the case of applying the multi–mechanism plastic theory.

Matsushima et al. [115] presented a finite deformation version of the theory of Chambon with two independent plastic mechanisms based on a incremental formulation in terms of Jaumann stress rate and an additive decomposition of first and second gradient–based rate of deformation measures. Two new independent variables are introduced and denoted as $\boldsymbol{f}$ which corresponds to the derivatives of the displacement field $\boldsymbol{u}$ and the Lagrange multiplier field $\boldsymbol{\lambda}$. They made use of the Lagrange multipliers to enforce the relation between the microkinematic gradient and the spatial derivatives of the corresponding displacements:

$$\boldsymbol{f} = \nabla \boldsymbol{u}, \qquad \boldsymbol{f}^{*} = \nabla \boldsymbol{u}^{*} \tag{4.10}$$

in this way, C^1 continuous elements are avoided.

The balance equation in the variational formulation, written in the current solid configuration (updated Lagrangian formulation), yields for any kinematically admissible fields $(\boldsymbol{u}^{*},\ \boldsymbol{f}^{*},\ \boldsymbol{\lambda}^{*})$:

$$\int_{\mathcal{B}^t} \left(\boldsymbol{\sigma}^t \cdot \nabla^s \boldsymbol{u}^{*} + \boldsymbol{\Sigma}^t \cdot \nabla^t \boldsymbol{f}^{*}\right) \mathrm{d}v^t - \int_{\mathcal{B}^t} \boldsymbol{\lambda}^t \cdot \left(\nabla^t \boldsymbol{u}^{*} - \boldsymbol{f}^{*}\right) \mathrm{d}v^t - W_e^{t*} = 0 \tag{4.11}$$

$$\int_{\mathcal{B}^t} \boldsymbol{\lambda}^{*} \cdot \left(\nabla^t \boldsymbol{u} - \boldsymbol{f}^t\right) \mathrm{d}v^t = 0 \tag{4.12}$$

where superscripts t denotes quantities at a given time t.

Bésuelle et al. [19] performed a bifurcation analysis using this version of the second gradient model. The authors indicate that after the bifurcation criterion is met, non

uniqueness of localized solutions are possible (see Figs. 4.1 and 4.2), and the result is controlled by fine details in the simulation parameters such as slight difference in time step size or the first guess of a given time step [39]. Therefore, second gradient model regularizes the solution but does not restore uniqueness consistent with the numerical results in Chambon et al. [35]. The results also indicate that the band thickness is reproducible regardless the position and the number of the localization bands (see Fig. 4.2).

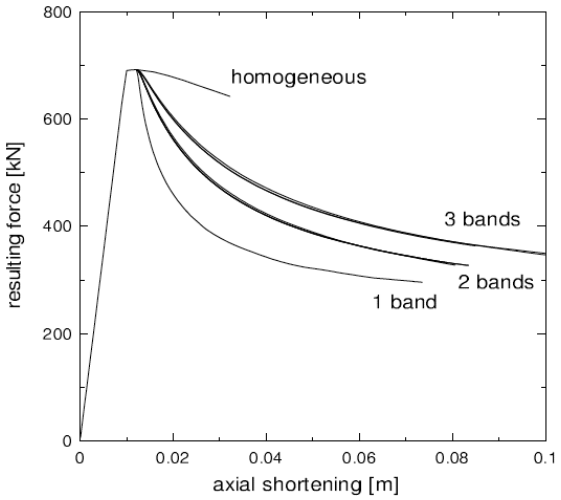

Figure 4.1: Global force versus axial shortening curves of a biaxial test with different shear band patterns obtained after a random initialization [19].

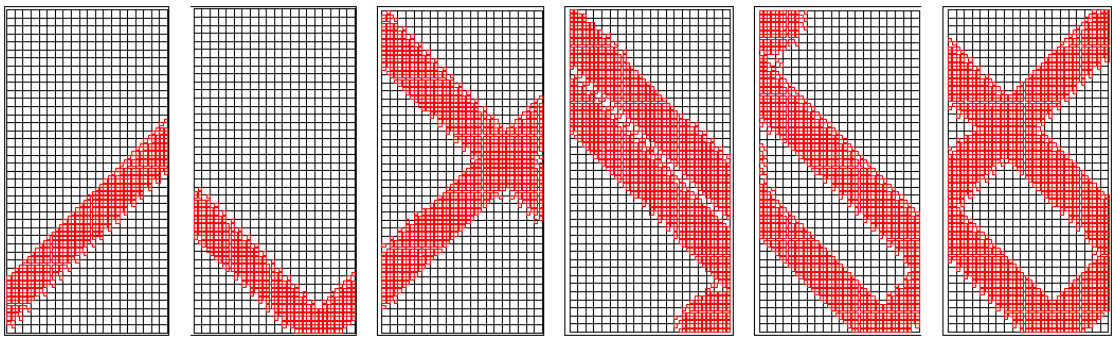

Figure 4.2: Localized solutions of a biaxial test obtained after a random initialization. The red squares correspond to the Gauss integration points which are in the softening loading part [19].

This formulation has been extensively applied in geomechanics and engineering applications with satisfactory results solving the mesh dependency issues in the localized zones

as we can see in the following sections.

We close this section by remarking that a theory for a full geometrically nonlinear theory based on a multiplicative split of the deformation gradient and an additive split of the second deformation gradient was developed in Chambon et al. [37], Tamagnini et al. [168] and Chambon et al. [38] but it has not yet numerically implemented.

4.2 Second gradient model for biphasic medium

The second gradient finite element model was then extended from monophasic medium to model saturated porous media by Collin et al. [44]. They account for a medium with incompressible solid grains, under isothermal and quasi–static conditions. The solid and fluid phases are considered as immiscible and phase changes, like evaporation and dissolution, are not taken into account.

Despite the fact that the pore fluid equation seems introducing its own internal scale, the second gradient effects are related only to the solid skeleton. This hypothesis was first formulated by Ehlers and Volk [59] on a Cosserat model for biphasic medium. A more general formulation is derived by Sciarra et al. [150] in which the second gradient effects are associated also to the fluid phase. Moreover, Collin et al. [44] assume that the pore fluid has no influence at the microstructure level and the double stress $\boldsymbol{\Sigma}$ has no link with the pore pressure. Therefore previous equations remain valid, provided that $\boldsymbol{\sigma}$ is the total stress, and Terzaghi's effective stress principle holds.

Eqs. (4.11) and (4.12) are completed with the mass balance equation for the fluid in a weak form, written in the current solid configuration (updated Lagrangian formulation). For every kinematically admissible virtual pore water pressure field p_w^*:

$$\int_{\mathcal{B}^t} \left(\dot{M}_w^t p_w^* - \boldsymbol{m}_w^t \cdot \nabla^t p_w^* \right) \mathrm{d}v^t = \int_{\mathcal{B}^t} Q_w^t p_w^* \, \mathrm{d}v^t - \int_{\partial \mathcal{B}_q^t} \overline{q}_w^t p_w^* \, \mathrm{d}v^t \tag{4.13}$$

where $\dot{M}_w^t$ is the specific fluid mass content, $\boldsymbol{m}_w^t$ is the fluid mass flow, Q_w^t is a source/sink term and $\overline{q}_w^t$ is the prescribed fluid flow per unit area.

Collin et al. [44] uses a 2D plane strain isoparametric finite element. The displacements, $\boldsymbol{u}$, and the pore pressure, p_w, are interpolated with quadratic Serendipity shape functions

while the displacement gradients, $\boldsymbol{f}$, are interpolated linearly. The Lagrange multipliers, $\boldsymbol{\lambda}$, are assumed constant within each element (see Fig. 4.3). The numerical integration is performed using a Gauss quadrature scheme.

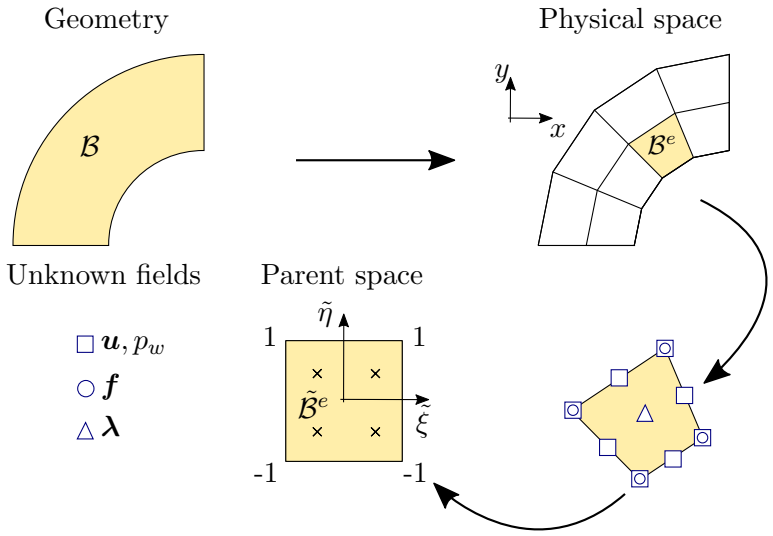

Figure 4.3: Geometry, spatial discretization in the physical space, quadrilateral element and parent element used in the second gradient model.

All these novelties have been implemented in the non–linear finite element code Lagamine developed at the University of Liège [40, 43] and has been continuously extended to different physical phenomena.

4.3 Recent advances using the local second gradient model

Fernandes et al. [62] developed a hydromechanical second gradient dilation model based on a second gradient model that considers only volumetric strain gradients under saturated conditions. This turns into a reduction of the number of degree of freedoms that allows the simulation of a very simple 3D problem, see Fernandes et al. [63]. It consisted in a triaxial test with a defect showing shear band localization.

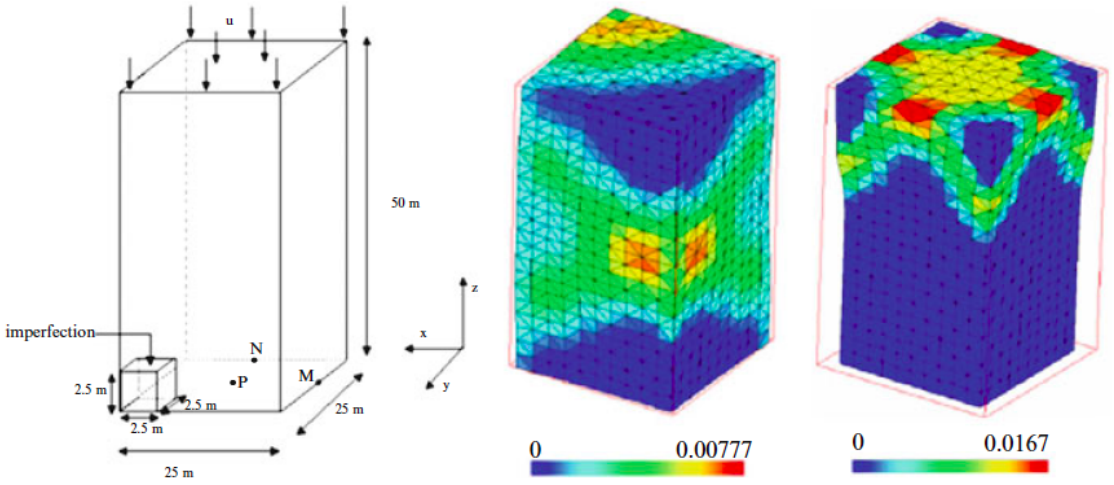

Figure 4.4: The 3D problem configuration and two different solutions [63].

Sieffert et al. [156] presented a local second gradient model with thermo–hydro–mechanical coupling, in which the thermal effects were added in the hydro–mechanical model developed by Collin et al. [44]. They studied the evolution of the Excavation Damage Zone with an increase of the temperature on the cavity of a borehole problem.

The second gradient model has been also extended to partially saturated conditions with constant gas pressure and applications of a gallery excavation in Callovo–Oxfordian claystone leading to good agreement with in–situ measurements and observations of the excavation damage zone [132].

The local second gradient model has been recently extended to the multi–scale approach by replacing the classical constitutive law with FE simulations performed at the micro–scale. In Marinelli [112] and Van Den Eijnden [173], the Finite element method was used at both scales, macro– and micro–scale and it is referred as FE^2 model (see Fig. 4.5). In this last work, second gradient model is used for hydro–mechanical modeling of Callovo–Oxfordian claystone. In Argilaga [6] the Finite Element method was used at the macro–scale with Discrete elements at the micro–scale (FEM–DEM approach), with applications to mechanical problems.

Through this chapter, we presented the main features of the second gradient model to obtain objective results when strain localization occurs. We also highlighted its flexibility to be used with any classical constitutive model and to be extended to coupled and

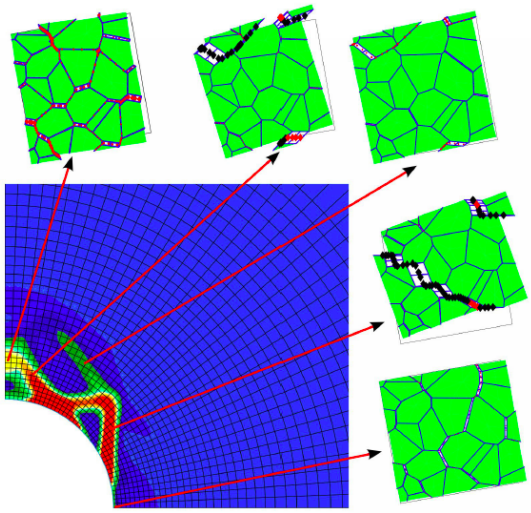

Figure 4.5: Mechanical simulation of quarter gallery and deformed microstructures for different integration points [173].

multiphysics phenomena. However, we believe second gradient model could be performed in a more efficient way if the C^1–continuity requirement is fulfilled with finite elements that introduces higher order continuity in a straightforward way such as the ones used in Isogeometric Analysis. We will see in the next chapter that in this way, the number of degrees of freedoms will decrease drastically and, in consequence, computations will be much more efficient.

Chapter 5

Isogeometric FE analysis: towards a more accurate spatial approximation with high degree of inter–element continuity

The idea of integrating computer–aided design (CAD) and Finite Element Analysis (FEA) dates back to the pioneering works of Gordon and Hall [75] and Gordon and Thiel [76]. The authors introduced the concept of *transfinite interpolation* in which the same basis functions are used for both the geometry description and the approximation of the unknown fields in the Finite Element. Aristodemo [7] used B–splines for the analysis of elastic problems with the objective of reducing the total number of degrees of freedoms. And the first attempts to incorporate NURBS in structural analysis is due to Schramm and Pilkey [149]. Most recent works can be found in Sabin [146], Kagan et al. [97] and Höllig [87]. But, it was Hughes et al. [89] who gave the decisive boost required to promote the benefits of integrating CAD functions into FEA by the name of Isogeometric Analysis (IGA).

Furthermore, the emergence of IGA in various engineering applications is due to the fact that IGA offers excellent control over the inter–element continuity conditions providing higher convergence rates with respect to C^0–continuous standard finite elements. This

implicit higher order–continuity has also implications in the formulation since will allow straightforward numerical implementations. These characteristics makes IGA the ideal candidate for the discretization of second gradient models.

This chapter provides a basic introduction of the IGA concept. We begin with some basic concepts, then we introduce the basis functions used in IGA along with the essential ingredients to be added in our second gradient IGA finite element formulation. This chapter concludes showing the numerical implications of implementing IGA with respect to standard FEA.

5.1 Isogeometric analysis concept

The basic idea of IGA is to employ the same basis functions (*i.e.* B–splines, non-uniform rational B–splines (NURBS), T–splines) used in CAD to describe both the geometry and physics fields in FEA rather than the traditional Lagrange or Serendipity basis functions. Since IGA uses the exact geometry from CAD, geometrical errors introduced by approximation of the physical domain are eliminated.

IGA introduces new concepts that are different from standard FEA. Geometries are usually modeled with macro–elements (or subdomains) called patches. Each patch has two representations, one in a physical space and one in a parametric space. A patch is an unit square or an unit cube in the parametric space, in two–dimensional (2D) and three–dimensional (3D) problems, respectively. Each patch is divided into knot spans (micro–elements or elements). Knot spans are convenient for numerical integration in the parent space. These knot spans are bounded by knots in each parametric direction. Many civil engineering problems can be modeled by a single patch; geometries requiring complex representation can be modeled by an assembly of multiple patches. Fig. 5.1 illustrates these new concepts. A two–dimensional geometry is discretized in four patches with eight quadratic NURBS elements each of them to model a hydromechanical coupled problem. The control points denoted with squares define the control mesh, which does not conform to the actual geometry. Rather, it is like a scaffold that controls the geometry, *i.e.* the nine blue squares that define the highlighted element on the first patch are not necessary embedded in the element as it happens with standard finite elements. It means that IGA basis functions are usually not interpolatory, and they would have to be projected to

the physical space as a part of a postprocess stage. The computations are carried on in the parametric space for each patch, and the numerical integration for each element are performed in the parent space. Following the isoparametric concept, the displacement $\boldsymbol{u}$ and pore pressure p_w are approximated using NURBS basis functions and are called control variables since they are located at the control points.

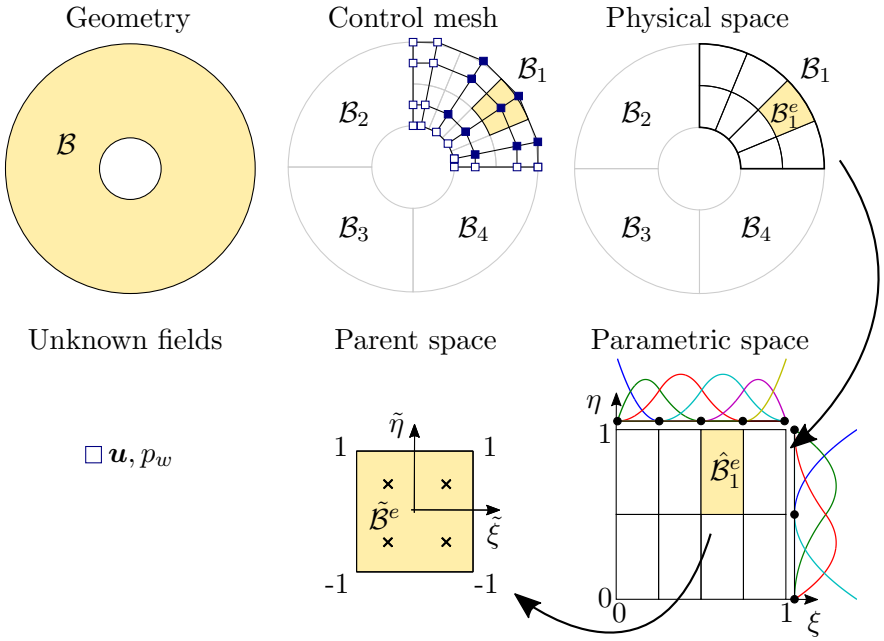

Figure 5.1: Schematic illustration of IGA concept using a NURBS geometry (four patches).

In this study, the domains for the boundary value problems will be modeled with one single patch. For an exhaustive description of B–splines and non-uniform rational B–splines (NURBS), we refer to Piegl and Tiller [136], whereas applications on a wide range of engineering problems are presented in Cottrell et al. [45].

Finally, the convention for the order of basis function $p = 1$, 2, 3, etc. refers to linear, quadratic, cubic, etc., piecewise polynomials, respectively.

5.2 Geometric modeling using IGA

5.2.1 B–spline and NURBS basis functions

5.2.1.1 B–spline basis functions

We start by defining B–spline basis functions as a function of the coordinate ξ in one–dimensional parametric space [0 1]. In order to construct a B–spline basis function of polynomial order p, one needs to define the so called *knot vector* which is a non–decreasing set of coordinates in the parametric space:

$$\Xi = [\xi_1, ..., \xi_i, ..., \xi_{n+p+1}] \tag{5.1}$$

where i is the knot index, $i = 1, 2, ..., n + p + 1$, $\xi_i \in \mathbb{R}$ is the i^{th} knot and n is the total number of basis functions. We assume in the following that $\xi_1 = 0$ and $\xi_{n+p+1} = 1$.

The knots divide the parameter space into knot spans, $[\xi_i, \xi_{i+1}]$. Note that since some values of ξ_i may be equal, some knot spans may not exist. Only knot spans with positive length are considered as elements. If a knot ξ_i appears m_i times, then it is said that ξ_i is a multiple knot of multiplicity m_i. In this work, we will restrict the discussion to open B–splines, the class of B–splines which is created using knot vectors in which the first and the last knots are repeated $p + 1$ times.

From the knot vector, the B–spline basis functions $N_{i,p}(\xi)$ of order $p = 0$ are defined as follows

$$N_{i,0}(\xi) = \begin{cases} 1, & \text{if } \xi_i \leq \xi \leq \xi_{i+1} \\ 0, & \text{otherwise} \end{cases} \tag{5.2}$$

and basis functions of order $p > 0$ are constructed recursively until the desired polynomial order of the functions [46, 49]:

$$N_{i,p}(\xi) = \frac{\xi - \xi_i}{\xi_{i+p} - \xi_i} N_{i,p-1}(\xi) + \frac{\xi_{i+p+1} - \xi}{\xi_{i+p+1} - \xi_{i+1}} N_{i+1,p-1}(\xi) \tag{5.3}$$

here it is formally assumed that $0/0 = 0$.

Fig. 5.2 shows B–spline basis functions for $p = 1$, that results in linear Lagrange elements, and $p = 2$.

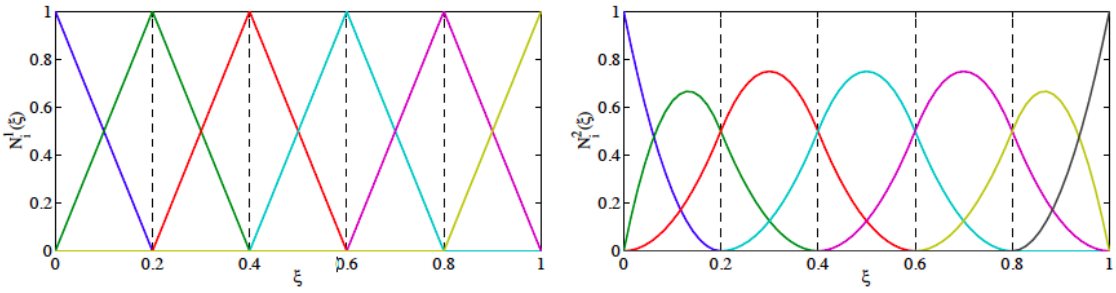

(a) Linear C^0 B-Spline basis functions (b) Quadratic C^1 B-Spline basis functions

Figure 5.2: B–splines basis functions for $p = 1$ and $p = 2$.

5.2.1.2 Derivatives

The first derivatives of B–spline basis functions are computed by

$$\frac{\mathrm{d}}{\mathrm{d}\xi} N_{i,p}(\xi) = \frac{p}{\xi_{i+p} - \xi_i} N_{i,p-1}(\xi) - \frac{p}{\xi_{i+p+1} - \xi_{i+1}} N_{i+1,p-1}(\xi) \tag{5.4}$$

and the second derivatives are given by

$$\frac{\mathrm{d}^2}{\mathrm{d}\xi^2} N_{i,p}(\xi) = \frac{p}{\xi_{i+p} - \xi_i} \frac{\mathrm{d}}{\mathrm{d}\xi} N_{i,p-1}(\xi) - \frac{p}{\xi_{i+p+1} - \xi_{i+1}} \frac{\mathrm{d}}{\mathrm{d}\xi} N_{i+1,p-1}(\xi) \tag{5.5}$$

5.2.1.3 Properties

We list the main properties of B–spline basis functions, some of them are shared with Lagrange and Serendipity basis functions commonly used in finite elements formulations:

1. All basis function are nonnegative over the entire domain:

$$N_{i,p}(\xi) \geq 0, \qquad \forall \xi \tag{5.6}$$

2. The number of basis functions which have support on any knot span (ξ_i, ξ_{i+1}), and thus over each element, is always $p + 1$. In this sense, univariate B–splines do

not differ from Lagrange and Serendipity basis functions. This implies that the bandwidth of the global matrix is $2p + 1$ regardless of whether we are using an FEA basis or B–splines.

3. The continuity of splines is controlled by the knot multiplicities. If a knot value is repeated m_i times, the continuity of the basis functions at that knot is C^{p-m}. Open B–splines are therefore C^{p-1} inside the domain and C^{-1} at the domain boundaries, a prerequisite for the application of Dirichlet boundary conditions.

4. The basis constitutes a partition of unity

$$\sum_{i=1}^{n} N_{i,p}(\xi) = 1, \qquad \forall \xi \tag{5.7}$$

5. B–splines are variation diminishing in the neighborhood of discontinuous data [61]. Most importantly, the Gibbs effect observed with Lagrange elements is not present. This property is illustrated in Fig. 5.3, and generally results in more stable discretizations, particularly in the presence of sharp gradients.

6. The geometry mapping is bijective (*i.e.* not self–penetrating), if and only if the image is a convex quadrilateral.

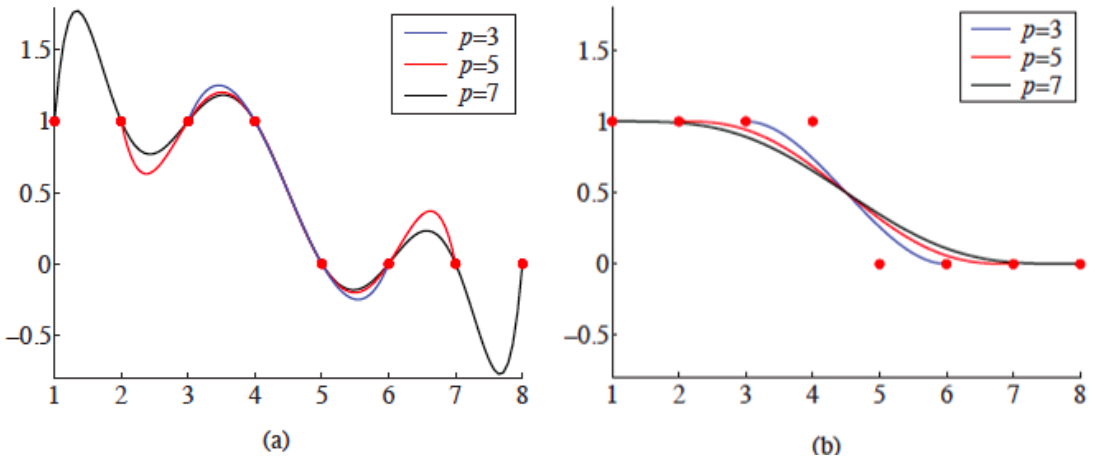

Figure 5.3: a) Lagrange interpolation oscillates when faced with discontinuous data. b) NURBS exhibit the variation diminishing property for the same data [45].

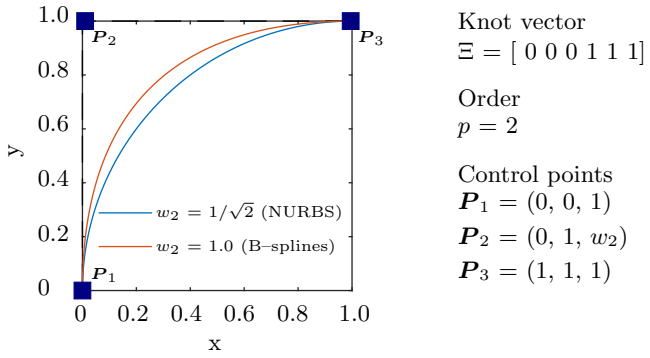

Figure 5.4: NURBS curve influenced by the value of the weight w_2.

5.2.1.4 NURBS basis functions

Despite the many advantages of splines, B–splines cannot exactly represent a number of objects that are of engineering interest, for instance, conic sections. NURBS are a rational generalization of B–splines:

$$R_{i,p}(\xi) = \frac{N_{i,p}(\xi)w_i}{W(\xi)} = \frac{N_{i,p}(\xi)w_i}{\sum_{\hat{i}=1}^{n} N_{\hat{i},p}(\xi)w_{\hat{i}}} \tag{5.8}$$

where w_i is a weight which provides an additional degree of freedom for geometry manipulation and $W(\xi)$ is the weighting function. Fig. 5.4 illustrates the influence of the weight on a curve defined by the knot vector, the polynomial order and the control points (coordinates and weights). NURBS offer the flexibility of adjusting the value of w_2 in order to construct a quarter of a circle having a unit radius.

NURBS share the properties of B–splines and the refinement procedure follows the same guidelines for the B–splines geometries. It is not our purpose to represent complex geometries. For this reason NURBS are not further developed in this work, nevertheless, no changes have to be made since their weighting functions are already considered in their basis functions.

5.2.2 B–spline geometries

5.2.2.1 Univariate B–spline curves

A B–spline curve is a linear combination of B–spline basis functions and control points as follows:

$$\boldsymbol{x}(\xi) = \sum_{i=1}^{n} N_{i,p}(\xi)\boldsymbol{P}_i \tag{5.9}$$

where $\boldsymbol{P}_i = (x_i, y_i, z_i)$ contains the coordinates of the i–th control point associated to the basis function $N_{i,p}(\xi)$.

5.2.2.2 Multivariate B–splines and NURBS geometries

Multivariate B–spline geometries are created by means of a tensor product of univariate B–splines. A 2D geometry modeled by B–splines of order p_ξ and p_η with parametric coordinates $\boldsymbol{\xi} = (\xi, \eta)$ is defined by:

$$\boldsymbol{x}(\xi, \eta) = \sum_{i=1}^{n_\xi}\sum_{j=1}^{n_\eta} N_{i,p_\xi}(\xi)M_{j,p_\eta}(\eta)\boldsymbol{P}_{ij} \tag{5.10}$$

where n_ξ and n_η are the number of basis functions in the parametric directions ξ and η, respectively. $\boldsymbol{P}_{ij} = (x_{ij}, y_{ij}, z_{ij})$ is the control point that is associated to the product of the basis functions $N_{i,p_\xi}(\xi)$ and $M_{j,p_\eta}(\eta)$. All the control points define a $n_\xi \times n_\eta$ net (control mesh).

Fig. 5.5 shows all the ingredients for the definition of a NURBS geometry in 2D discretized into two quadratic elements. The physical space and the control mesh are represented in the same figure with the particularity that two control points share location ($\boldsymbol{P}_{23}$ and $\boldsymbol{P}_{33}$). However, the two of them (as the rest of control points) are associated to different basis functions defined by the product of their respective basis functions in each parametric direction ($N_{2,2}M_{3,2}$ and $N_{3,2}M_{3,2}$, respectively). In terms of numerical analysis, these two control points are treated by means of static condensation.

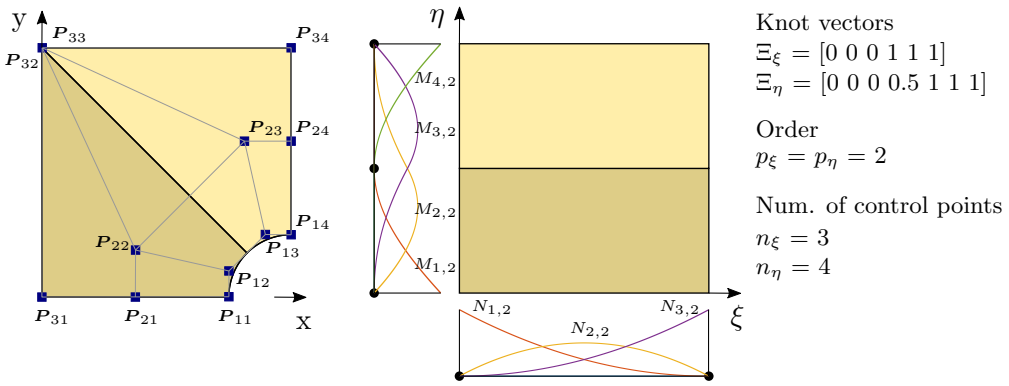

Figure 5.5: NURBS geometry.

In the case of a 3D geometry modeled by B–splines of order p_ξ, p_η and p_ζ with parametric coordinates $\boldsymbol{\xi} = (\xi, \eta, \zeta)$ is given by:

$$\boldsymbol{x}(\xi, \eta, \zeta) = \sum_{i=1}^{n_\xi} \sum_{j=1}^{n_\eta} \sum_{k=1}^{n_\zeta} N_{i,p_\xi}(\xi) M_{j,p_\eta}(\eta) L_{k,p_\zeta}(\zeta) \boldsymbol{P}_{ijk} \tag{5.11}$$

where n_ξ, n_η and n_ζ are the number of basis functions in the parametric directions ξ, η and ζ, respectively. $\boldsymbol{P}_{ijk} = (x_{ijk}, y_{ijk}, z_{ijk})$ is the control point that is associated to the product of the basis functions $N_{i,p_\xi}(\xi)$, $M_{j,p_\eta}(\eta)$ and $L_{k,p_\zeta}(\zeta)$. All the control points define a $n_\xi \times n_\eta \times n_\zeta$ lattice (control mesh).

In this study, we work with same order of approximation in each parametric direction. Furthermore, if we identify the coordinates (i, j) and (i, j, k) of each control point and set their values in a column vector in order to use the finite element notation, eq. (5.10) and (5.11) can be rewritten in the following general form:

$$\boldsymbol{x}(\boldsymbol{\xi}) = \sum_{A}^{n} N_A(\boldsymbol{\xi}) \boldsymbol{P}_A = \boldsymbol{N}(\boldsymbol{\xi}) \boldsymbol{P} \tag{5.12}$$

with

$$\sum_{A}^{n} N_A(\boldsymbol{\xi}) := \sum_{i=1}^{n_\xi} \sum_{j=1}^{n_\eta} N_{i,p_\xi}(\xi) M_{j,p_\eta}(\eta) \qquad (2D) \tag{5.13a}$$

$$\sum_{A}^{n} N_A(\boldsymbol{\xi}) := \sum_{i=1}^{n_\xi} \sum_{j=1}^{n_\eta} \sum_{k=1}^{n_\zeta} N_{i,p_\xi}(\xi) M_{j,p_\eta}(\eta) L_{k,p_\zeta}(\zeta) \qquad (3D) \tag{5.13b}$$

where $p_\xi = p_\eta = p_\zeta$ and N_A is the basis function associated to the control point $A = i + (j-1)n_\eta$ (2D), $A = i + (j-1)n_\eta + (k-1)n_\xi n_\eta$ (3D), $n = n_\xi n_\eta$ (2D) and $n = n_\xi n_\eta n_\zeta$ (3D).

5.2.3 Mesh refinement

Despite the fact that the geometry is considered exact and there is no need to refine it, in most cases the discretization needs to be refined for a better description of the approximated physical fields, mainly, in case of high gradients. The B–spline geometries can be refined by tree strategies which are termed h–, p– and k– refinements or, in computer–aided geometric design notation, knot insertion, order elevation, and order and continuity elevation, respectively. Each refinement strategy can be applied separately in each parametric direction.

First, h–refinement consists in inserting additional knots in the knot vector. Adding a single knot increases the number of basis functions/control points by one and the continuity of the new interfaces between the new elements does not vary with respect to the old interfaces. h–refinement is applied in the geometry of Fig. 5.5. Each element is subdivided into two elements, 0.5 is added in the ξ–direction and 0.25 and 0.75 in the η–direction. The new set of control points is a linear combination of the original set of control points (see Fig. 5.6a)), a detailed algorithm can be found in Piegl and Tiller [136].

The second refinement strategy is provided by first increasing the multiplicity of all existing knots, and subsequently increasing the order of the basis functions. If the the original knot vector is

$$\Xi = [\underbrace{0, ..., 0}_{p+1}, ..., \underbrace{\xi_r, ..., \xi_r}_{m_r}, ..., \underbrace{1, ..., 1}_{p+1}] \tag{5.14}$$

will now take the form:

$$\Xi' = [\underbrace{0, ..., 0}_{p+2}, ..., \underbrace{\xi_r, ..., \xi_r}_{m_r+1}, ..., \underbrace{1, ..., 1}_{p+2}] \tag{5.15}$$

where m_r is the multiplicity of the r internal knots in the original basis and p the order of the original basis functions. In this way, a basis function/control point is added for

each element and the continuity between elements remains unchanged. An example of order elevation can be seen in Fig. 5.6b) in which the order of the basis functions is elevated from quadratic to cubic. The interior knot in the η direction, 0.5, is repeated in order to keep the continuity across element interfaces unchanged.

In addition, IGA provides a third refinement strategy, referred as k–refinement. k–refinement is the action of combining the two previous refinement strategies. The mesh is refined by increasing the order of the basis functions followed by the knot insertion procedure. As a result, the continuity of the new interfaces created by the new elements are increased by an order from C^{p-1} to C^{p}, with p the order of the original B–spline. It is important to mention that the two previous refinement strategies are not commutative; therefore, applying knot insertion and then order elevation will not affect the continuity of the new interfaces. Comparing Fig. 5.6a) and Fig. 5.6c), it can be clearly seen that k–refinement procedure leads to a basis in which the continuity at the location of the inserted knot (new interfaces) is superior.

Local refinement is not possible in a single patch due to the tensor product structure, but can be achieved by combining multiple patches. However, connecting patches interfaces can easily be established only for C^0–continuity. Higher–order continuity requirements need implementation that can be cumbersome, and the range of possibilities is limited. For a true local refinement of spline meshes the global tensor product structure must be avoided. In the current literature there are three different developments: T–splines [151–153], locally refined (LR) B–splines [58, 95] and hierarchical splines [66, 184]. They have all been successfully applied in the context of IGA, but are beyond the scope of this thesis.

5.3 Isogeometric finite element method

5.3.1 General representation of physical fields using IGA

As it has been mentioned earlier in this chapter, IGA uses the isoparametric concept; the discretization of the unknown fields is carried out by the same basis functions adopted

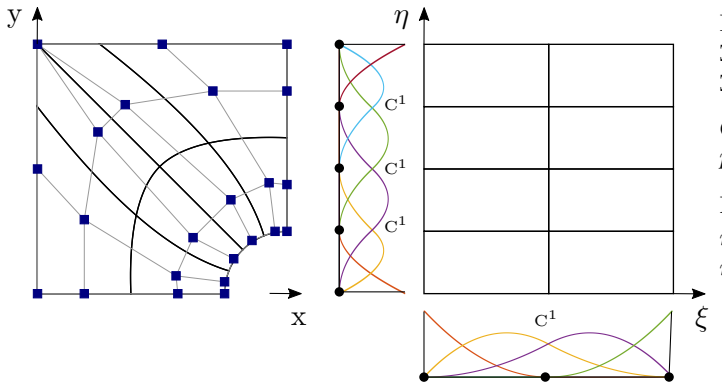

(a) Knot insertion (h–refinement)

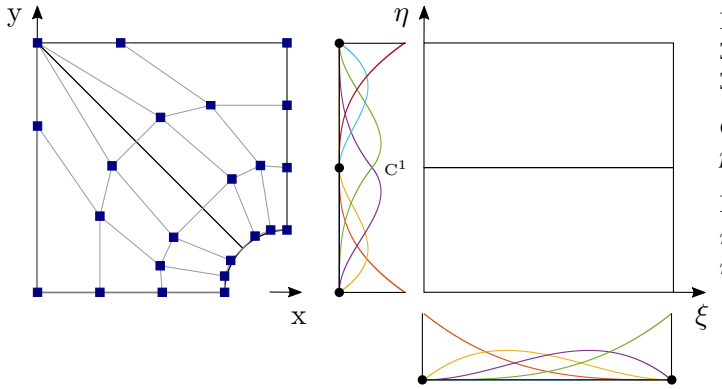

(b) Order elevation (p–refinement)

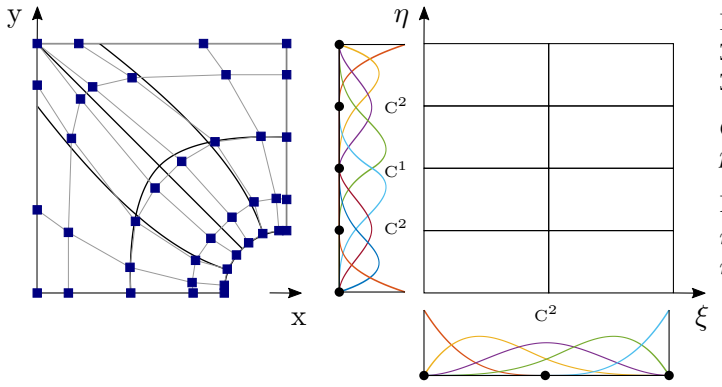

(c) Order and continuity elevation (k–refinement)

Figure 5.6: Refinement strategies in Isogeometric Analysis.

for the modeling of the geometry:

$$\phi(\boldsymbol{x}) = \sum_{A}^{n} N_A(\boldsymbol{\xi})\Phi_A = \boldsymbol{N}(\boldsymbol{\xi})\boldsymbol{\Phi} \tag{5.16}$$

where ϕ is a generic unknown scalar field and Φ_A denotes the values of this field (control variables or dofs) at the control point $\boldsymbol{P}_A$.

5.3.2 Spatial derivatives of shape functions

Second gradient model involves second order derivatives. Therefore, it requires the first and second order spatial derivatives of basis functions with respect to the physical coordinates:

$$\nabla \boldsymbol{N} = \frac{\partial}{\partial \boldsymbol{x}} \boldsymbol{N}(\boldsymbol{\xi}), \qquad \nabla\nabla \boldsymbol{N} = \frac{\partial^2}{\partial \boldsymbol{x} \otimes \partial \boldsymbol{x}} \boldsymbol{N}(\boldsymbol{\xi}) \tag{5.17}$$

Before computing the spatial derivatives, it is necessary to compute the Jacobian matrix:

$$\boldsymbol{J} = \frac{\partial \boldsymbol{x}}{\partial \boldsymbol{\xi}} = \frac{\partial}{\partial \boldsymbol{\xi}} \boldsymbol{N}(\xi)\boldsymbol{P} = \nabla_\xi \boldsymbol{N}(\xi)\boldsymbol{P} \tag{5.18}$$

that contains first derivatives of the geometric mapping, eq. (5.12), with respect to the parametric coordinates. The first order spatial derivatives with respect to the physical space are given by:

$$\nabla \boldsymbol{N} = \boldsymbol{J}^{-1} \nabla_\xi \boldsymbol{N}(\xi) \tag{5.19}$$

In order to obtain the second derivatives, one has to consider the following derivations:

$$\frac{\partial}{\partial \boldsymbol{J}} \left(\boldsymbol{J}\boldsymbol{J}^{-1} \right) = \mathbb{I}\boldsymbol{J}^{-1} + \boldsymbol{J} \frac{\partial \boldsymbol{J}^{-1}}{\partial \boldsymbol{J}} = \boldsymbol{0} \quad \Longrightarrow \frac{\partial \boldsymbol{J}^{-1}}{\partial \boldsymbol{J}} = -\boldsymbol{J}^{-1} \otimes \boldsymbol{J}^{-1} \tag{5.20}$$

$$\frac{\partial \boldsymbol{J}}{\partial \boldsymbol{x}} = \frac{\partial}{\partial x_k} \left(\frac{\partial x_i}{\partial \xi_j} \right) = \frac{\partial^2 x_i}{\partial \xi_j \partial \xi_m} \frac{\partial \xi_m}{\partial x_k} = \frac{\partial^2 x_i}{\partial \xi_j \partial \xi_m} J^{-1}_{mk} = \frac{\partial^2 \boldsymbol{x}}{\partial \boldsymbol{\xi}^2} \boldsymbol{J}^{-1} \tag{5.21}$$

where $\mathbb{I}$ is a second order identity tensor.

The second derivative is then determined by means of the following applications of the chain rule:

$$\begin{aligned}
\frac{\partial^2 N_A}{\partial x_i \partial x_j} &= \frac{\partial}{\partial x_j}\left(\frac{\partial N_A}{\partial \xi_k}\frac{\partial \xi_k}{\partial x_i}\right) \\
&= \frac{\partial}{\partial x_j}\left(\frac{\partial N_A}{\partial \xi_k} J^{-1}_{ki}\right) \\
&= \frac{\partial^2 N_A}{\partial \xi_k \partial \xi_l}\frac{\partial \xi_l}{\partial x_j} J^{-1}_{ki} + \frac{\partial N_A}{\partial \xi_k}\frac{\partial J^{-1}_{ki}}{\partial x_j} \\
&= \frac{\partial^2 N_A}{\partial \xi_k \partial \xi_l} J^{-1}_{lj} J^{-1}_{ki} + \frac{\partial N_A}{\partial \xi_k}\frac{\partial J^{-1}_{ki}}{\partial J_{lm}}\frac{\partial J_{lm}}{\partial x_j} \\
&= \frac{\partial^2 N_A}{\partial \xi_k \partial \xi_l} J^{-1}_{lj} J^{-1}_{ki} + \frac{\partial N_A}{\partial \xi_k}\left(-J^{-1}_{kl} J^{-1}_{mi}\right)\frac{\partial^2 x_l}{\partial \xi_m \partial \xi_n} J^{-1}_{nj} \\
&= \frac{\partial^2 N_A}{\partial \xi_k \partial \xi_l} J^{-1}_{lj} J^{-1}_{ki} - \frac{\partial N_A}{\partial x_l} J^{-1}_{mi}\frac{\partial^2 x_l}{\partial \xi_m \partial \xi_n} J^{-1}_{nj}
\end{aligned} \tag{5.22}$$

that in tensor notation is written as follows:

$$\nabla\nabla \boldsymbol{N} = \boldsymbol{J}^{-T}\left(\nabla_\xi \nabla_\xi \boldsymbol{N} - \nabla \boldsymbol{N} \boldsymbol{H}\right)\boldsymbol{J}^{-1} \tag{5.23}$$

where $\boldsymbol{H} := \partial^2 \boldsymbol{x} / \left(\partial \boldsymbol{\xi} \otimes \partial \boldsymbol{\xi}\right)$ is the Hessian matrix that contains the second derivatives of the geometric mapping, eq. (5.12), with respect to parametric coordinates.

5.3.3 Numerical integration

Integrals over the entire physical domain are split into element integrals with a domain denoted by $\mathcal{B}_e$. These integrals are pulled back to the parametric element $\mathcal{B}_e$ via geometry mapping. Finally, integrals over the parametric element are pulled back to the parent domain where numerical Gaussian quadrature is performed.

$$\begin{aligned}
\int_{\mathcal{B}} \phi(\boldsymbol{x})\,\mathrm{d}v &= \sum_{e=1}^{n_{el}} \int_{\mathcal{B}^e} \phi(\boldsymbol{x})\,\mathrm{d}v \\
&= \sum_{e=1}^{n_{el}} \int_{\hat{\mathcal{B}}_e} \phi\left[\boldsymbol{x}(\boldsymbol{\xi})\right] \left|\frac{\partial \boldsymbol{x}}{\partial \boldsymbol{\xi}}\right| \mathrm{d}\hat{v} \\
&= \sum_{e=1}^{n_{el}} \int_{\tilde{\mathcal{B}}_e} \phi\left\{\boldsymbol{x}\left[\boldsymbol{\xi}(\tilde{\boldsymbol{\xi}})\right]\right\} \left|\frac{\partial \boldsymbol{x}}{\partial \boldsymbol{\xi}}\frac{\partial \boldsymbol{\xi}}{\partial \tilde{\boldsymbol{\xi}}}\right| \mathrm{d}\tilde{v}
\end{aligned} \tag{5.24}$$

The mapping from the parent element domain $\tilde{\mathcal{B}}^e$ to a parametric domain $[\xi_i, \xi_{i+1}] \times [\eta_i, \eta_{i+1}] \times [\zeta_i, \zeta_{i+1}]$, $\hat{\mathcal{B}}^e$, is given by

$$\begin{aligned}
\xi &= \frac{1}{2}\left[(\xi_{i+1} - \xi_i)\,\tilde{\xi} + (\xi_{i+1} + \xi_i)\right] && \forall \xi \in [0,\ 1] \text{ and } \forall \tilde{\xi} \in [-1,\ 1] \\
\eta &= \frac{1}{2}\left[(\eta_{j+1} - \eta_j)\,\tilde{\eta} + (\eta_{j+1} + \eta_j)\right] && \forall \eta \in [0,\ 1] \text{ and } \forall \tilde{\eta} \in [-1,\ 1] \\
\zeta &= \frac{1}{2}\left[(\zeta_{k+1} - \zeta_k)\,\tilde{\zeta} + (\zeta_{k+1} + \zeta_k)\right] && \forall \zeta \in [0,\ 1] \text{ and } \forall \tilde{\zeta} \in [-1,\ 1]
\end{aligned} \tag{5.25}$$

then, the Jacobian of this transformation reads:

$$\left|\frac{\partial \boldsymbol{\xi}}{\partial \tilde{\boldsymbol{\xi}}}\right| = \frac{1}{8}\,(\xi_{i+1} - \xi_i)\,(\eta_{j+1} - \eta_j)\,(\zeta_{k+1} - \zeta_k) \tag{5.26}$$

5.4 IGA vs standard FEA

As we have seen in the previous sections, the major difference between standard FEA and IGA resides in the use of higher order–continuity basis functions (C^0 in FEA and C^{p-1} in IGA). Higher order–continuity has relevant implications in its computational cost, mainly in the assembly of the stiffness matrix and solution of the linear system. Schillinger et al. [148] and Veiga et al. [180] compared the influence of continuity of basis functions, C^0 or C^{p-1}, on these two stages. To simplify the analysis, they assumed periodic conditions (either, C^0 or C^{p-1}) are imposed at the boundaries.

On one side, the assembly stage is more time-consuming for the same number of degrees of freedom (dofs), n_{dofs}, in IGA, especially if a classical finite element code is adapted to implement IGA. Being d the dimension of the basis functions and p the order of the basis functions, $\mathcal{O}\left(n_{\text{dofs}}\, p^{3d}\right)$ operations are needed in the C^0 case, whereas $\mathcal{O}\left(n_{\text{dofs}}\, p^{3(d+1)}\right)$ in the case C^{p-1}. Optimal quadrature rules such as that presented in Auricchio et al. [11] and Hughes et al. [90] have been developed to reduce the quadrature effort.

On the other side, higher order–continuity increases the support of the basis functions and their interaction, affecting the sparsity pattern of the system matrix. In the C^0 case the total number of nonzeros is $n_{nz} = (p+2)^d n_{\text{dofs}}$, while it is $n_{nz} = (2p+1)^d n_{\text{dofs}}$ for C^{p-1} case. The sparsity of the stiffness matrix in the one–dimensional case is illustrated in Fig. 5.7. For the same n_{dofs}, higher order–continuity functions completely cover the

bandwidth, no matter the fact that the bandwidth is equal to $2p+1$ in both cases. Hence, IGA consumes more memory than FEA during the solution of the linear system when using direct solvers. For example, using a multi–frontal direct solver the computational cost is $\mathcal{O}\left(\left(n_{\text{dofs}}^{(d-1)/d}\right)^3\right)$ for the C^0 case and $\mathcal{O}\left(\left(n_{\text{dofs}}^{(d-1)/d}p\right)^3\right)$ for the C^{p-1} case [42]. In other words, IGA is $\mathcal{O}\left(p^3\right)$ times more expensive than traditional FEA per unknown. This difference is reduced when performing iterative solvers considering the cost of one iteration, the total number of iterations and precoditioning.

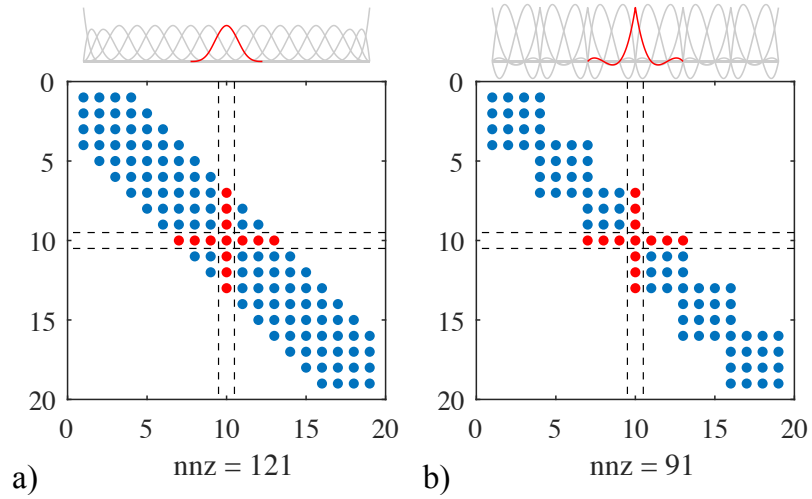

Figure 5.7: Sparsity of the stiffness matrix: a) Cubic B–splines b) Cubic Lagrange basis functions [adapted from 69].

Despite these drawbacks, Bazilevs et al. [15] showed that high inter–element continuity gives higher accuracy results in terms of dofs in comparison to C^0 finite elements.

Another important advantage is that the control over inter–element continuity allows for direct discretization of higher–order continuum such as second gradient continua. In the mixed formulation presented in the previous chapter, the discretization of the weak form requires the displacement, its gradient and the Lagrange multiplier as independent unknown fields. Therefore, a higher number of dofs has to be used in comparison to C^{p-1} continuous elements. This fact is clearly seen in Tab. 5.1, in which several finite elements have been proposed for a higher-order continuum: Hermite element in Petera and Pittman [134], Zervos A. et al. [188] and Papanicolopulos et al. [131]; Penalty Quad8U4P/Bri20U8P in Zervos [187]; Implicit element in Askes and Gutiérrez [10];

Element with Lagrange multipliers Matsushima et al. [115]; Element with QU34L4 Lagrange Shu et al. [155]; Form III, III9–70 Amanatidou and Aravas [3]. It is important to highlight the increase of dofs in the case of 3D finite elements.

Table 5.1: Number of degrees of freedom for different quadrilaterals and hexahedra used with gradient models (Adapted from Papanicolopulos et al. [131]). Number in parentheses are theoretical estimates, as the respective elements have not been presented in literature.

Element	2D dofs		3D dofs	
	total	u field	total	u field
Hermite element	32	32	192	192
Penalty Quad8U4P/Bri20U8P	32	16	132	60
Implicit element	32	8	(144)	(24)
Element with Lagrange multipliers	36	16	(141)	(60)
Element with QU34L4 Lagrange multipliers	38	18	(162)	(81)
Form III, III9–70	70	18	(396)	(81)

Our second gradient formulation should employ at least C^1 continuous basis functions for the displacement field. IGA elements satisfy this requirement without any additional assumption, *i.e.* Quadratic B–splines with 18 (2D case) and 81 (3D case) control variables (dofs); Cubic B–splines with 32 (2D case) and 192 (3D case) control variables (dofs). Fig. 5.8 shows the control points (blue squares) that define the quadratic and the cubic B–spline elements of a 2D geometry; hence two control variables per control point.

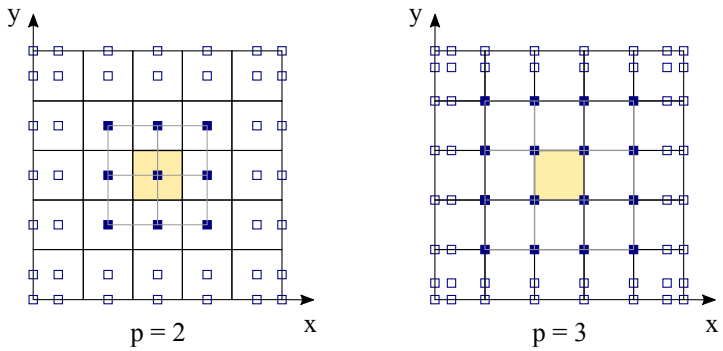

Figure 5.8: Control points for quadratic and cubic B–spline elements in 2D.

In practice, if we want to maximize computational efficiency, Quadratic B–splines should

be used. Marussig et al. [113] derived the floating point operations (FLOPS) for the evaluation of B–spline and NURBS basis functions and their derivatives. Fig. 5.9 shows a comparison of the number of FLOPS for different 2D basis functions and their derivatives: B–splines, NURBS and Lagrange and Serendipity. B–splines show the lowest computational cost for evaluating the basis functions and their derivatives. It is also important to remark that NURBS derivatives provide the highest computational cost due to the additional operations in which weights are involved.

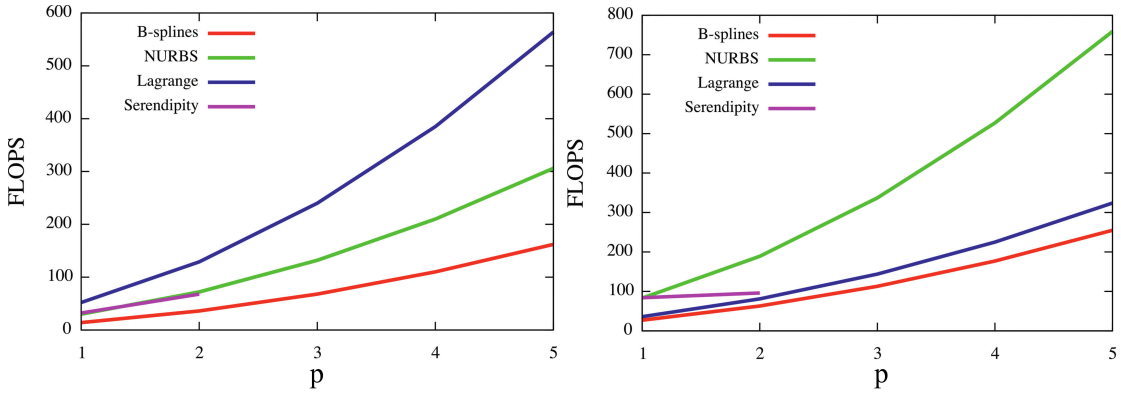

Figure 5.9: Number of floating point operations (FLOPS) for evaluating a) 2D basis functions of various orders p and b) their first derivatives. Results for serendipity functions are only shown for up to order 2 [16].

Part II

The development of a geomechanics IGA-FEM code

Chapter 6

Formulation of governing equations

This chapter develops the governing equations for the description of the coupled hydromechanical behavior of partially saturated soils.

There are two approaches for modeling multiphasic porous media. Phenomenological theory [24] and mixture theories [29], integrated by the concept of volume fractions with the balance equations written at macroscopic level, belong to the first strategy. Averaging theories [80, 81], belong to the second one, in which the corresponding equations at the macroscopic level are obtained by suitable averaging techniques after defining the conservation and constitutive equations at microscopic level.

Lewis and Schrefler [107] combine aspects of the classical mixture theories and averaging theories called hybrid mixture theory. In this approach, the balance equations are developed at the microscopic level and averaged to obtain the corresponding macroscopic equations. The constitutive equations are directly developed at the macroscopic level.

The mathematical model presented here is developed following the mixture theories. Thus, the governing equations are derived from the balance equations for each phase at the macroscopic scale, with proper exchange equations between phases.

6.1 Fundamental assumptions

The major assumptions made are that the gas pressure is negligible in comparison to the liquid pressure and the solid stresses, and the gas density is negligible in comparison to the solid and fluid densities. Therefore, the primary variables that describe the behavior of partially saturated soils are:

- Displacements
- Pore pressure in the liquid phase

The model is also restricted to the following assumptions:

a) Linear kinematics (small strains);

b) Solid phase is incompressible;

c) Compressibility of fluid is constant;

d) Inertia effects are negligible;

e) Darcy's law applies to pore fluid flow description;

f) Solid skeleton behaviour defined in terms of suction and Bishop–Schrefler stress; see Section 6.3;

g) Normal stresses are considered positive for traction, in agreement with continuum mechanics sign convention (pore fluid pressure is positive in compression);

h) No mass exchange between solid and liquid phases;

i) No thermal effects are taken into account.

6.2 Balance of Mass

6.2.1 Local and material time derivatives

This section starts by introducing the main concepts needed to develop the balance of mass of each phase. The material derivative of a quantity $f(\boldsymbol{x}, t)$, given in its spatial

description with respect to a moving particle of the π phase is given by:

$$\frac{\mathrm{d}^{\pi} f}{\mathrm{d}t} = \frac{\partial f}{\partial t} + \nabla f \cdot \boldsymbol{v}^{\pi} \tag{6.1}$$

where the first term of the right hand side (r.h.s) is the local time derivative and the second term represents the convective part, $\boldsymbol{v}^{\pi}$ being the velocity of the π phase in the spatial description.

If we consider the same particle moving with the α phase, the material time derivative of $f(\boldsymbol{x}, t)$ is

$$\frac{\mathrm{d}^{\alpha} f}{\mathrm{d}t} = \frac{\partial f}{\partial t} + \nabla f \cdot \boldsymbol{v}^{\alpha} \tag{6.2}$$

Subtraction of eq. (6.1) from eq. (6.2) yields the following relation:

$$\frac{\mathrm{d}^{\alpha} f}{\mathrm{d}t} = \frac{\mathrm{d}^{\pi} f}{\mathrm{d}t} + \nabla f \cdot \boldsymbol{v}^{\alpha\pi} \tag{6.3}$$

where $\boldsymbol{v}^{\alpha\pi}$ is the velocity of the α phase with respect to the π phase and it is expressed as follows:

$$\boldsymbol{v}^{\alpha\pi} = \boldsymbol{v}^{\alpha} - \boldsymbol{v}^{\pi} \tag{6.4}$$

The motion of the fluid and gas phases are described in terms of mass–averaged velocities relative to the solid phase in the poromechanics framework. The superscripts π now can be replaced by s for the solid phase, w for the liquid phase and g for the gas phase:

$$\boldsymbol{v}^{ws} = \boldsymbol{v}^{w} - \boldsymbol{v}^{s}, \qquad \boldsymbol{v}^{gs} = \boldsymbol{v}^{g} - \boldsymbol{v}^{s} \tag{6.5}$$

where $\boldsymbol{v}^{ws}$ and $\boldsymbol{v}^{gs}$ are the relative velocities of fluid and gas phases with respect to the solid phase, respectively.

The material time derivative of the material volume $\mathrm{d}v$ with respect to the phase π can be expressed as

$$\frac{\mathrm{d}^{\pi}}{\mathrm{d}t}\left(\mathrm{d}v\right) = \left(\nabla \cdot \boldsymbol{v}^{\pi}\right) \mathrm{d}v \tag{6.6}$$

6.2.2 Volume fractions of phases

Let v_s, v_w, and v_g be the volume fractions of the solid, liquid, and gas phases (see Fig. 6.1). Then

$$v_s + v_w + v_g = 1, \qquad v_v = v_w + v_g \tag{6.7}$$

where v_v is the volume fraction of void.

The parameters that are commonly used in poromechanics to measure the relations between the volumes of the constituents of a three–phase soil are:

$$\begin{aligned} S_w &= \frac{v_w}{v_v}, \qquad n = \frac{v_v}{v}, \qquad e = \frac{v_v}{v_s} \\ S_g &= 1 - S_w, \quad n = \frac{e}{1+e}, \quad e = \frac{n}{1-n} \end{aligned} \tag{6.8}$$

where S_w and S_g are the degree of saturation of the liquid and the gas phases respectively, n is the porosity, and e is the void ratio.

Let ρ_s, ρ_w and ρ_g be the solid particle, liquid and gas mass densities respectively, so that $(1-n)\rho_s \, \mathrm{d}v$ is the skeleton mass, $nS_w\rho_w \, \mathrm{d}v$ is the liquid mass, and $nS_g\rho_g \, \mathrm{d}v$ is the gas mass density, all of them are currently contained in the material volume $\mathrm{d}v$. Now the principle of the conservation of mass is applied to each phase separately.

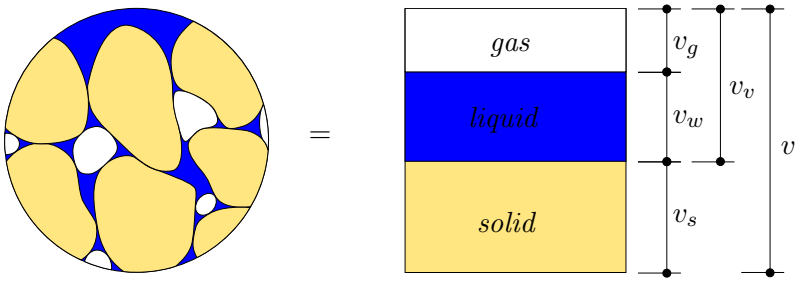

Figure 6.1: Soil composition.

6.2.3 Balance of mass

The principle of conservation of mass states that mass cannot be destroyed. When no mass change occurs, the balance of mass can be expressed in the form

$$\frac{\mathrm{d}^{\pi}}{\mathrm{d}t}\int_{\mathcal{B}}\mathrm{d}m = \frac{\mathrm{d}^{\pi}}{\mathrm{d}t}\int_{\mathcal{B}}\rho\,\mathrm{d}v = \int_{\mathcal{B}}\frac{\mathrm{d}^{\pi}}{\mathrm{d}t}\left(\rho\,\mathrm{d}v\right) = 0 \tag{6.9}$$

if we expand eq. (6.9) and then use (6.6), we rewrite eq. (6.9) in the form:

$$\int_{\mathcal{B}}\left(\frac{\mathrm{d}^{\pi}\rho}{\mathrm{d}t}\mathrm{d}v + \rho\frac{\mathrm{d}}{\mathrm{d}t}(\mathrm{d}v)\right) = \int_{\mathcal{B}}\left(\frac{\mathrm{d}^{\pi}\rho}{\mathrm{d}t} + \rho\nabla\cdot\boldsymbol{v}^{\pi}\right)\mathrm{d}v = 0 \tag{6.10}$$

eq. (6.1) allows us to write eq. (6.10) as

$$\int_{\mathcal{B}}\left(\frac{\partial\rho}{\partial t} + \nabla\cdot(\rho\boldsymbol{v}^{\pi})\right)\mathrm{d}v = 0 \tag{6.11}$$

or equivalently:

$$\frac{\partial\rho}{\partial t} + \nabla\cdot(\rho\boldsymbol{v}^{\pi}) = 0 \tag{6.12}$$

6.2.3.1 Solid phase

The local form of the balance of mass for the solid phase is written as

$$\frac{\partial}{\partial t}\left((1-n)\rho_s\right) + \nabla\cdot\left((1-n)\rho_s\boldsymbol{v}^{s}\right) = 0 \tag{6.13}$$

We develop the two terms of the left hand side (l.h.s) of eq. (6.13) and divide by ρ_s:

$$-\frac{\partial n}{\partial t} + (1-n)\frac{1}{\rho_s}\frac{\partial\rho_s}{\partial t} + (1-n)\frac{1}{\rho_s}\nabla\rho_s\cdot\boldsymbol{v}^{s} - \nabla n\cdot\boldsymbol{v}^{s} + (1-n)\nabla\cdot\boldsymbol{v}^{s} = 0 \tag{6.14}$$

Using eq. (6.1), we finally obtain:

$$-\frac{\mathrm{d}^{s}n}{\mathrm{d}t} + (1-n)\frac{1}{\rho_s}\frac{\mathrm{d}^{s}\rho_s}{\mathrm{d}t} + (1-n)\nabla\cdot\boldsymbol{v}^{s} = 0 \tag{6.15}$$

6.2.3.2 Liquid phase

The local form of the balance of mass for the liquid phase is written as

$$\frac{\partial}{\partial t}\left(nS_w\rho_w\right) + \nabla\cdot\left(nS_w\rho_w\boldsymbol{v}^w\right) = 0 \tag{6.16}$$

We develop the two terms of the l.h.s. of eq. (6.16), and then divide by $S_w\rho_w$:

$$n\frac{1}{\rho_w}\frac{\partial\rho_w}{\partial t} + \frac{\partial n}{\partial t} + n\frac{1}{S_w}\frac{\partial S_w}{\partial t} + n\frac{1}{\rho_w}\nabla\rho_w\cdot\boldsymbol{v}^w + \nabla n\cdot\boldsymbol{v}^w + n\frac{1}{S_w}\nabla S_w\cdot\boldsymbol{v}^w + n\nabla\cdot\boldsymbol{v}^w = 0 \tag{6.17}$$

Using eq. (6.1), and then considering the material derivative with respect to the solid phase (see eq. (6.3)), we have:

$$\frac{\mathrm{d}^w n}{\mathrm{d}t} + n\frac{1}{\rho_w}\frac{\mathrm{d}^w\rho_w}{\mathrm{d}t} + n\frac{1}{S_w}\frac{\mathrm{d}^w S_w}{\mathrm{d}t} + n\nabla\cdot\boldsymbol{v}^w = 0 \tag{6.18a}$$

$$\frac{\mathrm{d}^s n}{\mathrm{d}t} + \nabla n\cdot\boldsymbol{v}^{ws} + n\frac{1}{\rho_w}\frac{\mathrm{d}^s\rho_w}{\mathrm{d}t} + n\frac{1}{\rho_w}\nabla\rho_w\cdot\boldsymbol{v}^{ws} + n\frac{1}{S_w}\frac{\mathrm{d}^s S_w}{\mathrm{d}t} + \frac{n}{S_w}\nabla S_w\cdot\boldsymbol{v}^{ws} + n\nabla\cdot\boldsymbol{v}^{ws} + n\nabla\cdot\boldsymbol{v}^s = 0 \tag{6.18b}$$

and since:

$$\frac{1}{S_w\rho_w}\nabla\cdot\left(nS_w\rho_w\boldsymbol{v}^{ws}\right) = \nabla n\cdot\boldsymbol{v}^{ws} + n\frac{1}{\rho_w}\nabla\rho_w\cdot\boldsymbol{v}^{ws} + n\frac{1}{S_w}\nabla S_w\cdot\boldsymbol{v}^{ws} + n\nabla\cdot\boldsymbol{v}^s \tag{6.19}$$

we finally have:

$$\frac{\mathrm{d}^s n}{\mathrm{d}t} + \frac{n}{\rho_w}\frac{\mathrm{d}^s\rho_w}{\mathrm{d}t} + \frac{n}{S_w}\frac{\mathrm{d}^s S_w}{\mathrm{d}t} + n\nabla\cdot\boldsymbol{v}^s + \frac{1}{S_w\rho_w}\nabla\cdot\left(nS_w\rho_w\boldsymbol{v}^{ws}\right) = 0 \tag{6.20}$$

6.2.3.3 Solid phase + liquid phase

By summing eqs. (6.15) and (6.20), the balance of mass for the solid and liquid phases is obtained as

$$(1-n)\frac{1}{\rho_s}\frac{\mathrm{d}^s\rho_s}{\mathrm{d}t} + n\frac{1}{\rho_w}\frac{\mathrm{d}^s\rho_w}{\mathrm{d}t} + \frac{n}{S_w}\frac{\mathrm{d}^s S_w}{\mathrm{d}t} + \nabla\cdot\boldsymbol{v}^s + \frac{1}{S_w\rho_w}\nabla\cdot\left(nS_w\rho_w\boldsymbol{v}^{ws}\right) = 0 \tag{6.21}$$

Considering the solid as incompressible, $\mathrm{d}^s\rho_s/\mathrm{d}t = 0$, eq. (6.21) simplifies into (after multiplication by S_w):

$$\frac{nS_w}{\rho_w}\frac{\mathrm{d}^s\rho_w}{\mathrm{d}t} + n\frac{\mathrm{d}^sS_w}{\mathrm{d}t} + S_w\nabla\cdot\boldsymbol{v}^s + \frac{1}{\rho_w}\nabla\cdot(nS_w\rho_w\boldsymbol{v}^{ws}) = 0 \tag{6.22}$$

eq. (6.22) can be simplified further by assuming:

$$\nabla\rho_w \approx 0 \tag{6.23a}$$

$$\frac{1}{\rho_w}\frac{\mathrm{d}^w\rho_w}{\mathrm{d}t} \approx \frac{1}{\rho_w}\frac{\mathrm{d}^s\rho_w}{\mathrm{d}t} \tag{6.23b}$$

$$\nabla\cdot(nS_w\rho_w\boldsymbol{v}^{ws}) \approx \rho_w\nabla\cdot(nS_w\boldsymbol{v}^{ws}) \tag{6.23c}$$

Thus eq. (6.22) reads:

$$\frac{nS_w}{\rho_w}\frac{\mathrm{d}^w\rho_w}{\mathrm{d}t} + n\frac{\mathrm{d}^sS_w}{\mathrm{d}t} + \nabla\cdot\boldsymbol{w}^w + S_w\nabla\cdot\boldsymbol{v}^s = 0 \tag{6.24}$$

where $\boldsymbol{w}^w$ is the relative flow vector of fluid mass with respect to the solid phase:

$$\boldsymbol{w}^w = nS_w\boldsymbol{v}^{ws} \tag{6.25}$$

Eq. (6.24) will be further developed in chapter 8, once the constitutive equations are defined in the following chapter.

6.3 Balance of linear momentum (classical continuum mechanics)

The linear momentum equation for the solid phase is

$$\int_{\mathcal{B}}\rho\boldsymbol{b}\,\mathrm{d}v + \int_{\partial\mathcal{B}}\bar{\boldsymbol{t}}\,\mathrm{d}a = \boldsymbol{0} \tag{6.26a}$$

$$\int_{\mathcal{B}}\rho\boldsymbol{b}\,\mathrm{d}v + \int_{\mathcal{B}}\boldsymbol{\sigma}\cdot\boldsymbol{n}\,\mathrm{d}v = \boldsymbol{0} \tag{6.26b}$$

$$\int_{\mathcal{B}}\rho\boldsymbol{b}\,\mathrm{d}v + \int_{\mathcal{B}}\nabla\cdot\boldsymbol{\sigma}\,\mathrm{d}v = \boldsymbol{0} \tag{6.26c}$$

where $\boldsymbol{\sigma}$ is the total stress tensor, $\boldsymbol{n}$ is the outer normal to $\mathcal{B}$, $\bar{\boldsymbol{t}}$ is the traction force, $\boldsymbol{b}$ is the body force vector and ρ is the averaged density of the multiphase medium:

$$\rho = (1-n)\rho_s + nS_w\rho_w + nS_g\rho_g \approx (1-n)\rho_s + nS_w\rho_w \tag{6.27}$$

this leads to the following local form for the balance of linear momentum equilibrium:

$$\nabla \cdot \boldsymbol{\sigma} + \rho \boldsymbol{b} = \mathbf{0} \tag{6.28}$$

Regarding the mechanical behavior in fully saturated soils, the principle of classical soil mechanics states that the solid skeleton is governed by the Terzaghi's effective stress tensor:

$$\boldsymbol{\sigma}' = \boldsymbol{\sigma} + p_w \mathbf{1} \tag{6.29}$$

However, the mechanical behavior of partially saturated soils is different due to the fact that the liquid and the gas phases have a direct impact on the state of stress. Bishop [25] introduced the notion of generalized effective stress $\boldsymbol{\sigma}''$:

$$\boldsymbol{\sigma}'' = (\boldsymbol{\sigma} + p_g \mathbf{1}) - \chi\,(p_g - p_w)\,\mathbf{1} \tag{6.30}$$

in which, $\mathbf{1}$ is the identity tensor, $(\boldsymbol{\sigma} + p_g\mathbf{1})$ is the net stress tensor. In eq. (6.30), χ is Bishop's effective stress parameter which depends on degree of saturation S_w, being equal to zero for perfectly dry soil and unity for fully saturated soil. The difference $(p_g - p_w)$ between the pore gas pressure and pore liquid pressure is called matric suction, s, and is related to the degree of saturation by means of a specific constitutive equation (the soil–water characteristic curve).

Jennings and Burland [92] demonstrated the inability of eq. (6.30) to model partially saturated soils using the critical state framework defined for saturated soils. For example, to predict wetting induced collapse.

The first elastoplastic constitutive model for partially saturated soils was presented by Alonso et al. [2]. The Barcelona Basic Model (BBM) describes soil's behavior using two independent stress tensors. Jommi and Di Prisco [96], Wheeler et al. [186], Gallipoli et al. [67], Georgiadis [71], Sheng et al. [154], Nuth and Laloui [126] and others have

replaced χ by the degree of saturation, S_w. Other expressions for χ include some function of suction [98]. A detailed overview of the matter is given by Nuth and Laloui [126].

In this work, the mechanical behavior of partially saturated soil is modeled using the approach proposed by Jommi and Di Prisco [96]. They proposed to introduce the dependence of the hardening variables on S_w to simulate effects of suction in partially saturated soils (see chapter 7). In their work, eq. (6.30) is expressed as follows:

$$\boldsymbol{\sigma}'' = \boldsymbol{\sigma} + S_w p_w \mathbf{1} + (1 - S_w) p_g \mathbf{1} \tag{6.31}$$

and assuming that p_g is negligible in comparison to the liquid pressure and the solid stresses, we have:

$$\boldsymbol{\sigma}'' = \boldsymbol{\sigma} + S_w p_w \mathbf{1} \tag{6.32}$$

Note that we recover the fully saturated conditions for $S_w = 1$.

Finally, eq. 6.28 is rewritten in terms of constitutive stresses as follows:

$$\nabla \cdot \boldsymbol{\sigma}'' - \nabla(S_w p_w) + \rho \boldsymbol{b} = \mathbf{0} \tag{6.33}$$

6.4 Balance of angular momentum

The time–variation of the angular momentum of a material volume with respect to a fixed point is equal to the resultant moment with respect this fixed point.

$$\frac{\mathrm{d}}{\mathrm{d}t} \int_{\mathcal{B}} \boldsymbol{r} \times \rho \boldsymbol{v} \, \mathrm{d}v = \boldsymbol{M}_0(t) \tag{6.34}$$

where

$$\boldsymbol{M}_0(t) = \int_{\mathcal{B}} \boldsymbol{r} \times \rho \boldsymbol{b} \, \mathrm{d}v + \int_{\partial\mathcal{B}} \boldsymbol{r} \times \boldsymbol{t} \, \mathrm{d}a \tag{6.35}$$

The global form of the balance of angular momentum reads:

$$\int_{\mathcal{B}} \boldsymbol{r} \times \rho \boldsymbol{b} \, \mathrm{d}v + \int_{\partial\mathcal{B}} \boldsymbol{r} \times \boldsymbol{t} \, \mathrm{d}a = \frac{\mathrm{d}}{\mathrm{d}t} \int_{\mathcal{B}} \boldsymbol{r} \times \rho \boldsymbol{v} \, \mathrm{d}v \tag{6.36}$$

Knowing that $\boldsymbol{t} = \boldsymbol{\sigma}\boldsymbol{n}$ and using the divergence theorem,

$$\begin{aligned}\int_{\partial\mathcal{B}} \boldsymbol{r} \times \boldsymbol{t}\,\mathrm{d}a &= \int_{\partial\mathcal{B}} \boldsymbol{r} \times \boldsymbol{\sigma} \cdot \boldsymbol{n}\,\mathrm{d}a = \int_{\partial\mathcal{B}} (\boldsymbol{r} \times \boldsymbol{\sigma}) \cdot \boldsymbol{n}\,\mathrm{d}a \\ &= \int_{\mathcal{B}} \boldsymbol{\nabla} \cdot (\boldsymbol{r} \times \boldsymbol{\sigma})\ \mathrm{d}v = \int_{\mathcal{B}} \{(\boldsymbol{r} \times \nabla \cdot \boldsymbol{\sigma}) + \varepsilon_{ijk}\sigma_{jk}\hat{\boldsymbol{e}}_i\}\ \mathrm{d}v\end{aligned} \tag{6.37}$$

Applying Reynolds Lemma to the right–hand term of eq. (6.36) we have:

$$\begin{aligned}\frac{\mathrm{d}}{\mathrm{d}t}\int_{\mathcal{B}} \boldsymbol{r} \times \rho\boldsymbol{v}\,\mathrm{d}v &= \frac{\mathrm{d}}{\mathrm{d}t}\int_{\mathcal{B}} \rho\,(\boldsymbol{r} \times \boldsymbol{v})\ \mathrm{d}v = \int_{\mathcal{B}} \rho\frac{\mathrm{d}}{\mathrm{d}t}\,(\boldsymbol{r} \times \boldsymbol{v})\ \mathrm{d}v \\ &= \int_{\mathcal{B}} \rho\left(\frac{\mathrm{d}\boldsymbol{r}}{\mathrm{d}t} \times \boldsymbol{v} + \boldsymbol{r} \times \frac{\mathrm{d}\boldsymbol{v}}{\mathrm{d}t}\right)\mathrm{d}v = \int_{\mathcal{B}} \boldsymbol{r} \times \rho\frac{\mathrm{d}\boldsymbol{v}}{\mathrm{d}t}\,\mathrm{d}v\end{aligned} \tag{6.38}$$

Then, the global form is rewritten:

$$\int_{\mathcal{B}} \{\boldsymbol{r} \times (\rho\boldsymbol{b} + \nabla \cdot \boldsymbol{\sigma}) + \varepsilon_{ijk}\sigma_{jk}\hat{\boldsymbol{e}}_i\}\ \mathrm{d}v = \int_{\mathcal{B}} \boldsymbol{r} \times \rho\frac{\mathrm{d}\boldsymbol{v}}{\mathrm{d}t}\,\mathrm{d}v \tag{6.39}$$

Using eq. (6.28) and considering that for quasi–static processes $\mathrm{d}\boldsymbol{v}/\mathrm{d}t \approx \boldsymbol{0}$, eq. (6.39) finally yields:

$$\varepsilon_{ijk}\sigma_{jk} = 0 \tag{6.40}$$

Making use of the property $\varepsilon_{ijk} = \varepsilon_{irs}\varepsilon_{ijk} = \delta_{rj}\delta_{sk} - \delta_{rk}\delta_{sj}$, eq. (6.40) leads to

$$\boldsymbol{\sigma} = \boldsymbol{\sigma}^T, \quad \sigma_{jk} = \sigma_{kj} \tag{6.41}$$

The final outcome of the balance angular momentum is that the Cauchy total stress is symmetric.

6.5 Balance of linear momentum (local second gradient model)

Here we recall the balance of linear momentum for a second gradient continuum (see eq. (4.7)):

$$\nabla \cdot (\boldsymbol{\sigma} - \nabla \cdot \boldsymbol{\Sigma}) + \rho \boldsymbol{b} = \mathbf{0} \tag{6.42}$$

and remark that the double stress tensor $\boldsymbol{\Sigma}$ has no link with the pore pressure. Therefore, eq. (6.42) is rewritten as follows:

$$\nabla \cdot \left(\boldsymbol{\sigma}'' - S_w p_w - \nabla \cdot \boldsymbol{\Sigma}\right) + \rho \boldsymbol{b} = \mathbf{0} \tag{6.43}$$

Chapter 7

Formulation of constitutive models

The governing equations presented in the preceding chapter are completed in this chapter with the constitutive models describing the mechanical and hydraulic behavior of a porous medium in partially saturated conditions.

The mechanical behavior of the solid skeleton consisting in a second gradient material is described by two independent plastic mechanisms with their respective yield functions. Two elastoplastic constitutive models describing the standard part are outlined. The first one is used for validation purposes and the second one for describing a wide range of soils and soft rocks.

In addition to the constitutive model used in the works of Bésuelle et al. [19], Collin et al. [44], Matsushima et al. [115] for describing the second gradient part, a new isotropic elastic constitutive model is presented derived from the work of Mindlin [118] containing two elastic parameters. This model will be used for modeling 3D problems. Then, these linear models are extended to a simple elastoplastic second gradient constitutive model with two different hardening laws to incorporate inelastic behavior in the second gradient part of the constitutive equation.

7.1 Hydraulic constitutive models

7.1.1 Compressibility of water

In isothermal conditions, the density of the water depends only on the fluid pore pressure p_w and can be expressed as follows Lewis and Schrefler [107]:

$$\rho_w = \rho_{w0} \exp\{C_w(p_w - p_{w0})\} \tag{7.1}$$

where C_w is the liquid compressibility coefficient, ρ_{w0} the reference liquid density and p_{w0} the reference liquid pore pressure.

By retaining the first–order terms of the series expansion of eq. (7.1), we obtain:

$$\rho_w = \rho_{w0}\{1 + C_w(p_w - p_{w0})\} \tag{7.2}$$

Note that in this case, having assumed $\nabla\rho_w = 0$, we have:

$$\frac{1}{\rho_w}\frac{\mathrm{d}^w\rho_w}{\mathrm{d}t} \cong \frac{1}{\rho_w}\frac{\mathrm{d}^s\rho_w}{\mathrm{d}t} = C_w\frac{\mathrm{d}^s p_w}{\mathrm{d}t} \tag{7.3}$$

7.1.2 Soil–water characteristic curve

The soil–water characteristic curve (SWCC) describes the corresponding constitutive relationship between soil suction and soil–water content. The SWCC can describe either an adsorption (*i.e.*, wetting) process or a desorption (*i.e.* drying) process. Differentiation between wetting characteristic curves and drying characteristic curves is typically required to account for the significant hysteresis that can occur between the two branches of behavior. More water is generally retained by soil during a drying process than is adsorbed by the soil for the same value of suction during a wetting process [111]. However, in this work, hydraulic hysteresis effects are neglected for simplicity.

Van Genuchten [175], proposed a smooth SWCC that is expressed as:

$$S_e = (1 + (a_{sw}s)^{n_{sw}})^{-m_{sw}}\,, \qquad S_w = S_{\mathrm{res}} + (S_{\max} - S_{\mathrm{res}})\,S_e \tag{7.4}$$

where S_e, S_{res} and $S_{\max}$ are the effective, residual and maximum water degree of saturation respectively, a_{sw} is the inverse of air–entry pressure and n_{sw} is the pore–size distribution parameter. s is the matric suction that represents the difference between the pore gas pressure and pore fluid pressure. The parameter m_{sw} is frequently constrained by a direct relation to the parameter n_{sw}, assuming $m_{sw} = 1 - 1/n_{sw}$.

Considering the variation of suction in eq. (7.4), the definition of the time derivative of the degree of saturation is:

$$\frac{\mathrm{d}^s S_w}{\mathrm{d}t} = \frac{\partial S_w}{\partial s}\frac{\mathrm{d}^s s}{\mathrm{d}t} = \frac{\partial S_w}{\partial s}\left(\frac{\mathrm{d}^s p_g}{\mathrm{d}t} - \frac{\mathrm{d}^s p_w}{\mathrm{d}t}\right) \approx \frac{\partial S_w}{\partial s}\left(-\frac{\mathrm{d}^s p_w}{\mathrm{d}t}\right) \tag{7.5}$$

Setting

$$C_s := -n\frac{\partial S_w}{\partial s} \tag{7.6}$$

as the specific moisture content, we have:

$$\frac{\mathrm{d}^s S_w}{\mathrm{d}t} = \frac{C_s}{n}\frac{\mathrm{d}^s p_w}{\mathrm{d}t} \tag{7.7}$$

7.1.3 Permeability functions

Permeability is also influenced by the degree saturation. The permeability tensor is described as:

$$\boldsymbol{k}_w = k_w^{\text{rel}}\boldsymbol{k}_{\text{sat}} \tag{7.8}$$

where $\boldsymbol{k}_{\text{sat}}(e)$ is the permeability tensor in saturated conditions depending on the void ratio and $k_w^{\text{rel}}(S_e) \in [0,1]$, is the relative permeability. Mualem [121] uses the Van Genuchten constants to model the relative permeability, $k_w^{\text{rel}}(S_e)$ and it is expressed as follows:

$$k_w^{\text{rel}}(S_e) = \sqrt{S_e}\left[1 - \left(1 - S_e^{n_{sw}/(n_{sw}-1)}\right)^{1-1/n_{sw}}\right]^2 \tag{7.9}$$

where n_{sw} is the same constant as in eq. (7.4).

7.1.4 Darcy's law

Setting $\boldsymbol{w}^w = nS_w\boldsymbol{v}^{ws}$, the generalized Darcy's law for water flow in the porous medium is written as:

$$\boldsymbol{w}^w = -\frac{1}{\mu_w}\boldsymbol{k}_w(\nabla p_w - \rho_w \boldsymbol{b}) \tag{7.10}$$

where $\boldsymbol{k}_w$ is given by eq. (7.8) and μ_w is the dynamic viscosity of the fluid.

7.2 Mechanical constitutive models. First gradient part

In the representation of stress and strain states, the following invariant quantities will be used:

$$\begin{aligned} &p'' := \frac{1}{3}\operatorname{tr}(\boldsymbol{\sigma}''), \quad q := \sqrt{\frac{3}{2}}||\boldsymbol{\sigma}_{\text{dev}}|| = \sqrt{\frac{3}{2}\boldsymbol{\sigma}_{\text{dev}}\cdot\boldsymbol{\sigma}_{\text{dev}}}\ , \quad \sin(3\theta) := \sqrt{6}\frac{\operatorname{tr}\left(\boldsymbol{\sigma}_{\text{dev}}^3\right)}{\left\{\operatorname{tr}\left(\boldsymbol{\sigma}_{\text{dev}}^3\right)\right\}^{3/2}} \\ &\varepsilon_v := \operatorname{tr}(\boldsymbol{\varepsilon}) \qquad \varepsilon_s := \sqrt{\frac{2}{3}}||\boldsymbol{e}|| \end{aligned} \tag{7.11}$$

where p'' is the isotropic generalized stress invariant, q is the deviatoric stress invariant and θ is Lode's angle. ε_v is the volumetric strain and ε_s is the deviatoric strain. And

$$\boldsymbol{\sigma}_{\text{dev}} := \boldsymbol{\sigma}'' - p''\mathbf{1} \qquad\qquad \boldsymbol{e} := \boldsymbol{\varepsilon} - \frac{1}{3}\varepsilon_v\mathbf{1} \tag{7.12}$$

being the deviatoric stress and deviatoric strain, respectively.

Since small strain framework is assumed, the strain and its rate can be additively decomposed into elastic and plastic parts as:

$$\boldsymbol{\varepsilon} = \boldsymbol{\varepsilon}^e + \boldsymbol{\varepsilon}^p \qquad\qquad \dot{\boldsymbol{\varepsilon}} = \dot{\boldsymbol{\varepsilon}}^e + \dot{\boldsymbol{\varepsilon}}^p \tag{7.13}$$

where superscripts e and p denote elastic and plastic parts, respectively.

7.2.1 Prandtl–Reuss model

This first model is based on the Prandtl–Reuss elastoplastic model; it is a simple constitutive model that has been used in different works for validation purposes of second gradient models [see 19, 44, 115]. Therefore, this model will help us in this purpose and will allow us to develop confidence in the proposed computational approach before addressing the implementation of more realistic soil plasticity models. Fig. 7.1 shows the relationship given by the invariants S and E defined by:

$$S = ||\boldsymbol{\sigma}_{\text{dev}}|| = \sqrt{\boldsymbol{\sigma}_{\text{dev}} \cdot \boldsymbol{\sigma}_{\text{dev}}} \ , \qquad E = \sqrt{\boldsymbol{e} \cdot \boldsymbol{e}} \tag{7.14}$$

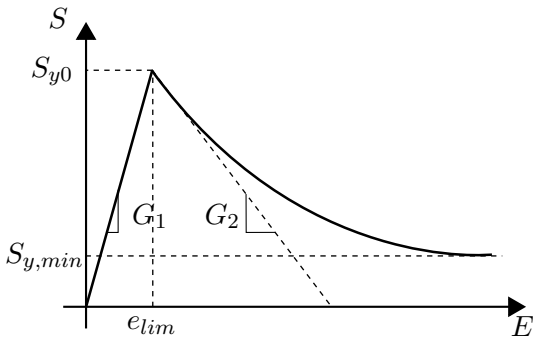

Figure 7.1: E–S relationship of the Prandtl–Reuss model with exponential hardening law.

The elastic constitutive equations for $E > e_{lim}$ are given by:

$$\dot{p}'' := K\dot{\varepsilon}_v^e \ , \qquad \dot{\boldsymbol{\sigma}}_{\text{dev}} := 2G_1\dot{\boldsymbol{e}}^e = 2G_1\left\{\dot{\boldsymbol{e}} - \dot{\boldsymbol{e}}^p\right\} \ , \qquad \dot{\boldsymbol{\sigma}}'' := \dot{\boldsymbol{\sigma}}_{\text{dev}} + \dot{p}''\mathbf{1} \tag{7.15}$$

where G_1 is the shear modulus and K is the bulk modulus.

The hydrostatic pressure is independent of plastic deformation, therefore the yield surface function is defined using the deviatoric stress alone:

$$f(S, S_y) = S - S_y = 0 \tag{7.16}$$

where S_y is the yield stress.

We assumed an associated flow rule:

$$\dot{e}^p = \dot{\lambda}_\varepsilon \frac{\partial f}{\partial \boldsymbol{\sigma}_{\text{dev}}} = \dot{\lambda}_\varepsilon \frac{\boldsymbol{\sigma}_{\text{dev}}}{S} = \dot{\lambda}_\varepsilon \boldsymbol{\eta} \tag{7.17}$$

where $\dot{\lambda}_\varepsilon$ is the plastic consistency parameter (plastic multiplier) and $\boldsymbol{\eta} := \boldsymbol{\sigma}_{\text{dev}}/S$ is a unit deviatoric tensor normal to the yield surface.

The hardening rule is given by an exponential softening law:

$$\dot{S}_y = \dot{\lambda}_\varepsilon H_\varepsilon (S_y - S_{y,min}) \tag{7.18}$$

with

$$H_\varepsilon = \frac{2G_1 G_2}{(G_1 - G_2)(S_{y0} - S_{y,min})} \tag{7.19}$$

where H_ε is the plastic modulus, G_2 a plastic parameter and S_{y0} and $S_{y,min}$ are the initial and minimum yield stresses, respectively.

The Kuhn–Tucker complementarity conditions can be written as:

$$\dot{\lambda}_\varepsilon \geq 0, \qquad f(S, S_y) \leq 0, \qquad \dot{\lambda}_\varepsilon f(S, S_y) = 0 \tag{7.20}$$

and the consistency condition:

$$\dot{\lambda}_\varepsilon \dot{f}(S, S_y) = 0 \tag{7.21}$$

7.2.2 Milan model

In order to capture the relevant features of behavior of most geomaterials, a three–invariant isotropic–hardening elastoplastic model materials is used. This model introduced in the works of Tamagnini et al. [167] and Nova et al. [125], is capable of reproducing accurately the observed behavior of a wide range of geomaterials such as soils, cemented soils and soft rocks undergoing mechanical and environmental degradation process.

The yield surface function (see Fig. 7.2) and the plastic potential function are assumed to be given by the expressions proposed by Lagioia et al. [103]. Furthermore, due to the assumption of material isotropy, the internal variables describing the effects of

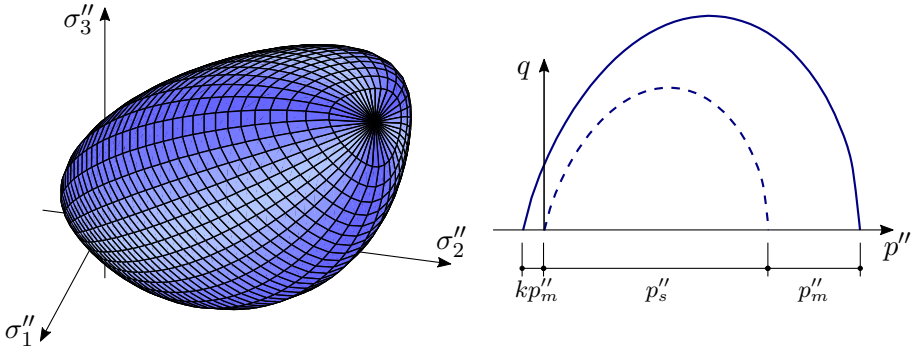

Figure 7.2: Yield surface in a) the principal stress space and b) the $p'' - q$ plane.

mechanical and non-mechanical processes are scalar and collected in vector $\boldsymbol{q}$. The yield surface function f and the plastic potential g depend on the generalized effective stress $\boldsymbol{\sigma}''$ through its invariants (p'', q, θ):

$$f(p'', q, \theta, p_s'', p_m'') = A_f^{K_{1f}/C_f} B_f^{-K_{2f}/C_f} p^* - p_c^* = 0 \tag{7.22}$$

$$g(p'', q, \theta, p_m'') = A_g^{K_{1g}/C_g} B_g^{-K_{2g}/C_g} p^* - \tilde{p}_c^* = 0 \tag{7.23}$$

where

$$K_{1\alpha} := \frac{m_\alpha\,(1 - a_\alpha)}{2\,(1 - m_\alpha)} \left\{ 1 + \sqrt{1 - \frac{4a_\alpha(1 - m_\alpha)}{m_\alpha(1 - a_\alpha)^2}} \right\} \tag{7.24a}$$

$$K_{2\alpha} := \frac{m_\alpha\,(1 - a_\alpha)}{2\,(1 - m_\alpha)} \left\{ 1 - \sqrt{1 - \frac{4a_\alpha(1 - m_\alpha)}{m_\alpha(1 - a_\alpha)^2}} \right\} \tag{7.24b}$$

$$A_\alpha := 1 + \frac{1}{K_{1\alpha} M_\alpha} \frac{q}{p^*} \tag{7.24c}$$

$$B_\alpha := 1 + \frac{1}{K_{2\alpha} M_\alpha} \frac{q}{p^*} \tag{7.24d}$$

$$C_\alpha := (1 - m_\alpha)(K_{1\alpha} - K_{2\alpha}) \tag{7.24e}$$

with $\alpha = f$ or g, and

$$p^* := p'' + p_t'' \;; \qquad p_c^* := p_c'' + p_t'' = p_s'' + p_m'' + p_t'' \;; \qquad \tilde{p}_c^* := \tilde{p}_c'' + p_t'' \tag{7.25}$$

in which

$$p_c'' := p_s'' + p_m'' \; ; \qquad\qquad p_t'' := k p_m'' \tag{7.26}$$

In the above expressions, the quantities a_f, m_f, a_g, m_g and k are material constants, while $\tilde{p}_c$ is a dummy parameter. p_s'' is an internal variable that plays the role of the preconsolidation pressure, as in classical critical–state models, and it is assumed to depend on soil microstructure in terms of grain arrangement and interactions (fabric) only. The internal variable p_m'' accounts for the effects of interparticle bonding. From the macroscopic point of view, the existence of such bonds is reflected by the development of a nonzero tensile strength.

In eqs. (7.24c) and (7.24d), the functions $M_\alpha = M_\alpha(\theta)$, which control the shape of the yield surface and plastic potential in the deviatoric plane, are taken from Van Eekelen [174].

The plastic strain rate tensor, $\dot{\boldsymbol{\varepsilon}}^p$, is provided by a standard flow rule:

$$\dot{\boldsymbol{\varepsilon}}^p = \dot{\lambda}_\varepsilon \frac{\partial g}{\partial \boldsymbol{\sigma}''} \left(\boldsymbol{\sigma}'', \boldsymbol{q} \right) \tag{7.27}$$

where $\boldsymbol{q}$ is the vector containing the internal variables p_s'' and p_m'':

$$\boldsymbol{q} := \left\{ p_s'', p_m'' \right\}^T \tag{7.28}$$

The evolution of the internal variables is provided by the following generalized hardening law [169]:

$$\dot{\boldsymbol{q}} = \dot{\lambda}_\varepsilon \boldsymbol{h}(\boldsymbol{\sigma}'', \boldsymbol{q}) + \boldsymbol{N} \left(\boldsymbol{q}, \boldsymbol{\alpha} \right) \dot{\boldsymbol{\alpha}} \tag{7.29}$$

where the first term in the r.h.s of eq. (7.29) controls the changes of the yield surface due to mechanical effects through of $\boldsymbol{h}$, and the second term controls the changes of the yield surface due to environmental processes, with

$$\boldsymbol{N} = [\boldsymbol{N}_{s_w}, \boldsymbol{N}_T, \boldsymbol{N}_c, \ldots] \tag{7.30}$$

and

$$\boldsymbol{\alpha} = \{S_w, T, c, ...\}^T \tag{7.31}$$

is an environmental process variable vector that may contains: the degree of saturation S_w, temperature T, concentration of chemical specie present in the soil responsible for chemo/mechanical processes c, etc.

Eq. (7.29) can be specialized for the case of having only the degree of saturation as environmental process variable:

$$\boldsymbol{N}_{s_w} = \begin{Bmatrix} N_{s,s_w} \\ N_{m,s_w} \end{Bmatrix} = \begin{Bmatrix} 0 \\ -G_r p_m'' \end{Bmatrix} \tag{7.32}$$

where G_r is a material constant that controls the rate of change in p_m'' caused by changes in the degree of saturation S_w. We assume that the changes in the degree of saturation affect only the bonding related internal variable. In this way, the yield surface depends only on p_s'' and reduces to a classical critical–state model in case of saturated conditions (S_w =1). Fig. 7.3 illustrates the reduction of the yield surface due to a wetting process in the case that p_m depends on S_w.

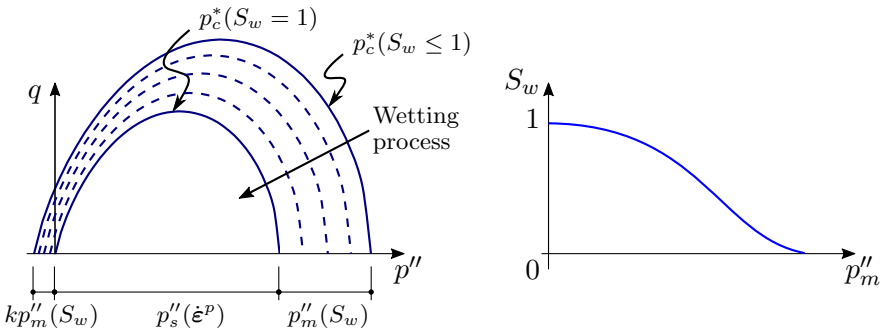

Figure 7.3: Reduction of the yield surface due to a wetting process.

The hardening laws corresponding to the mechanical changes are the same as in Tamagnini et al. [167]:

$$\boldsymbol{h} = \begin{Bmatrix} h_s \\ h_m \end{Bmatrix} = \begin{Bmatrix} \rho_s p_s'' \left(\dot{\varepsilon}_v^p + \xi_s \dot{\varepsilon}_s^p\right) \\ -\rho_m p_m'' \left(|\dot{\varepsilon}_v^p| + \xi_m \dot{\varepsilon}_s^p\right) \end{Bmatrix} \tag{7.33}$$

where ρ_s, ρ_m, ξ_s and ξ_m are material parameters. Consequently, eq. (7.29) accounting only for mechanical effects and degree of saturation reads:

$$\dot{\boldsymbol{q}} = \begin{Bmatrix} \dot{p}_s'' \\ \dot{p}_m'' \end{Bmatrix} = \dot{\lambda}_\varepsilon \begin{Bmatrix} \rho_s p_s'' \left(\dot{\varepsilon}_v^p + \xi_s \dot{\varepsilon}_s^p\right) \\ -\rho_m p_m'' \left(|\dot{\varepsilon}_v^p| + \xi_m \dot{\varepsilon}_s^p\right) \end{Bmatrix} + \dot{S}_w \begin{Bmatrix} 0 \\ -G_r p_m'' \end{Bmatrix} \tag{7.34}$$

The plastic multiplier $\dot{\lambda}_\varepsilon$ is subjected to the Kuhn–Tucker complementarity conditions:

$$f(\boldsymbol{\sigma}'', \boldsymbol{q}) \leq 0, \qquad \dot{\lambda}_\varepsilon \geq 0, \qquad \dot{\lambda}_\varepsilon f(\boldsymbol{\sigma}'', \boldsymbol{q}) = 0 \tag{7.35}$$

and the consistency condition:

$$\dot{\lambda}_\varepsilon \dot{f}(\boldsymbol{\sigma}'', \boldsymbol{q}) = 0 \tag{7.36}$$

The Milan model is completed by defining a hyper–elastic response of the material inside the yield surface. The stress–strain relationship and its respective elastic stiffness tensor, $\boldsymbol{D}^e$, are given by Tamagnini et al. [167]:

$$\boldsymbol{\sigma}'' = \left(1 + \frac{3\alpha}{2\hat{\kappa}} \left(\varepsilon_s^e\right)^2\right) \theta_\varepsilon \mathbf{1} + 2\left(G_0 + \frac{\alpha}{\hat{\kappa}} \tilde{\psi}\right) \boldsymbol{e}^e \tag{7.37}$$

and

$$\boldsymbol{D}^e := \left(1 + \frac{3\alpha}{2\hat{\kappa}} \left(\varepsilon_s^e\right)^2\right) K_\varepsilon \mathbf{1} \otimes \mathbf{1} + 2\left(G_0 + \frac{\alpha}{\hat{\kappa}} \tilde{\psi}\right) \left(\boldsymbol{I} - \frac{1}{3} \mathbf{1} \otimes \mathbf{1}\right) + 2\left(\frac{\alpha}{\hat{\kappa}}\right) \theta_\varepsilon \left(\mathbf{1} \otimes \boldsymbol{e}^e + \boldsymbol{e}^e \otimes \mathbf{1}\right) \tag{7.38}$$

where the three functions $\tilde{\psi}\left(\varepsilon_v\right)$, $\theta_\varepsilon\left(\varepsilon_v^e\right)$ and $K_\varepsilon\left(\varepsilon_v^e\right)$ are given by

$$\tilde{\psi}\left(\varepsilon_v\right) = \begin{cases} \hat{\kappa} p_r \exp\left(\varepsilon_v^e / \hat{\kappa} - 1\right), & \text{if } \varepsilon_v^e \geq \hat{\kappa} \\ p_r \varepsilon_v^e + p_r \left(\varepsilon_v^e - \hat{\kappa}\right)^2 / \left(2\hat{\kappa}\right) & \text{if } \varepsilon_v^e < \hat{\kappa} \end{cases} \tag{7.39}$$

$$\theta_\varepsilon := \frac{\mathrm{d}\tilde{\psi}}{\mathrm{d}\varepsilon_v^e} = \begin{cases} p_r \exp\left(\varepsilon_v^e / \hat{\kappa} - 1\right), & \text{if } \varepsilon_v^e \geq \hat{\kappa} \\ p_r \left(\varepsilon_v^e / \hat{\kappa}\right) & \text{if } \varepsilon_v^e < \hat{\kappa} \end{cases} \tag{7.40}$$

and

$$K_\varepsilon := \frac{\mathrm{d}\theta_\varepsilon}{\mathrm{d}\varepsilon_v^e} = \begin{cases} p_r/\hat{\kappa}\exp\left(\varepsilon_v^e/\hat{\kappa}-1\right), & \text{if } \varepsilon_v^e \geq \hat{\kappa} \\ p_r/\hat{\kappa} & \text{if } \varepsilon_v^e < \hat{\kappa} \end{cases} \tag{7.41}$$

in the above equations G_0 is the initial shear modulus, p_r is a reference mean stress, $\hat{\kappa}$ is a constitutive parameter that relates ε_v^e and p'', and α quantifies the rate of increase of shear modulus with mean stress p''.

7.3 Mechanical constitutive models. Second gradient part

7.3.1 Elastic constitutive model with one parameter

As there is little available information on the relation existing between the double stress and the second derivatives of displacements, a simple constitutive model was presented in the works of Bésuelle et al. [19], Collin et al. [44], Matsushima et al. [115]. It consists in an isotropic linear elastic constitutive model involving one parameter, D^{sg} with units of force, as a particular case of a more general isotropic linear relation derived by Mindlin [119]:

$$\boldsymbol{\Sigma} = \boldsymbol{D}_{sg}^e \nabla\nabla \boldsymbol{u} \tag{7.42}$$

For two–dimensional problems and in Voigt vector notation, it reads:

$$\begin{Bmatrix} \Sigma_{111} \\ \Sigma_{112} \\ \Sigma_{121} \\ \Sigma_{122} \\ \Sigma_{211} \\ \Sigma_{212} \\ \Sigma_{221} \\ \Sigma_{222} \end{Bmatrix} = D^{sg} \begin{bmatrix} 1 & 0 & 0 & 0 & 0 & 1/2 & 1/2 & 0 \\ 0 & 1/2 & 1/2 & 0 & -1/2 & 0 & 0 & 1/2 \\ 0 & 1/2 & 1/2 & 0 & -1/2 & 0 & 0 & 1/2 \\ 0 & 0 & 0 & 1 & 0 & -1/2 & -1/2 & 0 \\ 0 & -1/2 & -1/2 & 0 & 1 & 0 & 0 & 0 \\ 1/2 & 0 & 0 & -1/2 & 0 & 1/2 & 1/2 & 0 \\ 1/2 & 0 & 0 & -1/2 & 0 & 1/2 & 1/2 & 0 \\ 0 & 1/2 & 1/2 & 0 & 0 & 0 & 0 & 1 \end{bmatrix} \begin{Bmatrix} \gamma_{111} \\ \gamma_{112} \\ \gamma_{121} \\ \gamma_{122} \\ \gamma_{211} \\ \gamma_{212} \\ \gamma_{221} \\ \gamma_{222} \end{Bmatrix} \tag{7.43}$$

with:

$$\boldsymbol{\gamma} := \nabla\nabla\boldsymbol{u}, \quad \gamma_{ijk} := \frac{\partial^2 u_i}{\partial x_j x_k} \tag{7.44}$$

7.3.2 Elastic constitutive model with two independent length scales

This second elastic constitutive model follows the ideas in Tamagnini et al. [168] with the purpose of being used in two– and three–dimensions. The elastic second displacement gradient $\boldsymbol{\gamma}^e$ can be decomposed into a hydrostatic part, $\boldsymbol{\gamma}^{eH}$ and a deviatoric part $\boldsymbol{\gamma}^{eD}$:

$$\boldsymbol{\gamma}^e = \boldsymbol{\gamma}^{eH} + \boldsymbol{\gamma}^{eD} \tag{7.45}$$

with

$$\gamma^{eH}_{abc} := \frac{1}{4}\{\delta_{ab}\gamma^e_{kkc} + \delta_{ac}\gamma^e_{kkb}\} \tag{7.46a}$$

$$\gamma^{eD}_{abc} := \gamma^e_{abc} - \gamma^{eH}_{abc} \tag{7.46b}$$

The invariants of the deviatoric part of $\boldsymbol{\gamma}^e$ are given by

$$I^e_H = \boldsymbol{\gamma}^{eH} \cdot \boldsymbol{\gamma}^{eH} = \gamma^{eH}_{ijk}\gamma^{eH}_{ijk} \tag{7.47a}$$

$$I^e_D = \boldsymbol{\gamma}^{eD} \cdot \boldsymbol{\gamma}^{eD} = \gamma^{eD}_{ijk}\gamma^{eD}_{ijk} \tag{7.47b}$$

The second gradient part of the free energy function is then defined in terms of the norms of I^e_H and I^e_D as:

$$\Sigma_{abc} = \frac{\partial \Psi_\gamma}{\partial \gamma^e_{abc}} \tag{7.48}$$

with:

$$\Psi_\gamma = \frac{1}{2}G\{l_H^2 I^e_H + l_D^2 I^e_D\} \tag{7.49}$$

where G is the shear modulus of the material and l_H and l_D are constants with dimensions of length, representing two different internal length scales of the material.

By taking the first derivatives of eq. (7.48) with respect to $\boldsymbol{\gamma}^e$, we have:

$$\Sigma_{abc} = \frac{1}{2} G l_H^2 \frac{\partial I_H^e}{\partial \gamma_{abc}^e} + \frac{1}{2} G l_D^2 \frac{\partial I_D^e}{\partial \gamma_{abc}^e} \tag{7.50}$$

with

$$\frac{\partial I_H^e}{\partial \gamma_{abc}^e} = 2\gamma_{ijk}^{eH} \frac{\partial \gamma_{ijk}^{eH}}{\partial \gamma_{abc}^e} \tag{7.51}$$

and

$$\frac{\partial I_D^e}{\partial \gamma_{abc}^e} = 2\gamma_{ijk}^{eD} \frac{\partial \gamma_{ijk}^{eD}}{\partial \gamma_{abc}^e} \tag{7.52}$$

Substituting 7.51 and 7.52 into 7.50, we have:

$$\Sigma_{abc} = G \left\{ l_H^2 \gamma_{ijk}^{eH} \frac{\partial \gamma_{ijk}^{eH}}{\partial \gamma_{abc}^e} + l_D^2 \gamma_{ijk}^{eD} \frac{\partial \gamma_{ijk}^{eD}}{\partial \gamma_{abc}^e} \right\} \tag{7.53}$$

The expressions of the two tensors $\partial \gamma_{ijk}^{eH} / \partial \gamma_{abc}^e$ and $\partial \gamma_{ijk}^{eD} / \partial \gamma_{abc}^e$ are provided in the appendix A. The sixth–order second gradient constitutive tensor is obtained after derivation of eq. (7.53) with respect to $\boldsymbol{\gamma}^e$:

$$\boldsymbol{D}_{sg}^e = \frac{\partial \boldsymbol{\Sigma}}{\partial \boldsymbol{\gamma}^e} = \frac{\partial^2 \Psi}{\partial \boldsymbol{\gamma}^e \otimes \partial \boldsymbol{\gamma}^e} \tag{7.54}$$

that yields:

$$\begin{aligned} (\boldsymbol{D}_{sg}^e)_{ijkabc} = \frac{1}{8} G (l_H^2 - l_D^2) \{ & \delta_{ij}\delta_{ab}\delta_{kc} + \delta_{ik}\delta_{ab}\delta_{jc} \\ & + \delta_{ij}\delta_{ac}\delta_{bk} + \delta_{ik}\delta_{ac}\delta_{jb} \} + G l_D^2 (\delta_{ia}\delta_{jb}\delta_{kc}) \end{aligned} \tag{7.55}$$

7.3.3 Elastoplastic second gradient constitutive model

The second derivative of displacements $\boldsymbol{\gamma}$ is split into an elastic part $\boldsymbol{\gamma}^e$ and a plastic one $\boldsymbol{\gamma}^p$:

$$\boldsymbol{\gamma} = \boldsymbol{\gamma}^e + \boldsymbol{\gamma}^p \tag{7.56}$$

The elastic behavior is given by the double stress tensor in rate form:

$$\dot{\boldsymbol{\Sigma}} = \boldsymbol{D}^{e}_{sg}\left(\dot{\boldsymbol{\gamma}} - \dot{\boldsymbol{\gamma}}^{p}\right) \tag{7.57}$$

The simplest possible yield function for the second gradient part is a hypersphere of radius R^{sg} and is formulated as:

$$F(\boldsymbol{\Sigma}, R^{sg}) = ||\boldsymbol{\Sigma}|| - R^{sg} = 0$$

with:

$$||\boldsymbol{\Sigma}|| = \left\{\Sigma_{ijk}\Sigma_{ijk}\right\}^{1/2} \tag{7.58}$$

In lack of any experimental data on the plastic flow direction for $\dot{\boldsymbol{\gamma}}^{p}$, we assume an associative flow rule. Thus,

$$\dot{\boldsymbol{\gamma}}^{p} = \dot{\lambda}_{\gamma}\frac{\partial F}{\partial \boldsymbol{\Sigma}} \tag{7.59}$$

and considering that

$$\frac{\partial F}{\partial \boldsymbol{\Sigma}} = \frac{\partial}{\partial \boldsymbol{\Sigma}}\left\{\boldsymbol{\Sigma}\cdot\boldsymbol{\Sigma}\right\}^{1/2} \tag{7.60a}$$

$$= \frac{1}{2}\frac{1}{||\boldsymbol{\Sigma}||}\left\{\left(\frac{\partial \boldsymbol{\Sigma}}{\partial \boldsymbol{\Sigma}}\right)\boldsymbol{\Sigma} + \boldsymbol{\Sigma}\left(\frac{\partial \boldsymbol{\Sigma}}{\partial \boldsymbol{\Sigma}}\right)\right\} \tag{7.60b}$$

$$= \frac{\boldsymbol{\Sigma}}{||\boldsymbol{\Sigma}||} = \boldsymbol{N}_{\gamma} \tag{7.60c}$$

we can rewrite eq. (7.59) as:

$$\dot{\boldsymbol{\gamma}}^{p} = \dot{\lambda}_{\gamma}\boldsymbol{N}_{\gamma} \tag{7.61}$$

where $\dot{\lambda}_{\gamma}$ is the non–negative plastic multiplier for the second gradient mechanism. We assume two different hardening laws:

$$\dot{R}^{sg} = \dot{\lambda}_{\gamma}H_{\gamma}\ , \qquad \text{(linear)} \tag{7.62a}$$

$$\dot{R}^{sg} = \dot{\lambda}_{\gamma}H_{\gamma}(R^{sg}_{max} - R^{sg})\ , \qquad \text{(exponential)} \tag{7.62b}$$

where H_{γ} is the plastic modulus and R^{sg}_{max} is an asymptotic limit of R^{sg}.

The elastoplastic second gradient constitutive model is completed with the Kuhn–Tucker complementarity conditions:

$$\dot{\lambda}_\gamma \geq 0 \qquad F(\mathbf{\Sigma}, R^{sg}) \leq 0 \qquad \dot{\lambda}_\gamma F(\mathbf{\Sigma}, R^{sg}) = 0 \tag{7.63}$$

and the consistency condition:

$$\dot{\lambda}_\gamma \dot{F}(\mathbf{\Sigma}, R^{sg}) = 0 \tag{7.64}$$

Chapter 8

IGA–FEM implementation of the governing equations

This chapter presents the initial boundary value problem for modeling the coupled hydromechanical behavior of partially saturated soils. First, the constitutive equations presented in chapter 7 are now added to the governing equations of the porous media developed in chapter 6. Then, the variational equations and the time integration schemes are developed for the initial boundary value problem. Finally, the finite element discretization and their corresponding linearization are presented. The resulting system of non–linear algebraic equations governing the coupled hydromechanical formulation is solved by means of the Newton–Raphson method. The arc–length method, which becomes crucial in the solution of problems involving softening materials, is also described.

Moreover, the present chapter also addresses the different numerical strategies to solve the linear system of equations that yields the linearization of the variational equations. We finally summarize the main subroutines implemented in the GeoPDEs IGA–FEM code.

8.1 The initial boundary value problem definition

To define the initial boundary value problem (IBVP), we recall the balance of linear momentum given by eq. (6.43).

$$\nabla \cdot \left(\boldsymbol{\sigma}'' - S_w p_w - \nabla \cdot \boldsymbol{\Sigma} \right) + \rho \boldsymbol{b} = \mathbf{0} \tag{8.1}$$

and the balance of mass given by eq. (6.24) that is now completed with the constitutive equations presented in eqs. (7.3) and (7.7):

$$\left(C_{ww} + C_s \right) \dot{p}_w + S_w \nabla \cdot \boldsymbol{v}^s + \nabla \cdot \boldsymbol{w}^w = 0 \tag{8.2}$$

with:

$$C_{ww} := n S_w C_w \tag{8.3}$$

and

$$\boldsymbol{w}^w = -\frac{1}{\mu_w} \boldsymbol{k}_w (\nabla p_w - \rho_w \boldsymbol{b}) \tag{8.4}$$

8.1.1 Initial and Boundary Conditions

The definition of the IBVP requires specifications of initial and boundary conditions.

Initial conditions:

$$\boldsymbol{u}^s(\boldsymbol{x}, 0) = \boldsymbol{u}_0(\boldsymbol{x}), \qquad p_w(\boldsymbol{x}, 0) = p_{w0}(\boldsymbol{x}) \tag{8.5}$$

where $\boldsymbol{u}_0(\boldsymbol{x})$ and $p_{w0}(\boldsymbol{x})$ are the initial displacements and initial pore water pressures, respectively.

The boundary conditions have to be fulfilled for two unknowns fields, $\boldsymbol{u}^s$ and p_w. There are thus three sets of independent boundary conditions:

$$\partial\mathcal{B} = \overline{\partial\mathcal{B}_u \cup \partial\mathcal{B}_t}, \qquad \partial\mathcal{B}_u \cap \partial\mathcal{B}_t = \emptyset \tag{8.6a}$$

$$\partial\mathcal{B} = \overline{\partial\mathcal{B}_G \cup \partial\mathcal{B}_T}, \qquad \partial\mathcal{B}_G \cap \partial\mathcal{B}_T = \emptyset \tag{8.6b}$$

$$\partial\mathcal{B} = \overline{\partial\mathcal{B}_{p_w} \cup \partial\mathcal{B}_{q_w}}, \qquad \partial\mathcal{B}_{p_w} \cap \partial\mathcal{B}_{q_w} = \emptyset \tag{8.6c}$$

Boundary conditions:

$$\boldsymbol{u}^s(\boldsymbol{x},t) = \overline{\boldsymbol{u}} \qquad \forall \boldsymbol{x} \in \partial\mathcal{B}_u, \tag{8.7a}$$

$$D\boldsymbol{u}^s(\boldsymbol{x},t) = \overline{\boldsymbol{G}} \qquad \forall \boldsymbol{x} \in \partial\mathcal{B}_G \tag{8.7b}$$

$$(\boldsymbol{\sigma} - \nabla\cdot\boldsymbol{\Sigma})\,\boldsymbol{n} - (\overset{s}{\nabla}\cdot\boldsymbol{\Sigma})\boldsymbol{n} + \boldsymbol{\Sigma}\,(\boldsymbol{\beta} - \operatorname{tr}(\boldsymbol{\beta})\,\boldsymbol{n}\otimes\boldsymbol{n}) = \bar{\boldsymbol{t}} \qquad \forall \boldsymbol{x} \in \partial\mathcal{B}_t \tag{8.7c}$$

$$\boldsymbol{\Sigma}\,(\boldsymbol{n}\otimes\boldsymbol{n}) = \overline{\boldsymbol{T}} \qquad \forall \boldsymbol{x} \in \partial\mathcal{B}_T \tag{8.7d}$$

$$p_w(\boldsymbol{x},t) = \overline{p}_w \qquad \forall \boldsymbol{x} \in \partial\mathcal{B}_{p_w}, \tag{8.7e}$$

$$\boldsymbol{w}^w\cdot\boldsymbol{n} = \overline{q}_w \qquad \forall \boldsymbol{x} \in \partial\mathcal{B}_{q_w} \tag{8.7f}$$

where $\overline{\boldsymbol{u}}$ is the prescribed displacement on $\partial\mathcal{B}_u$, $\overline{\boldsymbol{G}}$ is the prescribed normal gradient displacement on $\partial\mathcal{B}_G$, $\bar{\boldsymbol{t}}$ is the prescribed traction vector on $\partial\mathcal{B}_t$, $\overline{\boldsymbol{T}}$ is the prescribed double traction vector on $\partial\mathcal{B}_T$, $\overline{p}_w$ is the prescribed pore water pressure on $\partial\mathcal{B}_{p_w}$, and $\overline{q}_w$ is the prescribed water flow per unit area on $\partial\mathcal{B}_{q_w}$.

8.2 Variational form

8.2.1 Balance of linear momentum

Following the standard arguments of variational principles, we define the following spaces:

$$\mathcal{S}_u := \left\{\boldsymbol{u}^s : \mathcal{B}\to\mathbb{R}^3 \mid \ \boldsymbol{u}^s \in H^2,\ \boldsymbol{u}^s = \overline{\boldsymbol{u}}^s \text{ on } \partial\mathcal{B}_u \text{ and } D\boldsymbol{u}^s = \overline{\boldsymbol{G}} \text{ on } \partial\mathcal{B}_G\right\} \tag{8.8a}$$

$$\mathcal{V}_u := \left\{\boldsymbol{u}^* : \mathcal{B}\to\mathbb{R}^3 \mid \ \boldsymbol{u}^* \in H^2,\ \boldsymbol{u}^* = \boldsymbol{0} \text{ on } \partial\mathcal{B}_u \text{ and } D\boldsymbol{u}^* = \boldsymbol{0} \text{ on } \partial\mathcal{B}_G\right\} \tag{8.8b}$$

where H^2 is the Sobolev space of degree two and it means that basis functions must satisfy at least C^1 continuity between elements.

The variational form of the balance of linear momentum requires that, for any test function, $\boldsymbol{u}^* \in \mathcal{V}_u$:

$$\int_{\mathcal{B}} \boldsymbol{u}^* \cdot \left\{\nabla\cdot\left(\boldsymbol{\sigma}'' - S_w p_w - \nabla\cdot\boldsymbol{\Sigma}\right) + \rho\boldsymbol{b}\right\}\,\mathrm{d}v = 0 \tag{8.9}$$

Given that $\boldsymbol{u}^* = 0$ on $\partial\mathcal{B}_u$ and the boundary conditions in eqs. (8.7c) and (8.7d), eq. (8.9) may be written as:

$$\int_{\mathcal{B}} \nabla^s \boldsymbol{u}^* \cdot \boldsymbol{\sigma}'' \,\mathrm{d}v - \int_{\mathcal{B}} (S_w p_w) \nabla \cdot \boldsymbol{u}^* \,\mathrm{d}v + \int_{\mathcal{B}} \boldsymbol{\Sigma} \cdot \nabla\nabla \boldsymbol{u}^* \,\mathrm{d}v \\ - \int_{\partial\mathcal{B}_t} \overline{\boldsymbol{t}} \cdot \boldsymbol{u}^* \,\mathrm{d}a - \int_{\partial\mathcal{B}_T} \overline{\boldsymbol{T}} \cdot D\boldsymbol{u}^* \,\mathrm{d}a - \int_{\mathcal{B}} \boldsymbol{u}^* \cdot (\rho \boldsymbol{b}) \,\mathrm{d}v = 0 \quad (8.10)$$

where $\nabla^s \boldsymbol{u}^*$ is the symmetric gradient of the virtual displacement field $\boldsymbol{u}^*$.

The l.h.s of eq. (8.10) is a functional $\mathcal{G} = \mathcal{G}(\boldsymbol{u}^s, p_w, \boldsymbol{u}^*)$. Hence eq. (8.10) also reads:

$$\mathcal{G}(\boldsymbol{u}^s, p_w, \boldsymbol{u}^*) = 0 \quad (8.11)$$

8.2.2 Balance of mass: Liquid + solid

The spaces for the liquid are given by:

$$\mathcal{S}_{p_w} := \left\{ p_w : \mathcal{B} \to \mathbb{R} \mid p_w \in H^1, p_w = \overline{p}_w \text{ on } \partial\mathcal{B}_{p_w} \right\} \quad (8.12a)$$

$$\mathcal{V}_{p_w} := \left\{ p_w^* : \mathcal{B} \to \mathbb{R} \mid p_w^* \in H^1, p_w^* = 0 \text{ on } \partial\mathcal{B}_{p_w} \right\} \quad (8.12b)$$

where H^1 is the Hilbert space requiring only C^1–continuity between elements.

The variational form of balance of mass is satisfied if, for any $p_w^* \in \mathcal{V}_{p_w}$:

$$\int_{\mathcal{B}} p_w^* \left\{ (C_{ww} + C_s) \dot{p}_w + S_{ww} \nabla \cdot \boldsymbol{v}^s + \nabla \cdot \boldsymbol{w}^w \right\} \,\mathrm{d}v = 0 \quad (8.13)$$

Considering that $\psi = 0$ on $\partial\mathcal{B}_{p_w}$ and the boundary conditions in eq. (8.7f), eq. (8.9) may be written as:

$$\int_{\mathcal{B}} p_w^* (C_{ww} + C_s) \dot{p}_w \,\mathrm{d}v + \int_{\mathcal{B}} p_w^* S_w \nabla \cdot \boldsymbol{v}^s \,\mathrm{d}v \\ - \int_{\mathcal{B}} \nabla p_w^* \cdot \boldsymbol{w}^w \,\mathrm{d}v + \int_{\partial\mathcal{B}_{q_w}} p_w^* \overline{q}_w \,\mathrm{d}a = 0 \quad (8.14)$$

The l.h.s. of (8.14) is a functional $\mathcal{H}_w = \mathcal{H}_w(\boldsymbol{u}^s, p_w, \dot{p}_w, p_w^*)$. Hence eq. 8.14 also reads:

$$\mathcal{H}_w(\boldsymbol{u}^s, p_w, \dot{p}_w, p_w^*) = 0 \tag{8.15}$$

8.3 Time discretization

The unknowns $\boldsymbol{u}^s$ and p_w are time dependent. The IBVP is then discretized in time. A Backward–Euler scheme is used to define the temporal evolution during a finite time step and the time derivatives:

$$\begin{aligned} \boldsymbol{v}_{n+1}^s &= \frac{1}{\Delta t}\left(\boldsymbol{u}_{n+1}^s - \boldsymbol{u}_n^s\right) = \frac{1}{\Delta t}\Delta \boldsymbol{u}^s \\ \dot{p}_{w,n+1} &= \frac{1}{\Delta t}\left(p_{w,n+1} - p_{w,n}\right) = \frac{1}{\Delta t}\Delta p_w \end{aligned} \tag{8.16}$$

Hence, writing eq. (8.14) at time t_{n+1} and using eqs. (8.16), we have:

$$\begin{aligned} \int_{\mathcal{B}} p_w^* \left(C_{ww} + C_s\right)_{n+1} \Delta p_w \,\mathrm{d}v + \int_{\mathcal{B}} p_w^* S_{w,n+1} \nabla \cdot \Delta \boldsymbol{u}^s \,\mathrm{d}v \\ - \Delta t \int_{\mathcal{B}} \nabla p_w^* \cdot \boldsymbol{w}_{n+1}^w \,\mathrm{d}v + \Delta t \int_{\partial \mathcal{B}_t} p_w^* \cdot \overline{q}_{w,n+1} \,\mathrm{d}a = 0 \end{aligned} \tag{8.17}$$

The functional of the l.h.s. of eq. (8.17) is:

$$\mathcal{H}_w^{\Delta t}(\boldsymbol{u}^s, p_w, p_w^*) = 0 \tag{8.18}$$

8.4 Discretization of variational equations

8.4.1 Finite element approximations

The field variables $\boldsymbol{u}^s$ (leaving the superscript s out for ease of notation) and p_w are discretized by different approximations basis functions. We follow the same procedure

for the virtual quantities. We thus have:

$$\boldsymbol{u}(\boldsymbol{x},t) \cong \sum_{A}^{n_u} \boldsymbol{N}_A^u \boldsymbol{d}_A = \boldsymbol{N}^u(\boldsymbol{x})\boldsymbol{d}(t) \; ; \qquad \boldsymbol{u}^*(\boldsymbol{x}) = \boldsymbol{N}^u(\boldsymbol{x})\boldsymbol{d}^* \tag{8.19a}$$

$$p_w(\boldsymbol{x},t) \cong \sum_{B}^{n_{p_w}} N_B^w p_{w,B} = \boldsymbol{N}^w(\boldsymbol{x})\boldsymbol{p}_w(t) \; ; \qquad p_w^*(\boldsymbol{x}) = \boldsymbol{N}^w(\boldsymbol{x})\boldsymbol{\psi}_w^* \tag{8.19b}$$

with

$$\boldsymbol{N}^u = [\boldsymbol{N}_1^u \; , \ldots \boldsymbol{N}_A^u \; , \ldots \boldsymbol{N}_n^u] \; , \qquad \boldsymbol{N}_A^u = \begin{bmatrix} N_A^u & 0 & 0 \\ 0 & N_A^u & 0 \\ 0 & 0 & N_A^u \end{bmatrix} \tag{8.20}$$

and

$$\boldsymbol{N}^w = [N_1^w \; , \ldots N_A^w \; , \ldots N_n^w] \; , \tag{8.21}$$

In the above equations, $\boldsymbol{d}$ and $\boldsymbol{p}_w$ are the displacement vector and the pore water pressure vector, respectively. $\boldsymbol{d}^*$ and $\boldsymbol{\psi}_w^*$ are the virtual displacement vector and the virtual pore water pressure vector, respectively. N_A^u and N_A^w are their corresponding B–spline basis functions, respectively.

The symmetric gradient, divergence and the second gradient of $\boldsymbol{u}$ and $\boldsymbol{u}^*$, adopting vector notation, are expressed as:

$$\nabla^s \boldsymbol{u}^s \cong \text{sym}\left(\sum_{A}^{n_u} \boldsymbol{N}_A^u \otimes \nabla \boldsymbol{d}_A\right) = \boldsymbol{B}^u \boldsymbol{d} \; ; \qquad \nabla^s \boldsymbol{u}^* = \boldsymbol{B}^u \boldsymbol{d}^* \tag{8.22a}$$

$$\nabla \cdot \boldsymbol{u}^s \cong \boldsymbol{m}^T \boldsymbol{B}^u \boldsymbol{d} \; ; \qquad \nabla \cdot \boldsymbol{u}^* = \boldsymbol{m}^T \boldsymbol{B}^u \boldsymbol{d}^* \tag{8.22b}$$

$$D\boldsymbol{u} \cong \sum_{A}^{n_u} (\nabla \boldsymbol{N}_A^u \cdot \boldsymbol{n}) \, \boldsymbol{d}_A = \boldsymbol{B}_s^u \boldsymbol{d} \; ; \qquad D\boldsymbol{u}^* = \boldsymbol{B}_s^u \boldsymbol{d}^* \tag{8.22c}$$

$$\nabla\nabla \boldsymbol{u} \cong \sum_{A}^{n_u} (\nabla\nabla \boldsymbol{N}_A^u) \otimes \boldsymbol{d}_A = \boldsymbol{S}^u \boldsymbol{d} \; ; \qquad \nabla\nabla \boldsymbol{u}^* = \boldsymbol{S}^u \boldsymbol{d}^* \tag{8.22d}$$

where $\boldsymbol{m}$ is the unit vector (equivalent to Kronecker's delta):

$$\boldsymbol{m} = \{1, \; 1, \; 1, \; 0, \; 0, \; 0\}^T \tag{8.23}$$

Discrete symmetric displacement gradient operator, $\boldsymbol{B}^u$:

$$\boldsymbol{B}^u = [\boldsymbol{B}^u_1,\ \ldots,\ \boldsymbol{B}^u_A,\ \ldots,\ \boldsymbol{B}^u_n]\ , \qquad \boldsymbol{B}^u_A = \begin{bmatrix} N^u_{A,1} & 0 & 0 \\ 0 & N^u_{A,2} & 0 \\ 0 & 0 & N^u_{A,3} \\ N^u_{A,2} & N^u_{A,1} & 0 \\ N^u_{A,3} & 0 & N^u_{A,1} \\ 0 & N^u_{A,3} & N^u_{A,2} \end{bmatrix} \tag{8.24}$$

with

$$N^u_{A,i} := \frac{\partial N^u_A}{\partial x_i} \tag{8.25}$$

Discrete normal derivative operator, $\boldsymbol{B}^u_s$:

$$\boldsymbol{B}^u_s = \left[\boldsymbol{B}^u_{s,1},\ \ldots,\ \boldsymbol{B}^u_{s,A},\ \ldots \boldsymbol{B}^u_{s,n}\right]\ , \qquad \boldsymbol{B}^u_{s,A} = \begin{bmatrix} P^u_A & 0 & 0 \\ 0 & P^u_A & 0 \\ 0 & 0 & P^u_A \end{bmatrix} \tag{8.26}$$

with

$$P^u_A = (\nabla N^u_A) \cdot \boldsymbol{n} = \frac{\partial N^u_A}{\partial x_j} n_j \tag{8.27}$$

Discrete second displacement gradient operator, $\boldsymbol{S}^u$:

$$\boldsymbol{S}^u = [\boldsymbol{S}^u_1,\ \ldots,\ \boldsymbol{S}^u_A,\ \ldots \boldsymbol{S}^u_n]\ , \qquad \boldsymbol{S}^u_A = \begin{bmatrix} \boldsymbol{Q}^u_A & \boldsymbol{0}_{9\times1} & \boldsymbol{0}_{9\times1} \\ \boldsymbol{0}_{9\times1} & \boldsymbol{Q}^u_A & \boldsymbol{0}_{9\times1} \\ \boldsymbol{0}_{9\times1} & \boldsymbol{0}_{9\times1} & \boldsymbol{Q}^u_A \end{bmatrix} \tag{8.28}$$

with

$$\boldsymbol{Q}^u_A = \left\{N^u_{A,11}\ , N^u_{A,12}\ , N^u_{A,13}\ , N^u_{A,21}\ , N^u_{A,22}\ , N^u_{A,23}\ , N^u_{A,31}\ , N^u_{A,32}\ , N^u_{A,33}\right\}^T \tag{8.29}$$

and

$$N^u_{A,ij} := \frac{\partial^2 N^u_A}{\partial x_i \partial x_j} \tag{8.30}$$

Gradients of p_w and ψ_w^* are given by:

$$\nabla p_w = \sum_B^{n_{p_w}} \nabla N_B^w p_{w,B} = \boldsymbol{E}^w \boldsymbol{p}_w \ , \qquad \nabla p_w^* = \boldsymbol{E}^w \boldsymbol{\psi}_w^* \tag{8.31}$$

Discrete hydraulic gradient operator

$$\boldsymbol{E}^w = \left[\boldsymbol{E}_1^w \ , \dots \boldsymbol{E}_B^w \ , \dots \boldsymbol{E}_{,n}^w\right] \ , \qquad \boldsymbol{E}_{w,B} = \begin{bmatrix} N_{B,1}^w & 0 & 0 \\ 0 & N_{B,2}^w & 0 \\ 0 & 0 & N_{B,3}^w \end{bmatrix} \tag{8.32}$$

with

$$N_{B,i}^w = \frac{\partial N_B^w}{\partial x_j} \tag{8.33}$$

8.4.2 Balance of linear momentum

By introducing the finite element approximations of the previous subsection and considering that, in Voigt notation:

$$\nabla^s \boldsymbol{u}^* \cdot \boldsymbol{\sigma}'' = \left(\nabla^s \boldsymbol{u}^*\right)^T \boldsymbol{\sigma}'' \qquad (\nabla\nabla \boldsymbol{u}^*) \cdot \boldsymbol{\Sigma} = \left(\nabla\nabla \boldsymbol{u}^*\right)^T \boldsymbol{\Sigma} \tag{8.34}$$

The discrete form of the eq. (8.10) reads:

$$\begin{aligned} \int_{\mathcal{B}} \boldsymbol{d}^{*T} \boldsymbol{B}^{uT} \boldsymbol{\sigma}'' \,\mathrm{d}v + \int_{\mathcal{B}} \boldsymbol{d}^{*T} \boldsymbol{S}^{uT} \boldsymbol{\Sigma} \,\mathrm{d}v - \int_{\mathcal{B}} \boldsymbol{d}^{*T} \boldsymbol{B}^{uT} \boldsymbol{m}(S_w p_w) \,\mathrm{d}v \\ - \int_{\mathcal{B}} \boldsymbol{d}^{*T} \boldsymbol{N}^{uT} (\rho \boldsymbol{b}) \,\mathrm{d}v - \int_{\partial \mathcal{B}_t} \boldsymbol{d}^{*T} \boldsymbol{N}^{uT} \overline{\boldsymbol{t}} \,\mathrm{d}a - \int_{\partial \mathcal{B}_T} \boldsymbol{d}^{*T} \boldsymbol{B}_s^{uT} \overline{\boldsymbol{T}} \,\mathrm{d}a = 0 \end{aligned} \tag{8.35}$$

i.e.:

$$\begin{aligned} \boldsymbol{d}^{*T} \Bigg(\int_{\mathcal{B}} \boldsymbol{B}^{uT} \boldsymbol{\sigma}'' \,\mathrm{d}v + \int_{\mathcal{B}} \boldsymbol{S}^{uT} \boldsymbol{\Sigma} \,\mathrm{d}v - \int_{\mathcal{B}} \boldsymbol{B}^{uT} \boldsymbol{m}(S_w p_w) \,\mathrm{d}v \\ - \int_{\mathcal{B}} \boldsymbol{N}^{uT} (\rho \boldsymbol{b}) \,\mathrm{d}v - \int_{\partial \mathcal{B}_t} \boldsymbol{N}^{uT} \overline{\boldsymbol{t}} \,\mathrm{d}a - \int_{\partial \mathcal{B}_T} \boldsymbol{B}_s^{uT} \overline{\boldsymbol{T}} \,\mathrm{d}a \Bigg) = 0 \end{aligned} \tag{8.36}$$

Due to the arbitrariness in the choice of $\boldsymbol{d}^*$, eq. (8.36) is equivalent to the algebraic system of nonlinear equations:

$$\boldsymbol{f}^{\text{int}}(\boldsymbol{d},\boldsymbol{p}_w)+\boldsymbol{f}^{\text{int}}_{\text{sg}}(\boldsymbol{d})-\boldsymbol{g}_s(\boldsymbol{p}_w)-\boldsymbol{f}^{\text{ext}}_b-\boldsymbol{f}^{\text{ext}}_t-\boldsymbol{f}^{\text{ext}}_T=\boldsymbol{0} \tag{8.37}$$

with

$$\begin{aligned}
\boldsymbol{f}^{\text{int}} &:= \int_{\mathcal{B}} \boldsymbol{B}^{uT}\boldsymbol{\sigma}''(\boldsymbol{\varepsilon}(\boldsymbol{d}),\boldsymbol{p}_w)\,\mathrm{d}v\ ; & \boldsymbol{f}^{\text{int}}_{\text{sg}} &:= \int_{\mathcal{B}} \boldsymbol{S}^T\boldsymbol{\Sigma}(\boldsymbol{\gamma}(\boldsymbol{d}))\,\mathrm{d}v\\
\boldsymbol{g}_s &:= \int_{\mathcal{B}} \boldsymbol{B}^T\boldsymbol{m}(S_w p_w)\,\mathrm{d}v\ ; & \boldsymbol{f}^{\text{ext}}_b &:= \int_{\mathcal{B}} \boldsymbol{N}^{uT}(\rho\boldsymbol{b})\,\mathrm{d}v\\
\boldsymbol{f}^{\text{ext}}_t &:= \int_{\partial\mathcal{B}_t} \boldsymbol{N}^{uT}\overline{\boldsymbol{t}}\,\mathrm{d}a\ ; & \boldsymbol{f}^{\text{ext}}_T &:= \int_{\partial\mathcal{B}_T} \boldsymbol{B}^{uT}_s\overline{\boldsymbol{T}}\,\mathrm{d}a
\end{aligned} \tag{8.38}$$

where $\boldsymbol{f}^{\text{int}}$ and $\boldsymbol{f}^{\text{int}}_{\text{sg}}$ are the internal force vectors associated to Cauchy stress and to the double stress, respectively; $\boldsymbol{g}_s$ is coupling nodal forces vector; $\boldsymbol{f}^{\text{ext}}_b$, $\boldsymbol{f}^{\text{ext}}_t$ and $\boldsymbol{f}^{\text{ext}}_T$ are the external force vectors associated to body forces, surface tractions and double tractions, respectively.

8.4.3 Balance of mass

Introducing the finite element approximations, eq. (8.17) is written as follows:

$$\begin{aligned}
\int_{\mathcal{B}} \boldsymbol{\psi}^{*T}_w \boldsymbol{N}^{wT}(C_{ww}+C_s)_{n+1}\Delta p_w\,\mathrm{d}v + \int_{\mathcal{B}} \boldsymbol{\psi}^{*T}_w \boldsymbol{N}^{wT} S_{w,n+1}\nabla\cdot\Delta\boldsymbol{u}\,\mathrm{d}v\\
-\Delta t\int_{\mathcal{B}} \boldsymbol{\psi}^{*T}_w \boldsymbol{E}^{wT}\boldsymbol{w}^w\,\mathrm{d}v + \Delta t\int_{\partial\mathcal{B}_{q_w}} \boldsymbol{\psi}^{*T}_w \boldsymbol{N}^{wT}\overline{q}_{w,n+1}\,\mathrm{d}a = 0
\end{aligned} \tag{8.39}$$

Factoring all the terms with respect to $\boldsymbol{\psi}^*_w$ we have:

$$\begin{aligned}
\boldsymbol{\psi}^{*T}_w\Bigg(\int_{\mathcal{B}} \boldsymbol{N}^{wT}(C_{ww}+C_s)_{n+1}\Delta p_w\,\mathrm{d}v + \int_{\mathcal{B}} \boldsymbol{N}^{wT} S_{w,n+1}\nabla\cdot\Delta\boldsymbol{u}\,\mathrm{d}v\\
-\Delta t\int_{\mathcal{B}} \boldsymbol{E}^{wT}\boldsymbol{w}^w\,\mathrm{d}v + \Delta t\int_{\partial\mathcal{B}_{q_w}} \boldsymbol{N}^{wT}\overline{q}_{w,n+1}\,\mathrm{d}a\Bigg) = 0
\end{aligned} \tag{8.40}$$

Since the virtual pore water pressure vector is arbitrary, it is deduced that

$$\boldsymbol{s}_w(\boldsymbol{p}_w) + \boldsymbol{g}_w(\boldsymbol{d}, \boldsymbol{p}_w) - \Delta t \boldsymbol{h}_w^{\text{int}}(\boldsymbol{d}, \boldsymbol{p}_w) + \Delta t \boldsymbol{h}_w^{\text{ext}} = \boldsymbol{0} \tag{8.41}$$

with

$$\begin{aligned} \boldsymbol{s}_w &:= \int_{\mathcal{B}} \boldsymbol{N}^{wT}(C_{ww} + C_s)_{n+1} \Delta p_w \, \mathrm{d}v \; ; \quad & \boldsymbol{h}_w^{\text{int}} &:= \int_{\mathcal{B}} \boldsymbol{E}^{wT} \boldsymbol{w}^w(\boldsymbol{d}, \boldsymbol{p}_w) \, \mathrm{d}v \\ \boldsymbol{g}_w &:= \int_{\mathcal{B}} S_{w,n+1} \nabla \cdot \Delta \boldsymbol{u} \boldsymbol{N}^{wT} \, \mathrm{d}v \; ; & \boldsymbol{h}_w^{\text{ext}} &:= \int_{\partial \mathcal{B}_{q_w}} \boldsymbol{N}^{wT} \overline{q}_{w,n+1} \, \mathrm{d}a \end{aligned} \tag{8.42}$$

where $\boldsymbol{s}_w$ is the storage term accounting for water compressibility; $\boldsymbol{g}_w$ is the coupling nodal flux vector; $\boldsymbol{h}^{\text{int}}$ is the internal nodal flux vector associated to Darcy's velocity, and $\boldsymbol{h}^{\text{ext}}$ is the external nodal flux vector.

8.5 Solution strategies: Newton–Raphson method and linearization

8.5.1 Partially saturated porous media: u–$p_w$formulation

Considering an infinitesimal perturbation of the discrete solution $(\boldsymbol{d}, \boldsymbol{p}_w) \in \mathcal{S}_u^h \times \mathcal{S}_{p_w}^h$ compatible with prescribed forced boundary conditions:

$$\{\delta \boldsymbol{d}, \delta \boldsymbol{p}_w\} \in \mathcal{V}_u^h \times \mathcal{V}_{pw}^h \tag{8.43}$$

8.5.1.1 Equilibrium equation

The corresponding variation of the residual:

$$\boldsymbol{r}^s := \boldsymbol{f}^{\text{int}}(\boldsymbol{d}, \boldsymbol{p}_w) + \boldsymbol{f}_{\text{sg}}^{\text{int}}(\boldsymbol{d}) - \boldsymbol{g}_s(\boldsymbol{p}_w) - \boldsymbol{f}_b^{\text{ext}} - \boldsymbol{f}_t^{\text{ext}} - \boldsymbol{f}_T^{\text{ext}} = \boldsymbol{0} \tag{8.44}$$

is given by:

$$\begin{aligned}\delta \boldsymbol{r}^u &= \frac{\partial \boldsymbol{f}^{\text{int}}}{\partial \boldsymbol{d}}\delta\boldsymbol{d} + \frac{\partial \boldsymbol{f}^{\text{int}}}{\partial \boldsymbol{p}_w}\delta\boldsymbol{p}_w + \frac{\partial \boldsymbol{f}^{\text{int}}_{\text{sg}}}{\partial \boldsymbol{d}}\delta\boldsymbol{d} - \frac{\partial \boldsymbol{g}_s}{\partial \boldsymbol{p}_w}\delta\boldsymbol{p}_w - \frac{\partial \boldsymbol{f}^{\text{ext}}}{\partial \boldsymbol{p}_w}\delta\boldsymbol{p}_w \\ &= \boldsymbol{K}^{ss}\delta\boldsymbol{d} + \boldsymbol{K}^{sw}\delta\boldsymbol{p}_w + \boldsymbol{K}^{ss}_{sg}\delta\boldsymbol{d} - \boldsymbol{G}^{sw}\delta\boldsymbol{p}_w - \boldsymbol{P}^{sw}\delta\boldsymbol{p}_w\end{aligned} \tag{8.45}$$

with

$$\begin{aligned}\boldsymbol{K}^{ss} &:= \frac{\partial \boldsymbol{f}^{\text{int}}}{\partial \boldsymbol{d}} = \int_{\mathcal{B}} \boldsymbol{B}^{uT}\boldsymbol{D}\boldsymbol{B}^u \,\mathrm{d}v \\ \boldsymbol{K}^{sw} &:= \frac{\partial \boldsymbol{g}_s}{\partial \boldsymbol{p}_w} = -\int_{\mathcal{B}} \boldsymbol{B}^{uT}\boldsymbol{M}\boldsymbol{N}^w \,\mathrm{d}v \\ \boldsymbol{G}^{sw} &:= \frac{\partial \boldsymbol{f}^{\text{int}}}{\partial \boldsymbol{p}_w} = \int_{\mathcal{B}} \left(S_w + p_w \frac{C_s}{n}\right) \boldsymbol{B}^{uT}\boldsymbol{m}\boldsymbol{N}^w \,\mathrm{d}v \\ \boldsymbol{K}^{ss}_{sg} &:= \frac{\partial \boldsymbol{f}^{\text{int}}_{\text{sg}}}{\partial \boldsymbol{d}} = \int_{\mathcal{B}} \boldsymbol{S}^{uT}\boldsymbol{D}_{sg}\boldsymbol{S}^u \,\mathrm{d}v \\ \boldsymbol{P}^{sw} &:= \frac{\partial \boldsymbol{f}^{\text{ext}}}{\partial \boldsymbol{p}_w} = \int_{\mathcal{B}} (nS_wC_w\rho_w + C_s\rho_w)\, \boldsymbol{N}^{uT}\boldsymbol{b}\boldsymbol{N}^w \,\mathrm{d}v\end{aligned} \tag{8.46}$$

The matrices $\boldsymbol{D}$, $\boldsymbol{M}$ and $\boldsymbol{D}^{sg}$ are respectively:

$$\boldsymbol{D} := \frac{\partial \boldsymbol{\sigma}''}{\partial \boldsymbol{\varepsilon}} \; ; \qquad \boldsymbol{M} := \frac{\partial \boldsymbol{\sigma}''}{\partial p_w} \; ; \qquad \boldsymbol{D}_{sg} := \frac{\partial \boldsymbol{\Sigma}}{\partial \boldsymbol{\gamma}} \tag{8.47}$$

and will be derived in chapter 9.

8.5.1.2 Balance of mass

For an infinitesimal perturbation of the solution at time t_{n+1}, the residual:

$$\boldsymbol{r}^{\Delta t}_{p_w} := \boldsymbol{s}_{ww}(\boldsymbol{p}_w) + \boldsymbol{g}_w(\boldsymbol{d}, \boldsymbol{p}_w) - \Delta t \boldsymbol{h}^{\text{int}}_w(\boldsymbol{d}, \boldsymbol{p}_w) + \Delta t \boldsymbol{h}^{\text{ext}}_w = \boldsymbol{0} \tag{8.48}$$

experiences a variation:

$$\begin{aligned}\delta \boldsymbol{r}^{\Delta t}_{p_w} &= \frac{\partial \boldsymbol{s}_{ww}}{\partial \boldsymbol{p}_w}\delta\boldsymbol{p}_w + \frac{\partial \boldsymbol{g}_w}{\partial \boldsymbol{d}}\delta\boldsymbol{d} + \frac{\partial \boldsymbol{g}_w}{\partial \boldsymbol{p}_w}\delta\boldsymbol{p}_w - \Delta t\frac{\partial \boldsymbol{h}^{\text{int}}_w}{\partial \boldsymbol{d}}\delta\boldsymbol{d} - \Delta t\frac{\partial \boldsymbol{h}^{\text{int}}_w}{\partial \boldsymbol{p}_w}\delta\boldsymbol{p}_w \\ &= \boldsymbol{S}^{ww}_w\delta\boldsymbol{p}_w + \boldsymbol{G}^{ws}\delta\boldsymbol{d} + \boldsymbol{G}^{ww}\delta\boldsymbol{p}_w - \Delta t\boldsymbol{H}^{ws}\delta\boldsymbol{d} - \Delta t\boldsymbol{H}^{ww}\delta\boldsymbol{p}_w\end{aligned} \tag{8.49}$$

where

$$\begin{aligned}
\boldsymbol{S}_w^{ww} &= \int_{\mathcal{B}} \xi_w^{ww} \boldsymbol{N}^{wT} \boldsymbol{N}^w \,\mathrm{d}v & \boldsymbol{G}^{ws} &= \int_{\mathcal{B}} S_w \boldsymbol{N}^{wT} \boldsymbol{m}^T \boldsymbol{B}^u \,\mathrm{d}v \\
\boldsymbol{G}^{ww} &= \int_{\mathcal{B}} \frac{C_s}{n} \Delta\varepsilon_v \boldsymbol{N}^{wT} \boldsymbol{N}^w \,\mathrm{d}v & \boldsymbol{H}^{ws} &= \int_{\mathcal{B}} \boldsymbol{E}^{wT} \boldsymbol{U}_e^w \boldsymbol{m}^T \boldsymbol{B}^u \,\mathrm{d}v \\
\boldsymbol{H}^{ww} &= -\int_{\mathcal{B}} \boldsymbol{E}^{wT} \left(\frac{k_w^{rel}}{\mu_w} \boldsymbol{k}_w \right) \boldsymbol{E}^w \,\mathrm{d}v + \int_{\mathcal{B}} \boldsymbol{E}^{wT} \left(\boldsymbol{U}_{sw}^w + \boldsymbol{B}^w \right) \boldsymbol{N}^w \,\mathrm{d}v
\end{aligned} \tag{8.50}$$

with

$$\xi_w^{ww} := C_{ww} + C_s + (C_w C_s - \frac{\mathrm{d}C_s}{\mathrm{d}s}) \Delta p_w \tag{8.51a}$$

$$\boldsymbol{\Xi} := (1 + e_0) \frac{\mathrm{d}\boldsymbol{k}_{sat}}{\mathrm{d}e} \tag{8.51b}$$

$$\boldsymbol{U}_e^w := -\frac{1}{\mu_w} k_w^{rel} \boldsymbol{\Xi} \left(\nabla p_w - \rho_w \boldsymbol{b} \right) \tag{8.51c}$$

$$\boldsymbol{U}_{sw}^w := -\frac{1}{\mu_w} \frac{\mathrm{d}k_w^{rel}}{\mathrm{d}s} \frac{C_s}{n} \boldsymbol{k}_w \left(\nabla p_w - \rho_w \boldsymbol{b} \right) \tag{8.51d}$$

$$\boldsymbol{B}^w := \frac{1}{\mu_w} k_w^{rel} C_w \rho_w \boldsymbol{k}_w \boldsymbol{b} \tag{8.51e}$$

8.5.1.3 Iterative solution of coupled problem

The linearization of the balance equations yields a linear system of equations to be solved by Newtown–Raphson method. We set for a generic iteration (k):

$$\boldsymbol{R}_{n+1}^{(k+1)} \simeq \boldsymbol{R}_{n+1}^{(k)} + \left(\frac{\partial \boldsymbol{R}}{\partial \boldsymbol{a}} \right)_{n+1}^{(k)} \delta \boldsymbol{a}_{n+1}^{(k)} \simeq 0 \tag{8.52}$$

where

$$\delta \boldsymbol{a}_{n+1}^{(k)} = \left\{ \begin{matrix} \delta \boldsymbol{d} \\ \delta \boldsymbol{p}_w \end{matrix} \right\}_{n+1}^{(k)} ; \qquad \boldsymbol{R}_{n+1}^{(k)} = \left\{ \begin{matrix} \boldsymbol{r}^s \\ \boldsymbol{r}_{\Delta t}^w \end{matrix} \right\}_{n+1}^{(k)} \tag{8.53}$$

the Jacobian matrix:

$$\left(\frac{\partial \boldsymbol{R}}{\partial \boldsymbol{a}} \right)_{n+1}^{(k)} = \begin{bmatrix} \boldsymbol{K}^{ss} + \boldsymbol{K}_{sg}^{ss} & -(\boldsymbol{G}^{sw} + \boldsymbol{P}^{sw}) \\ \boldsymbol{G}^{ws} - \Delta t \boldsymbol{H}^{ws} & \boldsymbol{S}^{ww} + \boldsymbol{G}^{ww} - \Delta t \boldsymbol{H}^{ww} \end{bmatrix}_{n+1}^{(k)} \tag{8.54}$$

and then solve for $\delta \boldsymbol{a}_{n+1}^{(k)}$.

The new guess $\boldsymbol{a}_{n+1}^{(k+1)}$ is obtained as:

$$\boldsymbol{a}_{n+1}^{(k+1)} = \boldsymbol{a}_n + \Delta \boldsymbol{a}_{n+1}^{(k+1)} \; ; \qquad \Delta \boldsymbol{a}_{n+1}^{(k+1)} = \Delta \boldsymbol{a}_{n+1}^{(k)} + \delta \boldsymbol{a}_{n+1}^{(k)} \tag{8.55}$$

where $\Delta \boldsymbol{a}_{n+1}^{(k)}$ and $\Delta \boldsymbol{a}_{n+1}^{(k+1)}$ contain, respectively, the incremental displacement vector and pore water pressure vector for the previous and current iterations. The computational procedure is presented in Algorithm 1.

Input : $\boldsymbol{a}_n$, $\Delta \boldsymbol{a}_{n+1}^{(0)}$
Output: $\boldsymbol{a}_{n+1}$

Set $k = 0$
while $k < k_{max}$ **do**
  Compute $\left(\frac{\partial \boldsymbol{R}}{\partial \boldsymbol{a}}\right)_{n+1}^{(k)}$ and $\boldsymbol{R}_{n+1}^{(k)}$
  if $\left\|(\boldsymbol{r}^s)_{n+1}^{(k)}\right\| < \epsilon_{tol}$ *and* $\left\|(\boldsymbol{r}_{\Delta t}^w)_{n+1}^{(k)}\right\| < \epsilon_{tol}$ **then Exit**
  Impose Dirichlet boundary conditions
  Solve $\delta \boldsymbol{a}_{n+1}^{(k+1)} = -\left(\left(\frac{\partial \boldsymbol{R}}{\partial \boldsymbol{a}}\right)_{n+1}^{(k)}\right)^{-1} \boldsymbol{R}_{n+1}^{(k)}$
  Updated $\Delta \boldsymbol{a}_{n+1}^{(k+1)} = \Delta \boldsymbol{a}_{n+1}^{(k)} + \delta \boldsymbol{a}_{n+1}^{(k)}$
  Set $k = k + 1$
end
Set $\Delta \boldsymbol{a}_{n+1} = \Delta \boldsymbol{a}_{n+1}^{(k+1)}$ and $\boldsymbol{a}_{n+1} = \boldsymbol{a}_n + \Delta \boldsymbol{a}_{n+1}$

Algorithm 1: Newton–Raphson method for coupled hydromechanical problems.

8.5.2 Saturated porous media

The saturated case is obtained by considering $S_w = 1$, $k_w^{rel} = 1$ and neglecting the variation in water density along with the simplifications already done in the partially saturated case.

$$\nabla \cdot \boldsymbol{\sigma}' - \nabla p_w + \rho \boldsymbol{b} = \boldsymbol{0} \tag{8.56a}$$

$$C_{ww} \dot{p}_w + \nabla \cdot \boldsymbol{v}^s + \nabla \cdot \boldsymbol{w}^w = 0 \tag{8.56b}$$

The mixture density now is $\rho = (1-n)\rho_s + n\rho_w$ and $C_{ww} = nC_w$. Finally, $\boldsymbol{\sigma}'$ is the Terzaghi's effective stress:

$$\boldsymbol{\sigma}' = \boldsymbol{\sigma} + p_w \mathbf{1} \tag{8.57}$$

The residual of the equilibrium equation and the mass of balance (integrated) are, respectively, given by:

$$\boldsymbol{r}^s = \boldsymbol{f}^{\text{int}}(\boldsymbol{d}) + \boldsymbol{f}^{\text{int}}_{\text{sg}}(\boldsymbol{d}) - \boldsymbol{g}_s(\boldsymbol{p}_w) - \boldsymbol{f}^{\text{ext}}_b - \boldsymbol{f}^{\text{ext}}_t - \boldsymbol{f}^{\text{ext}}_T \tag{8.58}$$

$$\boldsymbol{r}^w_{\Delta t} = \boldsymbol{s}_w(\boldsymbol{p}_w) + \boldsymbol{g}_w(\boldsymbol{d}) - \Delta t \boldsymbol{h}^{\text{int}}(\boldsymbol{d}, \boldsymbol{p}_w) - \Delta t \boldsymbol{h}^{\text{ext}} \tag{8.59}$$

where:

$$\begin{aligned}
\boldsymbol{f}^{\text{int}} &= \int_{\mathcal{B}} \boldsymbol{B}^{uT} \boldsymbol{\sigma}'(\boldsymbol{\varepsilon}(\boldsymbol{d}))\, \mathrm{d}v & \boldsymbol{f}^{\text{int}}_{\text{sg}} &= \int_{\mathcal{B}} \boldsymbol{S}^{uT} \boldsymbol{\Sigma}(\boldsymbol{\gamma}(\boldsymbol{d}))\, \mathrm{d}v \\
\boldsymbol{g}_s &= \int_{\mathcal{B}} \boldsymbol{B}^{uT} \boldsymbol{m} p_w\, \mathrm{d}v & \boldsymbol{f}^{\text{ext}}_b &= \int_{\mathcal{B}} \boldsymbol{N}^{uT} (\rho \boldsymbol{b})\, \mathrm{d}v \\
\boldsymbol{f}^{\text{ext}}_t &= \int_{\partial \mathcal{B}_t} \boldsymbol{N}^{uT} \overline{\boldsymbol{t}}\, \mathrm{d}a & \boldsymbol{f}^{\text{ext}}_T &= \int_{\partial \mathcal{B}_t} \boldsymbol{B}^{uT}_s \overline{\boldsymbol{T}}\, \mathrm{d}a
\end{aligned} \tag{8.60}$$

and:

$$\begin{aligned}
\boldsymbol{s}_w &= \int_{\mathcal{B}} \boldsymbol{N}^{wT} n C_w \Delta p_w\, \mathrm{d}v & \boldsymbol{g}_w &= \int_{\mathcal{B}} \boldsymbol{N}^{wT} \nabla \cdot \Delta \boldsymbol{u}\, \mathrm{d}v \\
\boldsymbol{h}^{\text{int}} &= \int_{\mathcal{B}} \boldsymbol{E}^{wT} \boldsymbol{w}^w(\boldsymbol{d}, \boldsymbol{p}_w)\, \mathrm{d}v & \boldsymbol{h}^{\text{ext}} &= \int_{\partial \mathcal{B}_{q_w}} \boldsymbol{N}^{wT} \overline{q}_w\, \mathrm{d}a
\end{aligned} \tag{8.61}$$

Eqs. (8.58) and (8.59) are also solved using Newton–Raphson method. Following the same procedure as in the partially saturated case, the linearization of eqs. (8.58) and (8.59) yield the following system of equations:

$$\begin{bmatrix} \boldsymbol{K}^{ss} + \boldsymbol{K}^{ss}_{sg} & -\boldsymbol{G}^{sw} \\ -\boldsymbol{G}^{ws} + \Delta t \boldsymbol{H}^{ws} & -\boldsymbol{S}^{ww} + \Delta t \boldsymbol{H}^{ww} \end{bmatrix}^{(k)}_{n+1} \begin{Bmatrix} \delta \boldsymbol{d} \\ \delta \boldsymbol{p}_w \end{Bmatrix}^{(k)}_{n+1} = - \begin{Bmatrix} \boldsymbol{r}^s \\ -\boldsymbol{r}^w_{\Delta t} \end{Bmatrix}^{(k)}_{n+1} \tag{8.62}$$

with

$$\begin{aligned}
\boldsymbol{K}^{ss} &:= \int_{\mathcal{B}} \boldsymbol{B}^{uT} \left(\frac{\partial \boldsymbol{\sigma}'}{\partial \boldsymbol{\varepsilon}} \right) \boldsymbol{B}^u\, \mathrm{d}v & \boldsymbol{K}^{ss}_{sg} &:= \int_{\mathcal{B}} \boldsymbol{S}^{uT} \left(\frac{\partial \boldsymbol{\Sigma}}{\partial \boldsymbol{\gamma}} \right) \boldsymbol{S}^u\, \mathrm{d}v \\
\boldsymbol{G}_{sw} &:= \int_{\mathcal{B}} \boldsymbol{B}^{uT} \boldsymbol{m} \boldsymbol{N}^w\, \mathrm{d}v
\end{aligned} \tag{8.63}$$

and

$$\begin{aligned} \boldsymbol{S}_w^{ww} &:= \int_{\mathcal{B}} C_{ww} \boldsymbol{N}_w^{wT} \boldsymbol{N}^w \, \mathrm{d}v \qquad & \boldsymbol{G}^{ws} &:= \int_{\mathcal{B}} \boldsymbol{N}^{wT} \boldsymbol{m}^T \boldsymbol{B}^u \, \mathrm{d}v \\ \boldsymbol{H}^{ws} &:= \int_{\mathcal{B}} \boldsymbol{E}^{wT} \boldsymbol{U}_e^w \boldsymbol{m}^T \boldsymbol{B}^u \, \mathrm{d}v \qquad & \boldsymbol{H}^{ww} &:= -\int_{\mathcal{B}} \boldsymbol{E}^{wT} \left(\frac{1}{\mu_w} \boldsymbol{k}_w \right) \boldsymbol{E}^w \, \mathrm{d}v \end{aligned} \tag{8.64}$$

where

$$\begin{aligned} \boldsymbol{\Xi} &:= (1 + e_0) \frac{\mathrm{d}\boldsymbol{k}_w}{\mathrm{d}e} \\ \boldsymbol{U}_e^w &:= -\frac{1}{\mu_w} \boldsymbol{\Xi} \left(\nabla p_w - \rho_w \boldsymbol{b} \right) \end{aligned} \tag{8.65}$$

8.6 Solution strategies. Arc–length method

Quadratic convergence makes Newton's method ideal when solving large systems of non-linear equations. However, a major drawback of this method is that it fails to reproduce correctly snap–through behavior under load control and snap–back behavior under load or displacement control. This might happen when modeling materials that exhibit softening. Arc length method is a path following technique able to reproduce correctly such behaviors.

The basic idea behind arc–length method is that instead of keeping the load (or the displacement) increment fixed during the iterations of a time step $[t_n, t_{n+1}]$, the load (or the displacement) increment varies through a load factor:

$$\lambda_{n+1} = \lambda_n + \Delta\lambda_{n+1} \tag{8.66}$$

where λ_n is the load factor at time t_n and $\Delta\lambda_{n+1}$ is the incremental load factor. Hence, the external force vector at time t_{n+1} is given by:

$$\boldsymbol{f}_{t,n+1}^{\mathrm{ext}} = \lambda_{n+1} \overline{\boldsymbol{f}}_t^{\mathrm{ext}} \tag{8.67}$$

where $\overline{\boldsymbol{f}}_t^{\mathrm{ext}}$ is the *fixed external force vector*.

Considering for simplicity the mechanical problem only, eq. (8.48) at time t_{n+1} can be written as follows:

$$\boldsymbol{r} := \boldsymbol{f}^{\text{int}}(\boldsymbol{d}_{n+1}) + \boldsymbol{f}^{\text{int}}_{\text{sg}}(\boldsymbol{d}_{n+1}) - \boldsymbol{f}^{\text{ext}}_{b,n+1} - \lambda_{n+1}\overline{\boldsymbol{f}}^{\text{ext}}_{t,n+1} - \boldsymbol{f}^{\text{ext}}_{T,n+1} = \boldsymbol{0} \tag{8.68}$$

where $\boldsymbol{f}^{\text{ext}}_{T}$ is considered as constant.

Since λ_{n+1} introduces an additional unknown to the system to be solved, an additional constraint function g must be supplied. The new equilibrium state of the augmented system of equations can now be determined by simultaneously solving:

$$\begin{bmatrix} \boldsymbol{K} & -\overline{\boldsymbol{f}}^{\text{ext}}_{t} \\ \boldsymbol{h}^T & s \end{bmatrix}^{(k)}_{n+1} \begin{Bmatrix} \delta\boldsymbol{d} \\ \delta\lambda \end{Bmatrix}^{(k)}_{n+1} = \begin{Bmatrix} -\boldsymbol{r} \\ g \end{Bmatrix}^{(k)}_{n+1} \tag{8.69}$$

with

$$\boldsymbol{K} := \boldsymbol{K}^{ss} + \boldsymbol{K}^{ss}_{sg}\ ; \qquad \boldsymbol{h} := \frac{\partial g}{\partial \boldsymbol{d}}\ ; \qquad s := \frac{\partial g}{\partial \lambda} \tag{8.70}$$

The first term on the l.h.s. of eq. (8.69) is a non-symmetric matrix. Therefore, the linear system of equations in eq. (8.69) is solved with a two–stage solution procedure in order to exploit the possibility of having a symmetric stiffness matrix, $\boldsymbol{K}$, as it is the case of the Prandtl–Reuss model (see chapter 9):

$$\delta\boldsymbol{d}^I = \left(\boldsymbol{K}^{(k)}_{n+1}\right)^{-1} \overline{\boldsymbol{f}}^{\text{ext}}_{n+1} \tag{8.71}$$

$$\delta\boldsymbol{d}^{II} = \left(\boldsymbol{K}^{(k)}_{n+1}\right)^{-1} (\boldsymbol{r}^u)^{(k)}_{n+1} \tag{8.72}$$

We have, then, the new increments for the next iteration:

$$\begin{aligned} \delta\boldsymbol{d}^{(k)}_{n+1} &= \delta\lambda^{(k)}_{n+1}\delta\boldsymbol{d}^I + \delta\boldsymbol{d}^{II} \\ \delta\lambda^{(k)}_{n+1} &= -\frac{g^{(k)}_{n+1} + \left(\boldsymbol{h}^{(k)}_{n+1}\right)^T \delta\boldsymbol{d}^{II}}{s^{(k)}_{n+1} + \left(\boldsymbol{h}^{(k)}_{n+1}\right)^T \delta\boldsymbol{d}^I} \end{aligned} \tag{8.73}$$

In this work we use a simplification version of the spherical arc–length constraint [47] presented by De Borst et al. [50]:

$$g = \Delta \boldsymbol{d}_n^T \delta \boldsymbol{d}_{n+1}^{(k)} + \beta^2 \Delta\lambda_n \delta\lambda_{n+1}^{(k)} \left(\overline{\boldsymbol{f}}_{n+1}^{\text{ext}}\right)^T \overline{\boldsymbol{f}}_{n+1}^{\text{ext}} \tag{8.74}$$

$$\delta\lambda_{n+1}^{(k)} = -\frac{\Delta \boldsymbol{d}_n^T \delta \boldsymbol{d}^{II}}{\Delta \boldsymbol{d}_n^T \delta \boldsymbol{d}^{I} + \beta^2 \Delta\lambda_n \left(\overline{\boldsymbol{f}}_{n+1}^{\text{ext}}\right)^T \overline{\boldsymbol{f}}_{n+1}^{\text{ext}}} \tag{8.75}$$

with β a user-specified value that weighs the importance of the contributions that stem from the displacement vector and the load increment. De Borst et al. [50] point out that *the value of β does not seem to influence the performance of the method very much* based on their numerical experiences. Thus, the nonlinear equilibrium problem defined in eq. (8.69) is solved by the algorithm summarized in Algorithm 2 and with $\beta = 0$.

8.7 Solution strategies. Linear equation system solvers

Newton–Raphson method and arc–length method require the computation of the Jacobian matrix $\partial \boldsymbol{R}/\partial \boldsymbol{a}$ and the solution of the linear system of equations at each iteration (*i.e.* line 6 of Algorithm 1 and line 7 of Algorithm 2). This last step implies using either direct solvers or iterative solvers. As we will see in next section, the partially saturated and fully saturated formulations presented in section 8.5 are implemented in GeoPDEs, an Octave/Matlab open source package. Matlab solves the linear system of equations with the backslash operator (\) using direct solvers which factorize the Jacobian matrix and uses this matrix decomposition to compute the solution.

For IBVPs in 3D where the dimension of the system may be several thousands, factorization methods are generally not efficient and the solution of such system may be extremely time expensive. MATLAB provides several iterative methods to generate a series of approximate solutions for large matrices. Two of these iterative techniques for solving such system of nonlinear equations are thus used in this work when modeling 3D domains: Minimum residual method, MINRES [see 12, 130], and Biconjugate gradient stabilized (l) method, BICGSTAB(I) [see 161].

Input : $\boldsymbol{d}_n$, λ_n, $\Delta\boldsymbol{d}_n, \Delta\boldsymbol{d}_{n+1}^{(0)}$, $\Delta\lambda_{n+1}^{(0)}$
Output: $\boldsymbol{d}_{n+1}$, λ_{n+1}

Set $k = 0$
while $k < k_{max}$ **do**
  Compute $\boldsymbol{K}_{n+1}^{(k)}$ and $\left(\boldsymbol{f}^{\text{int}}\right)_{n+1}^{(k)}$
  Compute $(\boldsymbol{r}^u)_{n+1}^{(k)} = \left(\lambda_n + \Delta\lambda_{n+1}^{(k)}\right)\overline{\boldsymbol{f}}_{n+1}^{\text{ext}} - \left(\boldsymbol{f}^{\text{int}}\right)_{n+1}^{(k)}$
  if $\left\|(\boldsymbol{r}^u)_{n+1}^{(k)}\right\| < \epsilon_{tol}$ **then Exit**
  Impose Dirichlet boundary conditions
  Solve $\delta\boldsymbol{d}^I = \left(\boldsymbol{K}_{n+1}^{(k)}\right)^{-1}\overline{\boldsymbol{f}}_{n+1}^{\text{ext}}$
    $\delta\boldsymbol{d}^{II} = \left(\boldsymbol{K}_{n+1}^{(k)}\right)^{-1}(\boldsymbol{r}^u)_{n+1}^{(k)}$;
  Compute $\delta\lambda_{n+1}^{(k)} = -\Delta\boldsymbol{d}_n^T\delta\boldsymbol{u}^{II} / \left(\Delta\boldsymbol{d}_n^T\delta\boldsymbol{d}^I\right)$
    $\delta\boldsymbol{d}_{n+1}^{(k)} = \delta\lambda_{n+1}^{(k)}\delta\boldsymbol{d}^I + \delta\boldsymbol{d}^{II}$
  Update $\Delta\boldsymbol{d}_{n+1}^{(k+1)} = \Delta\boldsymbol{d}_{n+1}^{(k)} + \delta\boldsymbol{d}_{n+1}^{(k)}$;
    $\Delta\lambda_{n+1}^{(k+1)} = \Delta\lambda_{n+1}^{(k)} + \delta\lambda_{n+1}^{(k)}$;
  set $k = k + 1$
end
set $\Delta\boldsymbol{d}_{n+1} = \Delta\boldsymbol{d}_{n+1}^{(k+1)}$ and $\Delta\lambda_{n+1} = \Delta\lambda_{n+1}^{(k+1)}$
  $\boldsymbol{d}_{n+1} = \boldsymbol{d}_n + \Delta\boldsymbol{d}_{n+1}$ and $\lambda_{n+1} = \lambda_n + \Delta\lambda_{n+1}$

Algorithm 2: Arc–lengh method for mechanical problems.

MINRES is used for large, sparse and symmetric non-positive definite matrices. This method is suitable for the fully saturated problem in eq. (8.62) if the effects of the void ratio considered in $\boldsymbol{H}^{ws}$ are neglected and matrices $\boldsymbol{K}^{ss}$ and $\boldsymbol{K}_{sg}^{ss}$ are symmetric. Hence, it can be also useful in the mechanical problem.

If the Jacobian matrix do not share these properties, BICGSTAB(I) will be used. This method solves linear system of equations with nonsymmetric matrices and is preconditioned by the incomplete LU factorization with a drop tolerance of 1e-5 in order to accelerate convergence.

8.8 GeoPDEs

GeoPDEs [51, 179] is an Octave/Matlab open source package in which IGA have been implemented for solving partial differential equations such as linear elasticity, Stokes, Maxwell equations, etc., each of them with their respective solvers (*i.e.* `solve_linear_elasticity.m`, `solve_stokes.m`, `solve_maxwell_eig.m`). These solvers make use of the different functions for the evaluation B-splines and NURBS basis functions as well as several operators for matrix and vector assembly available in the GeoPDEs package. Moreover, new capabilities are recently released such as IGA adaptive methods based on hierarchical B-splines, see Garau and Vázquez [68] for the details. Therefore, creating new solvers from existing functions only requires minor modifications with respect to the already existing examples. In this work, four additional solvers are implemented:

- `solve_meca_sg.m`: solves the mechanical problem for second gradient elastoplastic monophasic media using Newton–Rapshon method.
- `solve_meca_sg_arc.m`: solves the mechanical problem for second gradient elastoplastic monophasic media using the arc–length method in case of softening behavior under load control (Neumann boundary conditions).
- `solve_hidromeca_sat_sg.m`: solves the coupled hydromechanical problem for second gradient elastoplastic biphasic media in fully saturated conditions using Newton–Rapshon method.
- `solve_hidromeca_usat_uw_sg.m`: solves the coupled hydromechanical problem for second gradient elastoplastic biphasic media in partially saturated conditions using Newton–Rapshon method.

with three new operators:

- `op_meca_sg.m`: assembles the sum of the local matrices $\boldsymbol{K}^{uu}$ and $\boldsymbol{K}^{uu}_{sg}$ and the local internal force vectors $\boldsymbol{f}^{\text{int}}$ and $\boldsymbol{f}^{\text{int}}_{\text{sg}}$.
- `op_hidromeca_sat_sg.m`: assembles the local matrices given in eqs. (8.63) and (8.64) and the residual vectors given in eqs. (8.44) and (8.48) needed in line 6 of Algorithm 1.

- `op_hidromeca_usat_uw_sg.m`: assembles the matrices given in eqs. (8.46) and (8.50) and the residual vectors given in eqs. (8.58) and (8.59) needed in line 6 of Algorithm 1.

Finally, a new type of functions that updates the array containing the state variables, which are needed for the computation of stress and double stress at the gauss point level, after convergence of the current time step:

- `up_meca_sg.m`: updates the state variables needed for the numerical integration of the constitutive equations of the classical and the second gradient mechanical part and it is used in the solvers: `solve_meca_sg.m`, `solve_meca_sg_arc.m` and `solve_hidromeca_sat_sg.m`.
- `up_hidromeca_usat_uw_sg.m`: updates the state variables needed for the numerical integration of the constitutive equations of the classical and the second mechanical gradient part, density, void ratio and degree of saturation and it is used in the solver `solve_hidromeca_usat_uw_sg.m`.

Chapter 9

Numerical implementation of elastoplastic constitutive models

This chapter addresses the numerical integration schemes adopted to solve the initial value problems defined by the three elastoplastic models presented in chapter 7. The development of an implicit (backward Euler) integration scheme have been chosen in all three models. We make use of the additive decomposition of the infinitesimal strain (and second derivatives of displacement) into elastic and plastic parts. Thus, the rate forms of the constitutive relations and the evolution of the internal variables are split into two stages: elastic predictor and plastic corrector in order to performed the so–called return mapping algorithm [158]. Since the constitutive functions present nonlinearities a local Newton–Rapshon iteration is required.

One of the advantages of the proposed algorithm is its robustness and the possibility of the evaluation the consistent tangent operator in closed form after the linearization of the evolution equations of the constitutive models. In consequence, quadratic convergence is obtained in the global Newton–Rapshon algorithm derived in chapter 8. With the computation of the consistent tangent operators for the classical and the second gradient mechanical models, the IGA–FEM formulation is completed.

9.1 Prandtl–Reuss model

9.1.1 Return mapping algorithm

9.1.1.1 Evolution problem split

Given the stress state by $\boldsymbol{\sigma}_n$ and $S_{y,n}$ at time t_n, the goal is to find the stress state $\boldsymbol{\sigma}_{n+1}$ and $S_{y,n+1}$ at time t_{n+1} for a given strain increment $\Delta\boldsymbol{\varepsilon}_{n+1}$. Using the return mapping algorithm, the solution is split into two stages: elastic predictor and plastic corrector, as follows

$$
\begin{array}{lll}
\text{Evolution equations} & \text{Elastic predictor} \quad + & \text{Plastic corrector} \\
\dot{p} = K\dot{\varepsilon}_v & \dot{p} = K\dot{\varepsilon}_v & \dot{p} = 0 \\
\dot{\boldsymbol{\sigma}}_{\text{dev}} = 2G_1\left(\dot{\boldsymbol{e}} - \dot{\lambda}_\varepsilon\left(\partial f/\partial\boldsymbol{\sigma}_{\text{dev}}\right)\right) & \dot{\boldsymbol{\sigma}}_{\text{dev}} = 2G_1\dot{\boldsymbol{e}} & \dot{\boldsymbol{\sigma}}_{\text{dev}} = -2G_1\dot{\lambda}_\varepsilon\left(\partial f/\partial\boldsymbol{\sigma}_{\text{dev}}\right) \\
\dot{S}_y = \dot{\lambda}_\varepsilon H_\varepsilon(S_y - S_{y,min}) & \dot{S}_y = 0 & \dot{S}_y = \dot{\lambda}_\varepsilon H_\varepsilon(S_y - S_{y,min})
\end{array}
\tag{9.1}
$$

First, the elastic predictor is computed in which the strain increment is purely elastic. If the trial stress resides inside the elastic domain, then the stress and the internal variables are updated using the trial predictors. Otherwise, the trial stress is outside the elastic domain, and the plastic correction step follows by considering a reduction of the trial stress proportional to the plastic increment; the internal variable is also updated simultaneously with the stress according to the flow rule.

9.1.1.2 Elastic predictor

The solution of the elastic predictor step is given by:

$$p_{n+1} = p_n + K\Delta\varepsilon_{v,n+1} \tag{9.2a}$$

$$\left(\boldsymbol{\sigma}^{tr}_{\text{dev}}\right)_{n+1} = \left(\boldsymbol{\sigma}_{\text{dev}}\right)_n + 2G_1\Delta\boldsymbol{e}_{n+1} \tag{9.2b}$$

$$S^{tr}_{n+1} = \left\|\left(\boldsymbol{\sigma}^{tr}_{\text{dev}}\right)_{n+1}\right\| \tag{9.2c}$$

$$S^{tr}_{y,n+1} = S_{y,n} \tag{9.2d}$$

then, the following inequality is evaluated:

$$f_{n+1}^{tr} = S_{n+1}^{tr} - S_{y,n+1}^{tr} \leq 0? \tag{9.3}$$

If $f_{n+1}^{tr} \leq 0$, then, the stress and the internal variable are updated:

$$(\boldsymbol{\sigma}_{\text{dev}})_{n+1} = \left(\boldsymbol{\sigma}_{\text{dev}}^{tr}\right)_{n+1}, \qquad \boldsymbol{\sigma}_{n+1} = (\boldsymbol{\sigma}_{\text{dev}})_{n+1} + p_{n+1}\mathbf{1}, \qquad S_{y,n+1} = S_{y,n+1}^{tr} \tag{9.4}$$

9.1.1.3 Plastic corrector

If the trial stress is outside the elastic domain, *i.e.* $f_{n+1}^{tr} > 0$, the plastic corrector step is integrated numerically using the Backward Euler algorithm:

$$(\boldsymbol{\sigma}_{\text{dev}})_{n+1} = \left(\boldsymbol{\sigma}_{\text{dev}}^{tr}\right)_{n+1} - 2\Delta\lambda_{\varepsilon,n+1} G_1 \boldsymbol{\eta}_{n+1} \tag{9.5a}$$

$$\boldsymbol{\sigma}_{n+1} = (\boldsymbol{\sigma}_{\text{dev}})_{n+1} + p_{n+1}\mathbf{1} \tag{9.5b}$$

$$S_{n+1} = S_{n+1}^{tr} - 2\Delta\lambda_{\varepsilon,n+1} G_1 \tag{9.5c}$$

$$S_{y,n+1} = S_{y,n} + \Delta\lambda_{\varepsilon} H_{\varepsilon,n+1}(S_{y,n+1} - S_{y,min}) \tag{9.5d}$$

Eq. (9.5c) is obtained by observing that $\boldsymbol{\eta}_{n+1}^{tr}$ and $\boldsymbol{\eta}_{n+1}$ are parallel, which means that the final updated stress moves in the same direction as the trial stress.

Thus, at the return–mapped state, the yield condition must be satisfied:

$$f_{n+1} = S_{n+1} - S_{y,n+1} = 0 \tag{9.6}$$

which is a non–linear equation in terms of $\Delta\lambda_{\varepsilon}$. Eq. (9.6) can be solved using Newton–Raphson method:

$$f_{n+1}^{(k+1)} = f_{n+1}^{(k)} + \delta f_{n+1}^{(k)} = f_{n+1}^{(k)} + \frac{\partial f_{n+1}^{(k)}}{\partial \Delta\lambda_{\varepsilon}} \delta\Delta\lambda_{\varepsilon,n+1}^{(k)} = 0 \tag{9.7a}$$

$$\Delta\lambda_{\varepsilon,n+1}^{(k+1)} = \Delta\lambda_{\varepsilon,n+1}^{(k)} + \delta\Delta\lambda_{\varepsilon,n+1}^{(k)} \tag{9.7b}$$

where (k) denotes the iteration counter of this local Newton–Raphson iteration, presented in Algorithm 3 (with all subscripts $n+1$ dropped). Once the return–mapped state is found, the set of eqs. (9.5) are updated.

Input : S^{tr}, $S_{y,n}$ and $\Delta\lambda_\varepsilon^{(0)}$
Output: $\Delta\lambda_\varepsilon$

Set $k = 0$
while $k < k_{max}$ **do**
  Compute

$$\begin{aligned} S^{(k)} &= S^{tr} - 2\Delta\lambda_\varepsilon^{(k)} G_1 \\ S_y^{(k)} &= \left(S_{y,n} - \Delta\lambda_\varepsilon^{(k)} H_\varepsilon S_{y,min}\right) / \left(1 - \Delta\lambda_\varepsilon^{(k)} H_\varepsilon\right) \\ f^{(k)} &= S^{(k)} - S_y^{(k)} \end{aligned}$$

  if $\left\| f^{(k)} \right\| < \epsilon_{tol,f}$ **then Exit**
  Compute $\delta f^{(k)} = -2G_1 - H_\varepsilon \left(S_{y,n} - S_{y,min}\right) / \left(1 - H_\varepsilon \Delta\lambda_\varepsilon^{(k)}\right)^2$
  Solve $\delta\Delta\lambda_\varepsilon^{(k)} = -f^{(k)} / \delta f^{(k)}$
  Update $\Delta\lambda_\varepsilon^{(k+1)} = \Delta\lambda_\varepsilon^{(k)} + \delta\Delta\lambda_\varepsilon^{(k)}$
  set $k = k + 1$
end
Set $\Delta\lambda_\varepsilon = \Delta\lambda_\varepsilon^{(k+1)}$

Algorithm 3: Local Newton–Raphson iteration for determination of the plastic consistency parameter of Prandtl–Reuss model.

9.1.2 Consistent tangent operator

The consistent tangent stiffness operator for the integration algorithm of sect. 9.1.1 is evaluated at the end of the time step t_{n+1} as

$$\boldsymbol{D}_{n+1}^{(k)} = \frac{\partial \boldsymbol{\sigma}_{n+1}^{(k)}}{\partial \boldsymbol{\varepsilon}_{n+1}^{(k)}} \equiv \frac{\partial \boldsymbol{\sigma}_{n+1}^{(k)}}{\partial \boldsymbol{\varepsilon}_{n+1}^{tr,(k)}} \tag{9.8}$$

For an elastic process, the consistent tangent stiffness operator is equal to the elastic tangent stiffness matrix:

$$\boldsymbol{D} = \boldsymbol{D}^e = \left(K - \frac{2}{3} G_1\right) \mathbf{1} \otimes \mathbf{1} + 2G_1 \boldsymbol{I} \tag{9.9}$$

Otherwise, eq. (9.8) requires the linearization of the deviatoric stress given by eq. (9.5a) (subscripts $(n+1)$ and superscripts $(k+1)$ will be omitted for brevity):

$$\begin{aligned} \mathrm{d}\boldsymbol{\sigma}_{\mathrm{dev}} &= \mathrm{d}\left(\boldsymbol{\sigma}_{\mathrm{dev}}^{tr}\right)_{n+1} - 2G_1\Delta\lambda_\varepsilon \frac{\partial^2 f}{\partial\boldsymbol{\sigma}_{\mathrm{dev}} \otimes \partial\boldsymbol{\sigma}_{\mathrm{dev}}}\mathrm{d}\boldsymbol{\sigma}_{\mathrm{dev}} - 2G_1 \frac{\partial f}{\partial\boldsymbol{\sigma}_{\mathrm{dev}}}\mathrm{d}(\Delta\lambda_\varepsilon) \\ &= 2G_1\mathrm{d}\boldsymbol{e} - 2G_1\Delta\lambda_\varepsilon\left\{\frac{1}{S}\left(\boldsymbol{I} - \boldsymbol{\eta}\otimes\boldsymbol{\eta}\right)\right\}\mathrm{d}\boldsymbol{\sigma}_{\mathrm{dev}} + 2G_1\mathrm{d}(\Delta\lambda_\varepsilon) \end{aligned} \tag{9.10}$$

Rearranging terms, we have:

$$\mathrm{d}\boldsymbol{\sigma}_{\mathrm{dev}} = 2G_1\tilde{\boldsymbol{I}}^{-1}\left(\mathrm{d}\boldsymbol{e} - \boldsymbol{\eta}\mathrm{d}\left(\Delta\lambda_\varepsilon\right)\right) \tag{9.11}$$

with:

$$\tilde{\boldsymbol{I}} := \left(1 + 2G_1\frac{\Delta\lambda_\varepsilon}{S}\right)\boldsymbol{I} - 2G_1\frac{\Delta\lambda_\varepsilon}{S}\boldsymbol{\eta}\otimes\boldsymbol{\eta} \tag{9.12}$$

Since eq. (9.11) requires the differential of the plastic consistency parameter, the differential of the internal variable S_y is also computed:

$$\mathrm{d}S_y = \frac{H_\varepsilon(S_n - S_{y,min})}{(1-\Delta\lambda_\varepsilon H_\varepsilon)^2}\mathrm{d}(\Delta\lambda_\varepsilon) \tag{9.13}$$

and now using the consistency condition and the results in eqs. (9.11) and (9.13), one obtains:

$$\mathrm{d}(\Delta\lambda_\varepsilon) = \frac{1}{\tilde{K}_p}\left(2G_1\tilde{\boldsymbol{I}}^{-1}\boldsymbol{\eta}\right)\cdot\mathrm{d}\boldsymbol{e} \tag{9.14}$$

with

$$\tilde{\boldsymbol{I}}^{-1} = \frac{S}{S + 2G_1\Delta\lambda_\varepsilon}\boldsymbol{I} + \frac{2G_1\Delta\lambda_\varepsilon}{S + 2G_1\Delta\lambda_\varepsilon}\boldsymbol{\eta}\otimes\boldsymbol{\eta} \tag{9.15a}$$

$$\tilde{K}_p = 2G_1 + \frac{H_\varepsilon(S_n - S_{y,min})}{(1-\Delta\lambda_\varepsilon H_\varepsilon)^2} \tag{9.15b}$$

Thus, using the expression obtained in eq. (9.14), the differential of the deviatoric stress in eq. (9.11) may be written as

$$\mathrm{d}\boldsymbol{\sigma}_{\mathrm{dev}} = \boldsymbol{D}_{\mathrm{dev}}\mathrm{d}\boldsymbol{e} \tag{9.16}$$

where $\boldsymbol{D}$ is the deviatoric part of the elastoplastic tangent stiffness operator, given by:

$$\boldsymbol{D}_{dev} = 2G_1\tilde{\boldsymbol{I}}^{-1} - \frac{4G_1^2}{\tilde{K}_p}\boldsymbol{\eta}\otimes\boldsymbol{\eta} \tag{9.17}$$

Taking into account the volumetric part of the stress:

$$\begin{aligned} \mathrm{d}\boldsymbol{\sigma} &= \mathrm{d}\boldsymbol{\sigma}_{\mathrm{dev}} + \mathrm{d}p\mathbf{1} \\ &= \boldsymbol{D}_{\mathrm{dev}}\left(\boldsymbol{I} - \frac{1}{3}\mathbf{1}\otimes\mathbf{1}\right)d\boldsymbol{\varepsilon} + K(\mathbf{1}\otimes\mathbf{1})d\boldsymbol{\varepsilon} \\ &= \left(\boldsymbol{D}_{\mathrm{dev}}\boldsymbol{I}_{\mathrm{dev}} + K(\mathbf{1}\otimes\mathbf{1})\right)\mathrm{d}\boldsymbol{\varepsilon} \end{aligned} \tag{9.18}$$

Thus, the consistent tangent stiffness operator for the Prandtl–Reuss model is given by the following expression:

$$\begin{aligned} \boldsymbol{D} =& \boldsymbol{D}_{\mathrm{dev}}\boldsymbol{I}_{\mathrm{dev}} + K(\mathbf{1}\otimes\mathbf{1}) \\ =& \frac{2G_1S}{S+2G_1\Delta\lambda_\varepsilon}\boldsymbol{I} + \left\{K - \frac{2G_1S}{3(S+2G_1\Delta\lambda_\varepsilon)}\right\}(\mathbf{1}\otimes\mathbf{1}) \\ &+ \left(\frac{4G_1^2\Delta\lambda_\varepsilon}{S+2G_1\Delta\lambda_\varepsilon} - \frac{4G_1^2}{\tilde{K}_p}\right)(\boldsymbol{\eta}\otimes\boldsymbol{\eta}) \end{aligned} \tag{9.19}$$

9.2 Milan model

9.2.1 Return mapping algorithm

9.2.1.1 Evolution problem split

The return mapping algorithm for the Milan Model with generalized hardening will be only outlined since its numerical implementation follows the guidelines of Tamagnini et al. [167] and Tamagnini and Ciantia [169]. In this particular case, the elastic–plastic operator split is extended to account for the variation of the internal variable vector

$\boldsymbol{q} = \{p_s'',\ p_m''\}$ due to changes in degree of saturation S_w.

$$\begin{array}{lll} \text{Evolution equations} & \text{Elastic predictor} + & \text{Plastic corrector} \\ \dot{\boldsymbol{\varepsilon}} = \nabla^s \dot{\boldsymbol{u}} & \dot{\boldsymbol{\varepsilon}} = \nabla^s \dot{\boldsymbol{u}} & \dot{\boldsymbol{\varepsilon}} = \boldsymbol{0} \\ \dot{\boldsymbol{\varepsilon}}^e = \dot{\boldsymbol{\varepsilon}} - \dot{\lambda}_\varepsilon \left(\partial g / \partial \boldsymbol{\sigma}''\right) & \dot{\boldsymbol{\varepsilon}}^e = \dot{\boldsymbol{\varepsilon}} & \dot{\boldsymbol{\varepsilon}}^e = -\dot{\lambda}_\varepsilon \left(\partial g / \partial \boldsymbol{\sigma}''\right) \\ \dot{\boldsymbol{q}} = \dot{\lambda}_\varepsilon \boldsymbol{h} + \dot{S}_w \boldsymbol{N}_{S_w} & \dot{\boldsymbol{q}} = \dot{S}_w \boldsymbol{N}_{S_w} & \dot{\boldsymbol{q}} = \dot{\lambda}_\varepsilon \boldsymbol{h} \end{array} \tag{9.20}$$

9.2.1.2 Elastic predictor

The trial values of the strain tensor and the internal variables are provided by the integration of the elastic predictor problem:

$$\boldsymbol{\varepsilon}_{n+1}^{e,tr} = \boldsymbol{\varepsilon}_n^e + \Delta\boldsymbol{\varepsilon}_{n+1} \tag{9.21a}$$

$$\left(p_s''\right)_{n+1}^{tr} = p_n'' \tag{9.21b}$$

$$\left(p_m''\right)_{n+1}^{tr} = p_{m,n}'' \exp\left(-G_r \Delta S_{w,n+1}\right) \tag{9.21c}$$

The stress tensor associated to the trial elastic strain $\boldsymbol{\varepsilon}_{n+1}^{e,tr}$ is then obtained by the expression in eq. (7.37).

If $f_{n+1}^{tr} := f\left\{(\boldsymbol{\sigma}'')_{n+1}^{tr}, (p_s'')_{n+1}^{tr}, (p_m'')_{n+1}^{tr}\right\} \leq 0$, the trial state satisfies the constraints imposed by the Kuhn Tucker conditions. The process is then elastic and the trial state represents the actual final state of the material.

9.2.1.3 Plastic corrector

If $f_{n+1}^{tr} > 0$, the stress and internal variables are corrected by considering plastic deformation, solving the plastic corrector problem via the implicit Backaward Euler algorithm:

$$\boldsymbol{\varepsilon}_{n+1}^e = \boldsymbol{\varepsilon}_{n+1}^{e,tr} - \Delta\lambda_{\varepsilon,n+1} \left(\frac{\partial g}{\partial \boldsymbol{\sigma}''}\right)_{n+1} \tag{9.22a}$$

$$\boldsymbol{q}_{n+1} = \boldsymbol{q}_{n+1}^{tr} - \Delta\lambda_{\varepsilon,n+1} \boldsymbol{h}_{n+1} \tag{9.22b}$$

$$f_{n+1} = f\left(\boldsymbol{\sigma}_{n+1}'', \boldsymbol{q}_{n+1}\right) \tag{9.22c}$$

The set of eqs. (9.22) represents a system of nine nonlinear algebraic equations that can be reduced to six due to the assumption of isotropic behavior. If we represent the stress and strain tensors using the spectral decomposition and taking into account the isotropy of the elastic response, we obtain:

$$\sum_{J=1}^{3}(\varepsilon_J^e)_{n+1}\boldsymbol{n}_{n+1}^{(J)}\otimes\boldsymbol{n}_{n+1}^{(J)}=\sum_{J=1}^{3}\left(\varepsilon_J^{e,tr}\right)_{n+1}\boldsymbol{n}_{n+1}^{(J),tr}\otimes\boldsymbol{n}_{n+1}^{(J),tr} - \Delta\lambda_{\varepsilon,n+1}\sum_{j=1}^{3}\left(\frac{\partial\hat{g}}{\partial\sigma_J}\right)_{n+1}\boldsymbol{n}_{n+1}^{(J)}\otimes\boldsymbol{n}_{n+1}^{(J)} \quad (9.23)$$

in which $\boldsymbol{n}^{(J),tr}$ is the Jth unit eigenvector of $\boldsymbol{\varepsilon}_{n+1}^{e,tr}$. From eq. (9.23), it follows at once that

$$\boldsymbol{n}_{n+1}^{(J)}=\boldsymbol{n}_{n+1}^{(J),tr} \quad (9.24)$$

and

$$(\varepsilon_J^e)_{n+1}=\left(\varepsilon_J^{e,tr}\right)_{n+1}-\Delta\lambda_{\varepsilon,n+1}\left(\frac{\partial\hat{g}''}{\partial\sigma}_J\right)_{n+1} \quad (9.25)$$

for J =1,2 or 3. Note that, as the trial elastic strain is known, so are its principal directions. Therefore, the only unknown quantities to be determined remain the three principal elastic strains $(\varepsilon_J^e)_{n+1}$, the two internal variables $p_{s,n+1}$ and $p_{m,n+1}$ and the plastic consistency parameter $\Delta\lambda_{\varepsilon,n+1}$.

Introducing for convenience the following vector notation:

$$\hat{\boldsymbol{\varepsilon}}^e:=\begin{Bmatrix}\varepsilon_1^e\\ \varepsilon_2^e\\ \varepsilon_3^e\end{Bmatrix}\qquad \hat{\boldsymbol{\varepsilon}}^{e,tr}:=\begin{Bmatrix}\varepsilon_1^{e,tr}\\ \varepsilon_2^{e,tr}\\ \varepsilon_3^{e,tr}\end{Bmatrix}\qquad \hat{\boldsymbol{\sigma}}'':=\begin{Bmatrix}\sigma_1''\\ \sigma_2''\\ \sigma_3''\end{Bmatrix}\qquad \hat{\boldsymbol{Q}}:=\begin{Bmatrix}\partial\hat{g}/\partial\sigma_1''\\ \partial\hat{g}/\partial\sigma_2''\\ \partial\hat{g}/\partial\sigma_3''\end{Bmatrix} \quad (9.26)$$

the return mapping problem in principal elastic strain space can be recast as follows:

$$\hat{\boldsymbol{\varepsilon}}_{n+1}^e=\hat{\boldsymbol{\varepsilon}}_{n+1}^{e,tr}-\Delta\lambda_{\varepsilon,n+1}\hat{\boldsymbol{Q}}_{n+1} \quad (9.27a)$$

$$\boldsymbol{q}_{n+1}=\boldsymbol{q}_{n+1}^{tr}-\Delta\lambda_{\varepsilon,n+1}\boldsymbol{h}_{n+1} \quad (9.27b)$$

$$f_{n+1}=f\left(\hat{\boldsymbol{\sigma}}_{n+1}'',\boldsymbol{q}_{n+1}\right) \quad (9.27c)$$

A residual vector $\boldsymbol{R}_{n+1}$ is constructed from the set of eqs. (9.27):

$$\boldsymbol{R}_{n+1}\left(\boldsymbol{x}_{n+1}\right) := \begin{Bmatrix} \boldsymbol{r}^{\varepsilon}_{n+1} \\ \boldsymbol{r}^{q}_{n+1} \\ f_{n+1} \end{Bmatrix} := \begin{Bmatrix} -\hat{\boldsymbol{\varepsilon}}^{e}_{n+1} + \hat{\boldsymbol{\varepsilon}}^{e,tr}_{n+1} - \Delta\lambda_{\varepsilon,n+1}\hat{\boldsymbol{Q}}_{n+1} \\ -\boldsymbol{q}_{n+1} + \boldsymbol{q}^{tr}_{n+1} - \Delta\lambda_{\varepsilon,n+1}\boldsymbol{h}_{n+1} \\ f_{n+1} \end{Bmatrix} = \boldsymbol{0} \tag{9.28}$$

with a vector of unknowns:

$$\boldsymbol{x}_{n+1} := \left\{ \hat{\boldsymbol{\varepsilon}}^{eT}_{n+1},\ \boldsymbol{q}^{T}_{n+1},\ \Delta\lambda_{\varepsilon,n+1} \right\}^{T} \in \mathbb{R}^{6} \tag{9.29}$$

The unknown $\boldsymbol{x}_{n+1}$ must be determined by a local Newton–Raphson iteration:

$$\boldsymbol{R}\left(\boldsymbol{x}^{(k+1)}_{n+1}\right) = \boldsymbol{R}^{(k)}_{n+1} + \delta\boldsymbol{R}^{(k)}_{n+1} = \boldsymbol{R}^{(k)}_{n+1} + \left(\frac{\partial \boldsymbol{R}}{\partial \boldsymbol{x}}\right)^{(k)}_{n+1} \delta\boldsymbol{x}^{(k)}_{n+1} = \boldsymbol{0} \tag{9.30a}$$

$$\boldsymbol{x}^{(k+1)}_{n+1} = \boldsymbol{x}^{(k)}_{n+1} + \delta\boldsymbol{x}^{(k)}_{n+1} \tag{9.30b}$$

9.2.2 Consistent tangent operator

Since the internal variables of Milan Model are dependent also on the environmental variable S_w, two consistent tangent operators are computed:

$$\boldsymbol{D}^{(k)}_{n+1} = \frac{\partial \boldsymbol{\sigma}''^{(k)}_{n+1}}{\partial \boldsymbol{\varepsilon}^{(k)}_{n+1}}\ ; \qquad\qquad \boldsymbol{M}^{(k)}_{n+1} = \frac{\partial \boldsymbol{\sigma}''^{(k)}_{n+1}}{\partial p^{(k)}_{w,n+1}} \tag{9.31}$$

The developments for computing the first expression in eq. (9.31) remain the same as in Tamagnini et al. [167] and will not be repeated here. Thus, only the second expression in eq. (9.31) will be developed.

For an elastic process, the change in the degree of saturation has no effect on the current stress state. Thus, in this case:

$$\boldsymbol{M}^{(k)}_{n+1} = \boldsymbol{0} \tag{9.32}$$

If the process is plastic, any change in the degree of saturation may induce a variation in plastic strains and hence in the current stress state. Considering the spectral decomposition of the stress tensor (here it is assumed that the principal stress direction coincides with the unit vector in the principal elastic strain direction), the spectral form of the

second expression in eq. (9.31) reads:

$$\begin{aligned}\boldsymbol{M}_{n+1}^{(k)} &= \frac{\partial}{\partial p_{w,n+1}^{(k)}} \left\{ \sum_{A=1}^{3} (\sigma_A)_{n+1}^{(k)} \, \boldsymbol{m}_{n+1}^{(A)} \right\} \\ &= \frac{\partial}{\partial p_{w,n+1}^{(k)}} \left\{ \sum_{A=1}^{3} (\sigma_A)_{n+1}^{(k)} \, \boldsymbol{m}_{n+1}^{(A),tr} \right\} \\ &= \sum_{A=1}^{3} \frac{\partial \, (\sigma_A)_{n+1}^{(k)}}{\partial p_{w,n+1}^{(k)}} \boldsymbol{m}_{n+1}^{(A),tr}\end{aligned} \tag{9.33}$$

with:

$$\boldsymbol{m}_{n+1}^{(A)} := \boldsymbol{n}_{n+1}^{(A)} \otimes \boldsymbol{n}_{n+1}^{(A)}, \qquad\qquad \boldsymbol{m}_{n+1}^{(A),tr} := \boldsymbol{n}_{n+1}^{(A),tr} \otimes \boldsymbol{n}_{n+1}^{(A),tr} \tag{9.34}$$

of the tensors $\boldsymbol{\varepsilon}_{n+1}$ and $\boldsymbol{\varepsilon}_{n+1}^{tr}$.

The evaluation of the consistent tangent operator $\boldsymbol{M}_{n+1}^{(k)}$ thus reduces to the calculation of the three components of the vector

$$\left(\hat{\boldsymbol{d}}_{S_w} \right)_{n+1}^{(k)} := \frac{\partial \hat{\boldsymbol{\sigma}}_{n+1}^{(k)}}{\partial p_{w,n+1}^{(k)}} \tag{9.35}$$

From the hyperelastic constitutive equations we have

$$\mathrm{d}\hat{\boldsymbol{\sigma}} = \hat{\boldsymbol{d}}^{e} \frac{\partial \hat{\boldsymbol{\varepsilon}}^{e}}{\partial S_w} \frac{\partial S_w}{\partial p_w} \mathrm{d}p_w \tag{9.36}$$

where $\hat{\boldsymbol{d}}^{e}$ is the hyper–elastic stiffness matrix given in eq. (7.38) in principal directions. The subscript $(n+1)$ and the superscript (k) have been omitted to ease the notation.

The derivative $\partial\hat{\boldsymbol{\varepsilon}}/\partial S_w$ in eq. (9.36) is obtained by differentiating eqs. (9.22a) and (9.22a), keeping $\hat{\boldsymbol{\varepsilon}}^{e,tr}$ constant.

Knowing that

$$\mathrm{d}\boldsymbol{q}^{tr} = \boldsymbol{N}_{S_w} \mathrm{d}S_w \ , \qquad\qquad \boldsymbol{N}_{S_w} = \begin{Bmatrix} 0 \\ G_r p_{m,n} \end{Bmatrix} \tag{9.37}$$

we have

$$\boldsymbol{A}\mathrm{d}\tilde{\boldsymbol{x}} = \boldsymbol{C}\mathrm{d}S_w - \boldsymbol{U}\mathrm{d}\Delta\lambda_\gamma \tag{9.38}$$

where the differentials in eq. (9.38) are expressed as:

$$\boldsymbol{A} := \begin{bmatrix} \boldsymbol{I}_{(3\times3)} + \Delta\lambda_\varepsilon \left(\frac{\partial^2 \hat{g}}{\partial\hat{\boldsymbol{\sigma}}\otimes\partial\hat{\boldsymbol{\sigma}}}\right)\hat{\boldsymbol{d}}^e & \Delta\lambda_\varepsilon \left(\frac{\partial^2 \hat{g}}{\partial\hat{\boldsymbol{\sigma}}\otimes\partial\boldsymbol{q}}\right) \\ -\Delta\lambda_\varepsilon \left(\partial\boldsymbol{h}/\partial\hat{\boldsymbol{\sigma}}\right)\hat{\boldsymbol{d}}^e & \boldsymbol{I}_{(2\times2)} - \Delta\lambda_\varepsilon \left(\partial\boldsymbol{h}/\partial\boldsymbol{q}\right) \end{bmatrix} \tag{9.39a}$$

$$\boldsymbol{U} := \left\{\hat{\boldsymbol{Q}}^T, \ -\boldsymbol{h}^T\right\}^T \tag{9.39b}$$

$$\boldsymbol{C}^T := \{0,\ 0,\ 0,\ 0,\ p_{m,n}G_r\} \tag{9.39c}$$

Using the consistency condition, the following expression is obtained for the plastic consistency parameter $\mathrm{d}\left(\Delta\lambda_\varepsilon\right)$:

$$\mathrm{d}\left(\Delta\lambda_\varepsilon\right) = \frac{\boldsymbol{V}\boldsymbol{A}^{-1}\boldsymbol{C}}{\boldsymbol{V}\boldsymbol{A}^{-1}\boldsymbol{U}}\mathrm{d}S_w \tag{9.40}$$

where

$$\boldsymbol{V} := \left\{\hat{\boldsymbol{P}}^T\hat{\boldsymbol{d}}^e, \boldsymbol{W}^T\right\}, \qquad \hat{\boldsymbol{P}} := \frac{\partial\hat{f}}{\partial\hat{\boldsymbol{\sigma}}}\ , \qquad \boldsymbol{W} := \frac{\partial\hat{f}}{\partial\boldsymbol{q}} \tag{9.41}$$

Eq. (9.40) is substituted into eq. (9.38) that yields

$$\mathrm{d}\tilde{\boldsymbol{x}} = \left(\boldsymbol{A}^{-1} - \frac{\boldsymbol{A}^{-1}\boldsymbol{U}\boldsymbol{V}\boldsymbol{A}^{-1}}{\boldsymbol{V}\boldsymbol{A}^{-1}\boldsymbol{U}}\right)\boldsymbol{C}\mathrm{d}S_w \tag{9.42}$$

and

$$\mathrm{d}\hat{\boldsymbol{\varepsilon}}^e = \boldsymbol{\Xi}_{S_w}\mathrm{d}S_w, \qquad \boldsymbol{\Xi}_{S_w} := \boldsymbol{T}^T\left(\boldsymbol{A}^{-1} - \frac{\boldsymbol{A}^{-1}\boldsymbol{U}\boldsymbol{V}\boldsymbol{A}^{-1}}{\boldsymbol{V}\boldsymbol{A}^{-1}\boldsymbol{U}}\right)\boldsymbol{C} \tag{9.43}$$

Collecting the results in eqs. (9.42) and (9.36), it follows:

$$\left(\hat{\boldsymbol{d}}_{S_w}\right)_{n+1}^{(k)} = \hat{\boldsymbol{d}}_{n+1}^{e(k)}\left(\boldsymbol{\Xi}_{S_w}\right)_{n+1}^{(k)}\left(\frac{\partial S_w}{\partial p_w}\right)_{n+1}^{(k)} \tag{9.44}$$

9.3 Elastoplastic 2nd gradient model

9.3.1 Return mapping algorithm

9.3.1.1 Evolution problem split

As in the two previous models the problem to be solved consists in finding the double stress $\boldsymbol{\Sigma}_{n+1}$ and the internal variable R^{sg}_{n+1} at time t_{n+1} resulting from a given increment $\Delta\boldsymbol{\gamma}_{n+1}$, knowing the double stress $\boldsymbol{\Sigma}_n$ and the internal variable R^{sg}_n at time t_n. The split operator reads:

$$\begin{array}{lll} \text{Evolution equations} & \text{Elastic predictor} \quad + & \text{Plastic corrector} \\ \dot{\boldsymbol{\gamma}} = \nabla\nabla\dot{\boldsymbol{u}} & \dot{\boldsymbol{\gamma}} = \nabla\nabla\dot{\boldsymbol{u}} & \dot{\boldsymbol{\gamma}} = \mathbf{0} \\ \dot{\boldsymbol{\Sigma}} = \boldsymbol{D}^e_{sg}(\dot{\boldsymbol{\gamma}} - \dot{\lambda}_\gamma \boldsymbol{N}_\gamma) & \dot{\boldsymbol{\Sigma}} = \boldsymbol{D}^e_{sg}\dot{\boldsymbol{\gamma}} & \dot{\boldsymbol{\Sigma}} = -\boldsymbol{D}^e_{sg}(\dot{\lambda}_\gamma \boldsymbol{N}_\gamma) \\ \dot{R}^{sg} = \dot{\lambda}_\gamma \hat{H}_\gamma & \dot{R}^{sg} = 0 & \dot{R}^{sg} = \dot{\lambda}_\gamma \hat{H}_\gamma \end{array} \tag{9.45}$$

with $\hat{H}_\gamma$ being function of the internal variable R^{sg}.

9.3.1.2 Elastic predictor

We initially suppose the step to be elastic, and calculate the trial values for the state variables. Since $\boldsymbol{D}^e_{sg}$ is constant, the solution of the elastoplastic problem is trivial:

$$\boldsymbol{\Sigma}^{tr}_{n+1} = \boldsymbol{\Sigma}_n + \boldsymbol{D}^e_{sg}\Delta\boldsymbol{\gamma}_{n+1} \tag{9.46a}$$

$$R^{sg,tr}_{n+1} = R^{sg}_n \tag{9.46b}$$

If $F^{tr}_{n+1} := F(\boldsymbol{\Sigma}^{tr}_{n+1}, R^{sg,tr}_{n+1}) \leq 0$, then the process is purely elastic. The final state is:

$$\boldsymbol{\Sigma}_{n+1} = \boldsymbol{\Sigma}^{tr}_{n+1}, \qquad R^{sg}_{n+1} = R^{sg,tr}_{n+1} \tag{9.47}$$

9.3.1.3 Plastic corrector

If $F^{tr}_{n+1} > 0$, consistency is violated and the elastic predictor problem must be solved to restore it. Using Backward Euler algorithm to integrate the evolution equations of the plastic corrector problem, we have

$$\boldsymbol{\Sigma}_{n+1} = \boldsymbol{\Sigma}^{tr}_{n+1} - \Delta\lambda_{\gamma,n+1}\boldsymbol{D}^{e}_{sg}\boldsymbol{N}_{\gamma,n+1} \tag{9.48a}$$

$$R^{sg}_{n+1} = R^{sg}_{n} + \Delta\lambda_{\gamma,n+1}\hat{H}_{\gamma} \tag{9.48b}$$

$$F(\boldsymbol{\Sigma}_{n+1}, R^{sg}_{n+1}) = 0 \tag{9.48c}$$

Eq. 9.48 is a system of nonlinear algebraic equations to be solved for $\boldsymbol{\Sigma}_{n+1}$, R^{sg}_{n+1} and $\Delta\lambda_{\gamma,n+1}$ using a suitable iterative strategy.

Setting:

$$\boldsymbol{r}(\boldsymbol{x}_{n+1}) := \begin{Bmatrix} \boldsymbol{\Sigma}_{n+1} - \boldsymbol{\Sigma}^{tr}_{n+1} + \Delta\lambda_{\gamma,n+1}\boldsymbol{D}^{e}_{sg}\boldsymbol{N}_{\gamma,n+1} \\ R^{sg}_{n+1} - R^{sg,tr}_{n+1} - \Delta\lambda_{\gamma,n+1}\hat{H}(R^{sg}_{n+1}) \\ F(\boldsymbol{\Sigma}_{n+1}, R_{n+1}) \end{Bmatrix} = \begin{Bmatrix} \tilde{\boldsymbol{r}}_{1,n+1} \\ \tilde{r}_{2,n+1} \\ F_{n+1} \end{Bmatrix} = \boldsymbol{0} \tag{9.49}$$

the solution vector:

$$\boldsymbol{x}_{n+1} := \begin{Bmatrix} \boldsymbol{\Sigma}_{n+1} \\ R^{sg}_{n+1} \\ \Delta\lambda_{\gamma,n+1} \end{Bmatrix} \tag{9.50}$$

is determined using the Newton–Raphson method. For the iteration k, we have:

$$\boldsymbol{r}\left(\boldsymbol{x}^{(k+1)}_{n+1}\right) = \boldsymbol{r}^{(k)}_{n+1} + \delta\boldsymbol{r}^{(k)}_{n+1} = \boldsymbol{r}^{(k)}_{n+1} + \left(\frac{\partial \boldsymbol{r}}{\partial \boldsymbol{x}}\right)^{(k)}_{n+1} \delta\boldsymbol{x}^{(k)}_{n+1} = \boldsymbol{0} \tag{9.51}$$

which is solved for $\delta\boldsymbol{x}^{(k)}_{n+1}$ to yield:

$$\delta\boldsymbol{x}^{(k)}_{n+1} = -\left\{\left(\frac{\partial \boldsymbol{r}}{\partial \boldsymbol{x}}\right)^{(k)}_{n+1}\right\}^{-1} \boldsymbol{r}^{(k)}_{n+1} \tag{9.52}$$

or equivalently:

$$\begin{bmatrix} \boldsymbol{I}_{sg} + \Delta\lambda \boldsymbol{D}^e_{sg} \frac{\partial \boldsymbol{N}_\gamma}{\partial \boldsymbol{\Sigma}} & \boldsymbol{0} & \boldsymbol{D}^e_{sg}\boldsymbol{N}_\gamma \\ \boldsymbol{0} & 1 - \Delta\lambda_\gamma \frac{\partial \hat{H}}{\partial R^{sg}} & -\hat{H} \\ \boldsymbol{N}_\gamma & -1 & 0 \end{bmatrix}^{(k)}_{n+1} \begin{Bmatrix} \delta\boldsymbol{\Sigma}_1 \\ \delta R^{sg} \\ \delta\Delta\lambda_\gamma \end{Bmatrix}^{(k)}_{n+1} = - \begin{Bmatrix} \tilde{\boldsymbol{r}}_1 \\ \tilde{r}_2 \\ F \end{Bmatrix}^{(k)}_{n+1} \tag{9.53}$$

The system of eqs. (9.53) can be reduced by means of static condensation, solving first for $\delta R^{sg(k)}$ and $\delta\boldsymbol{\Sigma}^{(k)}$ (keeping only the superscripts):

$$\delta\boldsymbol{\Sigma}^{(k)} = \boldsymbol{H}^{(k)} \left(-\tilde{\boldsymbol{r}}_1^{(k)} - \boldsymbol{D}^e_{sg}\boldsymbol{N}_\gamma^{(k)} \delta\Delta\lambda_\gamma^{(k)} \right) \tag{9.54a}$$

$$\delta R^{sg(k)} = \frac{1}{1 - \Delta\lambda_\gamma^{(k)} \partial\hat{H}^{(k)}/\partial R^{sg}} \left(-\tilde{r}_2^{(k)} + \hat{H}^{(k)} \delta\Delta\lambda_\gamma^{(k)} \right) \tag{9.54b}$$

and replacing them in the last equation of the system (9.53), we have

$$\delta\Delta\lambda^{(k)} = \frac{\left(1 - \Delta\lambda_\gamma^{(k)} \partial\hat{H}^{(k)}/\partial R^{sg}\right) \left(F^{(k)} - \boldsymbol{N}_\gamma^{(k)} \boldsymbol{H}^{(k)} \tilde{\boldsymbol{r}}_1^{(k)}\right) + \tilde{r}_2^{(k)}}{\left(1 - \Delta\lambda_\gamma^{(k)} \partial\hat{H}^{(k)}/\partial R^{sg}\right) \boldsymbol{N}_\gamma^{(k)} \boldsymbol{H}^{(k)} \boldsymbol{D}^e_{sg} \boldsymbol{N}_\gamma^{(k)} + \hat{H}^{(k)}} \tag{9.55}$$

In the above equations:

$$\boldsymbol{H}^{(k)} = \left(\boldsymbol{I}_{sg} + \Delta\lambda_\gamma^{(k)} \boldsymbol{D}^e_{sg} \frac{\partial \boldsymbol{N}_\gamma}{\partial \boldsymbol{\Sigma}}^{(k)} \right)^{-1} \tag{9.56a}$$

$$\frac{\partial \boldsymbol{N}_\gamma^{(k)}}{\partial \boldsymbol{\Sigma}} = \frac{1}{\left\| \boldsymbol{\Sigma}^{(k)} \right\|} \left\{ \boldsymbol{I}_{sg} - \boldsymbol{N}_\gamma^{(k)} \otimes \boldsymbol{N}_\gamma^{(k)} \right\} \tag{9.56b}$$

where $\boldsymbol{I}_{sg}$ is an identity tensor of dimension 27×27.

The plastic corrector scheme is summarized in Algorithm 4.

9.3.2 Consistent tangent operator

For an elastic process, the consistent tangent operator is equal to the elastic second gradient constitutive tensor $\boldsymbol{D}^e_{sg}$. And since two second gradient elastic constitutive models were defined in chapter 7, which one is used in the numerical simulations will be specified in the following.

Input : $\boldsymbol{\Sigma}^{tr}$, $\boldsymbol{\Sigma}^{(0)}$, $R^{sg,tr}$, $R^{sg(0)}$, $\Delta\lambda_\gamma^{(0)}$
Output: $\boldsymbol{\Sigma}$, R^{sg}, $\Delta\lambda_\gamma$

Set $k = 0$
while $k < k_{max}$ **do**
  Compute

$$\begin{aligned} \boldsymbol{r}_1^{(k)} &= \boldsymbol{\Sigma}^{(k)} - \boldsymbol{\Sigma}^{tr} + \Delta\lambda_\gamma^{(k)} \boldsymbol{D}_{sg}^e \boldsymbol{N}_\gamma^{(k)} \\ r_2^{(k)} &= R^{sg(k)} - R^{sg,tr} - \Delta\lambda_\gamma^{(k)} \hat{H}^{(k)} \\ F^{(k)} &= \left\| \boldsymbol{\Sigma}^{(k)} \right\| - R^{sg(k)} \end{aligned}$$

  if $\left\|F^{(k)}\right\| < \epsilon_{tol,F}$ *and* $\left\|\boldsymbol{r}_1^{(k)}\right\| < \epsilon_{tol,r_1}$ *and* $\left\|r_2^{(k)}\right\| < \epsilon_{tol,r_2}$ **then**
    Exit
  end
  Solve

$$\begin{aligned} \delta\Delta\lambda^{(k)} &= \frac{\left(1-\Delta\lambda_\gamma^{(k)}\partial\hat{H}^{(k)}/\partial R^{sg}\right)\left(F^{(k)}-\boldsymbol{N}_\gamma^{(k)}\boldsymbol{H}^{(k)}\tilde{\boldsymbol{r}}_1^{(k)}\right)+\tilde{r}_2^{(k)}}{\left(1-\Delta\lambda_\gamma^{(k)}\partial\hat{H}^{(k)}/\partial R^{sg}\right)\boldsymbol{N}_\gamma^{(k)}\boldsymbol{H}^{(k)}\boldsymbol{D}_{sg}^e\boldsymbol{N}_\gamma^{(k)}+\hat{H}^{(k)}} \\ \delta\boldsymbol{\Sigma}^{(k)} &= \boldsymbol{H}^{(k)}\left(-\tilde{\boldsymbol{r}}_1^{(k)} - \boldsymbol{D}_{sg}^e\boldsymbol{N}_\gamma^{(k)}\delta\Delta\lambda_\gamma^{(k)}\right) \\ \delta R^{sg(k)} &= \frac{1}{1-\Delta\lambda_\gamma^{(k)}\partial\hat{H}^{(k)}/\partial R^{sg}}\left(-\tilde{r}_2^{(k)} + \hat{H}^{(k)}\delta\Delta\lambda_\gamma^{(k)}\right) \end{aligned}$$

  Update

$$\begin{aligned} \Delta\lambda_\gamma^{(k+1)} &= \Delta\lambda_\gamma^{(k)} + \delta\Delta\lambda_\gamma^{(k)} \\ \boldsymbol{\Sigma}^{(k+1)} &= \boldsymbol{\Sigma}^{(k)} + \delta\boldsymbol{\Sigma}^{(k)} \\ R^{sg(k+1)} &= R^{sg(k)} + \delta R^{sg(k)} \end{aligned}$$

  set $k = k + 1$
end
Set $\Delta\lambda_\gamma = \Delta\lambda_\gamma^{(k+1)}$, $\boldsymbol{\Sigma} = \boldsymbol{\Sigma}^{(k+1)}$, $R^{sg} = R^{sg(k+1)}$

Algorithm 4: Local Newton–Raphson iteration of the elastoplastic second gradient model.

For a plastic process, we consider that for a given perturbation $\mathrm{d}\boldsymbol{\gamma}$ of the increment $\Delta\boldsymbol{\gamma}_{n+1}^{(k)}$, eq. (9.48a) is written as follows (dropping subscripts and superscripts to ease the notation):

$$\mathrm{d}\boldsymbol{\Sigma} = \boldsymbol{D}_{sg}^e \mathrm{d}\boldsymbol{\gamma} - \mathrm{d}(\Delta\lambda_\gamma)\boldsymbol{D}_{sg}^e\boldsymbol{N}_\gamma - \Delta\lambda_\gamma\boldsymbol{D}_{sg}^e\frac{\partial\boldsymbol{N}_\gamma}{\partial\boldsymbol{\Sigma}}\mathrm{d}\boldsymbol{\Sigma} \tag{9.57}$$

Isolating $\mathrm{d}\boldsymbol{\Sigma}$ in eq. 9.57, we have:

$$\mathrm{d}\boldsymbol{\Sigma} = \boldsymbol{H}\boldsymbol{D}_{sg}^e\left\{\mathrm{d}\boldsymbol{\gamma} - \mathrm{d}(\Delta\lambda_\gamma)\boldsymbol{N}_\gamma\right\} \tag{9.58}$$

Since the consistency condition must be satisfied for all states between load step t_n and t_{n+1}, the differential of F must vanish:

$$\mathrm{d}F = \frac{\partial F}{\partial \boldsymbol{\Sigma}} \cdot \mathrm{d}\boldsymbol{\Sigma} + \frac{\partial F}{\partial R^{sg}} \mathrm{d}R^{sg} = \boldsymbol{N}_\gamma \cdot \mathrm{d}\boldsymbol{\Sigma} - \hat{H}_\gamma \mathrm{d}(\Delta\lambda_\gamma) = 0 \tag{9.59}$$

Incorporating eq. 9.58 in eq. 9.59, and solving for $\mathrm{d}(\Delta\lambda_\gamma)$ we get an algebraic equation:

$$\mathrm{d}(\Delta\lambda_\gamma) = \frac{1}{\hat{K}^p_{sg}} \left\{ \boldsymbol{N}_\gamma \cdot \left(\boldsymbol{H}\boldsymbol{D}^e_{sg} \right) \mathrm{d}\boldsymbol{\gamma} \right\} \tag{9.60}$$

with

$$\hat{K}^p_{sg} = \boldsymbol{N}_\gamma \cdot \left(\boldsymbol{H}\boldsymbol{D}^e_{sg} \right) \boldsymbol{N}_\gamma + \hat{H}_\gamma \tag{9.61}$$

then, we replace the expression given by eq. (9.60) in (9.58)

$$\mathrm{d}\boldsymbol{\Sigma} = \left\{ \boldsymbol{H}\boldsymbol{D}^e_{sg} - \frac{1}{\hat{K}^p_{sg}} \left[\left(\boldsymbol{H}\boldsymbol{D}^e_{sg} \right) \boldsymbol{N}_\gamma \right] \otimes \left[\left(\boldsymbol{H}\boldsymbol{D}^e_{sg} \right)^T \boldsymbol{N}_\gamma \right] \right\} \mathrm{d}\boldsymbol{\gamma} \tag{9.62}$$

Thus, from eq. 9.62 the consistent tangent stiffness becomes

$$\boldsymbol{D}_{sg} = \boldsymbol{H}\boldsymbol{D}^e_{sg} - \frac{1}{\hat{K}^p_{sg}} \left\{ \left(\boldsymbol{H}\boldsymbol{D}^e_{sg} \right) \boldsymbol{N}_\gamma \right\} \otimes \left\{ \left(\boldsymbol{H}\boldsymbol{D}^e_{sg} \right)^T \boldsymbol{N}_\gamma \right\} \tag{9.63}$$

Part III

Applications to relevant IVBPs

Chapter 10

Benchmarking

10.1 One–Dimensional localization problem

This example compares the results obtained with the IGA–FEM code against the work presented by Chambon et al. [35]. The mentioned work regularized the problem and proved that the second gradient regularization does not restore uniqueness of the solution for the boundary value problem, which still admits a finite number of solutions.

A bar of length $l = 1$ m is compressed by an external force (displacement–controlled) on its right side. All vertical displacements are constrained and the left boundary is fixed, see Fig. 10.1. Only the mechanical behavior of the bar is modeled. The bar is discretized with fifteen quadratic B–spline elements. The model chosen is the Prandlt–Reuss model along with the linear elastic second gradient law defined by the parameter D^{sg} (see Tab. 10.1). These unrealistic parameters have been chosen only to compare and validate the code in 1D.

Table 10.1: Material parameters for the 1D localization problem.

K	G_1	H_ε	S_{y0}	$S_{y,min}$	D^{sg}
[kPa]	[kPa]	[kPa]	[kPa]	[kPa]	[kN]
-7.50	16.88	0.00	2.76	0.55	0.08

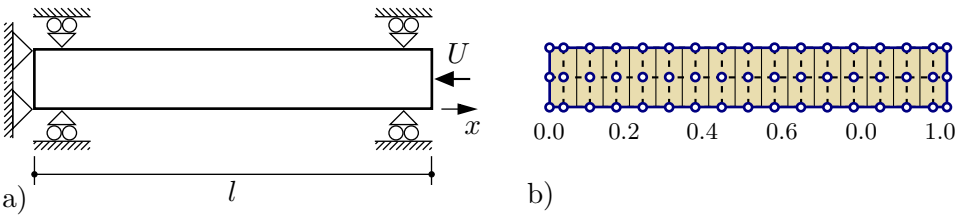

Figure 10.1: 1D localization problem: a) geometry, boundary conditions and b) B–spline mesh.

Four different analytical solutions exist for this set of materials: 1) homogeneous, 2) hardening–softening (HS), 3) hardening–softening–hardening (HSH), and 4) hardening–softening–hardening–softening (HSHS). The final U was set to 0.14 m for the HSH and HSHS solutions, and 0.1001 m for the HS solution. The problem was run several times using random values for the initial guess of the increment displacement field in a range of 0.0 and 0.001 m with a time step $\Delta t = 0.01$ until the three non–homogeneous solutions were found. This random initialization step was activated only once, after the global response of the bar reaches the peak stress.

Fig. 10.2 shows that the numerical solutions are in good agreement with the analytical solutions for the global response (reaction force at the left end of the bar and the global deformation) and the axial strain, with the exception of HS which may require a further refinement. Moreover, the results of the axial strain of the HS solution does not correspond to the end of the simulation but for $U = 0.1001$ m due to the large deformation it undergoes compared to the other solutions.

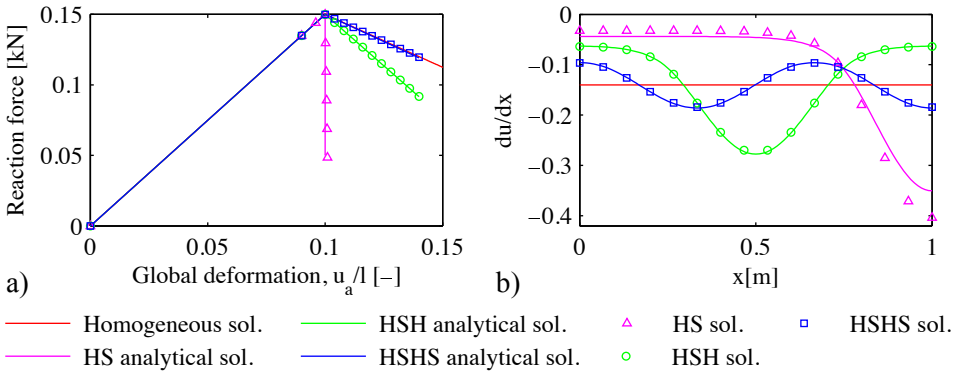

Figure 10.2: 1D localization problem: a) global response and b) axial strain.

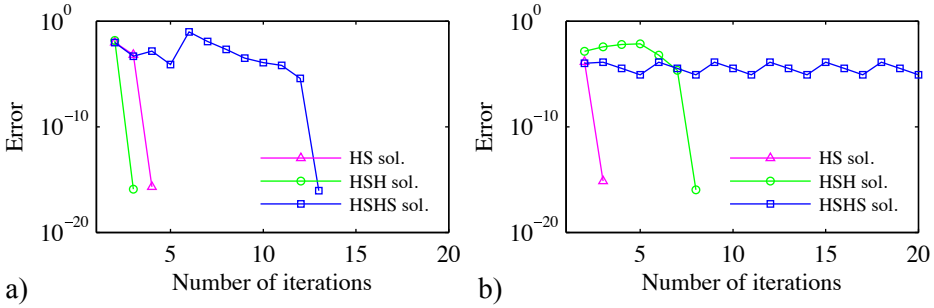

Figure 10.3: 1D localization problem: convergence at a) the random initialization step and b) subsequent step.

Fig. 10.3 illustrates the number of iterations required to reach convergence at the random initialization step and the subsequent step. The HSHS solution takes thirteen iterations to converge, but the following time step is not able to find a solution using zeros values as an initial guess. For this reason, the previous converged solution is taken as initial guess to continue the simulation and now converging in two iterations.

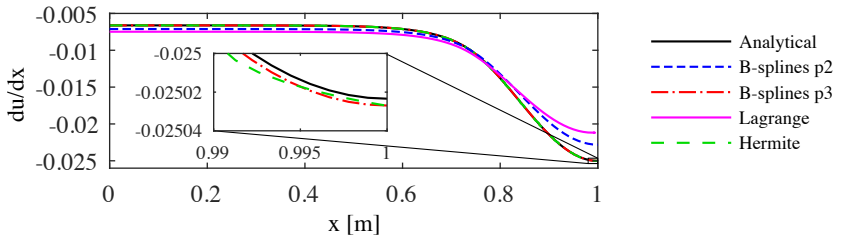

Figure 10.4: 1D localization problem: comparison of the axial strain (HSH solution) for different basis functions.

Finally, Fig. 10.4 compares the HS solution, using quadratic and cubic B–splines against the approximations functions used in the works of Chambon et al. [35] and Matsushima et al. [114], Hermite and Lagrangian functions, respectively. The latter uses a Lagrange multiplier field to enforce the C^1 requirement. We observe a better performance of cubic B–splines and Hermite basis functions over quadratic B–splines and Lagrange basis functions, due to the fact that their first derivatives are continuous in their connections. Fig. 10.5 shows that despite the fact that different basis functions have similar rate of convergence depending on the polynomial order, B–splines functions require much less number of degrees of freedoms (dofs) to achieve same level of accuracy.

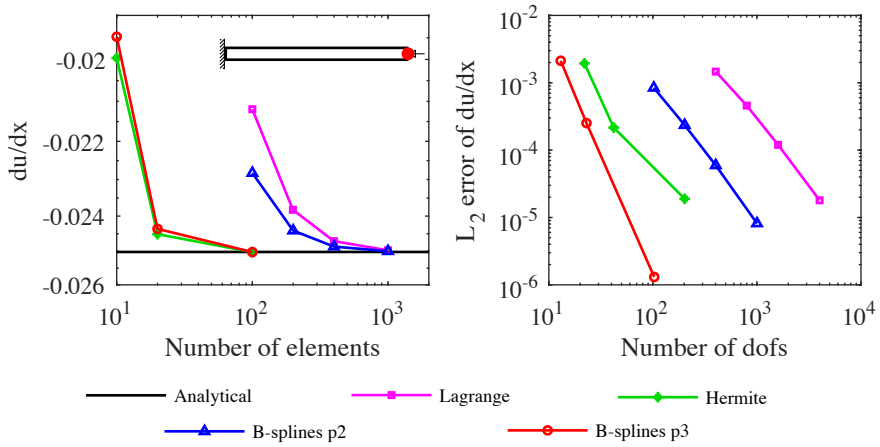

Figure 10.5: 1D localization problem: a) Relative error of du/dx at point x =1 m and b) L_2 error of du/dx along the bar.

10.2 Strip footing problem under undrained conditions

This example uses the Prandlt–Reuss model to predict the bearing capacity of a strip footing problem (PR strip footing problem). The problem has been studied by Smith et al. [163]. Fig. 10.6 a) shows half of a flexible strip footing on top of an undrained soil layer underlain by a rough rigid base. The footing, of half width $a = 2$ m, is subjected to an increasing vertical load, w, up to failure. The dimensions of the domain are $l = 12$ m and $h = 5$ m. Only vertical displacements are allowed along the lateral boundaries. The soil is assumed to be weightless.

We have run four simulations with: 1) 60×25 quadratic B–splines element 2) 60×25 cubic B–spline elements, 3) 120×50 quadratic B–spline elements, and 4) 240×100, quadratic B–spline elements. In all cases the meshes are homogeneous; the coarsest mesh is shown in Fig. 10.6 b).

The soil is assumed to be an elastoplastic material with perfect plasticity. The yield stress parameter S_{y0} is derived from the undrained shear strength $c_u = 100$kPa as $S_{y0} = \sqrt{2}c_u$. The second gradient model is defined by the elastic second gradient parameter D^{sg}. The material parameters used for the simulation are given in Tab. 10.2.

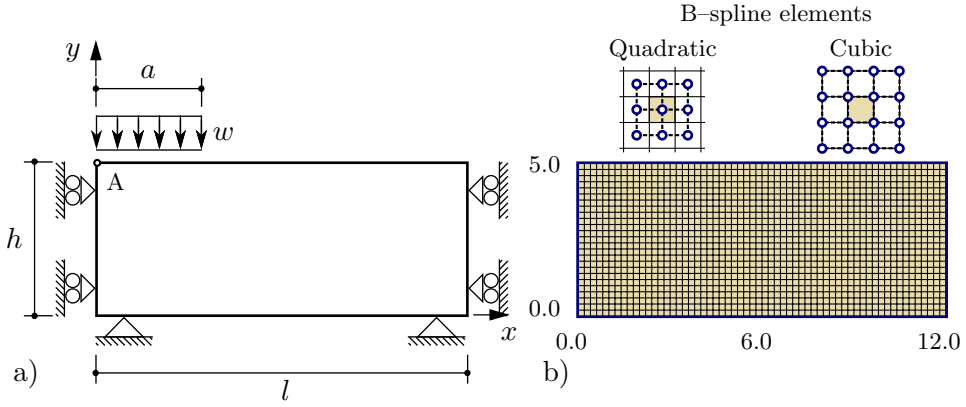

Figure 10.6: PR strip footing problem: a) geometry, boundary conditions and b) coarsest B–spline mesh.

Table 10.2: Soil parameters for the PR strip footing problem.

K [kPa]	G_1 [kPa]	H_ε [kPa]	S_{y0} [kPa]	$S_{y,min}$ [kPa]	D^{sg} [kN]
$3.33{\cdot}10^5$	$3.45{\cdot}10^4$	0.00	$1.41{\cdot}10^2$	–	0.2

The theoretical bearing capacity of this problem is given by Hill [85] and can be expressed as the bearing stress factor:

$$q_{ult}/c_u = (2+\pi) \approx 5.14 \tag{10.1}$$

The results of the normalized vertical displacement under the centerline (point A in Fig. 10.6 a)) vs bearing stress factor are plotted in Fig. 10.7. The four different cases show a good agreement with the theoretical solution (solid black line).

However, the coarsest mesh with quadratic approximation depicts a poor resolution of the failure mechanism as it can be seen when the equivalent deviatoric strains are plotted for the four meshes, as shown in Fig. 10.8. The strong gradients occurring along the line below the right edge of the footing are well modeled by the two other finer quadratic B–splines meshes. Moreover, the cubic B–splines element mesh performs similar results to the ones obtained with one level of refinement using quadratic B–splines. As in the previous example, the smoothness of the first derivatives of the cubic functions allows to achieve more accurate solutions compared to the quadratic functions having the same number of elements.

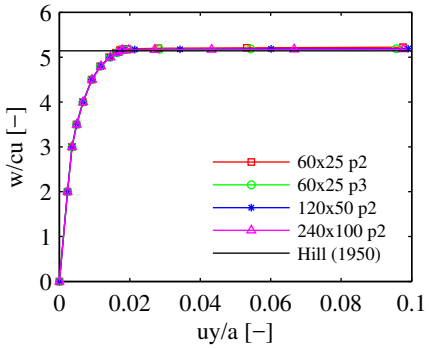

Figure 10.7: PR strip footing problem: normalized vertical displacement *vs.* bearing stress factor at point A.

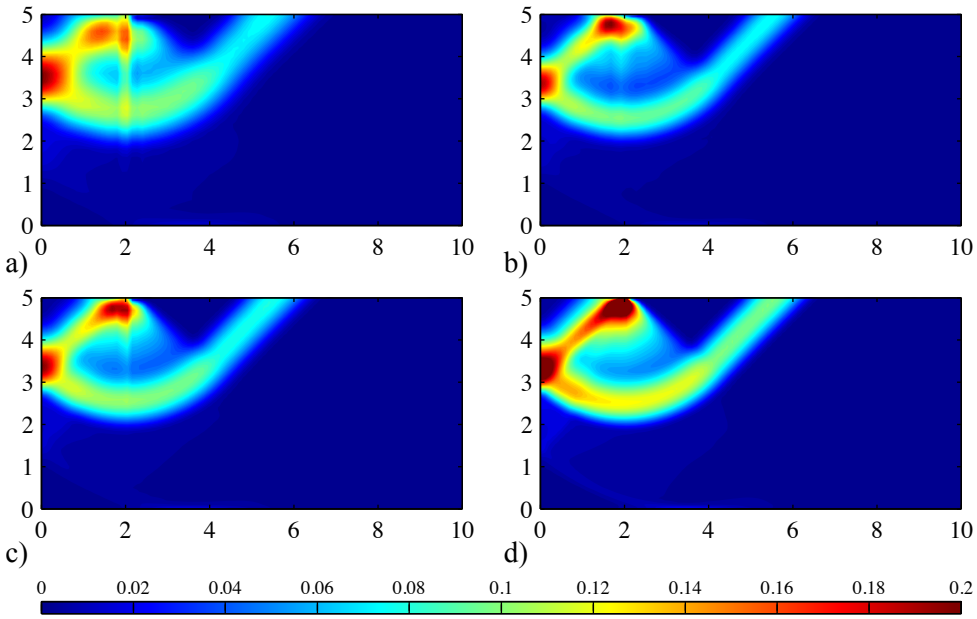

Figure 10.8: PR strip footing problem: isolines of equivalent deviatoric strain with a) 60×25 quadratic B–splines, b) 60×25 cubic B–splines, c) 120×50 quadratic B–splines, d) 240×100, quadratic B–splines

Concerning the regularization of the problem, the model is able to capture the shear band patterns and the problem is well regularized, since the occurring shear bands are mesh–independent; the shear band width remains constant through mesh refinement.

10.3 1D consolidation problem under saturated and unsaturated conditions

This example reproduces the results presented in Kim [101] who simulates the one–dimensional consolidation problem of an saturated/unsaturated sandy soil column. The IGA–FEM code is tested using the hydromechanical coupled formulation under fully saturated and partially saturated conditions.

A load $w = 100$ kPa is applied on the top surface of a soil layer $h = 10$ m thick, the lateral sides are prevented from moving in the horizontal direction and the bottom is fixed. Regarding the hydraulic boundary conditions, the top boundary is perfectly draining and the remaining boundaries are impervious. The initial pore pressure conditions will depend on the initial water table level, WT, and being assumed as hydrostatic, as it is depicted in Fig. 10.9 a). Three different initial water–table levels are considered: 10 m, 6 m, and 0 m above the bottom surface.

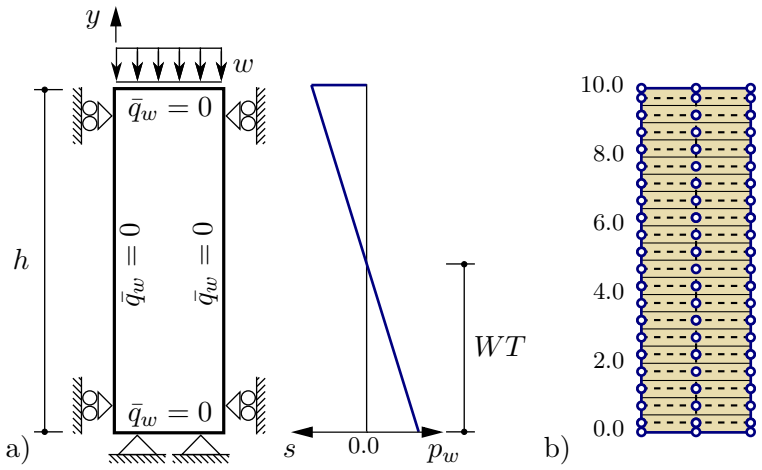

Figure 10.9: 1D consolidation problem: a) geometry, initial and boundary conditions and b) coarsest B–spline mesh.

The geometry is discretized into 20 and 40 quadratic B–spline elements as well as the displacement and pore pressure fields. Fig. 10.9 b) illustrates the coarsest mesh.

The soil is assumed to be elastic without second gradient effects, therefore, the mechanical parameters are given in terms of the Young modulus E and Poisson's ratio ν. The

water retention characteristic curve (WRCC) is given by the Van Genuchten model (see eq. (7.4)) and the relative permeability function by the Mualem model (see eq. 7.9). The rest of material parameters are listed in Tab. 10.3.

Table 10.3: Soil parameters for the 1D consolidation problem.

E	ν	n_{sw}	a_{sw}	m_{sw}	S_{y0}	$S_{y,min}$
[kPa]	[–]	[–]	[kPa^{-1}]	[–]	[–]	[–]
$1.9{\cdot}10^4$	0.3	2.5	$1.77{\cdot}10^{-1}$	1.0	1.0	0.00
ρ	ρ_{w0}	n_0	C_w	k_{sat}	μ_w	
[kg/m^3]	[kg/m^3]	[–]	[kPa^{-1}]	[m^2]	[kPa·s]	
$1.9{\cdot}10^3$	$1.0{\cdot}10^3$	0.45	$5.0{\cdot}10^{-7}$	$3.5{\cdot}10^{-12}$	$1.0{\cdot}10^{-6}$	

Another important aspect to be taken into account when solving coupled consolidation problems is the choice of the initial time step size, Δt_0. Vermeer and Verruijt [181] suggested a simple criterion for linear basis functions in order to avoid oscillating pore pressures close to the draining boundaries:

$$\Delta t_0 \geq \Delta t_c = \frac{1}{6}\frac{(\Delta h)^2}{c_v} \tag{10.2}$$

where Δt_c is the critical time step size, Δh is the element size (or $(\Delta h)^2$ the element area in 2D) near the draining surface, and c_v is the consolidation coefficient:

$$c_v = \frac{k_{sat}}{\mu_w(m_v + S)}, \qquad m_v = \frac{1}{K + 4/3G}, \qquad S = n_0 C_w \tag{10.3}$$

Due to the superior smoothness achieved with IGA, as observed in [91], it is possible to use a Δt smaller than Δt_c of eq. (10.2), taking as Δh the element size of the coarsest mesh. Therefore we set the initial time step size to $\Delta t_0 = 0.1$ seconds ($\Delta t_c = 0.5$ seconds). Then, the time domain is discretized for each k–time step with the following expression:

$$\Delta t_{k+1} = \zeta \Delta t_k = \zeta^{k+1} \Delta t_0 \tag{10.4}$$

with $\zeta = 1.20$ and $\Delta t_{k+1} \leq 6$ seconds.

For purposes of normalizing the results, we define the normalized time factor as $T = c_v t/h$. Fig. 10.10 shows the evolution with T of the excess pore water pressure and settlement at the bottom and top of the soil column, respectively. The numerical solutions

for $WT = 10$ m (solid lines) are compared with the analytical solution (dashed lines) derived by Terzaghi [171], which show good agreement. The results of this study for $WT = 6$ m (solid lines) also agree well with the results of [101] (circles). Fig. 10.10 b) illustrates an instantaneous settlement of 16 mm for $WT = 6$ m, which is mainly due to the deformation in the unsaturated zone. There is no consolidation for $WT = 0$ m since the initial and the final settlements are almost the same. The final settlement does not change with the initial water table, thus, the surface settlement is equal in all three cases.

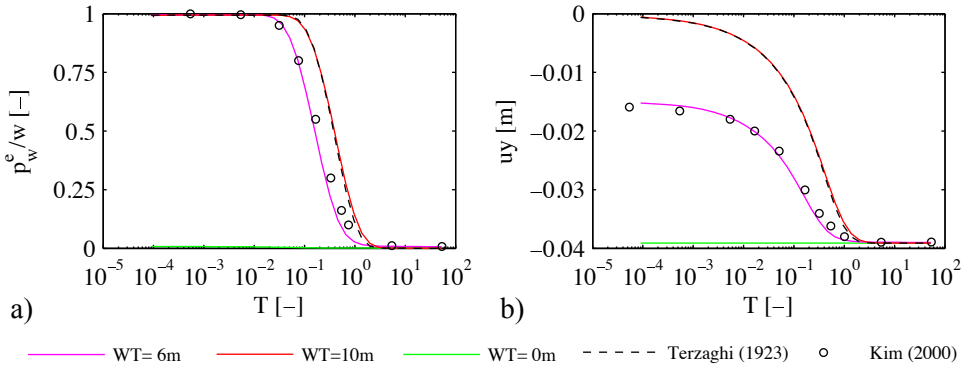

Figure 10.10: 1D consolidation problem: evolution of a) excess pore pressure at $y = 0$ m and b) vertical displacement at $y = 10$ m with 20 elements.

Fig. 10.11 shows the isochrones of the excess pore water pressure in the vertical direction for the case with $WT = 10$ m. Fig. 10.11 a) shows the results with 20 elements; we observe oscillations close to the surface after the load is applied that disappear with one refinement as illustrated in Fig. 10.11 b).

The isochrones of pore pressure for the case with $WT = 6$ m are shown in Fig. 10.12. After the load is applied, the pore water pressure increases by 100 kPa at the base of the soil column, that is, the entire load is absorbed by the pore water in the saturated zone, whereas the pore water pressure does not change at the top of the soil column. We observe that the water table level first increases slightly above the initial water table level and then it decreases with time. Another observation is that some oscillations appear in this zone; the sharp change in the pore pressure is not properly modeled with the coarse mesh (Fig. 10.12 a)) but the oscillations in the solution are mitigated by refining

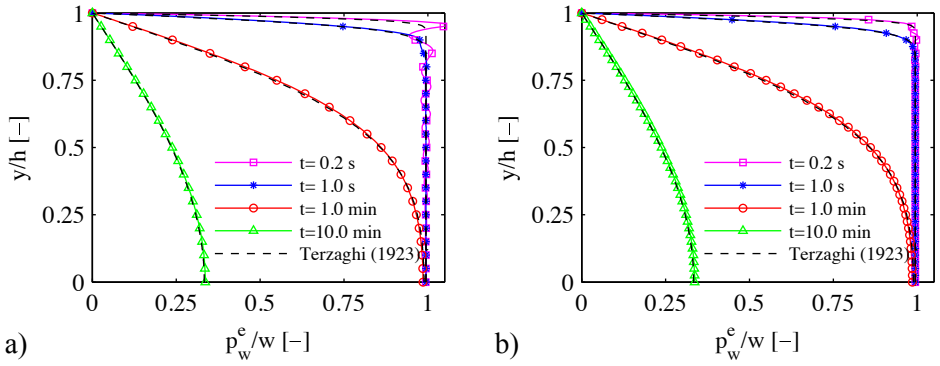

Figure 10.11: 1D consolidation problem ($WT = 10$ m): isochrones of excess pore pressure with a) 20 elements and b) 40 elements.

the mesh. It is important to remark that this numerical instability occurs just after the load is applied and it disappears completely for the subsequent steps.

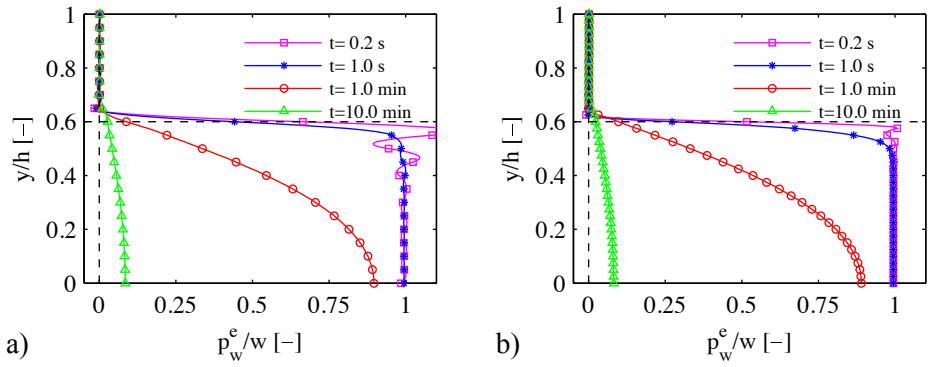

Figure 10.12: 1D consolidation problem ($WT = 6$ m): isochrones of pore pressure with a) 20 elements and b) 40 elements.

10.4 Desaturation of a sand column (Liakopoulos problem)

The proposed benchmark is based on an experimental drainage test on a Del Monte sand column carried out by Liakopoulos [108]. The test consists of a fully saturated soil column with a heigh of $h = 1.0$ m with free drainage along the vertical direction. The lateral walls are rigid and impervious, whereas the bottom is constrained in the horizontal and vertical directions. The simulation starts after instantaneous interruption of inflow at the

top of the column. The bottom boundary is kept pervious and the kinematics conditions remain unchanged. The initial stress state is geostatic and the simulation starts after removing the pore pressure from the sample. Fig. 10.13 a) shows the geometry with the initial and boundary conditions. The discretization of the column consists of ten quadratic B–spline elements is illustrated in Fig. 10.13 b). The time is equally discretized with $\Delta t = 20$ seconds.

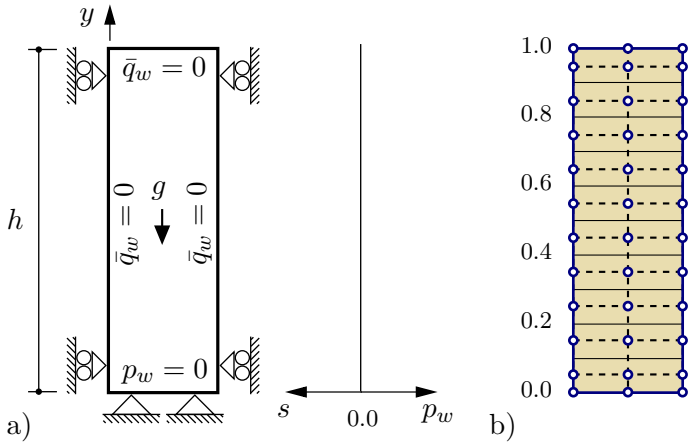

Figure 10.13: Liakopoulos problem: a) geometry, initial and boundary conditions and b) B–spline mesh.

The original report by Liakopoulos did not include mechanical parameters. For this reason, these parameters are taken from Lewis and Schrefler [107] for an elastic sand. All parameters are summarized in Tab. 10.4. The WRCC and the relative permeability are given by the following expressions:

$$S_w = 1 - 1.9722 \cdot 10^{-11} s^{2.4279} \tag{10.5}$$

$$k_w^{rel} = 1 - 2.207(1 - S_w)^{1.0121} \tag{10.6}$$

with $S_w > 0.91$.

Table 10.4: Soil parameters for the Liakopoulos problem.

E	ν	ρ	ρ_{w0}	n_0	C_w	k_{sat}	μ_w
[Pa]	[–]	[kg/m^3]	[kg/m^3]	[–]	[Pa^{-1}]	[m^2]	[Pa·s]
$1.3{\cdot}10^6$	0.4	$1.7{\cdot}10^3$	$1.0{\cdot}10^3$	0.3	$5.0{\cdot}10^{-10}$	$4.5{\cdot}10^{-13}$	$1.0{\cdot}10^{-3}$

In Fig. 10.14 the numerical results (solid lines) for the pore pressure and vertical displacements are given and compared to the ones obtained by Lewis and Schrefler [107] (dashed lines). We observe that both calculations agree reasonably well for all five time stations.

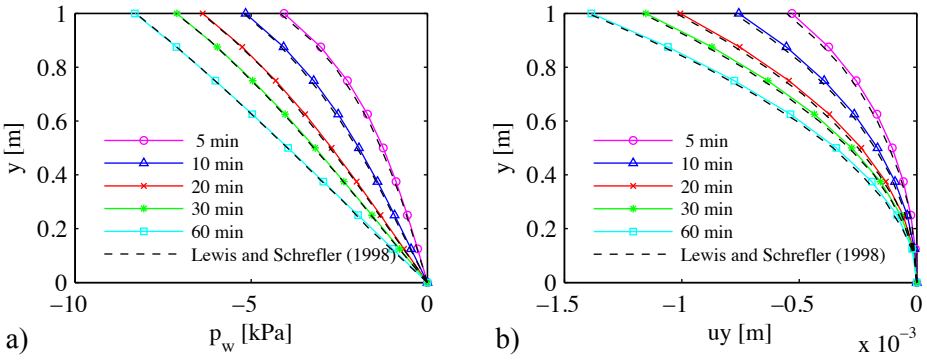

Figure 10.14: Liakopoulos problem: isochrones of a) pore pressure and b) vertical displacement.

10.5 Strip footing consolidation problem on an elastic soil layer

This last example was proposed by Ng and Small [124] to investigate how the initial degree of saturation influences the response of a strip footing in a consolidation problem (2D plane strain). The problem consists of a smooth flexible strip footing ($2a = 4$ m) resting on an elastic soil layer with $h = 10$ m and the water table level at the ground surface as shown in Fig. 10.15. A uniform load, $w = 100$ kPa, is applied instantaneously and remains constant with time. Gibson et al. [74] proposed an analytical solution for the saturated case with the assumption of an infinite horizontal layer resting on a smooth rigid base. Therefore, the domain is made relatively long in the horizontal direction ($l = 40$ m) with respect to the width of the loaded strip in order to minimize the boundary effects. And, unlike Ng and Small [124], the right boundary is constrained in the horizontal direction instead of considering it as a free surface. The geometry is discretized with 40×160 quadratic B–spline elements. The mesh is homogeneous in the vertical direction only. The time is discretized with $\Delta t_0 = \Delta t_c = 2.4{\cdot}10^{-4}$ days and then

the time steps are increased with a factor $\zeta = 1.50$. The material parameters are listed in Tab. 10.5.

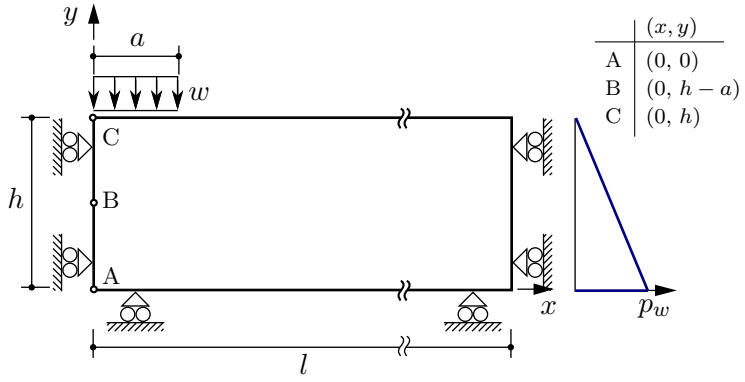

Figure 10.15: 2D consolidation problem: geometry, initial and boundary conditions.

Table 10.5: Soil parameters for the 2D consolidation problem.

E	ν	ρ	ρ_{w0}	n_0	C_w	k_{sat}	μ_w
[kPa]	[–]	[kg/m^3]	[kg/m^3]	[–]	[kPa^{-1}]	[m^2]	[kPa·days]
$1.0{\cdot}10^4$	0.0	$2.1{\cdot}10^3$	$1.0{\cdot}10^3$	0.33	0.0	$3.2{\cdot}10^{-15}$	$1.16{\cdot}10^{-11}$

This example assumes no influence of suction over permeability. The relationship between degree of saturation and suction used for this example are given by the following expression:

$$S_w = \frac{0.0099 p_w + 0.98 S_{w0}}{0.98 + 0.0097 p_w} \tag{10.7}$$

where S_{w0} is the initial degree of saturation. Three initial conditions were considered. The initial degree of saturation takes the values of: 85%, 95% and 100%.

The evolution with time of the pore pressure at point B for the three initial conditions is shown in Fig. 10.16 a). The plotted variations indicate that the Mandel–Crayer effect occurs in partially saturated soils, as well as in fully saturated soils, as would be expected. The evolution with time of the settlement at point C is plotted in Fig. 10.16 b). The saturated case is compared with the analytical solution given by Gibson et al. [74]. The difference between the numerical and the analytical solution is mainly due to the fact the right boundary were not chosen distance enough from the footing centerline.

Fig. 10.17 presents the pore pressure and total stress profiles along the section A–C throughout the consolidation process for the saturated case. The numerical solutions

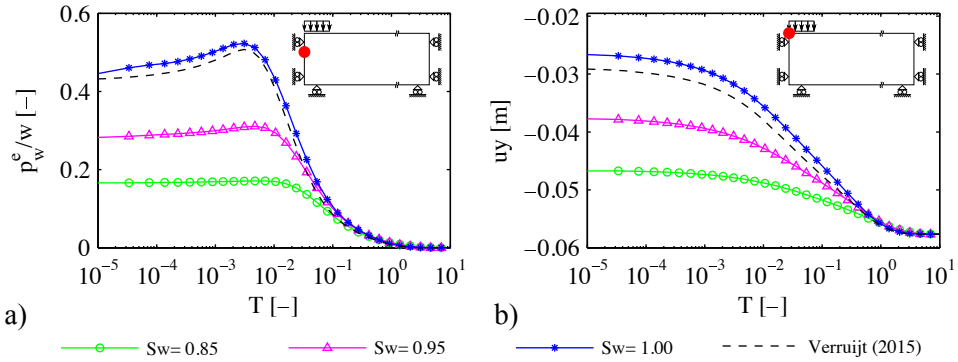

Figure 10.16: 2D consolidation problem: evolution of a) excess pore pressure at point B and b) vertical displacement at point C.

(solid lines) are compared with the analytical solution (dashed lines). Globally, the numerical solution is consistent with the analytical solution [182] and the small differences between both solutions are related to the location of the right boundary and not to the HM formulation. However, locally, numerical oscillations near the ground surface yield a maximum excess pore pressure and a minimum total stress totally different from their analytical counterparts. Such unrealistic solutions may lead to erroneous evaluation of the hydromechanical behavior of the strip footing. As in the 1D consolidation problem, refining the mesh will alleviate this oscillations.

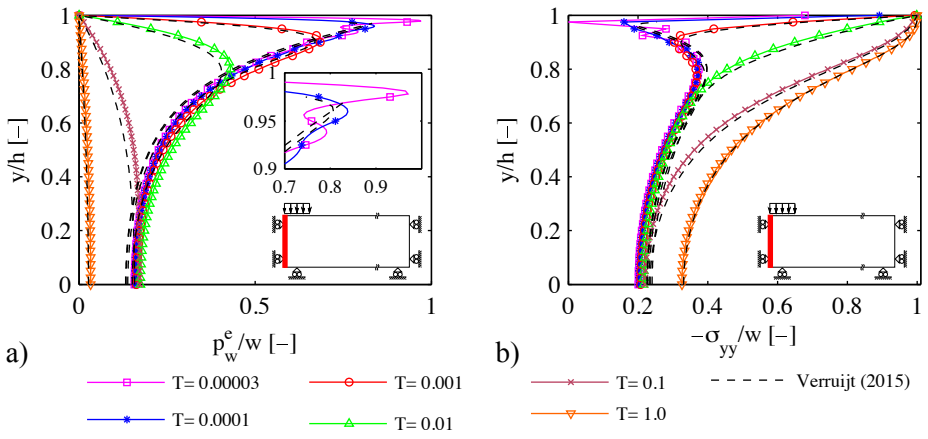

Figure 10.17: 2D consolidation problem (saturated case): isochrones of a) pore pressure along the segment A–C and b) total stress along the segment A–C.

Chapter 11

Shear band modeling and objectivity of numerical solutions

11.1 Mechanical biaxial test problem

In this section, a biaxial compression test (M biaxial test) is presented to study strain localization, in particular, the shear band width. We first perform a mesh dependency study on a biaxial test modeled with the Prandtl–Reuss model as it was done by Matsushima et al. [115] and Bésuelle et al. [19], but using small strains instead of the large strain formulation. Then, we analyze the evolution of the width and the orientation of the shear band during the numerical simulation. In the last part, we repeat the analysis using a second gradient plasticity model with three different hardening laws: 1) perfect plasticity, 2) linear hardening law, and 3) exponential hardening law.

A uniform downward displacement U is applied on the top surface of a biaxial sample. The material parameters are listed in Tab. 11.1. In order to obtain the same strain localization pattern in all computations, the yield strength is reduced to $0.9S_{y0}$ in an area of 0.05 m$\times$ 0.05 m at the bottom left corner of the sample, whose dimensions are $l = 0.5$ m and $h = 1.0$ m, as it is illustrated in Fig. 11.1 a). The rollers at the top and bottom boundaries simulates a frictionless interface between the soil and the bottom surface and only the left bottom corner is fixed. The geometry is discretized with four

meshes: 1) 10× 20, 2) 20× 30, 3) 30× 60, and 4) 40× 80 elements. In all cases the elements are quadratic B-splines. The coarsest mesh is shown in Fig. 11.1 b).

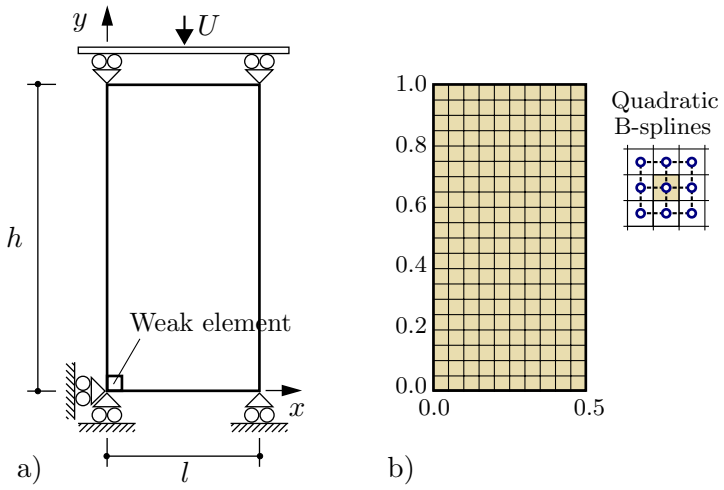

Figure 11.1: M biaxial test: a) geometry, boundary conditions and b) B–spline mesh.

Table 11.1: Material parameters for the M biaxial test.

K	G_1	H_ε	S_{y0}	$S_{y,min}$	D^{sg}
[kPa]	[kPa]	[kPa]	[kPa]	[kPa]	[kN]
$9.74{\cdot}10^4$	$5.00{\cdot}10^4$	-4.81	$1.00{\cdot}10^3$	$1.00{\cdot}10^3$	$2.00{\cdot}10^{-1}$

The curves of the loading force versus the axial shortening for the four meshes (see Fig. 11.2) show that they converge to a one solution. The small disagreement between the solutions obtained with the IGA formulation and the solution obtained by Bésuelle et al. [19] as the force decreases may be due to the finite strain approach used in the mentioned work.

Fig. 11.3 shows the shear band patterns of the first three meshes at the end of the test. The red squares correspond to the position of the Gauss points with a plastic stress state. The difference of the shear band width between the second and the third meshes is minimal. In order to have a quantitative idea of this difference, we track the first and the last gauss points in the vertical direction belonging to the shear band in the horizontal range 0.175 m–0.45 m in order to compute its upper and lower bounds by linear regression, as it is illustrated in Fig. 11.4.

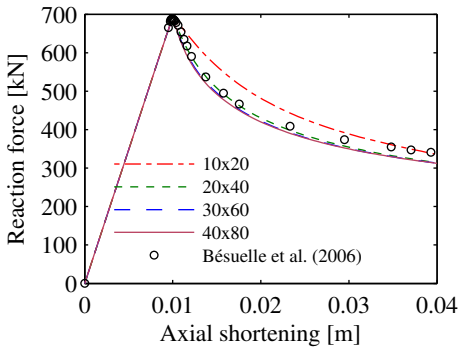

Figure 11.2: M biaxial test: axial shortening *vs.* reaction force of the specimen.

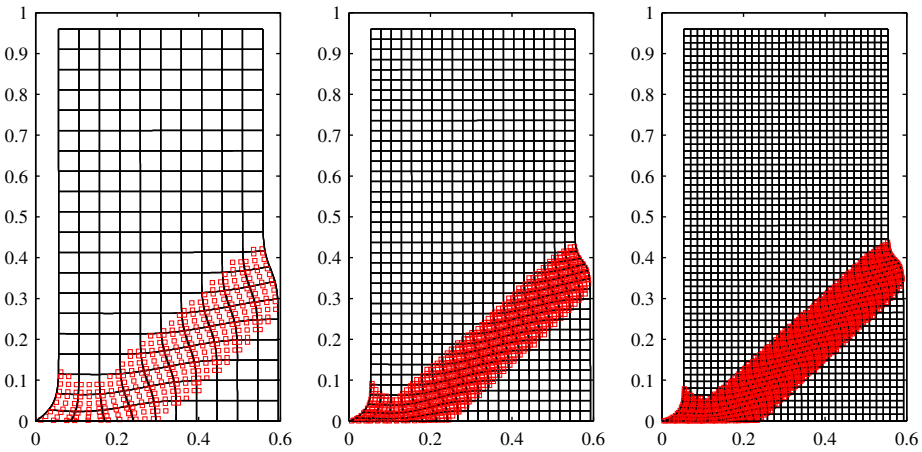

Figure 11.3: M biaxial test: Shear band patterns at the end of the simulation with: 10×20, 20×40, 30×60 elements.

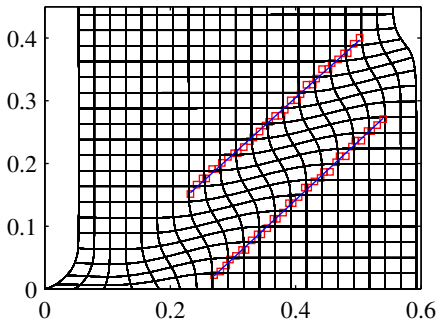

Figure 11.4: M biaxial test: boundaries of the shear band width for 20×40 element mesh.

Now, if we look at Fig. 11.5 b), we observe that the orientation of the shear band remains

constant during the test, and it tends to a value around 43° as we reduce the element size. On the other hand, despite the fact we obtain objective results, the shear band width increases constantly without reaching a stationary value as it is shown in Fig. 11.5 a).

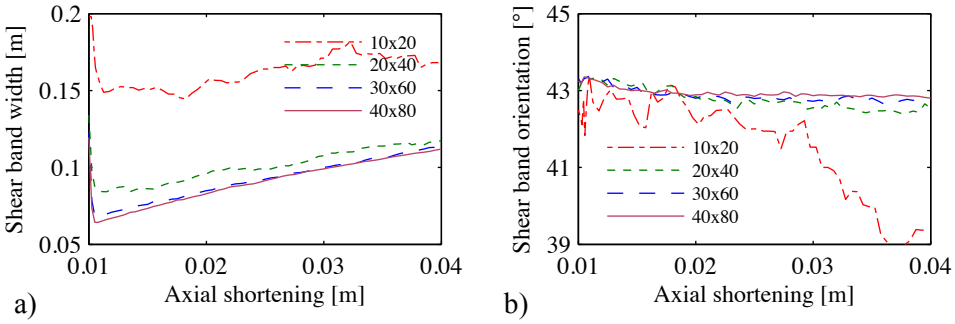

Figure 11.5: M biaxial test: evolution of a) the width and b) the orientation of the shear band.

This behavior is due to the fact that the shear band width is proportional to the ratio between the "magnitudes" of the first and second gradient constitutive tensors. In order to overcome this behavior predicted by the theory, we use the second gradient elastoplastic model with three different hardening laws: 1) perfect plasticity defined by the parameters D^{sg} and R_0^{sg}, 2) linear hardening defined by the parameters D^{sg}, R_0^{sg} and H_γ, and 3) exponential hardening law defined by the parameters D^{sg}, R_0^{sg}, H_γ and R_{max}^{sg}. Fig. 11.6 illustrates these three different hardening laws and the parameters for all these thee cases are listed in Tab. 11.2.

Table 11.2: Second gradient parameters for the M biaxial test.

D^{sg}	R_0^{sg}	H_γ	R_{max}^{sg}
[kN]	[kPa·m]	[kN]	[kPa·m]
$2.00{\cdot}10^{-1}$	2.00	$4.00{\cdot}10^{-1}$	4.25

The value R_0^{sg} was defined by looking at the maximum values of the double stresses obtained for the elastic second gradient law. As we can see in Fig. 11.7, the maximum value for the double stresses is around 6 kPa·m. Therefore, the yield double stress point was set to $2.00{\cdot}10^{-1}$ kPa·m. The remaining parameters were defined after a preliminary stage where they were tested in order to have reasonable results.

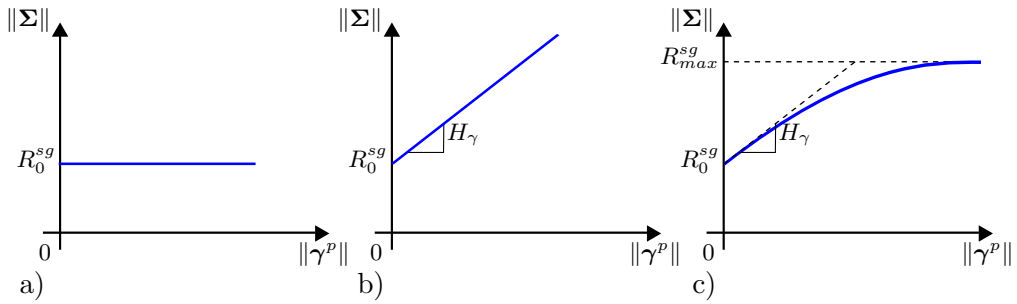

Figure 11.6: Elastoplastic second gradient hardening laws: a) Perfect plasticity, b) linear hardening and c) exponential hardening.

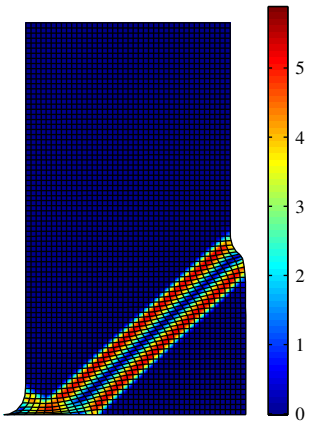

Figure 11.7: M biaxial test: isolines of the norm of the double stress [kN] at the end of the simulation.

Two different meshes were used for the simulations: 40×80 and 50×100. The evolution of the width and the orientation of the shear band can be seen in Fig. 11.8. The pair of curves sharing same color belong to the two meshes used for each case (the elastic second gradient law is also included). The perfect plasticity case shows an abrupt reduction of the shear band corresponding to the moment when the value of R_0^{sg} is reached inside the shear band thickness, which also leads to non-convergent results. Having a smooth transition between the elasticity and plasticity branch by setting a non–zero value for the hardening parameter H_γ it is possible to avoid any sharp discontinuity in the evolution of the shear band width. Furthermore, the exponential hardening law stabilizes the shear band width when the parameter R_{max}^{sg} is reached.

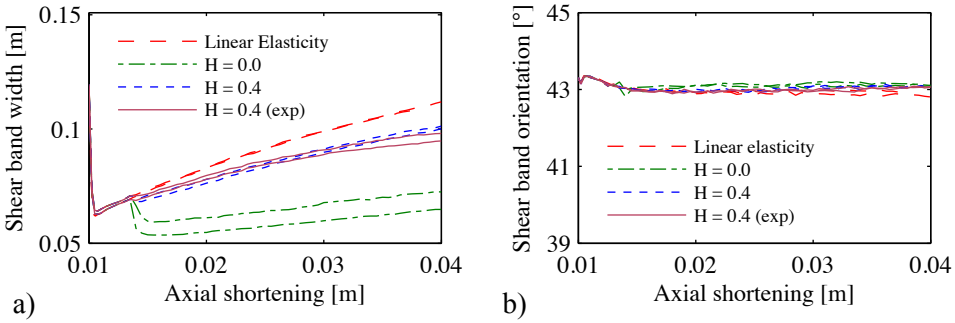

Figure 11.8: M biaxial test (second gradient elastoplastic model): evolution of a) the width and b) the orientation of the shear band.

11.2 Hydromechanical biaxial test problem

We consider the biaxial compression test shown in Fig. 11.9 using the hydromechanical formulation under saturated conditions (HM biaxial test). The specimen has a height h =1 m, and a width l = 0.5 m. Its lateral boundaries are considered as impervious and are subjected to a uniform, constant confinement pressure σ_0. The top and bottom boundaries of the sample are considered as smooth, rigid and perfectly draining ($\Delta p_w = 0$ during the entire simulation). The left bottom corner is fixed in order to avoid rigid body displacement. The vertical displacement of the top platen, $U(t)$ is applied considering two different loading rates: $(10^{-2}\%)$/days and $(10^{-4}\%)$/days, respectively.

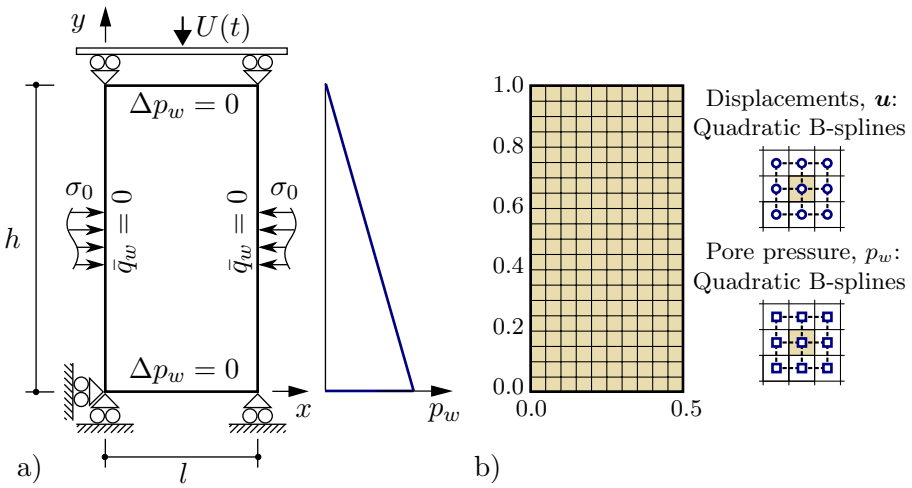

Figure 11.9: HM biaxial test: a) geometry, initial and boundary conditions and b) B–spline mesh.

The mechanical properties of the model adopted (Milan model) are taken from Tamagnini et al. [167] for a bonded soil with associative plastic flow (see Tab. 11.3). The initial values of the internal variables, controlling the size of the elastic domain, are assumed as $p'_{s0} = 200$ kPa and $p'_{m0} = 100$ kPa, respectively. The second gradient parameter D^{sg} has been assumed equal to 0.8 kN. The hydraulic parameters of the soil are summarized in Tab. 11.4.

Table 11.3: Mechanical parameters for the HM biaxial test.

α	$\hat{\kappa}$	G_0	p_{ref}	ρ_s	ξ_s	ρ_m	ξ_m	k
[–]	[–]	[kPa]	[kPa]	[–]	[–]	[–]	[–]	[–]
0.0	0.0024	77000.0	200.0	16.66	0.0	20.0	10.0	0.0
a_g	m_g	M_{gc}	M_{ge}	a_f	m_f	M_{fc}	M_{fe}	D^{sg}
[–]	[–]	[–]	[–]	[–]	[–]	[–]	[–]	[kN]
0.63	0.95	0.75	0.60	0.63	0.95	0.75	0.60	0.4

Table 11.4: Hydraulic parameters for the HM biaxial test.

ρ	ρ_{w0}	n_0	C_w	k_{sat}	μ_w
[kg/m^3]	[kg/m^3]	[–]	[kPa^{-1}]	[m^2]	[kPa·days]
$2.0{\cdot}10^3$	$1.0{\cdot}10^3$	0.15	$5.0{\cdot}10^{-7}$	$1.0{\cdot}10^{-19}$	$1.16{\cdot}10^{-11}$

Fig. 11.10 shows the global response – in terms of reaction force at the top platen *vs.* axial shortening of the specimen – obtained with the two different loading rates, for two different initial stress conditions. The first set of simulations have been performed assuming an initial isotropic stress with $\sigma_0 = 20$ kPa (highly overconsolidated soil, HOC), while in the second set of simulations, an initial isotropic stress with $\sigma_0 = 100$ kPa (slightly overconsolidated soil, SOC) has been adopted.

For the HOC soil (Fig. 11.10a), two different spatial discretizations, with 10×20 and 20×40 elements, have been used. The results show that force–displacement curves are indistinguishable for the case of low loading rate, and almost coincident when the high loading rate is considered, thus demonstrating the effectiveness of the second gradient regularization. It is worth noting that, as the loading rate increases, the global response of the specimen changes significantly, with a higher peak at much larger axial shortening values. This is a consequence of the different distributions of excess pore pressures within the specimen, which, in turns, affect the shear band pattern which develops upon bifurcation initiation, see Figs. 11.11 and 11.12. However, more investigations concerning

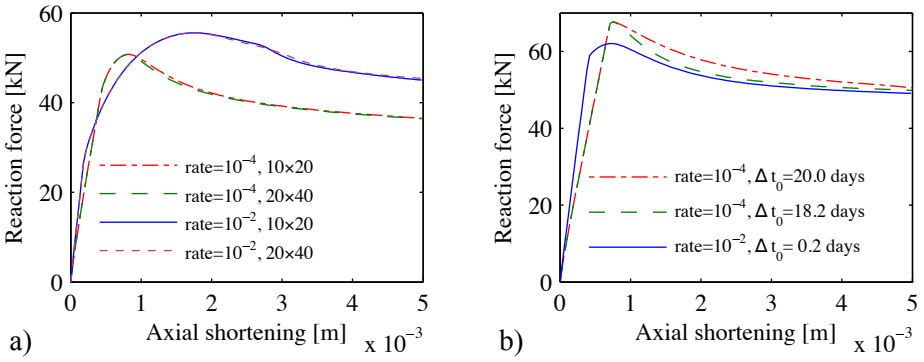

Figure 11.10: HM biaxial test: axial shortening *vs.* reaction force of the specimen for a) HOC soil and b) SOC soil.

non uniqueness of solutions would be necessary to better understand the effect of loading rate on the strain localization pattern.

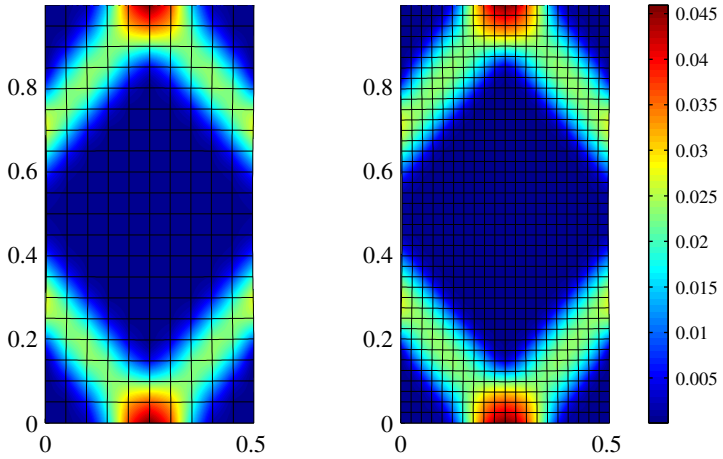

Figure 11.11: HM biaxial test (HOC, rate = $10^{-4}\%/days$): isolines of equivalent deviatoric strain at the end of the simulation with 10×20 and 20×40 elements.

Another interesting feature is observed in Fig. 11.13 for the HOC soil at low rate. Given an initial shear band pattern consisting in several bands, only one band becomes predominant as the loading progresses whereas the other ones start to unload and become inactive. This behavior is studied in Bésuelle et al. [19].

Fig. 11.10b provides the global response obtained for the SOC soil at different loading rates, using the 10×20 discretization. For the lower loading rate, two different initial

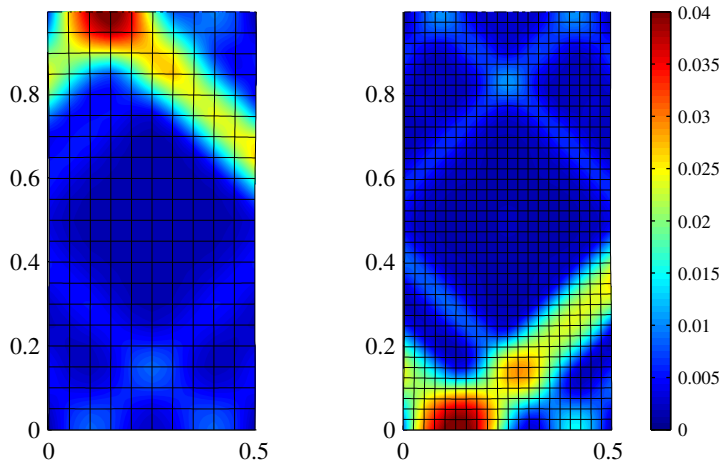

Figure 11.12: HM biaxial test (HOC, rate = 10^{-2}%/days): isolines of equivalent deviatoric strain at the end of the simulation with 10×20 and 20×40 elements.

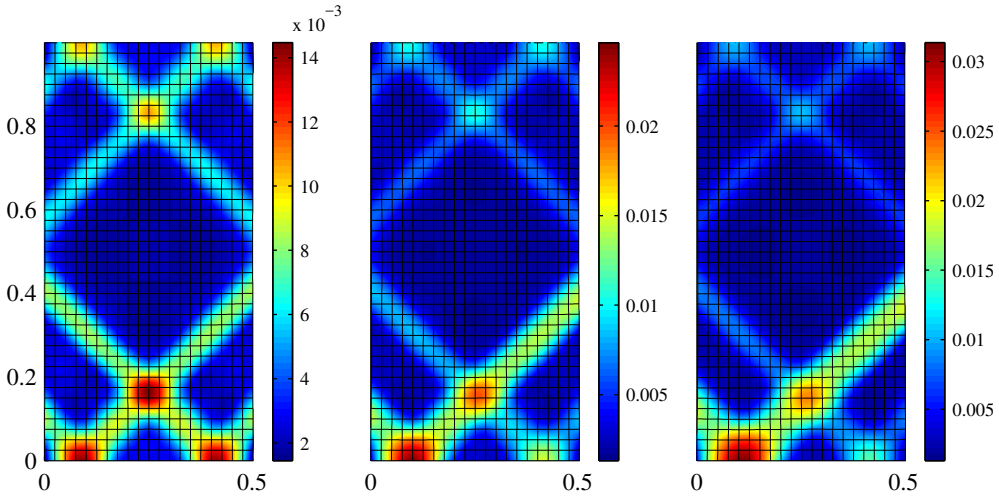

Figure 11.13: HM biaxial test (HOC, rate = 10^{-2}%/days): evolution of the shear band patterns with 20×40 elements at $U = 0.002$ m, $U = 0.003$ m and $U = 0.004$ m.

time step sizes have been considered, with Δt_0 equal to 18.2 and 20 days, respectively. Fig. 11.14 shows the shear band patterns corresponding to the two sizes. The results obtained indicate that, upon bifurcation, the post–peak response is significantly affected by the adopted step size. Again, this is a consequence of the impact that the choice of the step size has on the predicted deformation pattern in a context of non uniqueness of solutions [19], which, for the same applied boundary conditions, is dramatically different in the two cases considered. It is also interesting to note that the orientation of the shear

bands for HOC and SOC soils is slightly different, as typically observed in porous rocks [see, *e.g.*, 20].

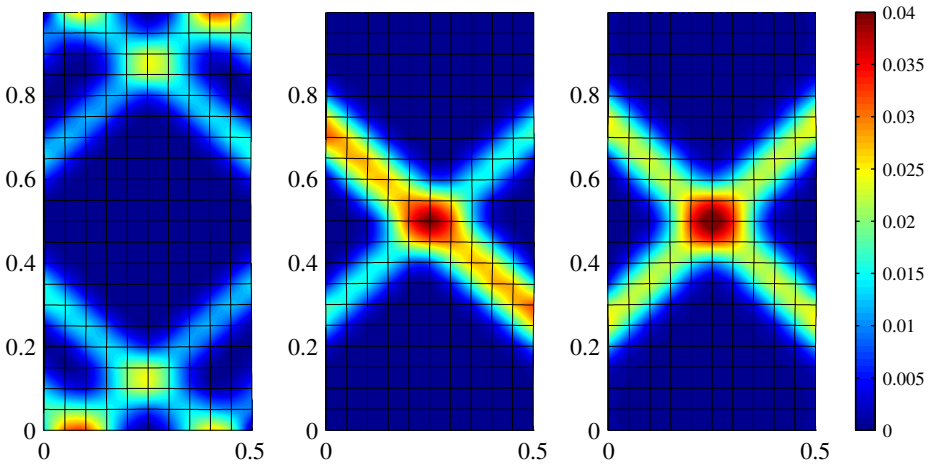

Figure 11.14: HM biaxial test (SOC soil): isolines of equivalent deviatoric strain at the end of the simulation with rate = 10^{-4}%/days, Δt_0 = 20.0 days, rate = 10^{-4}%/days, Δt_0 = 18.2 days and rate = 10^{-2}%/days, Δt_0 = 20.0 days.

Figs. 11.15 and 11.16 show the distribution of the excess pore pressure and the fluid flow field, respectively, for the SOC soil at the end of the simulation. The shear band pattern clearly influences the distribution of the pore pressure and the fluid flow as it is expected. The fluid flow is squeezed out from the shear band due to the contractancy behavior that the SOC soil experiences as the shear deformation increases.

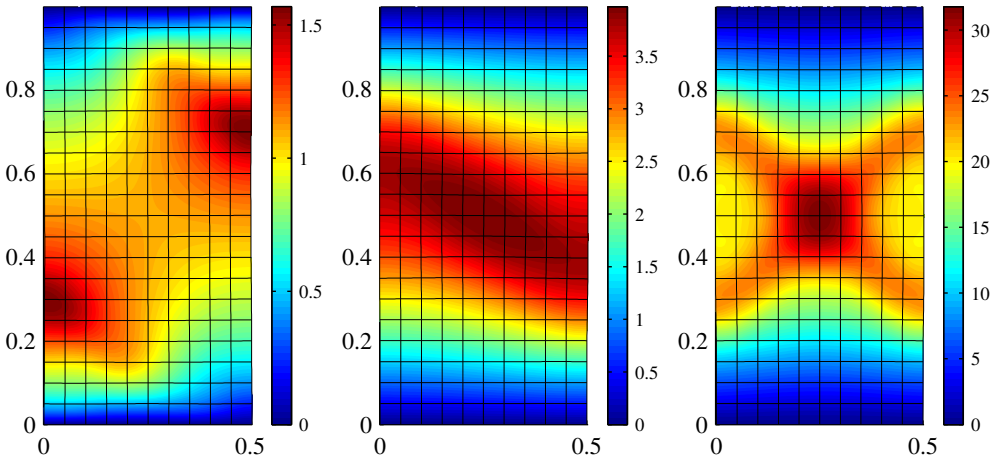

Figure 11.15: HM biaxial test (SOC soil): isolines of excess pore pressure [kPa] at the end of the simulation with rate = 10^{-4}%/days, Δt_0 = 20.0 days, rate = 10^{-4}%/days, Δt_0 = 18.2 days and rate = 10^{-2}%/days, Δt_0 = 20.0 days.

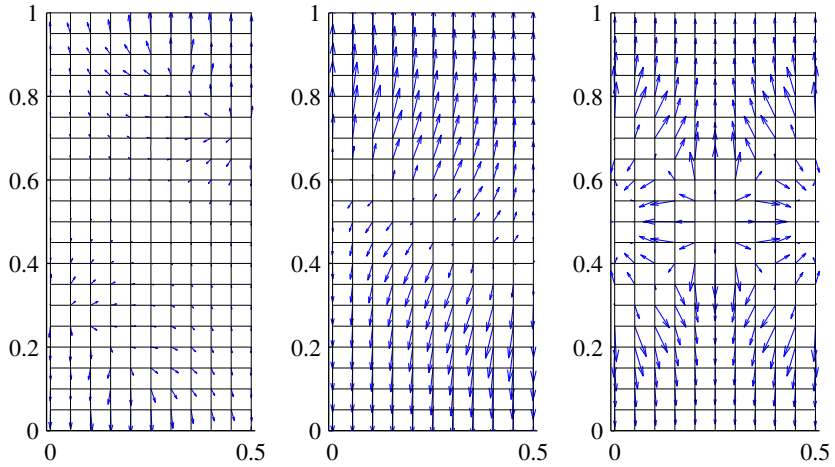

Figure 11.16: HM biaxial test (SOC soil): fluid flow field at the end of the simulation with rate = 10^{-4}%/days, Δt_0 = 20.0 days, rate = 10^{-4}%/days, Δt_0 = 18.2 days and rate = 10^{-2}%/days, Δt_0 = 20.0 days.

Chapter 12

One–phase modeling of geotechnical failure problems

12.1 Two–Dimensional Slope stability problem

A slope stability problem is presented to test the capability of the Arc Length Method implementation to advance the solution in time when modeling the softening response of a system under load–controlled conditions. The example considers an homogenous slope with a rigid, rough bedrock at the bottom and no horizontal displacement in its left lateral boundary. The dimensions of the slope are $h = 10$ m and $l = 20$ m as shown in Fig. 12.1. The initial stress field of the slope is reproduced by increasing the gravity up to 9.81m/s^2. At the end of the gravity state, the resulting displacements and strains are set to zero. Then, a flexible strip footing of width $a = 4$ m is placed on the top of the slope and its magnitude will gradually increase depending on the arc–length parameter λ. The groundwater table is assumed to be very deep. The slope geometry is discretized with two different meshes: 400 and 1600 quadratic B–splines elements.

The analyses is performed using the Milan model for a calcarenite soft rock of density $\rho = 2000.0$ kg/m^3, the initial internal variables are $p'_{s0} = 500$ kPa and $p'_{m0} = 100$ kPa. The second gradient constitutive law is given by $D^{sg} = 10.0$ kN. The rest of the soil parameters adopted in the analysis are given in Tab. 12.1.

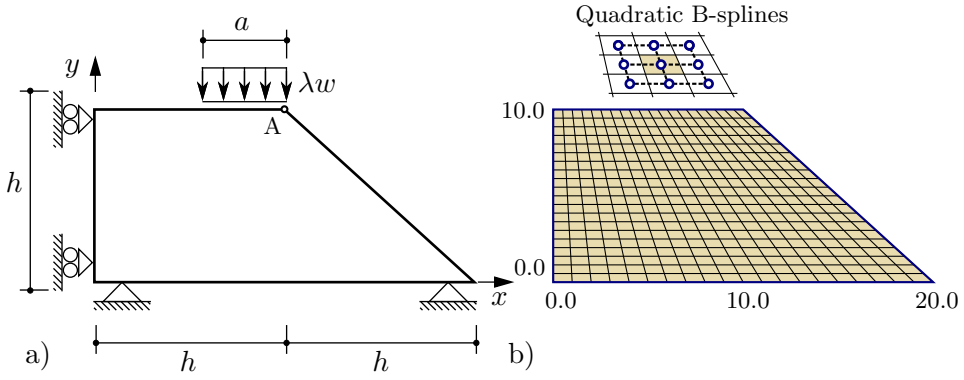

Figure 12.1: Slope stability problem: a) geometry, boundary conditions and b) B–spline mesh.

Table 12.1: Mechanical parameters for the slope stability problem.

α	$\hat{\kappa}$	G_0	p_{ref}	ρ_s	ξ_s	ρ_m	ξ_m	k
[–]	[–]	[kPa]	[kPa]	[–]	[–]	[–]	[–]	[–]
0.0	0.0024	77000.0	200.0	16.66	0.0	20.0	10.0	0.0
a_g	m_g	M_{gc}	M_{ge}	a_f	m_f	M_{fc}	M_{fe}	D^{sg}
[–]	[–]	[–]	[–]	[–]	[–]	[–]	[–]	[kN]
0.63	0.95	0.75	0.60	0.63	0.95	0.75	0.60	10.0

Fig. 12.2 presents the evolution of the vertical displacement at point A *vs.* the reaction force. A clearly visible softening response is predicted with the two meshes with a minor a difference between each other, thus objective solution is obtained regardless of the element size adopted for the mesh. Fig. 12.8 shows the displacement field at the end of

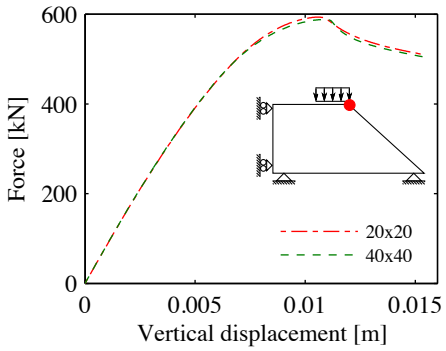

Figure 12.2: Slope stability problem: vertical displacement at point A *vs.* force.

the simulation with the coarse mesh. We observe that the deformations are concentrated

below the strip footing with displacement vectors which are mainly vertical beneath the footing, and almost horizontal along the slope face.

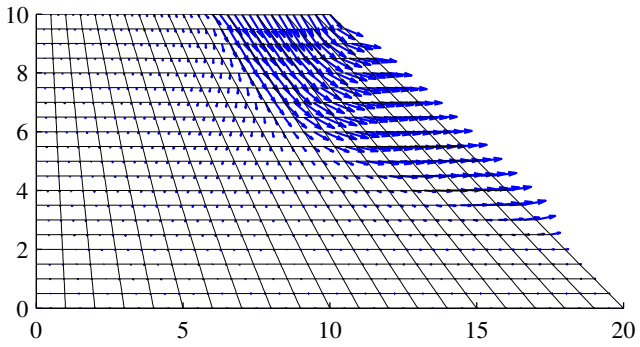

Figure 12.3: Slope stability problem: displacement field for the coarse mesh.

Fig. 12.4 shows the formation of the failure mechanisms for the two meshes at three instants of the loading process defined by the vertical displacement at point A. High strains develop beneath the strip footing with a diffuse shear band pattern which is only slightly affected by the sloping face. As the load progresses, a failure surface starts to develop until a clear failure mechanism is defined. The shear band formation and the failure of the slope is the one expected for both the coarse and fine meshes.

12.2 Square footing problem under undrained conditions

This example presents a flexible square footing problem with an inclined load in the x–direction whose magnitude is controlled by the arc–length parameter λ. The three dimensional model considers only half geometry taking advantage of the plane of symmetry as illustrated in Fig. 12.5. The depth of the layer is $h = 4$ m and the lateral boundaries are $a = 8$ m from the center of the loaded area, whose dimensions are $2b \times 2b = 1$ m^2. All lateral boundaries are fixed in the orthogonal direction whereas the bottom is fixed in the three directions.

The geometry is discretized with quadratic B–splines as well as the displacement field and reduced integration is applied over the elements. The mesh is not homogeneous and only the area below the foundation is refined where the strain localization is expected to occur.

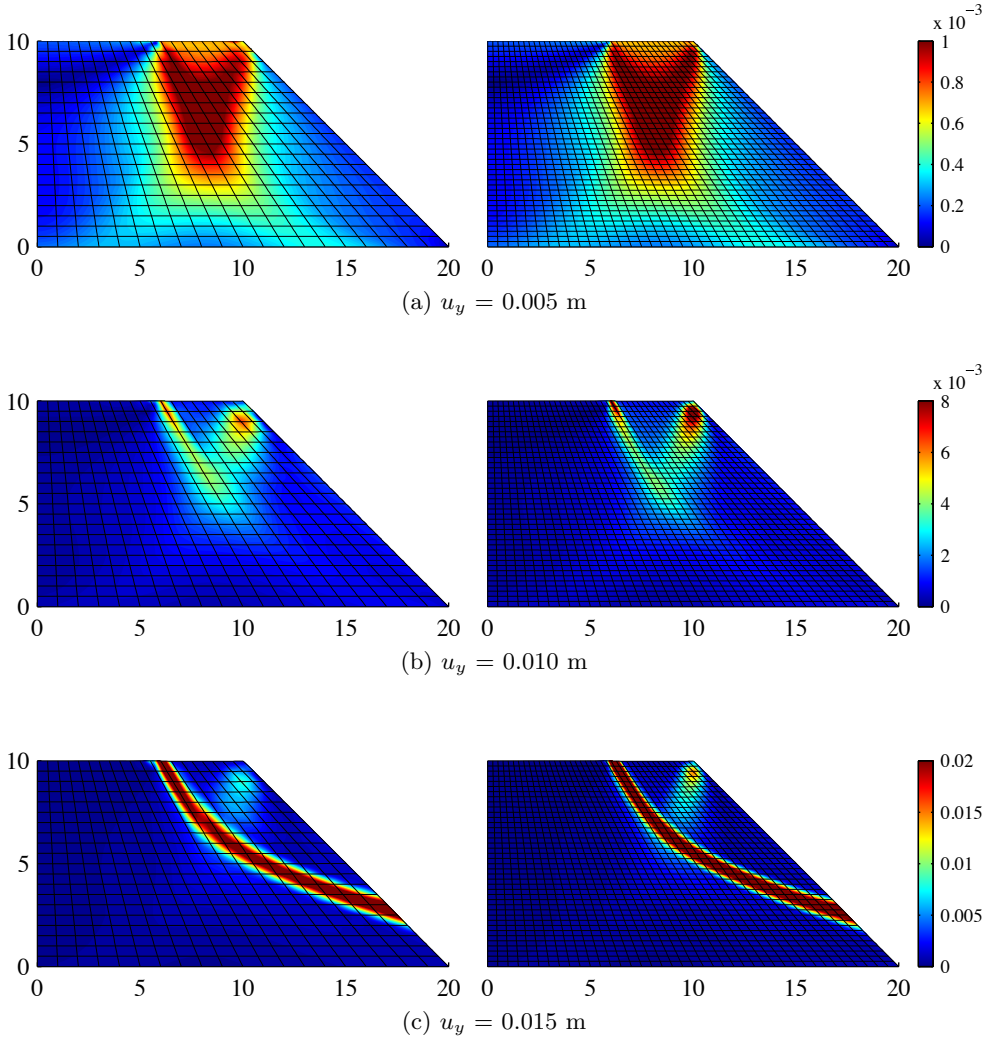

Figure 12.4: Slope stability problem: equivalent deviatoric strain for three different instants defined by the vertical displacement at point A.

The simulation is performed under undrained conditions and the soil is simulated with the Prandtl–Reuss model. The elastic second gradient law is defined by the parameters l_H and l_D. The mechanical parameters are shown in Tab. 12.2.

Table 12.2: Soil parameters for the square footing problem.

K	G_1	H_0	S_{y0}	$S_{y,min}$	l_H	l_D
[kPa]	[kPa]	[kPa]	[kPa]	[kPa]	[m]	[m]
$3.33{\cdot}10^5$	$3.45{\cdot}10^4$	-13.37	$1.41{\cdot}10^2$	$1.13{\cdot}10^2$	$4.0{\cdot}10^{-3}$	$2.0{\cdot}10^{-3}$

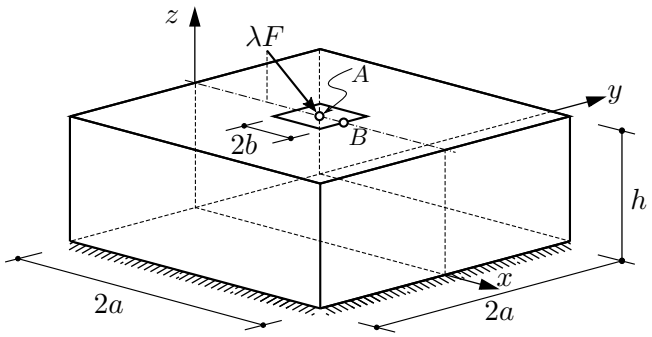

Figure 12.5: Square footing problem: a) geometry, boundary conditions and b) B-spline mesh.

The force–displacement curves at two points A and B for the two meshes are shown in Fig. 12.6. Vertical displacement at point A are larger and since it is located at the center of the footing. However, we observe that incremental vertical displacements at point B go downwards and then they start going upwards. Results with the two meshes are close but probably a further refinement will be required in order to achieve convergence of the solution with respect to the element size.

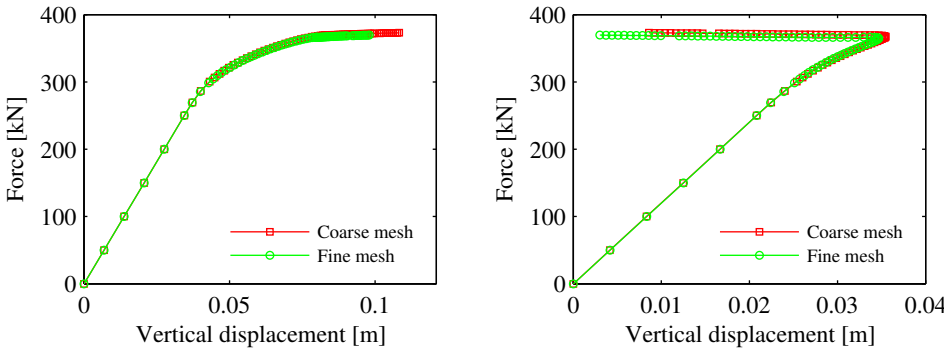

Figure 12.6: Square footing problem: vertical displacement *vs.* force at points A and B.

This becomes evident in Fig. 12.8 where the vertical displacements are plotted on the symmetry plane.

Fig. 12.8 plots the equivalent deviatoric strain for different planes along the x– and y–directions. The shear band localizes at the right edge of the square footing in the x–direction as expected. Another important aspect to highlight is the fact that the failure

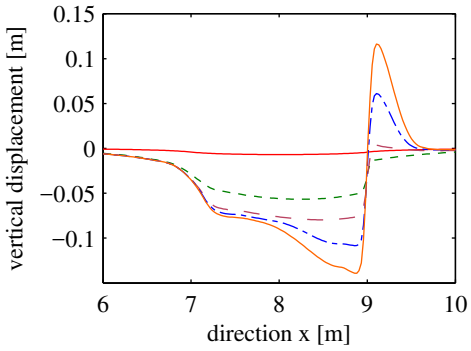

Figure 12.7: Square footing problem: vertical displacement on the symmetric plane.

mechanism is quite shallow, due to the significant inclination of the load, with a failure surface located only a few decimeters below the ground surface.

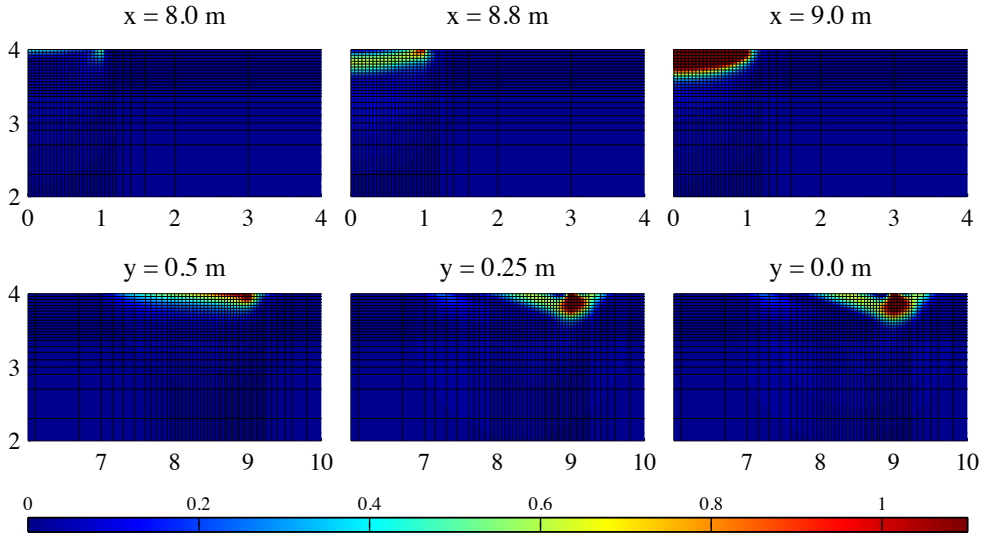

Figure 12.8: Equivalent deviatoric strain at different cut planes

Chapter 13

Multiphase modeling of consolidation problems

13.1 Strip footing on a calcarenite rock layer

A plane strain consolidation problem of a flexible strip footing on a fully saturated calcarenite rock is analyzed using the Milan model (Milan strip footing problem). Only one–half of the geometry is considered because of symmetry, as detailed in Fig. 13.1 a). The thickness of the layer is $h = 8$ m, and its extension in the horizontal direction is l =16 m. The bottom is assumed to be rigid and rough, and the lateral boundaries are constrained horizontally. A uniform pressure of w =260 kPa is applied over a footing of half–width $a = 2$ m and is increased linearly over a period of $t_0 = 0.21$ hours. Then, it remains constant during $t_f = 400$ days. Drainage is only assumed to occur on the ground surface.

Regarding the initial conditions, the internal variables controlling the size of the elastic domain are assumed equal to $p_{s0} = 200$ kPa and $p_{m0} = 200$ kPa. Only mechanical degradation effects are considered. The initial stress state is assumed to be geostatic with a preload of 30 kPa. And the at rest earth pressure coefficient is $K_0 = 0.8$. The domain is discretized into quadratic B–spline elements for the approximation of the displacement field and the pore pressure field. A mesh sensitivity study is carried out

with three meshes: 23×20 elements (coarse mesh), 43×40 elements (medium mesh) and 83×80 elements (fine mesh). The coarse mesh is described in Fig. 13.1 b), the last three column elements on the right side of the domain will not be taken into account for the mesh refinement.

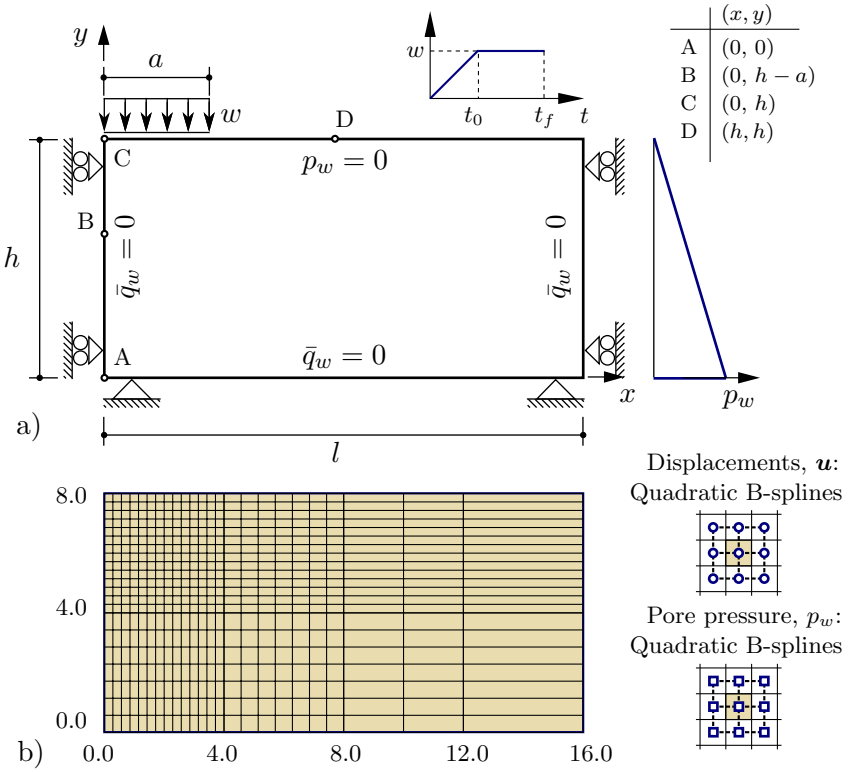

Figure 13.1: Milan strip footing problem: a) geometry, initial and boundary conditions and b) geometry discretization.

The mechanical and hydraulic parameters adopted in the simulations are presented in Tab. 13.1 and Tab. 13.2, respectively. The mechanical parameters that define the calcarenite rock are taken from Tamagnini et al. [167], whereas the second gradient effects have been modeled with the elastic parameter D^{sg}.

Fig. 13.2 shows the evolution of the normalized excess pore pressure and the normalized vertical displacement at points B and C, respectively (see Fig. 13.1). The normalized time factor T is given by the following expression:

$$T = \frac{c_{\text{ref}}\, t}{h^2} \qquad c_{\text{ref}} = \frac{p_{\text{ref}}}{\hat{\kappa}} \frac{k_{sat}}{\mu_w} \tag{13.1}$$

Table 13.1: Mechanical parameters for the Milan strip footing problem.

α	$\hat{\kappa}$	G_0	p_{ref}	ρ_s	ξ_s	ρ_m	ξ_m	k
[–]	[–]	[kPa]	[kPa]	[–]	[–]	[–]	[–]	[–]
0.0	0.0024	77000.0	200.0	16.66	0.0	20.0	10.0	0.1
a_g	m_g	M_{gc}	M_{ge}	a_f	m_f	M_{fc}	M_{fe}	D^{sg}
[–]	[–]	[–]	[–]	[–]	[–]	[–]	[–]	[kN]
0.40	0.90	0.86	0.86	0.40	0.90	0.86	0.86	1.0

Table 13.2: Hydraulic parameters for the Milan strip footing problem

ρ	ρ_{w0}	n_0	C_w	k_{sat}	μ_w
[kg/m^3]	[kg/m^3]	[–]	[kPa^{-1}]	[m^2]	[kPa·s]
2000.0	1000.0	0.41	$5.0{\cdot}10^{-7}$	$1.0{\cdot}10^{-16}$	$1.0{\cdot}10^{-6}$

Fig. 13.2 a) shows that the three FE models reproduce the Mandel–Cryer effect after the load is applied with an increase of the excess pore pressure. Then, the dissipation of the excess pore pressure is observed until $T \cong 10^{-1}$ when the excess pore pressure for the medium and the fine meshes start to increase again, reaching a local maximum and then finally dissipate. Fig. 13.2 b) also shows different results for the coarse mesh with respect to the other two meshes. When T approaches 10^{-1} a dramatic increase of the ground surface settlement is observed.

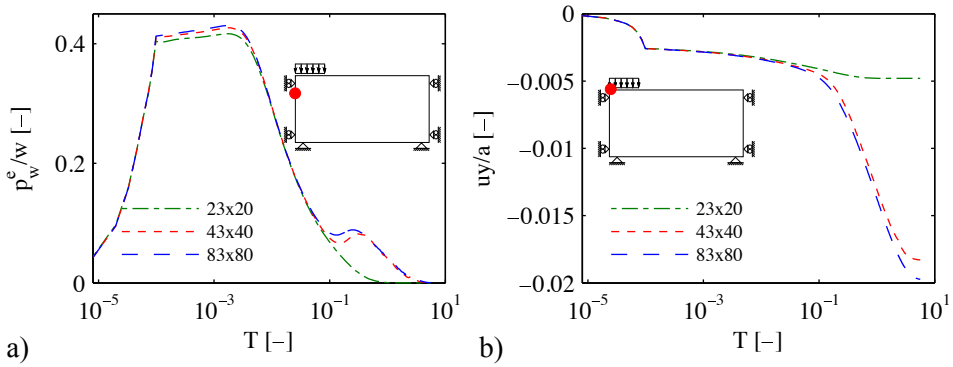

Figure 13.2: Milan strip footing problem: evolution of a) excess of pore pressure at point B and b) vertical displacement at point C.

Fig. 13.3 a) shows the evolution of the excess pore pressure along the centerline of the strip footing (segment A–C) at different time stations for the fine mesh. The excess pore pressure dissipates during the consolidation process until $T = 0.1$. Then, despite the drainage conditions imposed at the ground surface, the consolidation process near

the footing appears slower than at the bottom. Fig. 13.3 b) plots the isochrones of the surface settlements and confirms what was already observed in Fig. 13.2 b): the soft rock collapses beneath the strip footing, due to a concentration of plastic deformations, with a significant volumetric component.

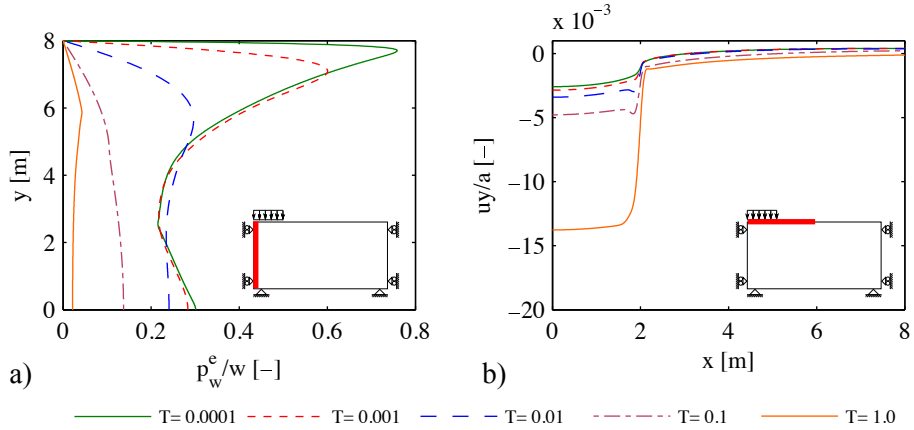

Figure 13.3: Milan strip footing problem: isochrones of a) excess pore pressure and b) vertical displacement for segments A–C and C–D, respectively.

Fig. 13.4 provides more insight on this process, by showing that the coarse mesh can not exactly reproduce the development of the shear band, which is clearly observed in the other two simulations performed with smaller elements.

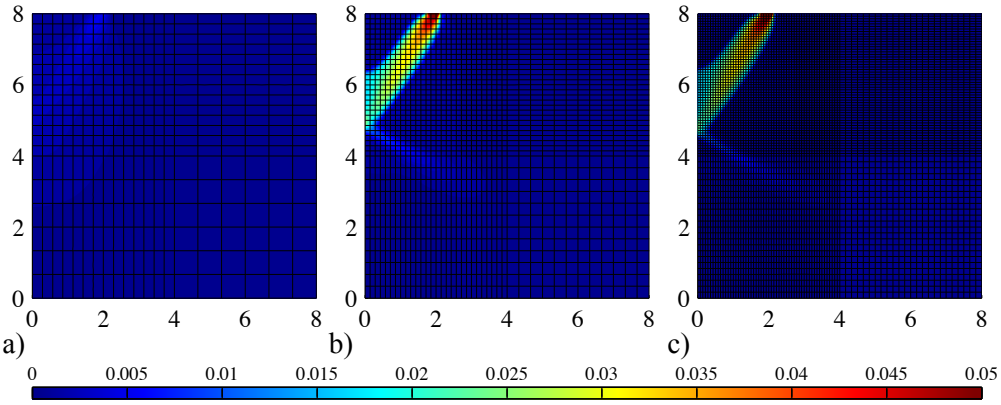

Figure 13.4: Milan strip footing problem: equivalent deviatoric strain: a) 23×20, b) 43×40 and c) 83×80 elements.

Figs. 13.4 b) and c) show that the shear band is captured by four and eight elements, respectively. Therefore, having less than four elements where high strains concentrations

develop may not be enough to properly model the strain localization phenomenon and, as consequence, the hydromechanical behavior of the strip footing under saturated conditions. From this figure, it is also clear that the soft rock layer fails due to a punching shear failure mechanism.

Fig. 13.5 shows the evolution of the internal variables p''_m and p''_s at point B. From this figure, it is possible to relate the punching shear failure mechanism to the debonding process of the highly structured soil, determined by the plastic deformations, which takes place in the zone around point B.

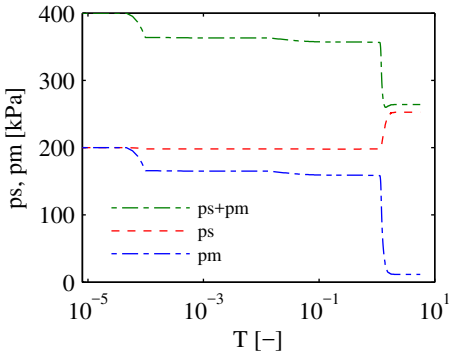

Figure 13.5: Milan strip footing problem: evolution with time of the internal variables at point B.

Figs. 13.6 and 13.7 show the excess pore pressure, volumetric strain, pore pressure and normalized vertical displacement obtained in the simulation with the fine mesh, plotted at the point B and on the segment C–D at four different time stations: $T = 0.001$, $T = 0.01$, $T = 0.1$ and $T = 1.0$.

These results show how the excess pore pressure around point A is constrained by additional excess pore pressure buildup as soon as the shear band starts to develop at the edge of the strip footing, when $T = 0.1$. Indeed, this is due to the fact that the plastic volume strains inside the band are contractant.

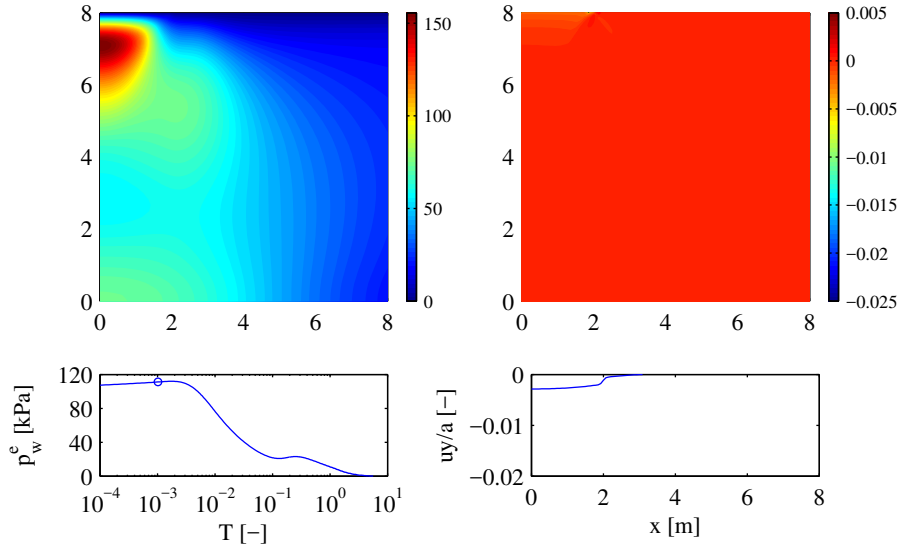

(a) $T = 0.001$

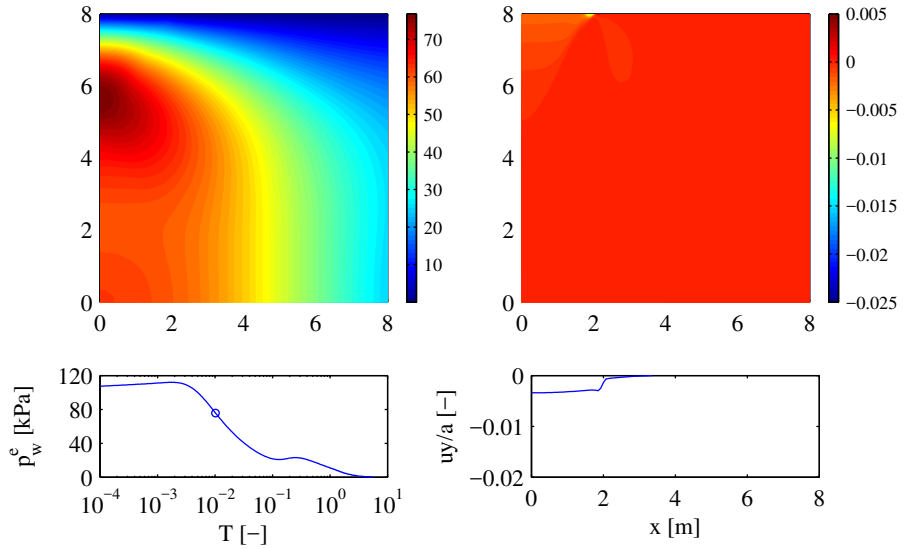

(b) $T = 0.01$

Figure 13.6: Top left: the excess pore pressure [kPa]. Top right: volumetric strain. Bottom left: excess pore pressure at point B. Bottom right: surface settlement.

13.2 Rainfall infiltration on a unsaturated slope

This example study the slope stability of an homogenous, unsaturated soil slope under rainfall infiltration. The dimensions of the domain are: $h_1 = 5$ m, $h_2 = 10$ m, $l_1 = 15$ m,

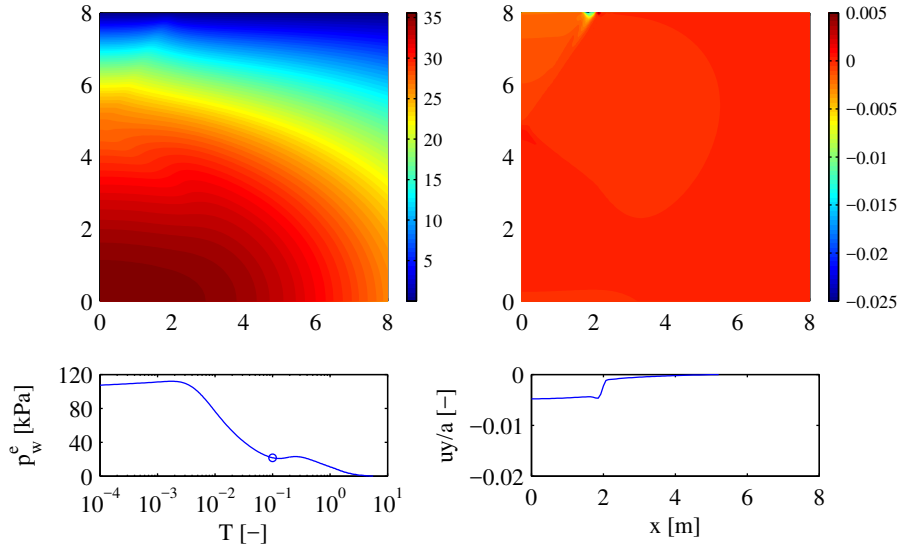

(a) $T = 0.1$

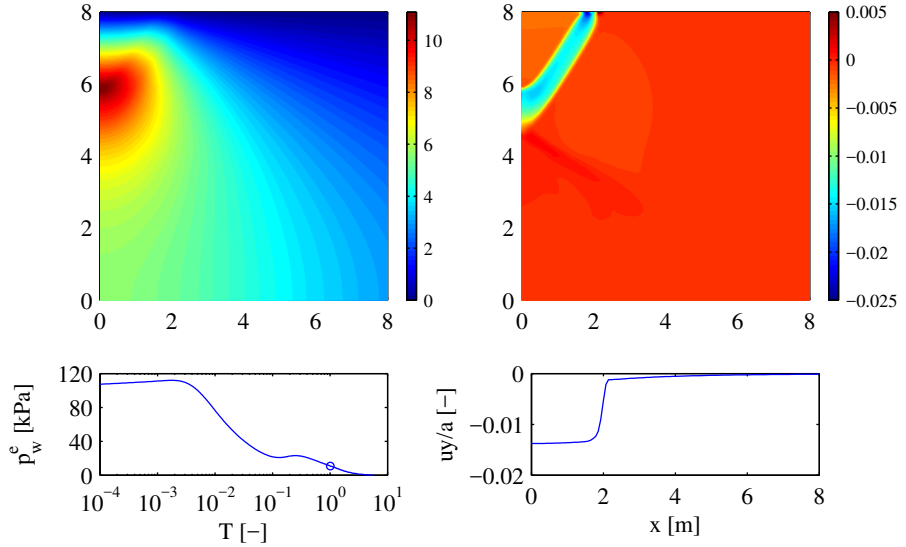

(b) $T = 1.0$

Figure 13.7: Top left: the excess pore pressure [kPa]. Top right: volumetric strain. Bottom left: excess pore pressure at point B. Bottom right: surface settlement.

$l_2 = 15$ m and $l_3 = 5$ m. The left and right boundaries are constrained in the horizontal direction and are assumed to be impervious. The bottom boundary is constrained in both vertical and horizontal directions and is assumed to be at constant hydraulic head. The water table level is assumed to be $WT = 3$ m above the bottom of the slope. The

initial pore pressure is hydrostatic with a maximum suction of 120 kPa at the top of the ground surface. The initial stress state is obtained by solving a geostatic step under the preceding initial/boundary conditions and increasing the gravity acceleration up to 9.81 m/s^2. At the end of the geostatic step, the resulting displacements and strains are reinitialized to zero. The rainfall linearly increases during the first $t_0 = 0.25$ days and lasts until $t_f = 3$ days with a constant intensity $I = 6.0$ mm/h. The initial and boundary conditions are shown in Fig. 13.8 a).

The domain is discretized with quadratic B–splines elements and so are the displacements and the pore pressure fields as depicted in Fig. 13.8 b). The mesh sensitivity study is carried out by two meshes: 64×30 (coarse mesh) and 122×60 elements (fine mesh).

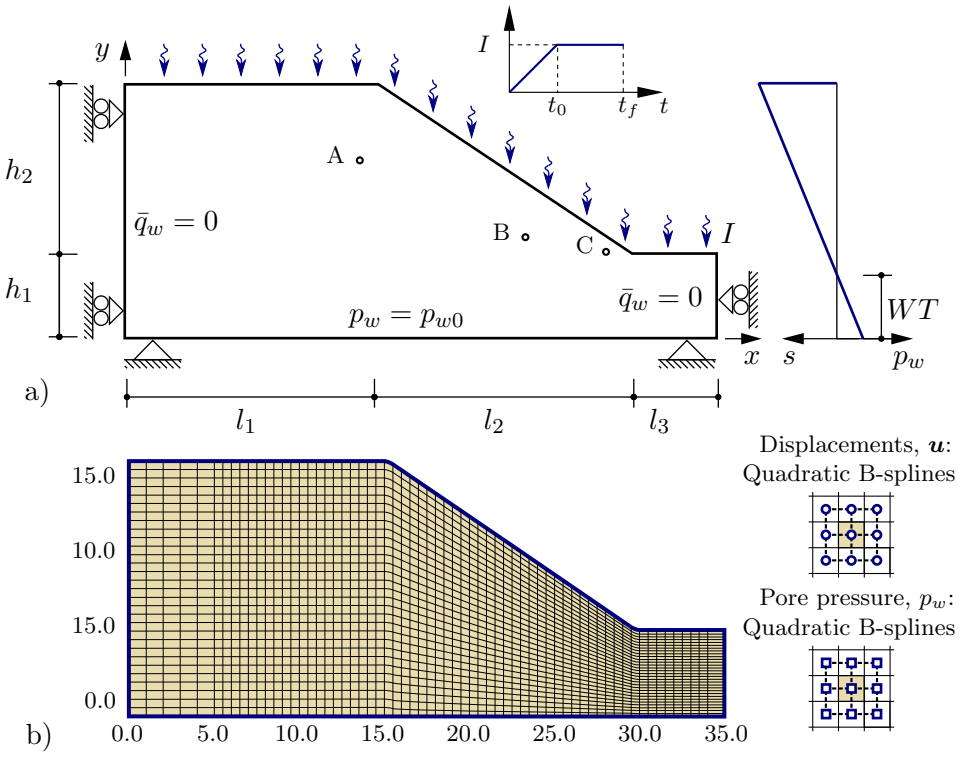

Figure 13.8: Rainfall infiltration problem: a) Geometry, initial and boundary conditions and b) geometry discretization.

The mechanical and hydraulic parameters adopted are typical of a silty soil and are listed in Tab. 13.3 and Tab. 13.4, respectively. The initial internal variable p''_{s0} is set equal to 100.0 kPa and the initial internal variable p''_{m0} is provided by the distribution

of the degree of saturation, S_w, in the slope. The hardening parameter ρ_m that controls the debonding due to mechanical effects is set to zero, therefore, the internal variable p''_m is affected only by the environmental variable S_w and its hardening parameter G_{rm}. In fully saturated conditions, the model becomes a conventional critical state model.

Table 13.3: Mechanical parameters for the rainfall infiltration problem.

α	$\hat{\kappa}$	G_0	p_{ref}	ρ_s	ξ_s	ρ_m	ξ_m	k	G_{rm}
[–]	[–]	[kPa]	[kPa]	[–]	[–]	[–]	[–]	[–]	[-]
0.0	0.0138	4334.2	100.0	13.85	0.0	0.0	0.0	0.1	20.9
a_g	m_g	M_{gc}	M_{ge}	a_f	m_f	M_{fc}	M_{fe}	D^{sg}	
[–]	[–]	[–]	[–]	[–]	[–]	[–]	[–]	[kN]	
0.40	0.90	0.86	0.68	0.40	0.90	0.86	0.68	1.0	

Table 13.4: Hydraulic parameters for the rainfall infiltration problem.

ρ	ρ_{w0}	n_0	C_w	k_{sat}	μ_w
[kg/m^3]	[kg/m^3]	[–]	[kPa^{-1}]	[m^2]	[kPa·hours]
$2.0{\cdot}10^{3}$	$1.0{\cdot}10^{3}$	0.41	$5.0{\cdot}10^{-7}$	$5.0{\cdot}10^{-13}$	$2.78{\cdot}10^{-10}$
n_{sw}	a_{sw}	m_{sw}	S_{max}	S_{res}	
[–]	[kPa^{-1}]	[–]	[–]	[–]	
1.2	$7.0{\cdot}10^{-2}$	$7.15{\cdot}10^{-1}$	1.0	0.6103	

The Van Genuchten model (see eq. (7.4)) and Mualem model (see eq. (7.9)) are adopted for the WRCC and the relative permeability function, respectively. Fig. 13.9 illustrates the relationships of the degree of saturation and permeability with suction and the evolution of the internal variable p''_m with S_r and suction, respectively.

Fig. 13.10 illustrates the evolution of the vertical and horizontal displacements during the rainfall at points A, B and C (see Fig. 13.8) for the two FE models. Both meshes yield similar results in these three critical points. Furthermore, the magnitude of both horizontal and vertical displacements, after three days of the rainfall event, are quite significant and indicate that the slope is approaching a limit equilibrium condition.

Fig. 13.11 shows the profiles of the pore pressure at three different sections of the domain. The upstream section shows a sharp wetting front after 2 hours of precipitations since the rain water infiltrates for about 1 m. Here, it is important to remark that IGA basis functions alleviate the numerical oscillations that commonly appear in the numerical

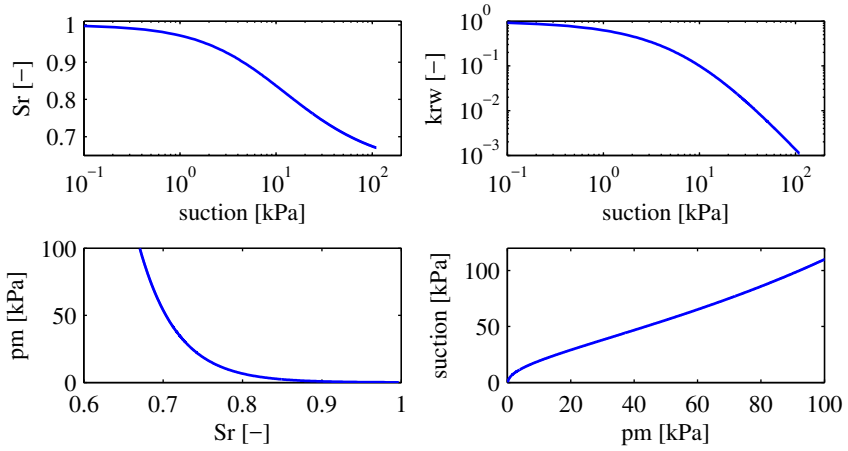

Figure 13.9: Top left: suction *vs.* degree of saturation. Top right: suction *vs.* relative permeability. Bottom left: degree of saturation *vs.* internal variable p''_m. Bottom right: internal variable p''_m *vs.* suction.

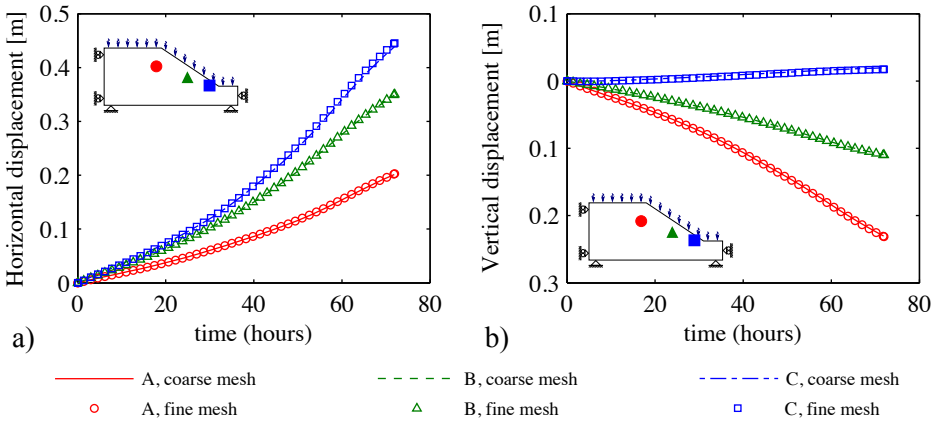

Figure 13.10: Rainfall infiltration problem: evolution of a) horizontal and b) vertical displacements at points A, B and C.

solutions with conventional FE methods when sharp wetting fronts develop under rainfall conditions.

The downstream section becomes almost fully saturated after three days, leading to an increase of the water table level, as we may expect during rainfall in real situations.

Under such conditions, it is obvious that any further rise of the water table could lead to a localized failure situation. This can be seen in Fig. 13.12 which shows the corresponding distribution of the equivalent deviatoric strain for the two simulations. No mesh

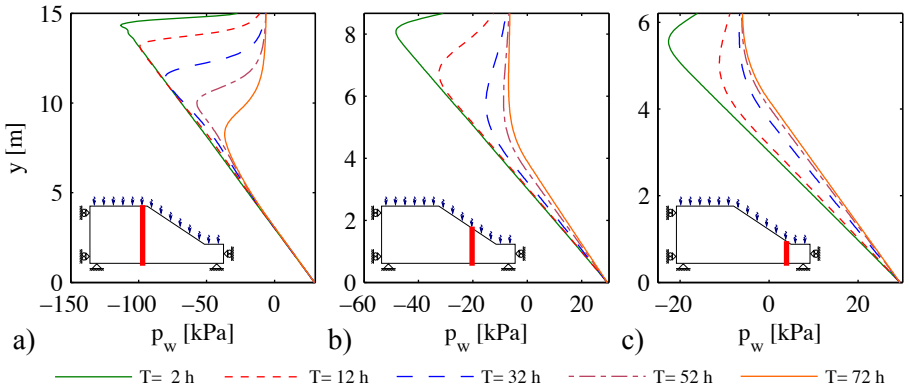

Figure 13.11: Rainfall infiltration problem: isochrones of the pore pressure at three different sections.

dependency is observed as a result of the second gradient regularization introduced by the parameter D^{sg}.

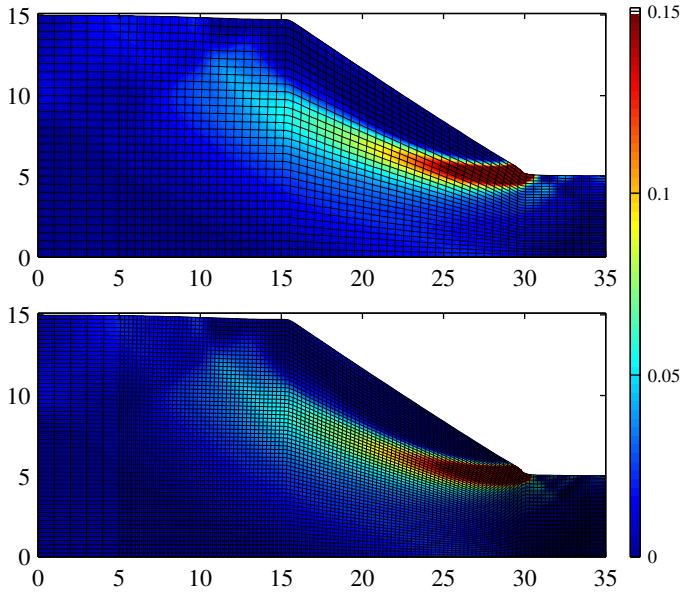

Figure 13.12: Rainfall infiltration problem: isolines of the equivalent deviatoric strain two meshes. Top: 64×30 elements. Bottom: 122×60 elements.

Fig. 13.13 shows a different view of the plastic mechanisms that are occurring in the entire domain, plotting the scalar quantity $\|\boldsymbol{\gamma}\|$ (norm of the second spatial gradient of displacement, see eq. (7.44)). To improve the readability of the figure, $\|\boldsymbol{\gamma}\|$ is plotted in log scale.

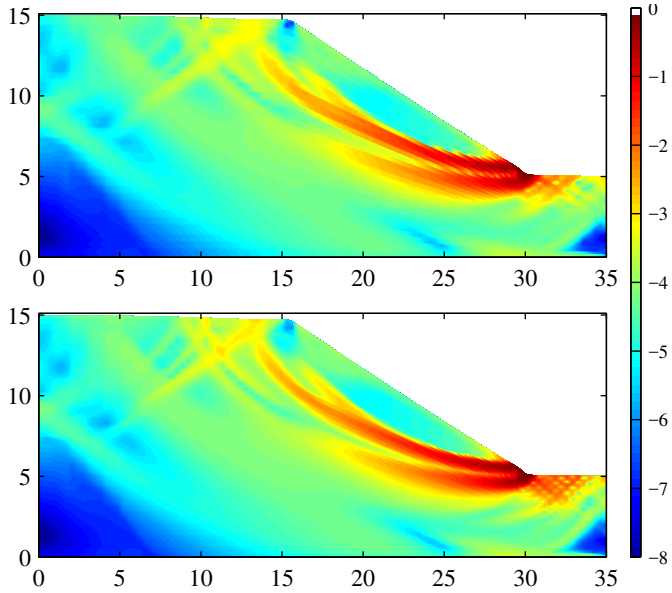

Figure 13.13: Rainfall infiltration problem: contours of the shear band given by the scalar quantity $\|\boldsymbol{\gamma}\|$ in log–scale with two meshes. Top: 64×30 elements. Bottom: 122×60 elements.

Figs. 13.14 and 13.15 illustrate the equivalent deviatoric strain, the degree of saturation, the equivalent deviatoric strain at points A and B, and the internal variable p_m'' at points A and B at four different times stations: $t = 12$ hours, $t = 32$ hours, $t = 52$ hours and $t = 72$ hours. We observe that the water table level starts to gradually rise below the toe and the slope (between 5 and 30 in the x–coordinates). According to the suction hardening mechanism incorporated in the model, the water infiltration may cause the loss of stability of the slope, due to the degradation of the suction–induced bonding effect. This can be observed from the time evolution of the internal variable p_m''. The debonding process is responsible for the triggering of the shear band which starts at the toe of the slope and then progresses upwards until it is almost fully developed at $t = 72$ h.

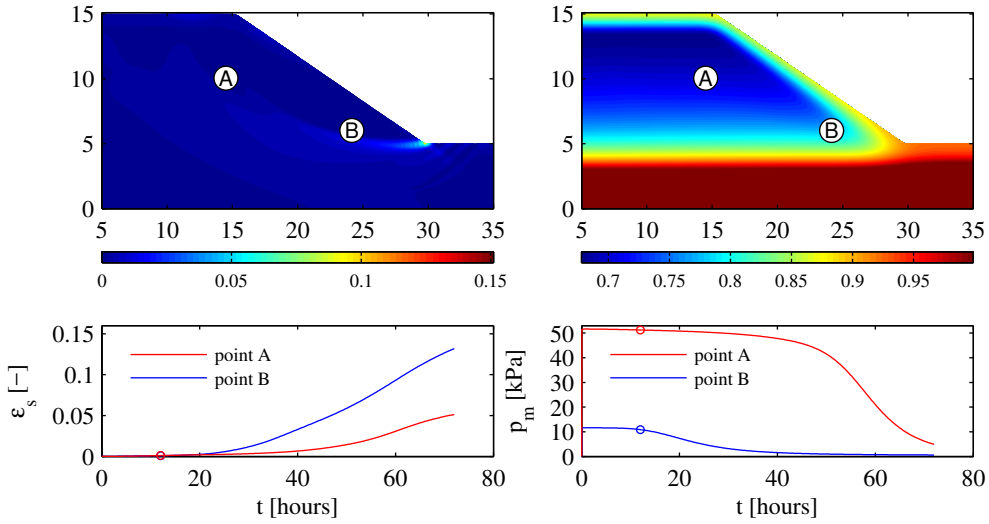

(a) $t = 12$ hours

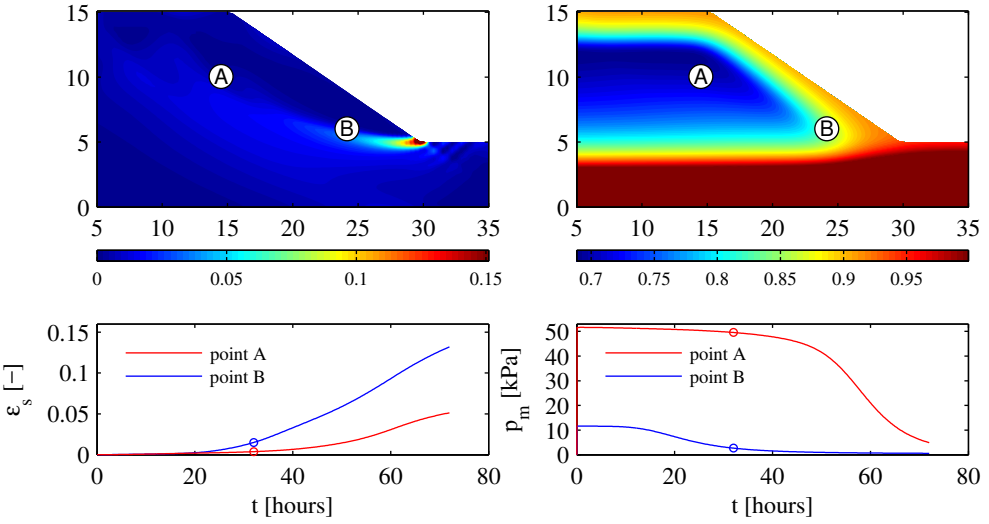

(b) $t = 32$ hours

Figure 13.14: Top left: equivalent deviatoric strain. Top right: degree of saturation [-]. Bottom left: equivalent deviatoric strain at points A and B. Bottom right: internal variable p_m'' at points A and B.

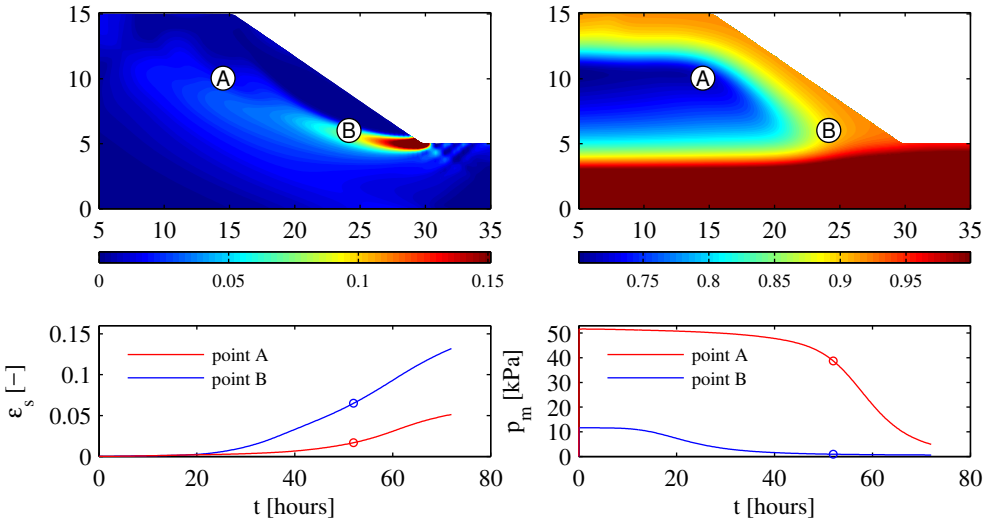

(a) $t = 52$ hours

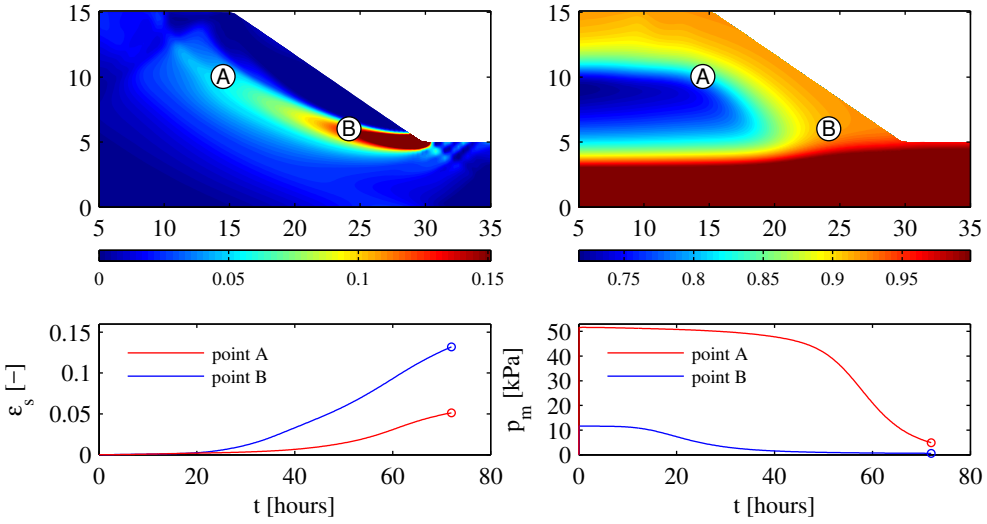

(b) $t = 72$ hours

Figure 13.15: Top left: equivalent deviatoric strain. Top right: degree of saturation [-]. Bottom left: equivalent deviatoric strain at points A and B. Bottom right: internal variable p''_m at points A and B.

Part IV

Conclusions and suggestions for further studies

Chapter 14

Concluding remarks and future work

14.1 Conclusions

In this work, IGA–FEM formulation of coupled hydromechanical problems for geomechanics applications was implemented in the open source code GeoPDEs. Benchmark problems were solved in order to validate the numerical implementation. Good agreement between the analytical and the numerical results were obtained. The regularization technique consisting in a second gradient model based on micromorphic continuum mechanics was also implemented in order to remove the pathological mesh dependence of conventional FE solutions in presence of strain localization. To demonstrate the capabilities of the IGA–FEM implementation, several geotechnical problems were analyzed for monophasic and biphasic media, the latter under both fully and partially saturated conditions.

The results obtained demonstrated that the model is able to capture the strong hydromechanical coupling occurring if a realistic constitutive model for the solid skeleton, capable of modeling correctly dilatancy and bond degradation is adopted. The implicit high continuity between elements and the smoothness properties of IGA basis functions helped in this respect, since geotechnical problems are typically characterized by strong

multiphysics couplings, highly nonlinear behavior of the soil, strongly localized displacement fields and high pore pressure gradients.

The contributions of this work can be summarized as follows:

- The IGA–FEM formulation has been proven an efficient approach in order to implement second gradient models since it allows a straightforward implementation with a significant reduction of degrees of freedom and computational time with respect to other implementation strategies.
- The classical constitutive equation for the solid skeleton has been extended in order to account for environmental effects in terms of the variability in the degree of saturation. These effects have been considered in the analysis of a slope stability problem under rainfall conditions. The results have demonstrated that the wetting process due to rainfall infiltration can trigger the shear localization that is responsible for the failure of the slope.
- Two improvements have been made in the second gradient constitutive law. First, an hyperelastic constitutive relation have been proposed which introduces two internal length scales related to the deviatoric and volumetric parts suitable for two and three dimensional problems. A three dimensional boundary value problem has been considered in order to study the localization patterns under undrained conditions with good results in terms of mesh dependency. And finally, an elastoplastic second gradient constitutive law with linear and exponential hardening laws has been proposed in order to improve the description of the evolution of the shear band width as shear strains increase.

14.2 Future work

Three main research lines are suggested in order to improve the work presented here and to spread the range of applications for more general engineering problems. First, The IGA–FEM formulation can take advantages of new IGA capabilities already available in the literature: local refinement and multipatch geometries. Generally, failure mechanisms can not be predicted in large scale geotechnical engineering problems and

homogeneous meshes are not efficient in terms of computational time. The GeoPDEs software package provides the option of use adaptive refinement based on hierarchical B–splines. This improvement will allow to apply local refinement only in the zone with high strains, such as shear bands, as the simulation progresses. Multipatch geometries will allow the applicabilities of IGA in terms of more complex geometries and boundaries conditions.

Second, theoretical, numerical and possibly experimental investigations of the link between shear band size and the elastoplastic second gradient constants should be carried out.

Regarding the IGA–FEM formulation, the extension of the small strain framework to finite deformations is of extreme importance. Strain localization implies large deformations resulting in severely distorted meshes. Under such conditions, the infinitesimal deformation approach is no longer valid. A fully unsaturated description for the porous media mechanics accounting for the gas phase is also fundamental in a wide range of geotechnical problems the influence of the gas flow cannot be neglected.

Bibliography

[1] Aifantis, E. C. (1984). On the microstructural origin of certain inelastic models. *ASME J. Eng. Mater. Technol*, 106(4):326–330.

[2] Alonso, E. E., Gens, A., and Josa, A. (1990). A constitutive model for partially saturated soils. *Géotechnique*, 40(3):405–430.

[3] Amanatidou, E. and Aravas, N. (2002). Mixed finite element formulations of strain-gradient elasticity problems. *Computer Methods in Applied Mechanics and Engineering*, 191(15):1723–1751.

[4] Andò, E. (2013). *Experimental investigation of microstructural changes in deforming granular media using x-ray tomography*. PhD thesis, Université Grenoble Alpes.

[5] Areias, P. M. A. and Belytschko, T. (2006). Two-scale shear band evolution by local partition of unity. *Int. J. Numer. Meth. Engng.*, 66(5):878–910.

[6] Argilaga, A. (2016). *Approche double échelle de type FEMxDEM avec régularization second gradient pour la modélisation des géomatériaux*. PhD thesis, Grenoble Alpes.

[7] Aristodemo, M. (1985). A high-continuity finite element model for two-dimensional elastic problems. *Computers & Structures*, 21(5).

[8] Armero, F. and Callari, C. (1999). An analysis of strong discontinuities in a saturated poro-plastic solid. *International journal for numerical methods in engineering*, 46(10):1673–1698.

[9] Armero, F. and Garikipati, K. (1995). Recent advances in the analysis and numerical simulation of strain localization in inelastic solids. *Computational Plasticity Fundamentals and Applications. I*, pages 547–561.

[10] Askes, H. and Gutiérrez, M. A. (2006). Implicit gradient elasticity. *Int. J. Numer. Meth. Engng.*, 67(3):400–416.

[11] Auricchio, F., Calabrò, F., Hughes, T. J. R., Reali, A., and Sangalli, G. (2012). A simple algorithm for obtaining nearly optimal quadrature rules for NURBS-based isogeometric analysis. *Comp. Methods Appl. Mech. Engrg.*, 249–252:15–27.

[12] Barrett, R., Berry, M. W., Chan, T. F., Demmel, J., Donato, J., Dongarra, J., Eijkhout, V., Pozo, R., Romine, C., and Van der Vorst, H. (1994). *Templates for the solution of linear systems: building blocks for iterative methods*, volume 43. Siam.

[13] Bažant, Z. P., Belytschko, T. B., and Chang, T.-P. (1984). Continuum theory for strain-softening. *Journal of Engineering Mechanics*, 110(12):1666–1692.

[14] Bazant, Z. P., Lin, F., and Pijaudier-Cabot, G. (1987). Yield limit degradation: non-local continuum model with local strain. In *Proc. Int. Conf. Computational Plasticity, Barcelona*, pages 1757–1780.

[15] Bazilevs, Y., Beirão Da Veiga, L., Cottrell, J. A., Hughes, T. J. R., and Sangalli, G. (2006). Isogeometric analysis: approximation, stability and error estimates for h-refined meshes. *Math. Models Methods Appl. Sci.*, 16(07):1031–1090.

[16] Beer, G. (2015). *Advanced Numerical Simulation Methods: From CAD Data Directly to Simulation Results*. CRC Press, Boca Raton.

[17] Belytschko, T. and Black, T. (1999). Elastic crack growth in finite elements with minimal remeshing. *Int. J. Numer. Meth. Engng.*, 45(5):601–620.

[18] Bésuelle, P. (1999). *Déformation et rupture dans les roches tendres et les sols indurés : comportement homogène et localisation*. phdthesis, Université Joseph-Fourier - Grenoble I.

[19] Bésuelle, P., Chambon, R., and Collin, F. (2006). Switching deformation modes in post-localization solutions with a quasibrittle material. *JOMMS*, 1(7):1115–1134.

[20] Bésuelle, P., Desrues, J., and Raynaud, S. (2000). Experimental characterisation of the localisation phenomenon inside a Vosges sandstone in a triaxial cell. *International Journal of Rock Mechanics and Mining Sciences*, 37(8):1223–1237.

[21] Bésuelle, P. and Rudnicki, J. W. (2004). Localization: shear bands and compaction bands. In *Mechanics of Fluid-Saturated Rocks*, volume 89, pages 219–321. Academic Press, Elsevier.

[22] Bigoni, D. and Hueckel, T. (1991a). Uniqueness and localization—I. Associative and non-associative elastoplasticity. *International Journal of Solids and Structures*, 28(2):197–213.

[23] Bigoni, D. and Hueckel, T. (1991b). Uniqueness and localization—II. Coupled elastoplasticity. *International Journal of Solids and Structures*, 28(2):215–224.

[24] Biot, M. A. (1941). General Theory of Three-Dimensional Consolidation. *Journal of Applied Physics*, 12(2):155–164.

[25] Bishop, A. W. (1959). The principle of effective stress. *Teknisk ukeblad*, 39:859–863.

[26] Borja, R. I. (2000). A finite element model for strain localization analysis of strongly discontinuous fields based on standard galerkin approximation. *Computer Methods in Applied Mechanics and Engineering*, 190(11):1529–1549.

[27] Borja, R. I. (2002). Finite element simulation of strain localization with large deformation: Capturing strong discontinuity using a Petrov-Galerkin multiscale formulation. *Comp. Methods Appl. Mech. Engrg.*, 191:2949–2978.

[28] Borja, R. I. (2008). Assumed enhanced strain and the extended finite element methods: A unification of concepts. *Computer Methods in Applied Mechanics and Engineering*, 197(33):2789–2803.

[29] Bowen, R. M. (1980). Incompressible porous media models by use of the theory of mixtures. *International Journal of Engineering Science*, 18(9):1129–1148.

[30] Brinkgreve, R. B. J. (1994). *Geomaterial Models and Numerical Analysis of Softening*. PhD thesis, Delt University of Technology.

[31] Butterfield, R., Harkness, R., and Andrews, K. (1970). A stero-photogrammetric method for measuring displacement fields. *Geotechnique*, 20(3):308–314.

[32] Callari, C., Armero, F., and Abati, A. (2010). Strong discontinuities in partially saturated poroplastic solids. *Computer Methods in Applied Mechanics and Engineering*, 199(23):1513–1535.

[33] Calvetti, F., Combe, G., and Lanier, J. (1997). Experimental micromechanical analysis of a 2d granular material: relation between structure evolution and loading path. *Mechanics of Cohesive-frictional Materials*, 2(2):121–163.

[34] Chambon, R. (2000). Uniqueness, second order work and bifurcation in hypoplasticity. In *Constitutive Modelling of Granular Materials*, pages 147–165. Springer.

[35] Chambon, R., Caillerie, D., and El Hassan, N. (1998). One-dimensional localisation studied with a second grade model. *Eur. J. of Mec. - A/Solids*, 17(4):637–656.

[36] Chambon, R., Caillerie, D., and Matsushima, T. (2001a). Plastic continuum with microstructure, local second gradient theories for geomaterials: localization studies. *International Journal of Solids and Structures*, 38(46–47):8503–8527.

[37] Chambon, R., Caillerie, D., and Tamagnini, C. (2001b). A finite deformation second gradient theory of plasticity. *Comptes Rendus de l'Académie des Sciences - Series IIB - Mechanics*, 329(11):797–802.

[38] Chambon, R., Caillerie, D., and Tamagnini, C. (2004). A strain space gradient plasticity theory for finite strain. *Computer Methods in Applied Mechanics and Engineering*, 193(27–29):2797–2826.

[39] Chambon, R., Crochepeyre, S., and Charlier, R. (2001c). An algorithm and a method to search bifurcation points in non-linear problems. *Int. J. Numer. Meth. Engng.*, 51(3):315–332.

[40] Charlier, R. (1987). *Approche unifiée de quelques problèmes non linéaires de mécanique des milieux continus par la méthode des éléments finis (grandes déformations des métaux et des sols, contact unilatéral de solides, conduction thermique et écoulements en milieu poreux)*. PhD thesis, Université de Liège.

[41] Chu, T., Ranson, W., and Sutton, M. A. (1985). Applications of digital-image-correlation techniques to experimental mechanics. *Experimental mechanics*, 25(3):232–244.

[42] Collier, N., Pardo, D., Dalcin, L., Paszynski, M., and Calo, V. M. (2012). The cost of continuity: A study of the performance of isogeometric finite elements using direct solvers. *Comp. Methods Appl. Mech. Engrg.*, 213–216:353–361.

[43] Collin, F. (2003). *Couplages thermo-hydro-mécaniques dans les sols et les roches tendres partiellement saturés*. PhD thesis, Université de Liège,? Liège,?? Belgique.

[44] Collin, F., Chambon, R., and Charlier, R. (2006). A finite element method for poro mechanical modelling of geotechnical problems using local second gradient models. *Int. J. Numer. Meth. Engng.*, 65(11):1749–1772.

[45] Cottrell, J. A., Hughes, T. J. R., and Bazilevs, Y. (2009). *Isogeometric Analysis: Toward Integration of CAD and FEA*. Wiley, Chichester, West Sussex, U.K. ; Hoboken, NJ.

[46] Cox, M. G. (1972). The Numerical Evaluation of B-Splines. *IMA J Appl Math*, 10(2):134–149.

[47] Crisfield, M. (1981). A fast incremental/iterative solution procedure that handles "snap-through". *Computers & Structures*, 13(1-3):55–62.

[48] Daneshyar, A. and Mohammadi, S. (2013). Strong tangential discontinuity modeling of shear bands using the extended finite element method. *Comput Mech*, 52(5):1023–1038.

[49] de Boor, C. (1972). On calculating with B-splines. *Journal of Approximation Theory*, 6(1):50–62.

[50] De Borst, R., Crisfield, M., and Remmers, J. J. C. (2012). *Nonlinear Finite Element Analysis of Solids and Structures*. Wiley, 2nd edition.

[51] de Falco, C., Reali, A., and Vázquez, R. (2011). GeoPDEs: A research tool for Isogeometric Analysis of PDEs. *Advances in Engineering Software*, 42(12):1020–1034.

[52] Desrues, J. (1984). *La localisation de la déformation dans les matériaux granulaires*. PhD thesis, Université Joseph-Fourier - Grenoble I.

[53] Desrues, J. and Chambon, R. (1989). Shear band analysis for granular materials: the question of incremental non-linearity. *Archive of Applied Mechanics*, 59(3):187–196.

[54] Desrues, J., Chambon, R., Mokni, M., and Mazerolle, F. (1996). Void ratio evolution inside shear bands in triaxial sand specimens studied by computed tomography. *Géotechnique*, 46(3):529–546.

[55] Desrues, J., Lanier, J., and Stutz, P. (1985). Localization of the deformation in tests on sand sample. *Engineering fracture mechanics*, 21(4):909–921.

[56] Desrues, J. and Viggiani, G. (2004). Strain localization in sand: an overview of the experimental results obtained in Grenoble using stereophotogrammetry. *International Journal for Numerical and Analytical Methods in Geomechanics*, 28(4):279–321.

[57] Díez, P., Arroyo, M., and Huerta, A. (2000). Adaptivity based on error estimation for viscoplastic softening materials. *Mech. Cohes.-Frict. Mater.*, 5(2):87–112.

[58] Dokken, T., Lyche, T., and Pettersen, K. F. (2013). Polynomial splines over locally refined box-partitions. *Computer Aided Geometric Design*, 30(3):331–356.

[59] Ehlers, W. and Volk, W. (1998). On theoretical and numerical methods in the theory of porous media based on polar and non-polar elasto-plastic solid materials. *International Journal of Solids and Structures*, 35(34):4597–4617.

[60] Engelen, R. A., Geers, M. G., and Baaijens, F. P. (2003). Nonlocal implicit gradient-enhanced elasto-plasticity for the modelling of softening behaviour. *International journal of Plasticity*, 19(4):403–433.

[61] Farin, G. (2002). *Curves and Surfaces for CACD. A Practical Guide*. Computer Graphics and Geometric Modeling. Morgan-Kaufmann, 5th edition.

[62] Fernandes, R., Chavant, C., and Chambon, R. (2008). A simplified second gradient model for dilatant materials: Theory and numerical implementation. *International Journal of Solids and Structures*, 45(20):5289–5307.

[63] Fernandes, R., Ducoin, B., and Chambon, R. (2011). 2d and 3d Modelling of Geomaterials Using a Second Gradient Dilation Model. In *Advances in Bifurcation and Degradation in Geomaterials*, Springer Series in Geomechanics and Geoengineering, pages 209–218. Springer, Dordrecht.

[64] Finno, R., Harris, W., Mooney, M. A., and Viggiani, G. (1997). Shear bands in plane strain compression of loose sand. *Geotechnique*, 47(1):149–165.

[65] Fleck, N. A. and Hutchinson, J. W. (1997). Strain gradient plasticity. *Adv. Appl. Mech.*, 33:296–361.

[66] Forsey, D. R. and Bartels, R. H. (1988). Hierarchical B-spline Refinement. In *Proceedings of the 15th Annual Conference on Computer Graphics and Interactive Techniques*, SIGGRAPH '88, pages 205–212, New York, NY, USA. ACM.

[67] Gallipoli, D., Gens, A., Sharma, R., and Vaunat, J. (2003). An elasto-plastic model for unsaturated soil incorporating the effects of suction and degree of saturation on mechanical behaviour. *Géotechnique*, 53(1):123–136.

[68] Garau, E. M. and Vázquez, R. (2018). Algorithms for the implementation of adaptive isogeometric methods using hierarchical B-splines. *Applied Numerical Mathematics*, 123(Supplement C):58–87.

[69] Garcia, D., Pardo, D., Dalcin, L., Paszyński, M., Collier, N., and Calo, V. M. (2017). The value of continuity: Refined isogeometric analysis and fast direct solvers. *Computer Methods in Applied Mechanics and Engineering*, 316:586–605.

[70] Garikipati, K. R. (1996). *On strong discontinuities in inelastic solids and their numerical simulation.* PhD thesis, Stanford University.

[71] Georgiadis, K. (2003). *Development, Implementation and Application of Partially Saturated Soil Models in Finite Element Analysis.* Ph.D. Thesis, Imperial College of Science, Technology and Medicine.

[72] Germain, P. (1973a). La méthode des puissances virtuelles en mécanique des milieux continus: Première partie: théorie du second gradient. *J. Mécanique*, 12:235 –274.

[73] Germain, P. (1973b). The method of virtual power in continuum mechanics. Part 2: Microstructure. *SIAM Journal on Applied Mathematics*, 25(3):556–575.

[74] Gibson, R. E., Schiffman, R. L., and Pu, S. L. (1970). Plane Strain and Axially Symmetric Consolidation of a Clay Layer on a Smooth Impervious Base. *Q J Mechanics Appl Math*, 23(4):505–520.

[75] Gordon, W. J. and Hall, C. A. (1973). Transfinite element methods: blending-function interpolation over arbitrary curved element domains. *Numerische Mathematik*, 21(2):109–129.

[76] Gordon, W. J. and Thiel, L. C. (1982). Transfinite mappings and their application to grid generation. *Applied Mathematics and Computation*, 10:171–233.

[77] Hall, S., Bornert, M., Desrues, J., Pannier, Y., Lenoir, N., Viggiani, G., and Bésuelle, P. (2010). Discrete and continuum analysis of localised deformation in sand using X-ray μCT and volumetric digital image correlation. *Géotechnique*, 60(5):315–322.

[78] Han, C. and Vardoulakis, I. (1991). Plane-strain compression experiments on water-saturated fine-grained sand. *Geotechnique*, 41(1):49–78.

[79] Hasan, A. and Alshibli, K. (2010). Experimental assessment of 3d particle-to-particle interaction within sheared sand using synchrotron microtomography. *Géotechnique*, 60(5):369–379.

[80] Hassanizadeh, M. and Gray, W. G. (1979a). General conservation equations for multi-phase systems: 1. Averaging procedure. *Advances in Water Resources*, 2:131–144.

[81] Hassanizadeh, M. and Gray, W. G. (1979b). General conservation equations for multi-phase systems: 2. Mass, momenta, energy, and entropy equations. *Advances in Water Resources*, 2:191–203.

[82] Higo, Y., Oka, F., Kimoto, S., Sanagawa, T., and Matsuhima, Y. (2011a). Observation of microstructural changes and strain localization of unsaturated sands using Microfocus X-ray CT. In *Advances in Bifurcation and Degradation in Geomaterials*, pages 37–43. Springer.

[83] Higo, Y., Oka, F., Kimoto, S., Sanagawa, T., and Matsushima, Y. (2011b). Study of strain localization and microstructural changes in partially saturated sand during triaxial tests using microfocus X-ray CT. *Soils and foundations*, 51(1):95–111.

[84] Higo, Y., Oka, F., Sato, T., Matsushima, Y., and Kimoto, S. (2013). Investigation of localized deformation in partially saturated sand under triaxial compression using microfocus X-ray CT with digital image correlation. *Soils and Foundations*, 53(2):181–198.

[85] Hill, R. (1950). *The Mathematical Theory of Plasticity*. Oxford University Press.

[86] Hill, R. and Hutchinson, J. W. (1975). Bifurcation phenomena in the plane tension test. *Journal of the Mechanics and Physics of Solids*, 23(4):239–264.

[87] Höllig, K. (2003). *Finite Element Methods with B-Splines*. Frontiers in Applied Mathematics. Society for Industrial and Applied Mathematics.

[88] Hounsfield, G. N. (1975). *Method of and apparatus for examining a body by radiation such as X or gamma radiation*. Google Patents.

[89] Hughes, T. J. R., Cottrell, J. A., and Bazilevs, Y. (2005). Isogeometric analysis: CAD, finite elements, NURBS, exact geometry and mesh refinement. *Comp. Methods Appl. Mech. Engrg.*, 194(39–41):4135–4195.

[90] Hughes, T. J. R., Reali, A., and Sangalli, G. (2010). Efficient quadrature for NURBS-based isogeometric analysis. *Comp. Methods Appl. Mech. Engrg.*, 199(5–8):301–313.

[91] Irzal, F., Remmers, J. J. C., Verhoosel, C. V., and de Borst, R. (2013). Isogeometric finite element analysis of poroelasticity. *Int. J. Numer. Anal. Meth. Geomech.*, 37(12):1891–1907.

[92] Jennings, J. E. B. and Burland, J. B. (1962). Limitations to the Use of Effective Stresses in Partly Saturated Soils. *Géotechnique*, 12(2):125–144.

[93] Jirásek, M. (2002a). Numerical modeling of strong discontinuities. *Revue française de génie civil*, 6(6):1133–1146.

[94] Jirásek, M. (2002b). Objective modeling of strain localization. *Revue française de génie civil*, 6(6):1119–1132.

[95] Johannessen, K. A., Kvamsdal, T., and Dokken, T. (2014). Isogeometric analysis using LR B-splines. *Computer Methods in Applied Mechanics and Engineering*, 269(Supplement C):471–514.

[96] Jommi, C. and Di Prisco, C. (1994). A simple theoretical approach for modelling the mechanical behaviour of unsaturated soils. In *Il ruolo dei fluidi nei problemi di Ingegneria geotecnica; Proc. Italian Conference*, volume 1, pages 167–188.

[97] Kagan, P., Fischer, A., and Bar-Yoseph, P. Z. (1998). New B-spline finite element approach for geometrical design and mechanical analysis. *International Journal for Numerical Methods in Engineering*, 41(3):435–458.

[98] Khalili, N. and Khabbaz, M. (1998). A unique relationship of chi for the determination of the shear strength of unsaturated soils. *Geotechnique*, 48(5).

[99] Khoei, A. R. and Haghighat, E. (2011). Extended finite element modeling of deformable porous media with arbitrary interfaces. *Applied Mathematical Modelling*, 35(11):5426–5441.

[100] Khoei, A. R. and Karimi, K. (2008). An enriched-FEM model for simulation of localization phenomenon in Cosserat continuum theory. *Computational Materials Science*, 44(2):733–749.

[101] Kim, J.-M. (2000). A fully coupled finite element analysis of water-table fluctuation and land deformation in partially saturated soils due to surface loading. *Int. J. Numer. Meth. Engng.*, 49(9):1101–1119.

[102] Kolymbas, D. (1981). Bifurcation analysis for sand samples with a non-linear constitutive equation. *Archive of Applied Mechanics*, 50(2):131–140.

[103] Lagioia, R., Puzrin, A. M., and Potts, D. M. (1996). A new versatile expression for yield and plastic potential surfaces. *Computers and Geotechnics*, 19(3):171–191.

[104] Lanatà, P. (2015). *Full-field experimental characterization of mechanical behaviour and failure in a porous rock in plane strain compression : homogeneous deformation and strain localization.* Theses, Université Grenoble Alpes.

[105] Lazari, M. (2016). *Finite Element Regularization for Post Localized Bifurcation in Variably Saturated Media.* PhD thesis, Università degli Studi di Padova.

[106] Lenoir, N., Bornert, M., Desrues, J., Bésuelle, P., and Viggiani, G. (2007). Volumetric digital image correlation applied to X-ray microtomography images from triaxial compression tests on argillaceous rock. *Strain*, 43(3):193–205.

[107] Lewis, R. W. and Schrefler, B. A. (1998). *The Finite Element Method in the Static and Dynamic Deformation and Consolidation of Porous Media, 2nd Edition.* Wiley, Chichester ; New York, 2 edition edition.

[108] Liakopoulos, A. C. (1964). *Transient flow through unsaturated porous media.* PhD thesis, University of California, Berkeley.

[109] Liu, P. (2015). Extended finite element method for strong discontinuity analysis of strain localization of non-associative plasticity materials. *International Journal of Solids and Structures*, 72(Supplement C):174–189.

[110] Loret, B. and Prevost, J. (1991). Dynamic strain localization in fluid-saturated porous media. *Journal of Engineering Mechanics*, 117(4):907–922.

[111] Lu, N. and Likos, W. J. (2004). *Unsaturated Soil Mechanics.* Wiley, Hoboken, N.J, 1 edition edition.

[112] Marinelli, F. (2013). *Comportement couplé des géo-matériaux : deux approches de modélisation numérique.* Ph.D., Université de Grenoble.

[113] Marussig, B., Zechner, J., Beer, G., and Fries, T.-P. (2014). Fast Isogeometric Boundary Element Method based on Independent Field Approximation. *Computer Methods in Applied Mechanics and Engineering*, 284.

[114] Matsushima, T., Chambon, R., and Caillerie, D. (2000). Second gradient models as a particular case of microstructured models: a large strain finite elements analysis. *Comptes Rendus de l'Académie des Sciences - Series IIB - Mechanics-Physics-Astronomy*, 328(2):179–186.

[115] Matsushima, T., Chambon, R., and Caillerie, D. (2002). Large strain finite element analysis of a local second gradient model: application to localization. *Int. J. Numer. Meth. Engng.*, 54(4):499–521.

[116] Matsushima, T., Saomoto, H., Tsubokawa, Y., and Yamada, Y. (2003). Grain rotation versus continuum rotation during shear deformation of granular assembly. *Soils and foundations*, 43(4):95–106.

[117] Melenk, J. M. and Babuška, I. (1996). The partition of unity finite element method: basic theory and applications. *Computer methods in applied mechanics and engineering*, 139(1-4):289–314.

[118] Mindlin, R. D. (1964). Micro-structure in linear elasticity. *Arch. Rational Mech. Anal.*, 16(1):51–78.

[119] Mindlin, R. D. (1965). Second gradient of strain and surface-tension in linear elasticity. *International Journal of Solids and Structures*, 1(4):417–438.

[120] Mohammadnejad, T. and Khoei, A. R. (2013). An extended finite element method for fluid flow in partially saturated porous media with weak discontinuities; the convergence analysis of local enrichment strategies. *Comput Mech*, 51(3):327–345.

[121] Mualem, Y. (1976). A new model for predicting the hydraulic conductivity of unsaturated porous media. *Water Resour. Res.*, 12(3):513–522.

[122] Mühlhaus, H. and Vardoulakis, I. (1987). The thickness of shear bands in granular materials. *Geotechnique*, 37(3):271–283.

[123] Needleman, A. (1988). Material rate dependence and mesh sensitivity in localization problems. *Computer Methods in Applied Mechanics and Engineering*, 67(1):69–85.

[124] Ng, A. K. L. and Small, J. C. (2000). Use of coupled finite element analysis in unsaturated soil problems. *Int. J. Numer. Anal. Meth. Geomech.*, 24(1):73–94.

[125] Nova, R., Castellanza, R., and Tamagnini, C. (2003). A constitutive model for bonded geomaterials subject to mechanical and/or chemical degradation. *Int. J. Numer. Anal. Meth. Geomech.*, 27(9):705–732.

[126] Nuth, M. and Laloui, L. (2008). Effective stress concept in unsaturated soils: clarification and validation of a unified framework. *Int. J. Numer. Anal. Meth. Geomech*, 32(7):771–801.

[127] Oda, M., Takemura, T., and Takahashi, M. (2004). Microstructure in shear band observed by microfocus X-ray computed tomography. *Geotechnique*, 54(8):539–542.

[128] Oliver, J., Huespe, A. E., and Samaniego, E. (2003). A study on finite elements for capturing strong discontinuities. *Int. J. Numer. Meth. Engng.*, 56(14):2135–2161.

[129] Oliver, J., Huespe, A. E., and Sánchez, P. J. (2006). A comparative study on finite elements for capturing strong discontinuities: E-FEM vs X-FEM. *Computer Methods in Applied Mechanics and Engineering*, 195(37):4732–4752.

[130] Paige, C. C. and Saunders, M. A. (1975). Solution of sparse indefinite systems of linear equations. *SIAM journal on numerical analysis*, 12(4):617–629.

[131] Papanicolopulos, S.-A., Zervos, A., and Vardoulakis, I. (2009). A three-dimensional C1 finite element for gradient elasticity. *International journal for numerical methods in engineering*, 77(10):1396–1415.

[132] Pardoen, B., Levasseur, S., and Collin, F. (2014). Using Local Second Gradient Model and Shear Strain Localisation to Model the Excavation Damaged Zone in Unsaturated Claystone. *Rock Mech Rock Eng*, 48(2):691–714.

[133] Peerlings, R., De Borst, R., Brekelmans, W., and De Vree, J. (1996). Gradient enhanced damage for quasi-brittle materials. *International Journal for numerical methods in engineering*, 39:3391–3403.

[134] Petera, J. and Pittman, J. F. T. (1994). Isoparametric Hermite elements. *Int. J. Numer. Meth. Engng.*, 37(20):3489–3519.

[135] Peters, W. and Ranson, W. (1982). Digital imaging techniques in experimental stress analysis. *Optical engineering*, 21(3):213427–213427.

[136] Piegl, L. and Tiller, W. (1997). *The NURBS Book*. Monographs in Visual Communication. Springer Berlin Heidelberg, Berlin, Heidelberg.

[137] Pijaudier-Cabot, G. and Bažant, Z. P. (1987). Nonlocal damage theory. *Journal of engineering mechanics*, 113(10):1512–1533.

[138] Pijaudier-Cabot, G. and Huerta, A. (1991). Finite element analysis of bifurcation in nonlocal strain softening solids. *Computer methods in applied mechanics and engineering*, 90(1-3):905–919.

[139] Regueiro, R. A. and Borja, R. I. (2001). Plane strain finite element analysis of pressure sensitive plasticity with strong discontinuity. *International Journal of Solids and Structures*, 38(21):3647–3672.

[140] Regueiro, R. A. and Foster, C. D. (2011). Bifurcation analysis for a rate-sensitive, non-associative, three-invariant, isotropic/kinematic hardening cap plasticity model for geomaterials: Part I. Small strain. *Int. J. Numer. Anal. Meth. Geomech.*, 35(2):201–225.

[141] Réthoré, J., Borst, R. d., and Abellan, M.-A. (2007a). A two-scale approach for fluid flow in fractured porous media. *Int. J. Numer. Meth. Engng.*, 71(7):780–800.

[142] Réthoré, J., Borst, R. d., and Abellan, M.-A. (2008). A two-scale model for fluid flow in an unsaturated porous medium with cohesive cracks. *Comput Mech*, 42(2):227–238.

[143] Réthoré, J., de Borst, R., and Abellan, M.-A. (2007b). A discrete model for the dynamic propagation of shear bands in a fluid-saturated medium. *Int. J. Numer. Anal. Meth. Geomech.*, 31(2):347–370.

[144] Rice, J. R. (1976). The localization of plastic deformation. In *in: WT Koiter (Ed.), Theoretical and Applied Mechanics*. Citeseer.

[145] Rudnicki, J. W. and Rice, J. R. (1975). Conditions for the localization of deformation in pressure-sensitive dilatant materials. *Journal of the Mechanics and Physics of Solids*, 23(6):371–394.

[146] Sabin, M. A. (1997). *Spline finite elements*. PhD Thesis, Ph. D. thesis, Leeds University, UK.

[147] Samaniego, E. and Belytschko, T. (2005). Continuum–discontinuum modelling of shear bands. *Int. J. Numer. Meth. Engng.*, 62(13):1857–1872.

[148] Schillinger, D., Evans, J. A., Reali, A., Scott, M. A., and Hughes, T. J. R. (2013). Isogeometric collocation: Cost comparison with Galerkin methods and extension to adaptive hierarchical NURBS discretizations. *Comp. Methods Appl. Mech. Engrg.*, 267:170–232.

[149] Schramm, U. and Pilkey, W. D. (1993). The coupling of geometric descriptions and finite elements using NURBs—A study in shape optimization. *Finite elements in analysis and design*, 15(1):11–34.

[150] Sciarra, G., dell'Isola, F., and Coussy, O. (2007). Second gradient poromechanics. *International Journal of Solids and Structures*, 44(20):6607–6629.

[151] Scott, M. A., Li, X., Sederberg, T. W., and Hughes, T. J. R. (2012). Local refinement of analysis-suitable T-splines. *Comp. Methods Appl. Mech. Engrg.*, 213–216:206–222.

[152] Sederberg, T. W., Cardon, D. L., Finnigan, G. T., North, N. S., Zheng, J., and Lyche, T. (2004). T-spline Simplification and Local Refinement. In *ACM SIGGRAPH 2004 Papers*, SIGGRAPH '04, pages 276–283, New York, NY, USA. ACM.

[153] Sederberg, T. W., Zheng, J., Bakenov, A., and Nasri, A. (2003). T-splines and T-NURCCs. In *ACM SIGGRAPH 2003 Papers*, SIGGRAPH '03, pages 477–484, New York, NY, USA. ACM.

[154] Sheng, D., Sloan, S., and Gens, A. (2004). A constitutive model for unsaturated soils: thermomechanical and computational aspects. *Computational Mechanics*, 33(6):453–465.

[155] Shu, J. Y., King, W. E., and Fleck, N. A. (1999). Finite elements for materials with strain gradient effects. *Int. J. Numer. Meth. Engng.*, 44(3):373–391.

[156] Sieffert, Y., Marinelli, F., and Chambon, R. (2011). Local Second Gradient Models for Thermo-Hydro-Mechanical Coupling in Rock Like Materials. In *9th International Workshop on Bifurcation and Degradation in Geomaterials*, volume 11 of *Geomechanics and Geoengineering*. Springer.

[157] Simo, J. and Oliver, J. (1994). A new approach to the analysis and simulation of strain softening in solids. *Fracture and damage in quasibrittle structures*, pages 25–39.

[158] Simo, J. C. and Hughes, T. J. R. (1998). *Computational Inelasticity*, volume 7 of *Interdisciplinary Applied Mathematics*. Springer-Verlag, New York.

[159] Simo, J. C., Oliver, J., and Armero, F. (1993). An analysis of strong discontinuities induced by strain-softening in rate-independent inelastic solids. *Computational mechanics*, 12(5):277–296.

[160] Simo, J. C. and Rifai, M. (1990). A class of mixed assumed strain methods and the method of incompatible modes. *International journal for numerical methods in engineering*, 29(8):1595–1638.

[161] Sleijpen, G. L., Van der Vorst, H. A., and Fokkema, D. R. (1994). BiCGstab (l) and other hybrid Bi-CG methods. *Numerical Algorithms*, 7(1):75–109.

[162] Sluys, L. J. and de Borst, R. (1992). Wave propagation and localization in a rate-dependent cracked medium—model formulation and one-dimensional examples. *International Journal of Solids and Structures*, 29(23):2945–2958.

[163] Smith, I. M., Griffiths, D. V., and Margetts, L. (2013). *Programming the Finite Element Method*. Wiley, Chichester, West Sussex, United Kingdom, 5 edition edition.

[164] Stankiewicz, A. (2007). *Numerical analysis of strain localization in one- and two-phase geomaterials*. PhD thesis, Cracow University of Technology.

[165] Sulem, J., Vardoulakis, I., Papamichos, E., Oulahna, A., and Tronvoll, J. (1999). Elasto-plastic modelling of Red Wildmoor sandstone. *Mechanics of Cohesive-frictional Materials*, 4(3):215–245.

[166] Tagliaferri, F., Waller, J., Andò, E., Hall, S. A., Viggiani, G., Bésuelle, P., and DeJong, J. T. (2011). Observing strain localisation processes in bio-cemented sand using x-ray imaging. *Granular Matter*, 13(3):247–250.

[167] Tamagnini, C., Castellanza, R., and Nova, R. (2002). A Generalized Backward Euler algorithm for the numerical integration of an isotropic hardening elastoplastic model for mechanical and chemical degradation of bonded geomaterials. *Int. J. Numer. Anal. Meth. Geomech.*, 26(10):963–1004.

[168] Tamagnini, C., Chambon, R., and Caillerie, D. (2001). A second gradient elastoplastic cohesive-frictional model for geomaterials. *Comptes Rendus de l'Académie des Sciences - Series IIB - Mechanics*, 329(10):735–739.

[169] Tamagnini, C. and Ciantia, M. O. (2016). Plasticity with generalized hardening: constitutive modeling and computational aspects. *Acta Geotech.*, 11(3):595–623.

[170] Tamagnini, C., Viggiani, G., and Chambon, R. (2000). A review of two different approaches to hypoplasticity. In *Constitutive Modelling of Granular Materials*, pages 107–145. Springer, Berlin, Heidelberg.

[171] Terzaghi, K. (1923). Die Berechnung der Durchlassigkeitsziffer des Tones aus dem Verlauf der hydrodyn. *Spannungsercsheinungen, Sitzber. Ak. Wiss. Wien, Abt. IIa*, 123.

[172] Toupin, R. A. (1962). Elastic materials with couple-stresses. *Archive for Rational Mechanics and Analysis*, 11(1):385–414.

[173] Van Den Eijnden, B. (2015). *Modélisation multi-échelle du comportement hydro-méchanique des roches argileuses.* PhD thesis, Grenoble Alpes.

[174] Van Eekelen, H. (1980). Isotropic yield surfaces in three dimensions for use in soil mechanics. *International Journal for Numerical and Analytical Methods in Geomechanics*, 4(1):89–101.

[175] Van Genuchten, M. T. (1980). A closed-form equation for predicting the hydraulic conductivity of unsaturated soils. *Soil science society of America journal*, 44(5):892–898.

[176] Vardoulakis, I. (1984). Rock bursting as a surface instability phenomenon. In *International Journal of Rock Mechanics and Mining Sciences & Geomechanics Abstracts*, volume 21, pages 137–144. Elsevier.

[177] Vardoulakis, I., Goldscheider, M., and Gudehus, G. (1978). Formation of shear bands in sand bodies as a bifurcation problem. *International Journal for numerical and analytical methods in Geomechanics*, 2(2):99–128.

[178] Vardoulakis, I. and Sulem, J. (1995). *Bifurcation analysis in geomechanics.* Hapman & Hall.

[179] Vázquez (2016). A new design for the implementation of isogeometric analysis in Octave and Matlab: GeoPDEs 3.0. *Computers and Mathematics with Applications*, 72:523–554.

[180] Veiga, L. B. d., Buffa, A., Sangalli, G., and Vázquez, R. (2014). Mathematical analysis of variational isogeometric methods. *Acta Numerica*, 23:157–287.

[181] Vermeer, P. A. and Verruijt, A. (1981). An accuracy condition for consolidation by finite elements. *Int. J. Numer. Anal. Meth. Geomech.*, 5(1):1–14.

[182] Verruijt, A. (2015). *Theory and problems of poroelasticity.* Delft University of Technology.

[183] Viggiani, G., Bésuelle, P., Hall, S., and Desrues, J. (2010). Sand deformation at the grain scale quantified through X-ray imaging. *Advances in Computed Tomography for Geomaterials: GeoX 2010*, pages 1–16.

[184] Vuong, A. V., Giannelli, C., Jüttler, B., and Simeon, B. (2011). A hierarchical approach to adaptive local refinement in isogeometric analysis. *Comp. Methods Appl. Mech. Engrg.*, 200(49–52):3554–3567.

[185] Wang, W., Sluys, L., and De Borst, R. (1997). Viscoplasticity for instabilities due to strain softening and strain-rate softening. *International Journal for Numerical Methods in Engineering 40 (20), 3839-3864.(1997).*

[186] Wheeler, S., Sharma, R., and Buisson, M. (2003). Coupling of hydraulic hysteresis and stress-strain behaviour in unsaturated soils. *Géotechnique*, 53(1):41–54.

[187] Zervos, A. (2008). Finite elements for elasticity with microstructure and gradient elasticity. *Int. J. Numer. Meth. Engng.*, 73(4):564–595.

[188] Zervos A., Papanicolopulos S.-A., and Vardoulakis I. (2009). Two Finite-Element Discretizations for Gradient Elasticity. *Journal of Engineering Mechanics*, 135(3):203–213.

[189] Zhang, H. W. and Schrefler, B. A. (2000). Gradient-dependent plasticity model and dynamic strain localisation analysis of saturated and partially saturated porous media: one dimensional model. *European Journal of Mechanics - A/Solids*, 19(3):503–524.

Appendix A

Calculation of $\frac{\partial \gamma^{eH}_{ijk}}{\partial \gamma^{e}_{abc}}$ and $\frac{\partial \gamma^{eD}_{ijk}}{\partial \gamma^{e}_{abc}}$

Calculation of $\partial \gamma^{eH}_{ijk} / \partial \gamma^{e}_{abc}$

$$P_{ijkabc} = \frac{\partial \gamma^{eH}_{ijk}}{\partial \gamma^{e}_{abc}} \tag{A.1a}$$

$$= \frac{\partial}{\partial \gamma^{e}_{abc}} \left\{ \frac{1}{4} (\delta_{i} j \gamma^{e}_{ppl} + \delta_{ik} \gamma^{e}_{ppj}) \right\} \tag{A.1b}$$

$$= \frac{1}{4} \delta_{ij} \frac{\partial \gamma^{e}_{ppk}}{\partial \gamma^{e}_{abc}} + \frac{1}{4} \delta_{ik} \frac{\partial \gamma^{e}_{ppj}}{\partial \gamma^{e}_{abc}} \tag{A.1c}$$

Eq. A.1c is symmetric in j and k. We have

$$\frac{\partial \gamma^{e}_{ppk}}{\partial \gamma^{e}_{abc}} = \delta_{ab} \delta_{kc} \tag{A.2a}$$

$$\frac{\partial \gamma^{e}_{ppj}}{\partial \gamma^{e}_{abc}} = \delta_{ab} \delta_{jc} \tag{A.2b}$$

Equations A.2a and A.2b are not symmetric in b and c. These two terms will produce non-minor symmetric hyperstress tensors Σ. In order to restore symmetry, the definition of $\boldsymbol{\gamma}^{eH}$ is changed as follows:

$$\tilde{\gamma}^{eH}_{ijk} = \frac{1}{8} \left\{ \delta_{ij} \gamma^{e}_{ppk} + \delta_{ik} \gamma^{e}_{ppj} + \delta_{ij} \gamma^{e}_{pkp} + \delta_{ik} \gamma^{e}_{pjp} \right\} \tag{A.3}$$

and, consequently:

$$\tilde{\gamma}_{ijk}^{eD} = \gamma_{ijk}^{e} - \tilde{\gamma}_{ijk}^{eH} \tag{A.4a}$$

$$\tilde{\Psi}_g = \frac{1}{2} G \left\{ l_H^2 \tilde{I}_H^e + l_D^2 \tilde{I}_D^e \right\} \tag{A.4b}$$

$$\tilde{I}_H^e = \tilde{\gamma}_{ijk}^{eH} \tilde{\gamma}_{ijk}^{eH} \tag{A.4c}$$

$$\tilde{I}_D^e = \tilde{\gamma}_{ijk}^{eD} \tilde{\gamma}_{ijk}^{eD} \tag{A.4d}$$

$$\Sigma_{abc} = G \left\{ l_H^2 \tilde{\gamma}_{ijk}^{eH} \frac{\partial \tilde{\gamma}_{ijk}^{eH}}{\partial \gamma_{abc}^{e}} + l_D^2 \tilde{\gamma}_{ijk}^{eD} \frac{\partial \tilde{\gamma}_{ijk}^{eD}}{\partial \gamma_{abc}^{e}} \right\} \tag{A.5}$$

Calculation of $\partial \tilde{\gamma}_{ijk}^{eH} / \partial \gamma_{abc}^{e}$

$$P_{ijkabc} = \frac{\partial \tilde{\gamma}_{ijk}^{eH}}{\partial \gamma_{abc}^{e}} \tag{A.6a}$$

$$= \frac{1}{8} \left\{ \delta_{ij}\delta_{ab}\delta_{kc} + \delta_{ik}\delta_{ab}\delta_{jc} + \delta_{ij}\delta_{ac}\delta_{bk} + \delta_{ik}\delta_{ac}\delta_{jb} \right\} \tag{A.6b}$$

Calculation of $\partial \tilde{\gamma}_{ijk}^{eD} / \partial \gamma_{abc}^{e}$

$$Q_{ijkabc} = \frac{\partial \tilde{\gamma}_{ijk}^{eD}}{\partial \gamma_{abc}^{e}} \tag{A.7a}$$

$$= \frac{\partial \gamma_{ijk}^{e}}{\partial \gamma_{abc}^{e}} - \frac{\partial \tilde{\gamma}_{ijk}^{eH}}{\partial \gamma_{abc}^{e}} \tag{A.7b}$$

$$= \delta_{ia}\delta_{jb}\delta_{kc} - P_{ijkabc} \tag{A.7c}$$

Calculation of $\tilde{\gamma}^{eH}_{ijk} P_{ijkabc}$:

$$
\begin{aligned}
M_{ijkabc} =& \tilde{\gamma}^{eH}_{ijk} P_{ijkabc} && \text{(A.8a)}\\
=& \frac{1}{8}\left\{\delta_{ij}\gamma^{e}_{ppk} + \delta_{ik}\gamma^{e}_{ppj} + \delta_{ij}\gamma^{e}_{pkp} + \delta_{ik}\gamma^{e}_{pjp}\right\}\\
& \frac{1}{8}\left\{\delta_{ij}\delta_{ab}\delta_{kc} + \delta_{ik}\delta_{ab}\delta_{jc} + \delta_{ij}\delta_{ac}\delta_{bk} + \delta_{ik}\delta_{ac}\delta_{jb}\right\} && \text{(A.8b)}\\
=& \frac{1}{64}\big\{3\gamma^{e}_{ppc}\delta_{ab} + \gamma^{e}_{ppc}\delta_{ab} + 3\gamma^{e}_{ppb}\delta_{ac} + \gamma^{e}_{ppb}\delta_{ac}\\
& + \gamma^{e}_{ppc}\delta_{ab} + 3\gamma^{e}_{ppc}\delta_{ab} + \gamma^{e}_{ppb}\delta_{ac} + 3\gamma^{e}_{ppb}\delta_{ac}\\
& + 3\gamma^{e}_{pcp}\delta_{ab} + \gamma^{e}_{pcp}\delta_{ab} + 3\gamma^{e}_{pbp}\delta_{ac} + \gamma^{e}_{pbp}\delta_{ac}\\
& + \gamma^{e}_{pcp}\delta_{ab} + 3\gamma^{e}_{pcp}\delta_{ab} + \gamma^{e}_{pbp}\delta_{ac} + 3\gamma^{e}_{pbp}\delta_{ac}\big\} && \text{(A.8c)}\\
=& \frac{1}{64}\left\{8\gamma^{e}_{ppc}\delta_{ab} + 8\gamma^{e}_{ppb}\delta_{ac} + 8\gamma^{e}_{pcp}\delta_{ab} + 8\gamma^{e}_{pbp}\delta_{ac}\right\} && \text{(A.8d)}
\end{aligned}
$$

Calculation of $\tilde{\gamma}^{eD}_{ijk} P_{ijkabc}$:

$$
\begin{aligned}
N_{abc} =& \tilde{\gamma}^{eD}_{ijk} P_{ijkabc} && \text{(A.9a)}\\
=& (\gamma^{e}_{ijk} - \tilde{\gamma}^{eH}_{ijk}) P_{ijkabc} && \text{(A.9b)}\\
=& \gamma^{e}_{ijk} P_{ijkabc} - M_{abc} && \text{(A.9c)}\\
=& \gamma^{e}_{ijk} P_{ijkabc} - \tilde{\gamma}^{eH}_{abc} && \text{(A.9d)}
\end{aligned}
$$

And since:

$$
\begin{aligned}
\gamma^{e}_{ijk} P_{ijkabc} =& \gamma^{e}_{ijk} \frac{1}{8}\left(\delta_{ij}\delta_{ab}\delta_{kc} + \delta_{ik}\delta_{ab}\delta_{jc} + \delta_{ij}\delta_{ac}\delta_{bk} + \delta_{ik}\delta_{ac}\delta_{jb}\right) && \text{(A.10a)}\\
=& \frac{1}{8}\left\{\gamma^{e}_{iic}\delta_{ab} + \gamma^{e}_{ici}\delta_{ab} + \gamma^{e}_{iib}\delta_{ac} + \gamma^{e}_{ibi}\delta_{ac}\right\} && \text{(A.10b)}\\
=& \tilde{\gamma}^{eH}_{abc} && \text{(A.10c)}
\end{aligned}
$$

we have:

$$
N_{abc} = \tilde{\gamma}^{eH}_{abc} - \tilde{\gamma}^{eH}_{a} bc = 0 \qquad \text{(A.11)}
$$

Collecting the results A.6, A.8 and A.11 into eq. A.5 we obtain:

$$
\begin{aligned}
\Sigma_{abc} =& G\left\{l^2_H \tilde{\gamma}^{eH}_{abc} + l^2_D \tilde{\gamma}^{eD}_{ijk}\left(\delta_{ia}\delta_{jb}\delta_{kc} - P_{ijkabc}\right)\right\} && \text{(A.12a)}\\
=& G\left\{l^2_H \tilde{\gamma}^{eH}_{abc} + l^2_D \tilde{\gamma}^{eD}_{abc}\right\} && \text{(A.12b)}
\end{aligned}
$$

Elastic hyperstiffness matrix:

$$(\boldsymbol{D}_{sg}^{e})_{ijkabc} = \frac{\partial \Sigma_{ijk}}{\partial \gamma_{abc}^{e}} \tag{A.13a}$$

$$= Gl_H^2 \frac{\partial \tilde{\gamma}_{ijk}^{eH}}{\partial \gamma_{abc}^{e}} + Gl_D^2 \frac{\partial \tilde{\gamma}_{ijk}^{eD}}{\partial \gamma_{abc}^{e}} \tag{A.13b}$$

$$= Gl_H^2 \frac{\partial \tilde{\gamma}_{ijk}^{eH}}{\partial \gamma_{abc}^{e}} + Gl_D^2 \frac{\partial}{\partial \gamma_{abc}^{e}} \{\gamma_{ijk}^{e} - \tilde{\gamma}_{ijk}^{eH}\} \tag{A.13c}$$

$$= G(l_H^2 - l_D^2) \frac{\partial \tilde{\gamma}_{ijk}^{eH}}{\partial \gamma_{abc}^{e}} + Gl_D^2 (\delta_{ia}\delta_{jb}\delta_{kc}) \tag{A.13d}$$

$$(\boldsymbol{D}_{sg}^{e})_{ijkabc} = \frac{1}{8} G(l_H^2 - l_D^2)\{\delta_{ij}\delta_{ab}\delta_{kc} + \delta_{ik}\delta_{ab}\delta_{jc} + \delta_{ij}\delta_{ac}\delta_{bk} + \delta_{ik}\delta_{ac}\delta_{jb}\} + Gl_D^2(\delta_{ia}\delta_{jb}\delta_{kc}) \tag{A.14}$$